Part 2 – Detailed Report

Pool Fund Study TPF-5-297

Led by the Oklahoma DOT

Bahaa N. Abdelrahman, M. Tyler Ley, Lichun Chen, Hope Becker, Amir Behravan, Guoliang Fan, Nicholas F. Materer, Jair Simon, Andrew Young

Oklahoma State University

Stillwater, Oklahoma

Rita M. Ghantous, K. Zetterberg, O. Burkan Isgor, W. Jason Weiss

Oregon State University

Corvallis, Oregon

December 2025

Table of Contents

The Influence of Air Voids and Fluid Absorption on Salt-Induced Calcium Oxychloride Damage

Quantifying Calcium Oxychloride Formation Using Micro-Computed Tomography

Field-Based Measurement of Freeze–Thaw Damage in Cementitious Materials

Predicting Concrete Freeze–Thaw Damage with Weather Data-Based Machine Learning

Creating Maps of Freeze–Thaw Exposure Based for Concrete

The Effects of Concrete Temperature on Air Void Parameters in Pumped Concrete

.

The Influence of Air Voids and Fluid Absorption on Salt-Induced Calcium Oxychloride Damage

Rita M. Ghantous[1], Keegan Zetterberg[1], Hope Hall Becker[2], Amir Behravan[2], M. Tyler Ley[2], O. Burkan Isgor[1], and W. Jason Weiss[1]

[1]School of Civil and Construction Engineering, Oregon State University, 1491 SW Campus Way, Corvallis, OR 97331, USA

{ritamaria.ghantous; zetterbk; Burkan.Isgor ; Jason.Weiss}@oregonstate.edu

[2]Oklahoma State University, Department of Civil and Environmental Engineering, Stillwater, OK 74078, USA

{hhall; tyler.ley}@okstate.edu

Abstract

Calcium and magnesium deicing salts may damage concrete due to calcium oxychloride formation (CaOXY). Previous work has shown that replacing a portion of the cement in a mixture with supplementary cementitious materials reduce CaOXY formation. AASHTO PP-84 was developed to help specify damage-resistant mixtures by limiting the CaOXY amount in paste. This limit was established based on empirical observations; however, this did not consider other aspects of the mixture such as paste volume or air content. This paper investigates how fluid absorption, paste volume, and air content are all key parameters in determining damage from CaOXY. Concrete with a higher paste volume has more CaOXY and is more susceptible to damage. Concrete with a higher air content is less susceptible to damage as the voids provide space for fluid absorption and CaOXY formation; however this only occurs for mixtures with a specific range of calcium hydroxide ($Ca(OH)_2$) (between 7 and 12 g $Ca(OH)_2$/100g paste). This paper incorporates these factors to provide a more comprehensive explanation for CaOXY-induced damage in concrete.

Keywords: Deicing salts, calcium chloride, calcium oxychloride, salt damage, air void content, concrete pavements.

Introduction

Some portland cement concrete pavements (PCCP) have exhibited premature deterioration at the joints [1-5]. This distress has been related to the accumulation of fluid in the joints that contains deicing chemicals specifically in the form of calcium and/or magnesium chloride [1-5]. When the salt concentration is low, this fluid can increase the degree of saturation and increase the potential for freezing and thawing damage [6-10]. As the salt concentration increases, the accumulating fluid can result in the formation of several solid phases such as Friedel's salt (FS), Kuzel's salt, and calcium oxychloride (CaOXY) [11-23].

Calcium monosulfoaluminate present in the cementitious paste ($C_4A\bar{S}H_{12}$) reacts with the chloride ions (Cl^-) to form FS ($C_3A.CaCl_2.H_{10}$) (equation (1)) [20, 24-26]. The release of sulfate ions (SO_4^{2-}) when Friedel's salt forms can react with the remaining calcium monosulfualuminate to form secondary ettringite (SE) ($C_6A\bar{S}_3H_{32}$) (Equation (2)) [20, 24-26].

$$C_4A\bar{S}H_{12} + 2Cl^- \rightarrow C_3A.CaCl_2.H_{10} + SO_4^{2-} \quad (1)$$

$$C_4A\bar{S}H_{12} + 2{SO_4}^{2-} \rightarrow C_6A\bar{S}_3H_{32} \quad (2)$$

Equation (3) describes the chemical reaction that occurs when calcium hydroxide ($Ca(OH)_2$) reacts with the salt solution ($CaCl_2 + H_2O$) to form CaOXY [27-38]. Various forms of CaOXY have been reported in the literature [22, 39-42]; however, the form shown in equation (3) ($3Ca(OH)_2.CaCl_2.12H_2O$) has been widely reported as responsible for concrete deterioration [6, 7, 12, 14, 18-20, 24, 42-50].

$$3\,Ca(OH)_2 + CaCl_2 + 12\,H_2O \rightleftharpoons 3Ca(OH)_2.CaCl_2.12H_2O \quad (3)$$

Equation (3) is a reversible phase change that is dependent on the temperature and the $CaCl_2$ content as illustrated in Figure 1 [51]. The dashed line in Figure 1 is the liquidus line for CaOXY. For a given $CaCl_2$ concentration, when the temperature is above the dashed line the system is a fluid and there is no CaOXY present. When the temperature falls below the liquidus line, a phase change occurs and solid CaOXY begins to form. This occurs at temperatures

above freezing (i.e., the solid lines shown in Figure 1). For instance, Figure 1 shows that with $CaCl_2$ concentrations of 10%, solid CaOXY forms at approximately room temperature.

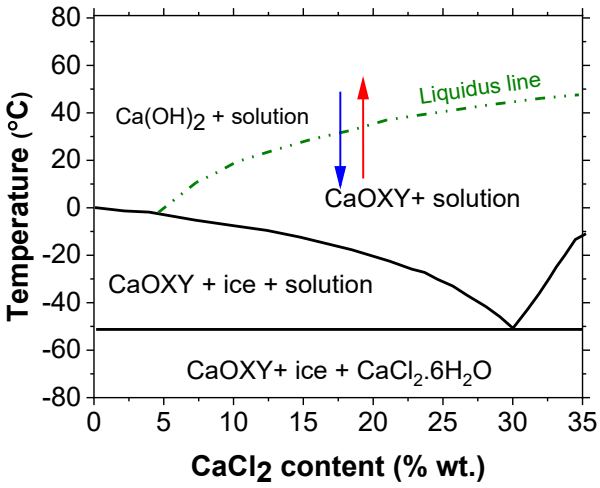

Figure 1- Phase isopleth of $Ca(OH)_2$-$CaCl_2$-H_2O [51]

CaOXY is particularly problematic since its volume is 303% larger than the volume of $Ca(OH)_2$ [45, 47, 48]. This expansion can cause pressure that may exceed the tensile strength of the paste, which often results in damage [14, 23, 52-54]. Qiao et al. [55] demonstrated measurements that showed that CaOXY formation induced a decrease in volume during the phase change to a solid (i.e., cooling), followed by a volume increase when CaOXY went through a phase change from solid to liquid during heating (Figure 1). This is important as it indicates that damage is less likely to occur on cooling than heating. Further, this indicates that the reason of damage development may be more complicated than a simple volume change. Previous studies [15, 48] showed that damage development increased when the samples were immersed in salt solution and less damage occurred for samples not in solution [48]. However, a full explanation of the role of immersion in fluid on damage development was not provided in those studies. As such, it is essential to understand the role that access to fluid has in salt damage development and this work attempt to provide insight into the role that submersion in fluid plays.

Several approaches have been recommended to reduce the potential for CaOXY-induced damage. The vast majority of these approaches outline reducing the formation of CaOXY. For example, one approach is to use supplementary cementitious materials (SCM) that reduce $Ca(OH)_2$ content to levels where damage is reduced or eliminated [56-62]. Another approach

is to use topical treatments [33, 63-65] to provide a barrier between the $Ca(OH)_2$ and the deicing salts. A third approach is to carbonate the concrete [66, 67] which reduces CaOXY due to both a reaction that reduces the $Ca(OH)_2$ and the formation of a barrier around the $Ca(OH)_2$. A fourth approach is to reduce the paste content of concrete, which reduces the $Ca(OH)_2$ and thus CaOXY [64]; however, a specific amount of paste reduction was not recommended. Current specifications have focused on limiting the CaOXY content to 15g per 100g of paste based on empirical evidence [57] as measured using low temperature differential scanning calorimetry according to AASHTO T-365. It has been speculated that air may reduce damage and some experimental evidence has been gathered to confirm this speculation but this has not been fully confirmed [68]. Further, the CaOXY specification limit was established empirically and was assumed to not depend on the paste content, air content, or other aspects of the mixture. These approaches do not identify the air content that is necessary to accommodate the CaOXY formation and delay the onset of damage. Research is needed to examine this hypothesis and to develop approaches to quantify this effect.

This paper examines three factors to determine their influence on the potential CaOXY-induced damage: First, a series of experiments are performed to evaluate the hypothesis that fluid absorption is a critical part of CaOXY damage development. If validated, this has a practical implication on the use of topical treatments to limit fluid ingress as a potential solution for CaOXY-induced damage. In addition, this would open the possibility that CaOXY-induced damage requires cumulative fluid absorption (i.e., repeated CaOXY formation through heating and cooling cycles). Second, the paper examines whether concrete with a higher air content is less susceptible to damage and whether a higher air-to-paste content ratio will lead to lower salt induced damage. The hypothesis is based on the fact that the voids would permit more space for fluid absorption and CaOXY formation with reduced damage (i.e., concrete with higher air content has a lower degree of saturation). While the current AASHTO PP-84 limit on the amount of CaOXY that can form is a strong first step to limiting damage, if damage is dependent on the ratio of air content to paste content, this would indicate that this threshold may be able to be modified based on concrete mixture design.

Experimental Procedure

Materials

Type I ordinary portland cement (OPC - ASTM C150 - 19a) and Class C fly ash (FA) (ASTM C618) were used. The physical and chemical properties of the cement and FA are described in Table 1. The reactivity of the FA was 27.47% as measured using the Pozzolanic Reactivity Test [69]. The Blaine finesses of the cement was 386 m^2/kg. Natural river sand was used as a fine aggregate. The natural sand had a specific gravity of 2.61 and an absorption of 0.44%. Two coarse aggregates were used in this study with specific gravity of 2.75 and 2.72, an absorption of 0.73% and a maximum size of 19.1 mm. A wood rosin air-entraining admixture (AEA) was added to the mixtures.

Mixture preparation, sample curing and sample conditioning

Twelve different concrete mixtures were prepared, with varying air void and $Ca(OH)_2$ content. The $Ca(OH)_2$ content was varied by varying the FA content (0, 20, 25, 30, 35, 40% replacement levels by mass). For each fly ash replacement level, two different air void content were targeted: low air void content (~2%) and high air void content (~5%). The paste content was kept constant for mixtures with different air void content. The water-to-binder ratio for all mixtures is equal to 0.45. The fresh concrete was mixed using the procedure described in [70]. The Sequential Air Method (SAM) number was used to indicate the air void quantity and quality (air void content, size, and spacing) based on AASHTO TP 118-17 [70-72]. The mixture characteristics are shown in Table 2. The mortar was obtained from the fresh concrete by removing the coarse aggregates by wet sieving according to ASTM C172-17. Wet sieving was done by hand in less than 10 minutes. The concrete was placed on a #4 sieve (4.76 mm) and the large aggregates were removed. Next, the remaining material was pushed through the openings. It should be noted that a small loss in air content (averaged to 0.5% when the air content is determined by pressure [73]) was caused by wet sieving as mentioned in ASTM C172-17. The air content in mortar is listed in Table 2. Please note that in all the figures of this manuscript, the air content of the parent concrete will be displayed. The mortar was cast in cylindrical plastic molds of 102 mm (4 inches) in diameter and 203 mm in height (8 inches). The mortar was cured in the molds (i.e., under sealed conditions) for 91 days at 23 ± 2°C.

Table 1. Properties of the cement used in this study

Cement Oxides	Type I cement (OPC)	Class C fly ash
	Percent by mass (%)	Percent by mass (%)
Silicon Dioxide (SiO_2)	21.10	27.04
Aluminum Oxide (Al_2O_3)	4.70	18.11
Ferric Oxide (Fe_2O_3)	2.60	4.56
Calcium Oxide (CaO)	62.10	30.51
Magnesium Oxide (MgO)	2.40	6.36
Sulfur Trioxide (SO_3)	3.20	2.56
Sodium Oxide (Na_2O)	0.20	2.73
Potassium Oxide (K_2O)	0.30	1.07
Loss on Ignition (LOI)	2.70	0.12
Bogue phase composition	Percent by mass (%)	
Tricalcium Silicate (C_3S)	56.70	-
Dicalcium Silicate (C_2S)	17.80	-
Tricalcium Aluminate (C_3A)	8.20	-
Tetracalcium Aluminoferrite (C_4AF)	7.80	-
Specific gravity	3.15	2.74

Table 2. The mixture proportions and fresh properties of the concrete mixtures

Mixture	CA* (kg/m^3)	Sand (kg/m^3)	Cement (kg/m^3)	FA* (kg/m^3)	Water (kg/m^3)	AEA (g/m^3)	A_C* (%)	A_m* (%)	SAM number	A/P* (%)
1	1161	754	340	0.0	153	2.7	2.6	4.5	0.51	9.9
2	1123	729	329	0.0	148	16.7	5.8	9.8	0.13	22.9
3	1120	729	296	74	167	1.6	2.6	4.3	0.35	9.0
4	1088	707	287	72	162	5.2	5.4	9.0	0.16	19.4
5	1105	722	274	91	165	3.0	2.1	3.6	0.66	7.5
6	1048	685	260	87	156	11.0	7.2	11.9	0.10	26.5
7	1107	723	257	110	165	2.5	1.8	3.14	0.63	6.4
8	1064	695	247	106	159	10.6	5.7	9.5	0.13	20.6
9	1104	721	238	128	165	2.9	2.0	3.4	0.55	6.9
10	1046	683	225	121	156	10.8	7.1	11.8	0.10	26.2
11	1117	724	222	147	166	2.2	2.6	4.3	0.57	8.9
12	1079	700	214	142	160	5.8	5.9	9.7	0.10	20.9

CA is coarse aggregate, FA is fly ash, A_C is the air content in concrete, A_m is the air content in mortar, A/P is the air to paste content ratio

After curing, the mortar samples were demolded and cut using a water-cooled diamond saw into slabs before being cored to cylinders with 10 mm diameter and 30 mm heights. These cylinders edges were then trimmed using a precision diamond saw that was water cooled in order to have parallel surfaces as described in [74]. The final dimensions of the cylindrical cores are 10 mm in diameter and 20 mm in height. The cores were thereafter exposed to 60°C temperature until reaching a constant mass (mass evolution over 24 hours is less than 0.01%). The change in the microstructure of the samples after drying was not assessed in this study. The samples were then vacuum saturated with lime-water solution under a vacuum pressure of 0.8 MPa according to AASHTO 1.6a. The mortar cores were immersed in lime solution for an additional 24 hours at 23 ± 2°C. They were then kept immersed in lime solution at 50 ± 1°C for an additional 24 hours. The samples were removed from the lime solution and placed directly in 20% $CaCl_2$ solution that was equilibrated at 50 ± 1°C for an additional 24 hours. The immersion in salt solution at 50°C was to allow the saturation of the pores of the mortar cores with chloride ions without the formation of CaOXY [55] (as illustrated in Figure 1, where values above the liquidus lines are solutions without CaOXY). During the immersion of the samples in salt solution at 50°C, the chloride ions diffused through the pore solution until reaching equilibrium. The uniformity of the chloride profiles throughout the cross section of

the sample was confirmed using EDAX Orbis micro X-ray fluorescence (mXRF) spectroscopy [75].

Salt damage testing procedure

After the saturation, the samples were exposed to 15 temperature cycles from 50°C to 5°C as illustrated in Figure 2. At the end of each temperature cycle, the samples were kept at 50°C for a duration of 30 minutes. It should be noted that the temperature of the samples remained above the solidus temperature as well as above freezing (-20°C for a 20% $CaCl_2$ solution by weight) as shown in Figure 1. Consequently, any damage that is observed is primarily caused by the formation of CaOXY and not by ice formation. As stated in the introduction, Equation (3) is completely reversible and thus CaOXY is expected to undergo a phase change forming a solid when the temperature is reduced below the liquidus line and then forming a liquid again when the temperature is raised above the liquidus line (Figure 1). According to Figure 1, at 50°C the pores of the samples will be filled with dissolved $Ca(OH)_2$ and salt solution, and at 5°C CaOXY will solidify and form in the pores of concrete.

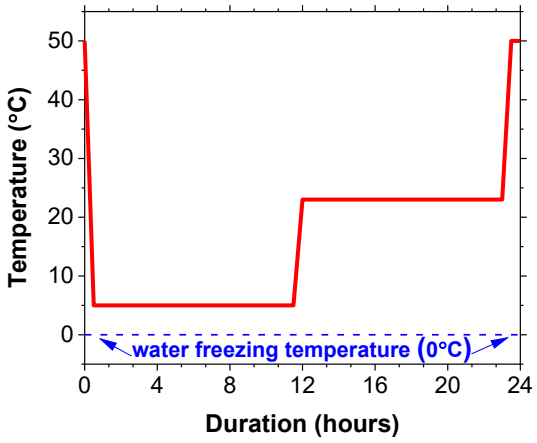

Figure 2- Temperature cycle during the salt damage testing

Three conditions were tested as illustrated in Figure 3.

- Condition #1 (Figure 3(a)): samples were saturated by 20% $CaCl_2$ solution and exposed to temperature cycling while being immersed in 20% $CaCl_2$ solution. This condition was used to study the impact of fluid absorption and air void content on salt damage development in mortar samples.

- Condition #2 (Figure 3(b)): Samples were saturated by 20% $CaCl_2$ solution and exposed to temperature cycling while wrapped in aluminum tape. This was done to limit moisture evaporation and not allow solution to enter the samples during the cycles. The impact of fluid absorption on salt damage development can be determined by comparing the damage on samples exposed to this condition with the one measured on samples exposed to condition # 1.
- Condition #3 (Figure 3(c)): samples were only saturated with lime-water solution without any salt exposure and exposed to temperature cycling while being immersed in lime solution. The samples in this condition were used as a control sample where no salt damage is expected.

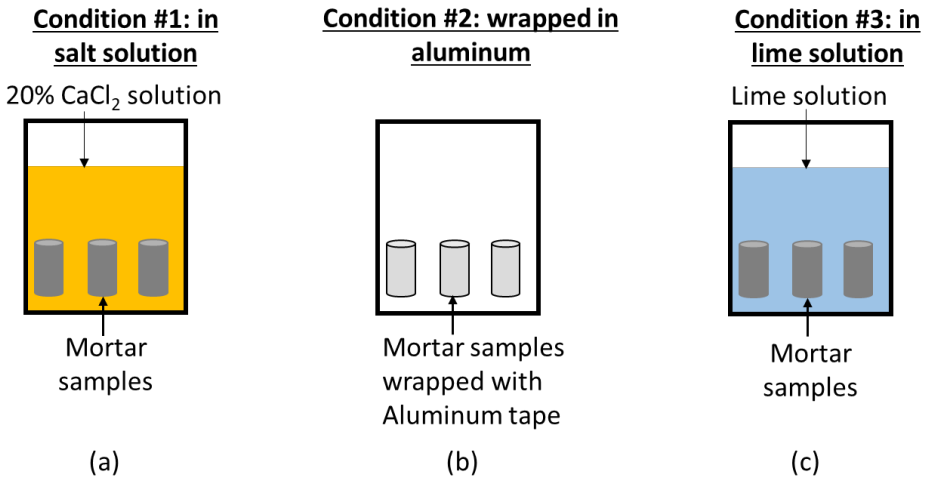

Figure 3- Testing conditions during temperature cycling (a) in salt solution, (b) wrapped in aluminium, (c) in lime solution

The length change of the cores was measured using a micrometer with 2.54 µm resolution at the beginning and end of each cycle. The residual strain was then calculated according to equation (4):

$$\varepsilon = \frac{l - l_0}{l_0} \tag{4}$$

where, ε is the residual strain, l is the length of the sample at the end of each cycle, l_0 is the initial length of the sample. A positive residual strain value indicates expansion which is likely due to damage development as shown in earlier studies [74, 76-78].

The mass was measured at each cycle and the change in mass was determined using equation (5).

$$\Delta M = \frac{M - M_0}{M_0} \quad (5)$$

where, ΔM is the change in mass, M is the mass of the sample during the test, M_0 is the initial mass of the sample.

A visual inspection for the mortar cores was also performed at the end of each temperature cycle in order to investigate the development of cracks. The samples were imaged using a camera at the beginning of the test and during the test in order to provide a qualitative comparison of the damage between different samples.

CaOXY content determination

The CaOXY content was measured using the Low-Temperature Differential Scanning Calorimetry (LT-DSC) according to the procedure for mortar defined in [79] and in AASHTO T365. A portion of the central part of the mortar cylinder (102 mm in diameter and 203 mm in height) was ground using a lathe grinder. The collected powder was then sieved through a 75 µm sieve. The particles that did not pass the sieve were ground using a mortar and pestle to pass through the 75 µm sieve. 20 mg of the ground powder was then mixed in a high volume stainless steel pan with 5 mg of 20% $CaCl_2$ solution according to the procedure defined in [79]. The pan was then sealed and subjected to temperature cycling inside the low-temperature differential scanning calorimetry (LT-DSC). The temperature was kept constant at 25°C for 60min, and then decreased to -90°C at 3°C/min rate; this was followed by a temperature loop from -90°C to -70°C to -90°C at the same rate. The temperature was then increased at 0.25°C/min up to 50°C [80]. The amount of CaOXY was quantified according to equation (6).

$$M_{CaOXY} = \frac{L}{L_0} \quad (6)$$

where, M_{CaOXY} is the amount of CaOXY (g/g_{mortar}), L is the latent heat measured during the phase transition of CaOXY at a temperature around 30°C, L_0 is 186 J/g which is the latent heat of pure CaOXY. For each mixture design, three LT-DSC tests were performed from the ground powder. The average and standard deviation values of CaOXY content were then calculated from these three tests for each mixture.

$Ca(OH)_2$ content determination

Thermo-gravimetric analysis (TGA) was performed to determine the amount of $Ca(OH)_2$ using the mass loss of the sample between 400°C and 500°C. For each mixture design, a small

powder sample (35-50 mg) was collected from the powder that was sieved through the 75 µm sieve as described previously [79]. This powder sample was oven dried at 105°C, placed in a platinum crucible, and then loaded into the TGA Q50 TA instrument. The sample was first kept at an isothermal condition (23°C) for 3 min and then heated up to 990°C at 10°C/min under a nitrogen purge.

$Ca(OH)_2$ content was calculated using equation (7) [81].

$$M_{Ca(OH)_2} = \frac{74.1}{18} \times \frac{M^S_{Start} - M^S_{end}}{M_0} \quad (7)$$

where, $M_{Ca(OH)_2}$ is the $Ca(OH)_2$ content (g/g_{mortar}), M^S_{Start} and M^S_{end} are the sample masses (g) recorded at the start point and the end point of decomposition of $Ca(OH)_2$, respectively [81], and M_0 is the mass of the mortar powder used during the TGA test. For each mixture design, three TGA tests were performed from the ground powder. The average and standard deviation values of $Ca(OH)_2$ content were then calculated from these three tests for each mixture.

Theoretical calculations

Thermodynamic modeling

Thermodynamic modeling was used to determine the volume of hydration products, mainly calcium monosulfoaluminate and $Ca(OH)_2$, that form in the mixture designs listed in Table 2 [82]. Once the $Ca(OH)_2$ content and calcium monosulfoaluminate content are known for each mixture, the filling of air voids by FS, SE, and CaOXY can be calculated using the procedures described later in this paper. The thermodynamic calculations are done using GEMS3K [83] which uses the Gibbs free energy minimization technique to determine the reaction products for a given set of inputs compositions and mixture proportions. CemData v18.01 [84] and PSI/Nagra [85] databases are used in conjunction with the GEMS3K for the calculation of reaction products of cementitious systems. These calculations provide the amounts of solid, aqueous, and gaseous species that form in these reactions, including key compositions for this work such as $Ca(OH)_2$ and calcium monosulfoaluminate.

The prediction of hydration products using thermodynamic modeling and kinetic model has been validated in several studies in the literature for both ordinary plain cement systems (OPC)

[86-88] and OPC+SCM cementitious systems [84, 89-92]. In order to determine the hydration products at 91 days of sealed curing, the mass fraction of oxide phases that dissolve from the FA was considered to be equal to the reactivity of the FA (27.47% as measured using the Pozzolanic Reactivity Test [69]) [84, 89-92]. The mass of alkali oxides (Na_2O, K_2O, MgO, SO_3) that dissolve from OPC was calculated based on the clinker dissolution as described in [93]. The Modified Parrot-Killoh kinetic model [82] was used to calculate the mass fractions of clinker phases (C_3S, C_2S, C_3A, C_4AF) that dissolves from OPC.

Volume of void filling due to FS and SE

The volume of void filling due to calcium monosulfualuminate consumption was determined using equation (8).

$$V_1 = (V_{\mathrm{FS}} + V_{\mathrm{SE}}) - (V_{\mathrm{Afm,r1}} + \mathrm{V_{Afm,r2}}) \quad (8)$$

where, V_1 is the volume of void reduction induced by FS and SE, $V_{\mathrm{Afm,r1}}$ is the volume of calcium monosulfoaluminate that reacted to form FS according to equation (1), $V_{\mathrm{Afm,r2}}$ is the volume of monosulfoaluminate that reacted to form SE according to equation (2). V_{FS} and V_{SE} are the volume of FS and SE respectively.

Using equation (1) and equation (2), the volume of FS and SE can be determined as a function of $V_{\mathrm{Afm,r1}}$, and $V_{\mathrm{Afm,r2}}$ according to equation (9) and (10) respectively.

$$V_{\mathrm{FS}} = \frac{\frac{\rho_{\mathrm{Afm}} \cdot V_{Afm,r1}}{M_{\mathrm{Afm}}} M_{\mathrm{FS}}}{\rho_{\mathrm{FS}}} = 0.88\, V_{Afm,r1} \quad (9)$$

$$V_{\mathrm{SE}} = \frac{\frac{\rho_{Afm} \cdot V_{Afm,r2}}{M_{\mathrm{Afm}}} M_{\mathrm{SE}}}{\rho_{\mathrm{SE}}} = 2.28\, V_{\mathrm{Afm,r2}} \quad (10)$$

where, ρ_{Afm} is the density of calcium monosulfomaluminate (2.015 g/cm^3), M_{Afm} is the molar mass of calcium monosulfoaluminate (622.53 g/mol), ρ_{FS} and M_{FS} are the density (2.064 g/cm3) and molar mass (561.33 g/mol) of FS respectively, ρ_{SE} and M_{SE} are the density (1.778 g/cm^3) and molar mass (1255.11 g/mol) of SE respectively [94].

The maximum volume of FS (V_{FS}) that can develop in cement paste samples with varying FA content was determined based on the work by Qiao et al. [95]. The volume of calcium monosulfoaluminate ($V_{\mathrm{Afm,r1}}$) that is needed to react in order to form this maximum amount FS was calculated using equation (9) for each mixture in Table 3.

Using equation (1), the number of moles of sulfate generated with the formation of the maximum amount of FS was determined and used in order to compute the number of moles of calcium monosulfoaluminate that can react with these sulfate to form SE according to equation (2). $V_{Afm,r2}$ was then determined for all mixtures and illustrated in Table 3.

Table 3. Original volume of calcium monosulfoalumionate and the volumes consumed to form Friedel's salt and secondary ettringite for different mixture designs

Fly ash (%)	V_{Afm} (cm^3/cm^3 paste)	V_{FS} ** (cm^3/cm^3 paste)	$V_{Afm,r1}$ (cm^3/cm^3 paste)	$V_{Afm,r2}$ (cm^3/cm^3 paste)
0	0.171	0.041	0.047	0.023
20	0.160	0.059	0.067	0.033
25	0.152	0.065	0.074	0.037
30	0.144	0.070	0.080	0.040
35	0.136	0.075	0.085	0.042
40	0.128	0.080	0.091	0.036*

**Limited due to percentage of AFm consumed to form Friedel's salt*

*** Maximum amount of Friedel's Salt that can be produced*

Consequently, the volume of void filling (V_1) due to the formation of FS and SE can be determined using equation (11).

$$V_1 = 1.28V_{Afm,r2} - 0.12V_{Afm,r1} \quad (11)$$

The values of $V_{Afm,r1}$ and $V_{Afm,r2}$ are illustrated in Table 3 for the different FA content tested in this study.

Volume of void filling by the solution absorbed after CaOXY formation

Qiao et al. [55] measured a volume decrease when CaOXY formed, this is in accordance with the stoichiometry of equation (3). It is hypothesized in this study that the solution surrounding the concrete, if available, will be drawn by suction into the voids generated by CaOXY formation and this hypothesis has been confirmed based on mass measurements that will be shown later in this study. The volume of the solution absorbed by the concrete at each

temperature cycle was assumed equal to the volume reduction accompanying CaOXY formation according to equation (12).

$$V_2 = V_{Ca(OH)_2,r} + V_s - V_{CaOXY} \quad (12)$$

where, V_2 is the volume of absorbed solution accompanying CaOXY formation, $V_{Ca(OH)_2,r}$ is the volume of $Ca(OH)_2$ dissolving to react with salt solution, V_s is the volume of salt solution reacting with $Ca(OH)_2$ to form CaOXY, V_{CaOXY} is the volume of CaOXY developing at each temperature cycle.

Using equation (3), the volume of salt solution (V_S) and CaOXY (V_{CaOXY}) can be determined as a function of $V_{Ca(OH)_2,r}$ according to equation (13) and (14).

$$V_{CaOXY} = \frac{\frac{V_{Ca(OH)_2,r}\,\rho_{Ca(OH)_2}}{3\,M_{Ca(OH)_2}} \times M_{CaOXY}}{\rho_{CaOXY}} = 3.02\,V_{Ca(OH)_2,r} \quad (13)$$

$$V_S = \frac{\frac{V_{Ca(OH)_2,r}\,\rho_{Ca(OH)_2}}{3\,M_{Ca(OH)_2}} \times M_{CaCl2} + \frac{V_{Ca(OH)_2,r}\,\rho_{Ca(OH)_2}}{3\,M_{Ca(OH)_2}} \times 12 M_{H2O}}{\rho_s} = 2.45\,V_{Ca(OH)_2,r} \quad (14)$$

where, $\rho_{Ca(OH)_2}$ is the density of $Ca(OH)_2$ (2.21 g/cm^3), ρ_S is the density of the solution (1.325 g/cm^3), ρ_{CaOXY} is the density of the CaOXY (1.805 g/cm^3 [96, 97]; $M_{Ca(OH)2}$, M_{CaOXY}, M_{CaCl2}, and M_{H2O} are the molar mass of $Ca(OH)_2$ (74.093 g/mol), CaOXY (549.259 g/mol), calcium chloride (110.98 g/mol) and water (18 g/mol) respectively.

Consequently, the volume of void filling (V_2) due to the absorption of solution after CaOXY formation can be determined as a function of the volume of $Ca(OH)_2$ reacting with the salt solution $\left(V_{Ca(OH)_2,r}\right)$ according to equation (15).

$$V_2 = 0.428 V_{Ca(OH)_2,r} \quad (15)$$

where, $V_{Ca(OH)_2,r}$ is dependent on the volume of $Ca(OH)_2$ obtained from thermodynamic simulation for each of the mixtures in Table 2. The correlation between $V_{Ca(OH)_2,r}$ and the volume of $Ca(OH)_2$ for each mixture will be defined later in this paper based on the results of the LT-DSC and TGA measurements.

Number of temperature cycles needed to fill the voids of the concrete

Figure 4 is an illustration for the filling of voids (i.e., unfilled porosity) for mixture 2 in Table 2 as the temperature is cycled. Some phases are not shown in Figure 4. These phases corresponds to those that does not react: coarse aggregate with a volume fraction of 41%, fine aggregate with a volume fraction of 28%, unhydrated cement with a volume fraction of 1.1%, C-S-H with a volume fraction of 9.3%, other minor hydration products (such as Goethite and Brucite) with a volume fraction of 0.6%, pore solution that will not react with $Ca(OH)_2$ with a volume fraction of 0.31%. In this illustration, after exposure to salt, the matrix pores were assumed to be filled with calcium chloride solution of 20% concentration by mass. In field, this will not be the case and longer duration is needed for calcium chloride ions to diffuse and fill all the matrix pores with 20% concentration. Consequently, the results of the theoretical calculations aim only to illustrate dependency of salt damage on volume of air voids and paste content and not to show the duration it takes for the chloride ions to diffuse in the concrete and start inducing damage.

After exposure to salt solution, there is a reduction in the void space from the formation of FS and SE (equation (11)) [98, 99]. With each temperature cycle, CaOXY forms and leads to additional void space. This additional void space develops because the volume of the CaOXY solid is smaller than its liquid constituents. This creates additional void space that will allow solution to be absorbed from the surrounding environment. With the temperature increase and CaOXY phase change to a liquid, there is an increase in volume because of the previously absorbed fluid. This absorbed fluid is expected to fill the open void space. This process of fluid movement may cause damage to the concrete if no space is available to accommodate for its volume.

This work assumes that all dissolved $Ca(OH)_2$ will react with the salt solution to form CaOXY during the first temperature cycle. In reality, it may take several temperature cycles for this to happen. Consequently, the evolution of the volume of void space in concrete with respect to temperature cycles can be determined according to equation (16).

$$V_r = V_0 - V_1 - iV_2 \tag{16}$$

where, V_r is the remaining volume of void space in the concrete after chemical interaction with salt solution, V_0 is the original volume of void space, V_1 is the volume of voids filled by FS

and SE as described by equation (11), i is the number of temperature cycles as shown in Figure 2, V_2 is the volume of voids filled by the solution absorbed after CaOXY formation as described by equation (15). In this work, V_0 is assumed equal to the volume of entrained air voids because the matrix porosity is assumed to be filled with solution.

By rearranging equation (16), the number of cycles needed to fill the void space (i.e., all unfilled pores) can be determined. The filling of the void space could be thought of as one way to quantify when damage should occur. As such determining the number of cycles to fill the voids can be determined as shown in equation (17).

$$i = \frac{V_0 - V_1}{0.428 \times V_{Ca(OH)_2,r}} \quad (17)$$

The impact of the air void content, $Ca(OH)_2$ content (i.e. FA content), and paste content of the concrete on this number of cycles needed before damage development was investigated in this research study. It should be noted that the cycles reported in this paper are not directly applied for a field application in concrete slabs due to differences in sample size, thermal gradients and fluid availability. Ongoing work will relate the cycles in field conditions for use in pavement prediction.

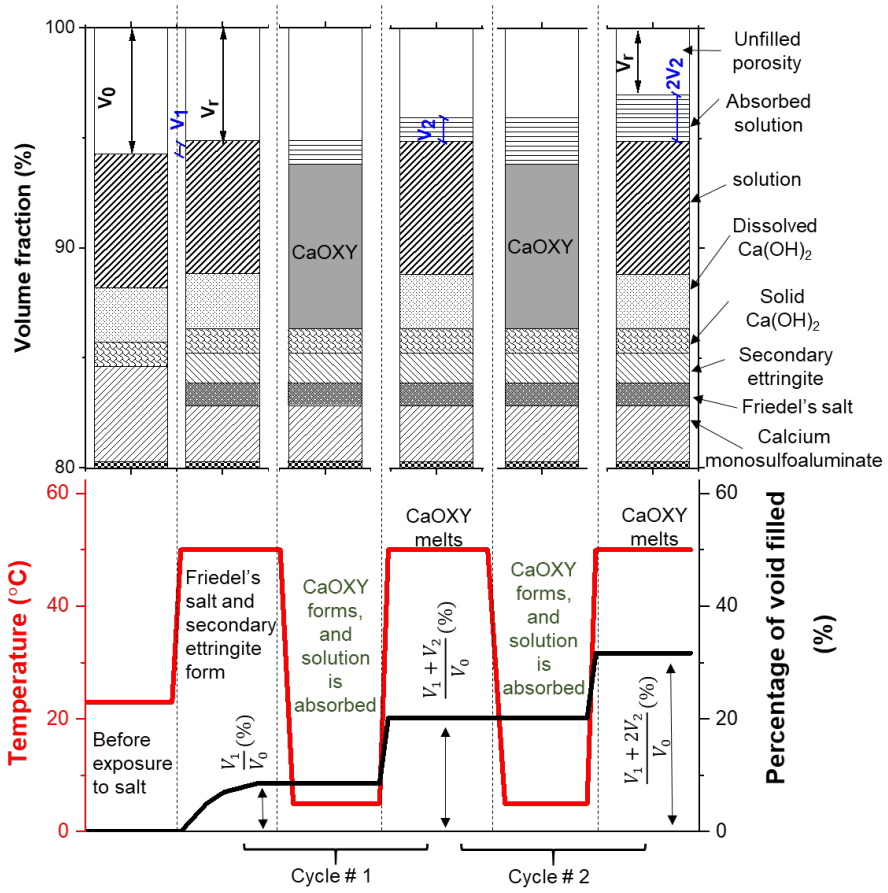

Figure 4. Illustration of the filling of void space with temperature cycles due to the absorption of solution accompanying CaOXY, Friedel's salt and secondary ettringite formation in mixture 2.

Results and Discussion

$Ca(OH)_2$ and CaOXY content

$Ca(OH)_2$ content and CaOXY content as a function of the FA replacement level by mass of cement are illustrated in Figure 5(a) and Figure 5(b) respectively. As the FA content increases, the $Ca(OH)_2$ and CaOXY values decrease [6, 60].

Filled circles are the experimental values of $Ca(OH)_2$ content obtained from TGA measurements, while the line represents the $Ca(OH)_2$ content obtained from thermodynamic simulation. There is a strong correlation between the experimental measurements and the theoretically predicted values of $Ca(OH)_2$.

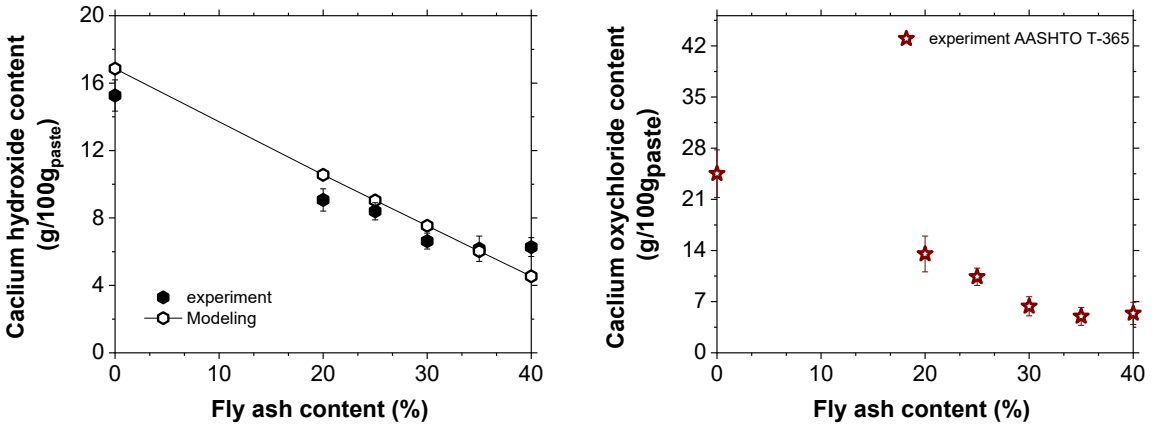

(a) (b)

Figure 5- (a) $Ca(OH)_2$ content with respect to fly ash, (b) CaOXY content with respect to fly ash

In Figure 6, the experimental values for $Ca(OH)_2$ and CaOXY content collected in this study were added to data points existing in the literature [6, 60, 80]. A line was fitted to these experimental data points while fixing the slope to the theoretical stoichiometric value of 2.47. An intercept of -3.27 was obtained from the fit with an R^2 value of 0.94. This indicates that approximately 1.32g/100g_{paste} of $Ca(OH)_2$ does not react with $CaCl_2$ solution to form CaOXY. Consequently, $V_{Ca(OH)_2,r}$, needed for equation (15), was determined according to equation (18). The value 1.32g/100g paste may vary depending on what portion of the $Ca(OH)_2$ is inaccessible because it is possibly surrounded by hydration products, similar to the mechanism described in [67], but this seems to be a good value for the data points summarized in Figure 6.

$$V_{Ca(OH)_{2,r}} = V_{Ca(OH)_2} - \frac{1.32/\rho_{Ca(OH)2}}{100(\frac{1}{\rho_{paste}})} \quad (18)$$

where, $V_{Ca(OH)_2}$ is the volume fraction of $Ca(OH)_2$ determined for each mixture using thermodynamic simulation, ρ_{paste} is the density of the paste. This plot illustrates that the potential for CaOXY production can be determined by knowing the amount of $Ca(OH)_2$ produced in the material.

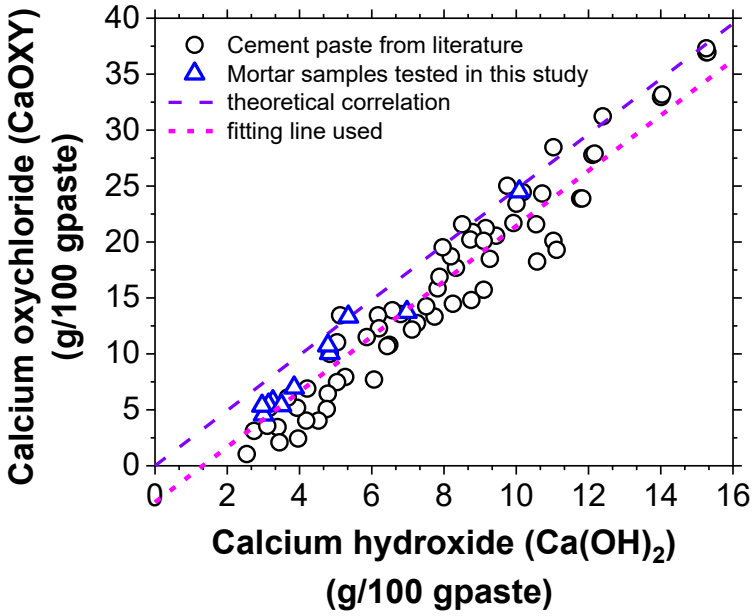

Figure 6- CaOXY content with respect to $Ca(OH)_2$ content for both cement paste and mortar samples

Impact of salt solution suction on the salt damage development

Figure 7 illustrates the residual strain that develops in mortar samples as a function of the number of temperature cycles for three different exposure conditions illustrated in Figure 3. It should be noted that the strains reported on the y-axis are quite large, much larger than the strains typically observed for mechanical failures of cementitious systems in tension. However, when expansion occurs in the paste matrix, as in the case of delayed ettringite formation where strains of 10,000 με were observed [100], these large strains can be expected.

The residual strain increases more for the samples surrounded by salt solution than it does for the sealed samples or samples in lime solution. The damage that develops in the sample surrounded by salt solution is significant. In fact, several of the samples broke before reaching 15 cycles (6 and 9 cycles respectively) and their length became non-measurable.

The residual strain measurements collected on samples saturated with salt solution and sealed during the temperature cycles are comparable to those collected on samples saturated with lime solution. The samples saturated with lime solution and exposed to temperature cycling while being immersed in this solution are not expected to develop damage because the temperature

remained above freezing temperature (>0°C) and no CaOXY is forming due to the absence of salt.

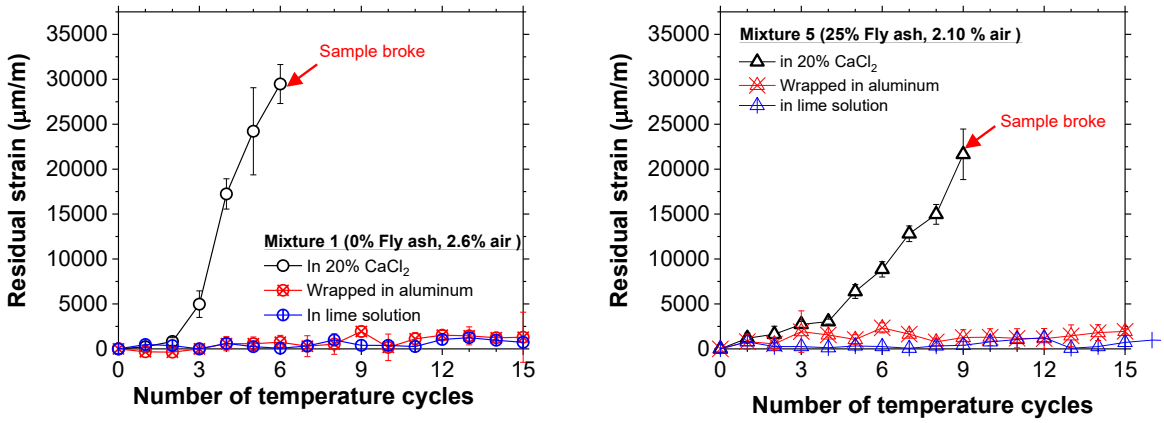

(a) (b)

Figure 7. Residual strain with respect to the number of cycles for the three different conditions tested in this study (a) in 0% fly ash (high $Ca(OH)_2$ content), (b) in 25% fly ash (lower $Ca(OH)_2$ content)

Figure 8 provides a plot illustrating the mass evolution in mortar samples with respect to the number of temperature cycles for the three different exposure conditions. The samples surrounded with salt solution had a measurable increase in mass (1.9 % in Figure 8(a) and 1.3% in Figure 8(b)) before visible damage was observed (3.5 cycles in Figure 8(a) and 7.5 cycles in Figure 8(b)). The average maximum mass gain recorded in this study from all the samples immersed in salt before visible damage was +2.0 ± 0.6%, while a value of 0.4 ± 0.2 % was determined for samples immersed in lime solution. This mass increase was not observed for sealed samples. The sealed samples showed a slight mass loss on average value of -1.2 ± 0.2 % after 15 temperature cycles for all mixtures tested in this study due to evaporation.

Figure 4 illustrated that the formation of CaOXY is accompanied by a volume reduction of the materials in the pores of the sample. This volume reduction appears to occur with a suction stress that causes fluid to be absorbed from the solution surrounding it to fill in vacancies created by CaOXY formation. This increase in fluid can explain the increase in the samples' mass (Figure 8). The mass increases with an increase in the number of thermal cycles, almost like a 'pumping' effect where more and more solution is absorbed. As the fluid moves through the paste it may cause microcracks. These microcracks may also allow more solution to be absorbed, which would also increase the mass of the sample. The mass increase in all the mixtures tested in this study is illustrated in [101].

After 3.5 temperature cycles in Figure 8(a) and 7.5 temperature cycles in Figure 8(b)), cracking increases, which can result in flaking off of particles from the sample leading to a decrease in the mass of the sample. The salt damage was first visible and localized around the aggregates. This is likely due to the high $Ca(OH)_2$ content at aggregates surface [102], and it is the dissolution of the $Ca(OH)_2$ and reaction with $CaCl_2$ (Equation(1)) that results in the reaction product resulting in CaOXY formation [64]. As the number of thermal cycles increases, additional loss of paste and particles from the sample cause a continuous mass decrease. This observation holds for all the mixture designs tested in this study as shown in the [101].

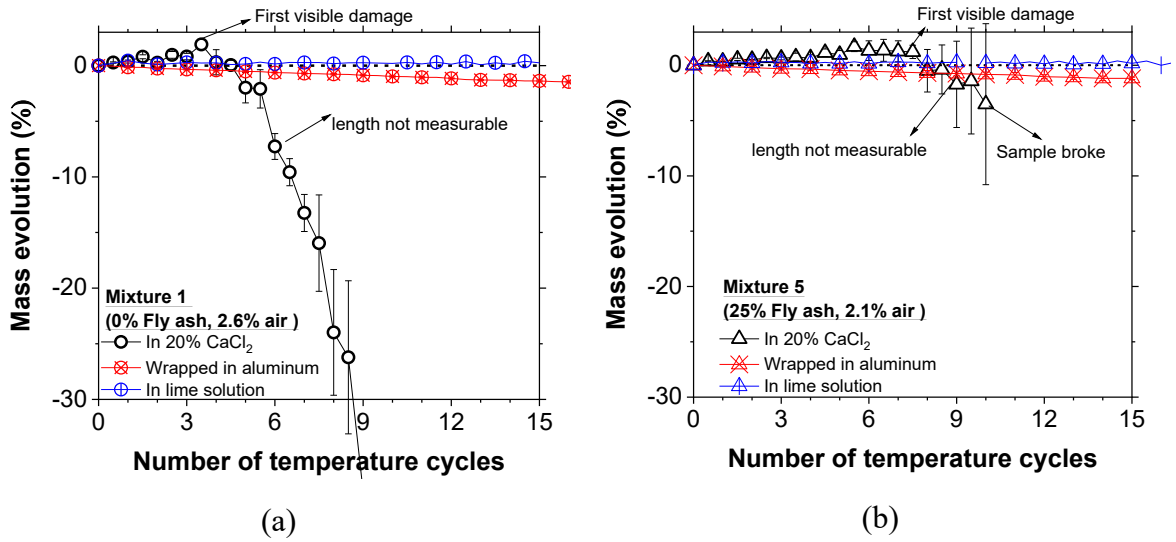

(a) (b)

Figure 8- Mass evolution with respect to the number of cycles for the three different conditions tested in this study (a) in 0% fly ash, (b) in 25% fly ash

Figure 9 illustrates the residual strain as a function of the $Ca(OH)_2$ content (and FA content) for the three exposure conditions tested in this study after 9 temperature cycles for the sample with the low air content of 2.3%. This shows the performance of a mixture by only varying the $Ca(OH)_2$ content. Visible damage was clearly identified in the samples with a residual strain of 15,000 µm/m, and as such, this value was selected as a limit for the residual strain measurements. Samples with $Ca(OH)_2$ content higher than 6 $g/100g_{paste}$ developed higher residual strain values when surrounded with salt solution during CaOXY formation as compared to samples wrapped in aluminum, or just immersed in lime solution. The absorption of fluid during CaOXY formation appears to be critical for salt damage development in these mixtures. This reinforces that the pumping or movement of solution surrounding the sample is important for the damage.

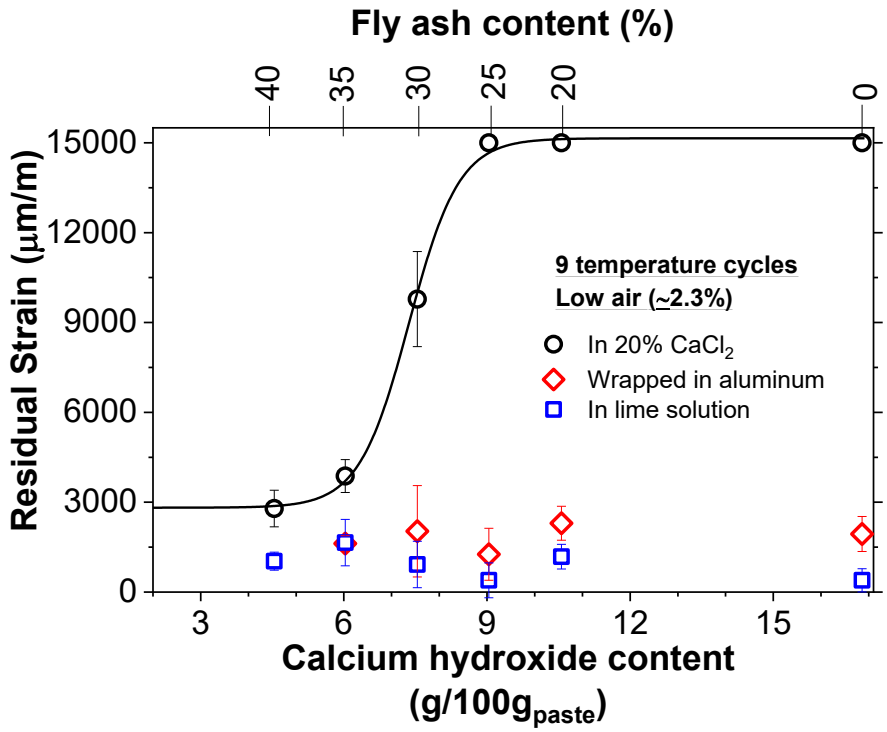

Figure 9- Comparison of the residual strain measured after 9 temperature cycles with respect to the Ca(OH)$_2$ content and three different conditions of testing

Impact of the air void content on the salt damage development

The impact of air void content on the salt damage development is shown in Figure 10. The evolution of the residual strain is plotted with respect to the number of temperature cycles for samples with different Ca(OH)$_2$ contents (achieved by varying the FA content from 0% to 40%) and different air voids contents. As shown in Figure 9 and 10, as the Ca(OH)$_2$ content decreases, the damage decreases.

The residual strain for mixtures with a Ca(OH)$_2$ content of 16.9 g/100g$_{paste}$ and 10.6g/100g$_{paste}$ increased with temperature cycling as illustrated in Figure 10(a) and Figure 10(b), independently from the air void content. However, samples with high air void content lasted three more temperature cycles than low air void content.

This shows that air void content can influence salt damage development in mixtures with intermediate Ca(OH)$_2$ content of 9 g/100g$_{paste}$ and 7.5g/100g$_{paste}$ (i.e. obtained by a FA content of 25% and 30% FA by mass respectively). Samples with 7.5 g/100g$_{paste}$ Ca(OH)$_2$ and a high air void content lasted up to 15 cycles while samples with a low air void content broke and their length became non-measurable after 12 cycles (Figure 10 (d)). The impact of air void

content on mixtures containing 9 g/100g_{paste} $Ca(OH)_2$ is visible but less advanced as compared to mixtures with 7.5 g/100g_{paste} $Ca(OH)_2$ (Figure 10 (c)).

The salt damage measured in both mixtures containing low $Ca(OH)_2$ content (35% FA or 40% FA) is negligible as illustrated in Figure 10 (e) and Figure 10 (f) respectively. This is due to the pozzolanic reaction that consumes $Ca(OH)_2$ and reduces its availability to react with $CaCl_2$. This results in a reduction in CaOXY content and thus in salt damage development regardless of the air void content [57].

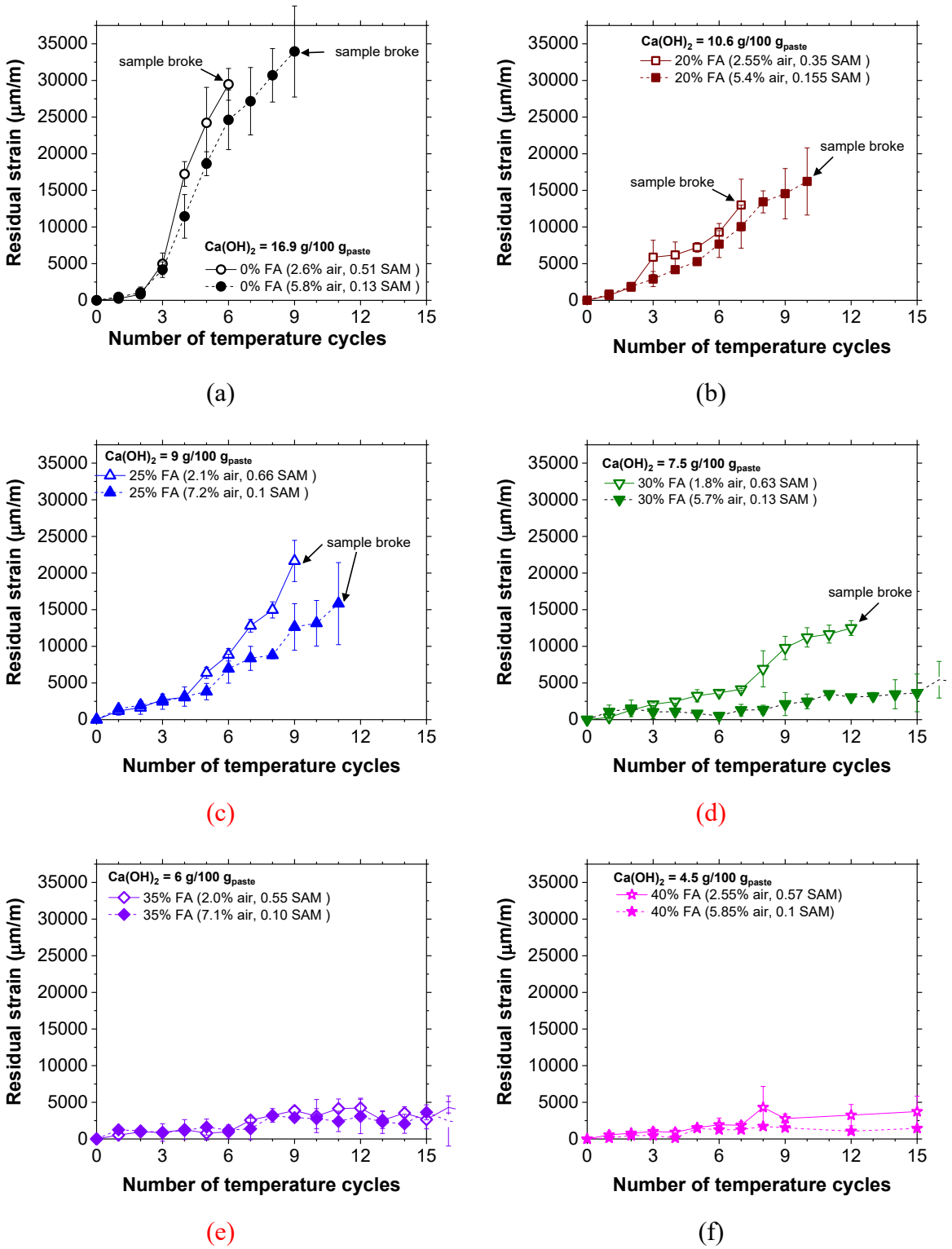

Figure 10- Residual strain with respect to the number of temperature cycle for mortar samples with 2 different air void content (a) Mixture 1 and 2, (b) Mixture 3 and 4, (c) Mixture 5 and 6, (d) Mixture 7 and 8, (e) Mixture 9 and 10, (f) Mixture 11 and 12.

Figure 11 illustrates the residual strain measurements after 9 temperature cycles as a function of $Ca(OH)_2$ content, and air void content. As illustrated in Figure 11, the impact of air void content on salt damage development become more significant for mixtures with intermediate $Ca(OH)_2$ content (mixtures with 25% and 30% FA content by mass) and this is in accordance with the visual inspection of the sample as illustrated in [101]. The $Ca(OH)_2$ threshold value corresponding to 15g CaOXY/100 g paste is theoretically equal to 6g $Ca(OH)_2$/100g paste (Figure 6). For the mortar samples tested in this study with a low air void content (empty dots in Figure 11), this threshold value seems to hold true as samples with $Ca(OH)_2$ content higher than 6g/100 g paste developed significant damage while samples with a lower $Ca(OH)_2$ content did not display significant damage. While for mortar samples with a higher air void content (filled dots in Figure 11), this threshold value seems to be conservative and can be increased to the value of about 8g $Ca(OH)_2$/100g paste. This observation illustrates that the threshold value for CaOXY to limit salt damage is dependent on air void content rather than being a constant single value.

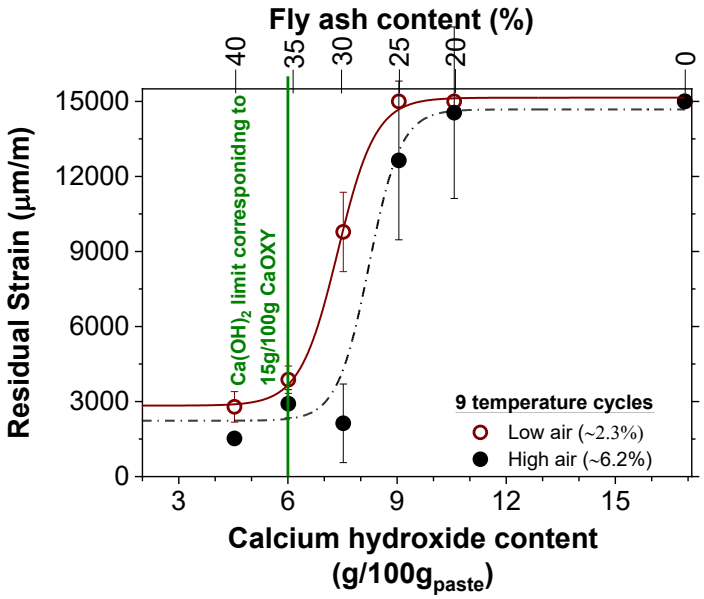

Figure 11- Residual strain measured on samples with different $Ca(OH)_2$, and different air voids content after 9 temperature cycles

Impact of paste content and air void on CaOXY threshold value

Figure 12 illustrates the number of cycles needed to fill the void spaces of concrete, determined using equation (17) with respect to the air to paste content ratio and fly ash content. The number of cycles needed to fill voids increased with the FA content (i.e. increased with a decrease in $Ca(OH)_2$ content), and with the air to paste content.Based on Figure 12, it can be noted that mixtures with a high air void content, low paste content and low $Ca(OH)_2$ content (i.e. high fly ash content) will resist longer against salt damage development. It should be noted that the number of cycles illustrated in this figure is not representative to the number of cycles of a concrete pavement exposed to real environmental conditions. The calculations in this paper do not apply for a full-scale application with different size samples, environmental boundary conditions and aims only to illustrate the dependency of salt damage on the paste content, air void content and $Ca(OH)_2$ content. Consequently, CaOXY threshold limit may vary depending on these parameters.

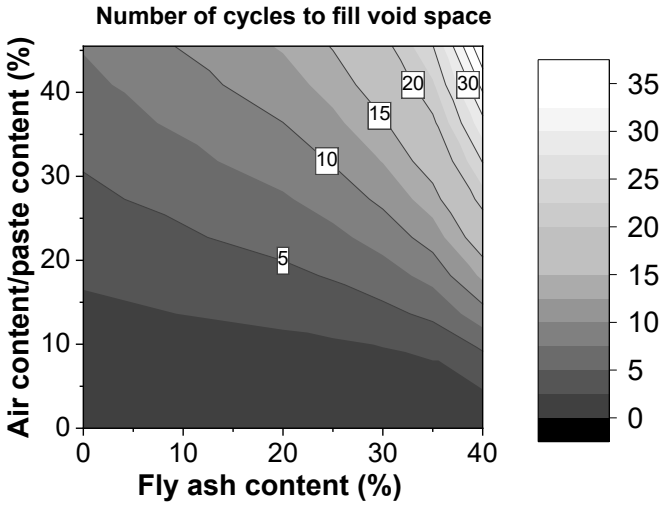

Figure 12. Number of cycles needed to fill the void space in concrete with respect to the air void content to paste content ratio, and fly ash content. Note the number of cycle in this figure only applies to the laboratory sample sizes and boundary conditions.

By combining equation (17) and equation (13), the amount of CaOXY that can develop in a mixture before filling the unfilled voids of concrete can be determined as a function of the number of temperature cycles, original volume of voids in a concrete mixture (V_0), and paste content of the concrete mixture according to equation (19).

$$M_{CaOXY-limit} = \frac{V_0 - V_1}{0.43i} \times \frac{3.02}{C} \times \frac{\rho_{CaOXY}}{\rho_{paste}} \times 100 \quad (19)$$

where, $M_{CaOXY\text{-}limit}$ is the amount of CaOXY that can develop before filling all the voids of concrete with solution ($g/100g_{paste}$), C is the paste content of the concrete mixture.

For a given number of temperature of cycles, the impact of the air void content to paste content ratio on the threshold value of CaOXY to limit salt damage development can be determined according to (19).

Conclusion

AASHTO PP-84-20 recommend that mixtures be designed using SCMs to limit the amount of CaOXY that forms to be less than $15g/100g_{paste}$. This limit has been established empirically and does not consider other aspects of the mixture design. This paper discusses the impact of fluid absorption, entrained air void content, and paste content (i.e, air content /paste content) on CaOXY-induced damage. This was studied on mixtures containing different $Ca(OH)_2$ content and different air void contents.

The air void content did not influence salt damage development in mixtures with high $Ca(OH)_2$ content (FA replacement was between 0 and 20% of the cement by mass)), due to the large amount of CaOXY that can form (i.e., the volume of voids was insufficient to control the expansion).

Similarly, the air void content did not impact the salt damage development in mixtures with a low $Ca(OH)_2$ content (FA replacement higher than 35% by mass)). That is due to the dilution and pozzolanic reaction leading to a reduction in the $Ca(OH)_2$ content and CaOXY content (i.e., there was not a sufficient expansion to result in substantial damage in either case).

The air void content does however impact salt damage in mixtures with moderate $Ca(OH)_2$ content (FA replacement of 25% and 30% by mass)). Samples in this range of $Ca(OH)_2$ content with higher air content had improved resistance to salt damage (compared to those with a lower entrained air content). This indicates the value of the void space (i.e., air content) in reducing the expansive pressure caused by CaOXY.

This study showed that the absorption of fluid during CaOXY formation is an important factor for salt damage development. CaOXY formation at low temperatures is accompanied by a

volume reduction of the materials in the pores of the mortar. The sample absorbs fluid from the solution surrounding the sample, due to capillary suction, and fills in void space created by CaOXY formation. When the temperature increases, a phase change occurs of solid CaOXY into liquid, which has a bigger volume than the solid phase. The absorbed solution at low temperature will reduce the available volume to accommodate for the volume expansion accompanying the phase change of CaOXY with the temperature increase. This may lead to pressure development and salt damage.

Acknowledgments

The authors gratefully acknowledge support for this work from the pooled fund study (Project No. U1117C) managed by the Oklahoma Department of Transportation. The authors are grateful to the discussions with Doctor Alexander Chemey about the rate of calcium hydroxide dissolution. The authors are grateful to Audrey Collins and Gannon Holland, under-graduate research assistants at Oregon State University, who helped in conducting some of the experiments. The contents of this paper reflect the views of the authors, who are responsible for the facts and the accuracy of the data presented herein. The contents do not necessarily reflect the official views or policies of the sponsors. These contents do not constitute a standard, specification, or regulation.

References

1. M. Del Mar Arribas-Colón, M. Radlinski, J. Olek, N.M. Whiting, Investigation of Premature Distress Around Joints in PCC Pavements: Parts I & II, Joint Transportation Research Program, Indiana Department of Transportation and Purdue University, 2016.

2. W. Jones, Y. Farnam, P. Imbrock, J. Spiro, C. Villani, J. Olek, J., W.J. Weiss, An overview of joint deterioration in concrete pavement: Mechanisms, solution properties, and sealers, Indiana, 2013.

3. J. Castro, W. Li, M. Pour-Ghaz, M. Golias, B. Tao, H. Sun, W.J. Weiss, Durability of saw-cut joints in plain cement concrete pavements, Joint Transportation Research Program, Indiana Department of Transportation and Purdue University, 2011.

4. C. Graveen, E.M. Falker, M. Beaver, N. Neithalath, W.J. Weiss, J. Olek, T.E. Nantung, V.L. Gallivan, Performance Related Specifications (PRS) for Concrete Pavements in Indiana, Volume 2: Technical Report, Joint Transportation Research Program, Indiana Department of Transportation and Purdue University, 2009.

5. J. Olek, M. Radlinski, M. Del Mar Arribas, Premature deterioration of joints in selected Indiana portland cement concrete pavements, Proceedings, 23rd Conference on Structural Failures, Poland, 2007, pp.859-868.

6. C. Jones, S. Ramanathan, P. Suraneni, W.M. Hale, Calcium oxychloride: a critical review of the literature surrounding the formation, deterioration, testing procedures, and recommended mitigation techniques, Cement and Concrete Composites. 113 (2020) 19. https://doi.org/10.1016/j.cemconcomp.2020.103663.

7. S. Smith, Q. Chunyu, P. Suraneni, K.E. Kurtis, W.J. Weiss, Service-life of Concrete in Freeze-Thaw Environments: Critical Degree of Saturation and Calcium Oxychloride Formation, Cement and Concrete Research. 122 (2019) 93-106. https://doi.org/10.1016/j.cemconres.2019.04.014

8. H. Cai, X. Liu, Freeze-thaw durability of concrete: ice formation process in pores, Cement and Concrete Research. 28 (1998) 1281-1287. doi:10.1016/S0008-8846(98)00103-3

9. J. Tanesi, R. Meininger, Freeze-thaw resistance of concrete with marginal air content, Transportation research record, report FHWA-HRT-06-117, 2006, pp.96.

10. D.J. Janssen, M.B. Snyder, Resistance of concrete to freezing and thawing, No. SHRP-C-391, 1994, pp.201.

11. L. Sutter, K. Peterson, S. Touton, T. Van Dam, D. Johnston, Petrographic evidence of calcium oxychloride formation in mortars exposed to magnesium chloride solution, Cement and Concrete Research. 36 (2006) 1533-1541. https://doi.org/10.1016/j.cemconres.2006.05.022

12. S. Monosi, Chemical attack of calcium chloride on the Portland cement paste, Cemento. 86 (1989) 97-104.

13. S. Monosi, Research on $3CaO \cdot CaCl_2 \cdot 15H_2O$ identified in concretes damaged by $CaCl_2$ attack, Cemento. 87 (1990) 3-8.

14. M. Collepardi, L. Coppola, C. Pistolesi, Durability of concrete structures exposed to $CaCl_2$ based deicing salts, Special Publication in ACI. 145 (1994) 107-120.

15. L. Sutter, K. Peterson, G. Julio-Betancourt, D. Hooton, T. Van Dam, K. Smith, The Deleterious Chemical Effects of Concentrated Deicing Solutions on Portland Cement Concrete, Technical Report, Michigan Tech Transportation Insitute, South Dakota Department of Transportation, 2008, pp.216.

16. X. Shi, L. Fay, M.M. Peterson, Z. Yang, Freeze–thaw damage and chemical change of a portland cement concrete in the presence of diluted deicers, Materials and Structures. 43 (2010) 933-946. https://doi.org/10.1617/s11527-009-9557-0.

17. A.E. Janusz, Investigation of deicing chemicals and their interactions with concrete materials, master thesis, Purdue University, 2010.

18. H. Lee, R.D. Cody, A.M. Cody, P.G. Spry, Effects of various deicing chemicals on pavement concrete deterioration, proceedings of the Mid-Continent Transportation Symposium, 2000.

19. K. Wang, D.E. Nelsen, W.A. Nixon, Damaging effects of deicing chemicals on concrete materials, Cement and Concrete Composites. 28 (2006)173-188. https://doi.org/10.1016/j.cemconcomp.2005.07.006.

20. M. Lawrence, H.E. Vivian, Action of calcium chloride on mortar and concrete, Australian Journal of Applied Science. 11 (1960) 490-496.

21. C.B. Van Niejenhuis, C.M. Hansson, Detrimental Effects of Anti-Icing Brines on Concrete Durability, Concrete International. 41 (2019) 30-34.

22. A. Ghazy, M.T. Bassuoni, Resistance of concrete to different exposures with chloride-based salts, Cement and Concrete Research. 105 (2017) 144-158. https://doi.org/10.1016/j.cemconres.2017.09.001

23. S. Chatterji, Mechanism of the $CaCl_2$ attack on Portland cement concrete, Cement and Concrete Research. 8 (1978) 461-467. https://doi.org/10.1016/0008-8846(78)90026-1.

24. H.G. Smolczyk, Chemical Reactions of strong Chloride-Solution with Concrete, Proceedings of the 5th International Congress on the Chemistry of Cement, 1968, pp. 274-280.

25. C. Qiao, P. Suraneni, T.N.W. Ying, A. Choudhary, W.J. Weiss, Chloride binding of cement pastes with fly ash exposed to $CaCl_2$ solutions at 5 and 23° C, Cement and Concrete Composites. 97 (2019) 43-53. https://doi.org/10.1016/j.cemconcomp.2018.12.011

26. U.A. Birnin-Yauri, F.P. Glasser, Friedel's salt, $Ca_2Al(OH)_6(Cl,OH)\cdot 2H_2O$: Its solid solutions and their role in chloride binding, Cement and Concrete Research. 28 (1998) 1713-1723. https://doi.org/10.1016/S0008-8846(98)00162-8 .

27. W. Li, M. Pour-Ghaz, J. Castro, W.J. Weiss, Water Absorption and Critical Degree of Saturation Relating to Freeze-Thaw Damage in Concrete Pavement Joints, Journal of Materials in Civil Engineering. 24 (2012) 299-307. https://doi.org/10.1061/(ASCE)MT.1943-5533.0000383

28. G.G. Litvan, Frost action in cement in the presence of de-icers, Cement and Concrete Research. 6 (1976) 351-356. https://doi.org/10.1016/0008-8846(76)90097-1.

29. R.P. Spragg, J. Castro, W. Li, M. Pour-Ghaz, P.T. Huang, W.J. Weiss, Wetting and drying of concrete using aqueous solutions containing deicing salts, Cement and Concrete Composites. 33 (2011) 535-542. 10.1016/j.cemconcomp.2011.02.009.

30. P. Taylor, L. Sutter, W.J. Weiss, Investigation of deterioration of joints in concrete pavements, InTrans Project 09-361, 2012.

31. L. Sutter, T. Van Dam, K.R. Peterson, D.P. Johnston, Long-term effects of magnesium chloride and other concentrated salt solutions on pavement and structural Portland cement concrete, Transportation research record. 1979 (2006) 60-68. https://doi.org/10.1177/0361198106197900109 .

32. M. Pour-Ghaz, F. Rajabipour, J. Couch, W.J. Weiss, Numerical and experimental assessment of unsaturated fluid transport in saw-cut (notched) concrete elements, in ACI fall convention, 2009, pp.73-85.

33. M. Golias, J. Castro, A. Peled, T. Nantung, B. Tao, W.J. Weiss, Can Soy Methyl Esters Improve Concrete Pavement Joint Durability?, Transportation research record. 2290 (2012) 60-68. https://doi.org/10.3141/2290-08

34. K.T. Hall, S.D. Tayabji, J. Sherwood, S. Tyson, Performance of Sealed and Unsealed Concrete Pavement Joints, report number FHWA-HIF-09-013, 2009.

35. C. MacInnis, Y.R. Nathawad, The effects of a deicing agent on the absorption and permeability of various concretes, Durability of Building Materials and Components, ASTM International, 1980, pp.485-496.

36. J. Castro, P. Kompare, P. Poursaee, T. Nantung, W.J. Weiss, Portland cement concrete pavement performance relative to permeability, JTRP Rep. SPR-3093, Indiana Department of Transportation, 2010.

37. V. Barde, A. Radlinska, M. Cohen, W.J. Weiss, Relating material properties to exposure conditions for predicting service life in concrete bridge decks in Indiana, Publication FHWA/IN/JTRP-2007/27, Joint Transportation Research Program, Indiana Department of Transportation and Purdue University, 2009.

38. P.R. Rangaraju, Investigating premature deterioration of a concrete highway, Transportation research record. 1798 (2002) 1-7. DOI: 10.3141/1798-01.

39. P.J. Tumidajski, G.W. Chan, Durability of high performance concrete in magnesium brine, Cement and Concrete Research. 26 (1996) 557-565. doi:10.1016/0008-8846(96)00034-8.

40. F. Häusler, H. Schmidt, D. Freyer, Calcium Hydroxide Chlorides: The Ternary System $Ca(OH)_2$-$CaCl_2$-H_2O at 25, 40, and 60° C, Phase Stoichiometry and Crystal Structure, Zeitschrift für anorganische und allgemeine Chemie. 645 (2019) 723-731. https://doi.org/10.1002/zaac.201900051.

41. P. Brown, J. Bothe Jr, The system CaO-Al_2O_3-$CaCl_2$-H_2O at 23±2 °C and the mechanisms of chloride binding in concrete, Cement and Concrete Research. 34 (2004) 1549-1553. DOI: 10.1016/j.cemconres.2004.03.011.

42. G.A. Julio-Betancourt, R.D. Hooton, Calcium and magnesium chloride attack on cement-based materials: formation, stability, and effects of oxychlorides, In 2nd International RILEM Workshop on Concrete Durability and Service Life Planning, 2009, pp.432-439.

43. K. Peterson, G. Julio-Betancourt, L. Sutter, R.D. Hooton, D. Johnston, Observations of chloride ingress and calcium oxychloride formation in laboratory concrete and mortar at 5° C, Cement and Concrete Research. 45 (2013) 79-90. https://doi.org/10.1016/j.cemconres.2013.01.001.

44. T. Demediuk, W.F. Cole, H.V. Hueber, Studies on magnesium and calcium oxychlorides, Australian Journal of Chemistry. 8 (1955) 215-233. https://doi.org/10.1071/CH9550215.

45. H. Mori, R. Kuga, S. Ogawa, Y. Kubo, Deterioration of hardened cement pastes immersed in calcium chloride solution, Cement Science and Concrete Technology. 66 (2012) 79-86. https://doi.org/10.14250/cement.66.79.

46. C. Qiao, P. Suraneni, M.T. Chang, W.J. Weiss, The Influence of calcium chloride on flexural strength of cement-based materials, in High Tech Concrete: Where Technology and Engineering Meet, Springer International Publishing: Cham., 2018, pp.2041-2048. DOI: https://doi.org/10.1007/978-3-319-59471-2_233.

47. C. Qiao, P. Suraneni, W.J. Weiss, Flexural strength reduction of cement pastes exposed to $CaCl_2$ solutions, Cement and Concrete Composites. 86 (2018) 297-305. https://doi.org/10.1016/j.cemconcomp.2017.11.021.

48. Y. Farnam, S. Dick, A. Wiese, J. Davis, D. Bentz, W.J. Weiss, The influence of calcium chloride deicing salt on phase changes and damage development in cementitious materials, Cement and Concrete Composites. 64 (2015) 1-15. DOI: 10.1016/j.cemconcomp.2015.09.006.

49. L. Berntsson, S. Chandra, Damage of concrete sleepers by calcium chloride, Cement and Concrete Research. 12 (1982) 87-92.

50. S. Chatterji, J. Ad, Studies of the mechanism of calcium chloride attack on Portland cement concrete, 1975.

51. C. Qiao, P. Suraneni, W.J. Weiss, Phase diagram and volume change of the $Ca(OH)_2$-$CaCl_2$-H_2O system for varying $Ca(OH)_2/CaCl_2$ molar ratios, Journal of Materials in Civil Engineering. 30 (2018). https://doi.org/10.1061/(ASCE)MT.1943-5533.0002145.

52. E.M. Winkler, P.C. Singer, Crystallization Pressure of Salts in Stone and Concrete, Geological Society of America Bulletin. 83 (1972) 3509-3514. https://doi.org/10.1130/0016-7606(1972)83[3509:CPOSIS]2.0.CO;2.

53. G.W. Scherer, Crystallization in pores, Cement and Concrete Research. 29 (1999) 1347-1358.

54. G.W. Scherer, Stress from crystallization of salt, Cement and Concrete Research, 34 (2004) 1613-1624. https://doi.org/10.1016/j.cemconres.2003.12.034.

55. C. Qiao, P. Suraneni, W.J. Weiss, Measuring volume change due to calcium oxychloride phase transformation in a $Ca(OH)_2$-$CaCl_2$-H_2O system, Advances in Civil Engineering Materials. 6 (2017) 157-169. DOI: 10.1520/ACEM20160065.

56. Y. Farnam, B. Zhang, W.J. Weiss, Evaluating the use of supplementary cementitious materials to mitigate damage in cementitious materials exposed to calcium chloride deicing salt, Cement and Concrete Composites. 81 (2017) 77-86. DOI: 10.1016/j.cemconcomp.2017.05.003.

57. P. Suraneni, V.J. Azad, O.B. Isgor, W.J. Weiss, Use of fly ash to minimize deicing salt damage in concrete pavements, Journal of the Transportation Research Board. 2629 (2017) 24-32. https://doi.org/10.3141/2629-05.

58. K.O. Ampadu, K. Torii, M. Kawamura, Beneficial effect of fly ash on chloride diffusivity of hardened cement paste, Cement and Concrete Research. 29 (1999) 585-590. DOI: 10.1016/S0008-8846(99)00047-2.

59. K. Torll, T. Sasatani, M. Kawamura, Effects of Fly Ash, blast Furnace Slag, and Silica Fume on Resistance of Mortar to Calcium Chloride Attack, ACI Special Publication. 153 (1995) 931-950.

60. P. Suraneni, V.J. Azad, O.B. Isgor, W.J. Weiss, Role of supplementary cementitious material type in the mitigation of calcium oxychloride formation in cementitious pastes, Journal of Materials in Civil Engineering. 30 (2018) 1-10. https://doi.org/10.1061/(ASCE)MT.1943-5533.0002425.

61. P. Suraneni, V.J. Azad, O.B. Isgor, W.J. Weiss, Calcium oxychloride formation in pastes containing supplementary cementitious materials: Thoughts on the role of cement and supplementary cementitious materials reactivity, RILEM Technical Letters. 1 (2016) 24-30. http://orcid.org/0000-0002-0899-2601.

62. S.N. Whatley, P. Suraneni, V.J. Azad, O.B. Isgor, W.J. Weiss, Mitigation of Calcium Oxychloride Formation in Cement Pastes Using Undensified Silica Fume, Journal of Materials in Civil Engineering. 29 (2017) 9. https://doi.org/10.1061/(ASCE)MT.1943-5533.0002052.

63. X. Wang, S. Sadati, P. Taylor, C. Li, X. Wang, A. Sha, Material characterization to assess effectiveness of surface treatment to prevent joint deterioration from oxychloride formation mechanism, Cement and Concrete Composites. 104 (2019) 15. DOI: 10.1016/j.cemconcomp.2019.103394.

64. W.J. Weiss, M.T. Ley, L. Sutter, D. Harrington, J. Gross, S.L. Tritsch, Guide to the Prevention and Restoration of Early Joint Deterioration in Concrete Pavements, No. IHRB Project TR-697, 2016, pp.41.

65. J. Monical, E. Unal, T. Barrett, Y. Farnam, W.J. Weiss, Reducing Joint Damage in Concrete Pavements: Quantifying Calcium Oxychloride Formation for Concrete Made with Portland Cement, Portland Limestone Cement, Supplementary Cementitious Materials, and Sealers, Transportation Research Board. 2577 (2016) 17-24. https://doi.org/10.3141/2577-03.

66. M. Collepardi, S. Monosi, Effect of the carbonation process on the concrete deterioration by $CaCl_2$ aggression, 9th international congress on the Chemistry of Cement, New Delhi, 1992, pp.389-395.

67. R.M. Ghantous, Y. Farnam, E. Unal, W.J. Weiss, The influence of carbonation on the formation of calcium oxychloride, Cement and Concrete Composites. 73 (2016) 185-191. https://doi.org/10.1016/j.cemconcomp.2016.07.016.

68. N. Hosseinzadeh, P. Suraneni, Synergistic Effects of Air Content and Supplementary Cementitious Materials in Reducing Damage Caused by Calcium Oxychloride Formation in Concrete, 2021.

69. P. Suraneni, W.J. Weiss, Examining the pozzolanicity of supplementary cementitious materials using isothermal calorimetry and thermogravimetric analysis, Cement and Concrete Composites. 83 (2017) 273-278. https://doi.org/10.1016/j.cemconcomp.2017.07.009.

70. M.T. Ley, D. Welchel, J. Peery, S. Khatibmasjedi, J. LeFlore, Determining the air-void distribution in fresh concrete with the Sequential Air Method, Construction and Building Materials. 150 (2017) 723-737. https://doi.org/10.1016/j.conbuildmat.2017.06.037.

71. R.V. Felice, J.M. Freeman, M.T. Ley, Durable Concrete with Modern Air-Entraining Admixtures, Concrete International. 36 (2014) 37-45.

72. H. Hall, M.T. Ley, D. Welchel, J. Peery, J. Leflore, M. Khatibmasjedi, J.M. Gudimettla, M. Praul, Field and laboratory validation of the sequential air method, Materials and Structures. 53 (2020). https://doi.org/10.1617/s11527-020-1444-8.

73. WM. Whipple, Investigation of field methods for determining air content of mass concrete. Corps of Engineers, U.S. Army, Vicksburg, Mississippi, 1952, p. 59.

74. R.M. Ghantous, H. Madland, J. Kwong, W.J. Weiss, Examining the influence of the Degree of Saturation on Length Change and Freeze Thaw Damage, Advances in Civil Engineering Materials. 8 (2019) 365-374. DOI: 10.1520/ACEM20190001.

75. M.K. Moradllo, B. Sudbrink, Q. Hu, M. Aboustait, B. Tabb, M.T. Ley, J.M. Davis, Using micro X-ray fluorescence to image chloride profiles in concrete, Cement and Concrete Research. 92 (2017) 128-141. https://doi.org/10.1016/j.cemconres.2016.11.014.

76. R.M. Ghantous, M.K. Moradllo, H.H. Becker, M.T. Ley, W.J. Weiss, Determining the freeze-thaw performance of mortar samples using length change measurements during freezing, cement and concrete composite. 116 (2021) 10. DOI: 10.1016/j.cemconcomp.2020.103869.

77. B.Y. Trofimov, L.Y. Kramar, K.V. Schuldyakov, On Deterioration Mechanism of Concrete Exposed to Freeze-Thaw Cycles, in IOP Conference Series: Materials Science and Engineering. 262 (2017) 7. doi:10.1088/1757-899X/262/1/012019.

78. J.J. Beaudoin, C. MacInnis, Dimensional changes of hydrated portland cement paste during slow cooling and warming, Cement and Concrete Research. 2 (1972) 225-240. https://doi.org/10.1016/0008-8846(72)90044-0.

79. P. Suraneni, W.J. Weiss, Extending Low-Temperature Differential Scanning Calorimetry from Paste to Mortar and Concrete to Quantify the Potential for Calcium Oxychloride Formation, Advances in Civil Engineering Materials. 7 (2018) 1-16. DOI: 10.1520/ACEM20190001.

80. J. Monical, C. Villani, Y. Farnam, E. Unal, W.J. Weiss, Using Low-Temperature Differential Scanning Calorimetry to Quantify Calcium Oxychloride Formation for

Cementitious Materials in the Presence of Calcium Chloride, Advances in Civil Engineering Materials. 5 (2016) 142-156. DOI: 10.1520/ACEM20150024.

81. T. Kim, J. Olek, Effects of sample preparation and interpretation of thermogravimetric curves on calcium hydroxide in hydrated pastes and mortars, Transportation research record. 2290 (2012) 10-18. https://doi.org/10.3141/2290-02.

82. D. Glosser, P. Suraneni, O.B. Isgor, W. J. Weiss, Estimating reaction kinetics of cementitious pastes containing fly ash, Cement and Concrete Composites. 112 (2020) 11. https://doi.org/10.1016/j.cemconcomp.2020.103655.

83. D.A. Kulik, T. Wagner, S.V. Dmytrieva, G. Kosakowski, F.F Hingerl, K.V Chudnenko, U.R. Berner, GEM-Selektor geochemical modeling package: revised algorithm and GEMS3K numerical kernel for coupled simulation codes, Computational Geosciences. 17 (2013) 1-24. https://doi.org/10.1007/s10596-012-9310-6.

84. B. Lothenbach, D.A. Kulik, T. Matschei, M. Balonis, L. Baquerizo, B. Dilnesa, G.D. Miron, R.J. Myers, Cemdata 18: A chemical thermodynamic database for hydrated Portland cements and alkali-activated materials, Cement and Concrete Research. 115 (2019) 472-506. https://doi.org/10.1016/j.cemconres.2018.04.018.

85. T. Thoenen, W. Hummel, U. Berner, E. Curti, The PSI/Nagra Chemical Thermodynamic Database 12/07, 2014.

86. B. Lothenbach, T. Matschei, G. Möschner, F.P. Glasser, Thermodynamic modelling of the effect of temperature on the hydration and porosity of Portland cement, Cement and Concrete Research. 38 (2008) 1-18. https://doi.org/10.1016/j.cemconres.2007.08.017.

87. V.J. Azad, P. Suraneni, O.B. Isgor, W.J. Weiss, Interpreting the pore structure of hydrating cement phases through a synergistic use of the Powers-Brownyard model, hydration kinetics, and thermodynamic calculations, Advances in Civil Engineering Materials. 6 (2017) 1-16. DOI: 10.1520/ACEM20160038.

88. B. Lothenbach, F. Winnefeld, Thermodynamic modelling of the hydration of Portland cement, Cement and Concrete Research. 36 (2006) 209-226. https://doi.org/10.1016/j.cemconres.2005.03.001.

89. V. J. Azad, P. Suraneni, D. Trejo, W. J. Weiss, O. B. Isgor, Thermodynamic investigation of allowable admixed chloride limits in concrete, ACI Materials Journal. 115 (2018) 727-738.

90. K. Bharadwaj, R.M. Ghantous, F. Sahan, O.B. Isgor, W.J. Weiss, Predicting Pore Volume, Compressive Strength, Pore Connectivity, and Formation Factor in Cementitious Pastes Containing Fly Ash, Cement and Concrete Composites. 122 (2021) 13. https://doi.org/10.1016/j.cemconcomp.2021.104113.

91. D. Glosser, V. Jafari Azad, P. Suraneni, O.B. Isgor, W.J. Weiss, An extension of the Powers-Brownyard model to pastes containing SCM, ACI Materials Journal, 2019.

92. D. Glosser, A. Choudhary, J. Ideker, D. Trejo, W.J. Weiss, O.B. Isgor, Thermodynamic Investigation of Cementitious Mixtures Incorporating Off-Spec Fly Ashes, In the world of coal ash 2019 proceedings, Missouri, 2019.

93. H.F. Taylor, Cement chemistry, Thomas Telford London, V. 2, 1997, pp. 459

94. M. Balonis, F.P. Glasser, The density of cement phases, Cement and Concrete Research. 39 (2009) 733-739. https://doi.org/10.1016/j.cemconres.2009.06.005.

95. C. Qiao, P. Suraneni, W.J. Weiss, Damage in cement pastes exposed to NaCl solutions, Construction and Building Materials. 171 (2018) 120-127. https://doi.org/10.1016/j.conbuildmat.2018.03.123.

96. U.A. Birnin-Yauri, Chloride in cement: study of the system CaO-Al_2O_3-$CaCl_2$-H_2O, PhD thesis, University of Aberdeen, United Kingdom, 1993.

97. I. Galan, L. Perron, F.P. Glasser, Impact of chloride-rich environments on cement paste mineralogy, Cement and Concrete Research. 68 (2015) 174-183. https://doi.org/10.1016/j.cemconres.2014.10.017.

98. C. Qiao, N. Hosseinzadeh, P. Suraneni, S. Wei, D. Rothstein, Petrographically quantifying the damage to field and lab-cast mortars subject to freeze-thaw cycles and deicer application, Journal of Infrastructure Preservation and Resilience. 2 (2021) 1-12. https://doi.org/10.1186/s43065-021-00024-3.

99. W.J. Weiss, J. Olek, N.M. Whiting, P. Panchmatia, C. Qiao, P. Suraneni, Synthesis: Accelerating Implementation of Research Findings to Reduce Potential Concrete

Pavement Joint Deterioration, Report for a joint transportation research program, 2018, pp.59.

100. H.F.W. Taylor, C. Famy, K.L. Scrivener, Delayed ettringite formation, Cement and Concrete Research. 31 (2001) 683-693. https://doi.org/10.1016/S0008-8846(01)00466-5.

101. Rita M. Ghantous, K. Zetterberg, H. H. Becker, A. Behravan, M. T. Ley, O. B. Isgor, W. J. Weiss, A Dataset on the influence of air voids and fluid absorption on salt-induced calcium oxychloride damage, Dataset version 1.0, Oregon State University, School of Civil and Construction Engineering, Corvallis, Oregon, USA. (2022) 26 pages. https://doi.org/10.7267/z890s2587.

102. B.D. Barnes, S. Diamond, W.L. Dolch, Micromorphology of the interfacial zone around aggregates in Portland cement mortar, Journal of the American Ceramic Society. 62 (1979) 21-24. https://doi.org/10.1111/j.1151-2916.1979.tb18797.x.

Quantifying Calcium Oxychloride Formation Using Micro-Computed Tomography

Corresponding author: Hope Hall Becker, e-mail: hopebecker@jdh-gc.com

Hope Hall Becker[a], M. Tyler Ley[a], Qinang Hu[a], Rita M. Ghantous[b], and W. Jason Weiss[b]

[a] Department of Civil and Environmental Engineering, Oklahoma State University, Stillwater, OK 74074, USA

[b] School of Civil and Construction Engineering, Oregon State University, 1491 SW Campus Way, Corvallis, OR 97331, USA

Abstract

Deicing salts may accumulate within concrete paving joints which, over time, may cause damage due to calcium oxychloride formation. This study looks at mixtures with similar air contents and 20% and 40% fly ash replacement by mass that are saturated in calcium chloride solution and cycled through a range of temperatures. 3D X-ray micro-computed tomography scans are used to sequentially image the changes in the same sample after different temperature cycles. These images are correlated, and the damage propagation can be observed. This study shows the formation of a damage gradient within the sample that is the highest at the surface. The cracking is also observed to begin at the aggregate interface and progress into the matrix. These observations provide insights into the mechanisms of the damage and provide guidance to design concrete to resist this deterioration.

Keywords: Concrete, Air entrained concrete, Fly ash, Calcium oxychloride, Micro-Computed Tomography

1.0 Introduction

Concrete pavements have experienced damage near the joints due to the accumulation of deicing salts solution [1-6]. The absorption of this solution can result in an increase in the degree of saturation, which increases the potential for freezing and thawing damage for solutions with a low chloride concentration [7-11]. As the salt concentration increases, the potential for deleterious reactions between the solution and reacted products in the concrete increases resulting in the potential formation of Friedel's salt (FS), Kuzel's salt, and calcium oxychloride (CaOXY) [12-24].

Specifically, the calcium hydroxide $Ca(OH)_2$ that occurs as a part of the hydration reaction is susceptible to reaction with the deicing salt [25-36]. A typical chemical reaction for CaOXY is shown in Equation (1) [7, 8, 13, 15, 19-21, 37-47]; however, the amount and form of water may change with temperature and $CaCl_2$ concentration.

$$3\,Ca(OH)_2 + CaCl_2 + 12\,H_2O \rightleftharpoons 3Ca(OH)_2.CaCl_2.12H_2O \qquad (20)$$

Equation (1) is a reversible phase change that depends on the temperature and the $CaCl_2$ content as illustrated in Figure 1 [6, 47]. For systems in which the temperature is above the liquidus line, the $Ca(OH)_2$ + H_2O + $CaCl_2$ solution is a miscible fluid. When the temperature of the solution is decreased to below the liquidus line, the solution undergoes a phase change, and solid CaOXY begins to form. This phase change occurs above the temperatures necessary to freeze water. Figure 1 shows that at 20 percent $CaCl_2$ and 20ºC, solid CaOXY is present within the solution that can cause damage to the concrete.

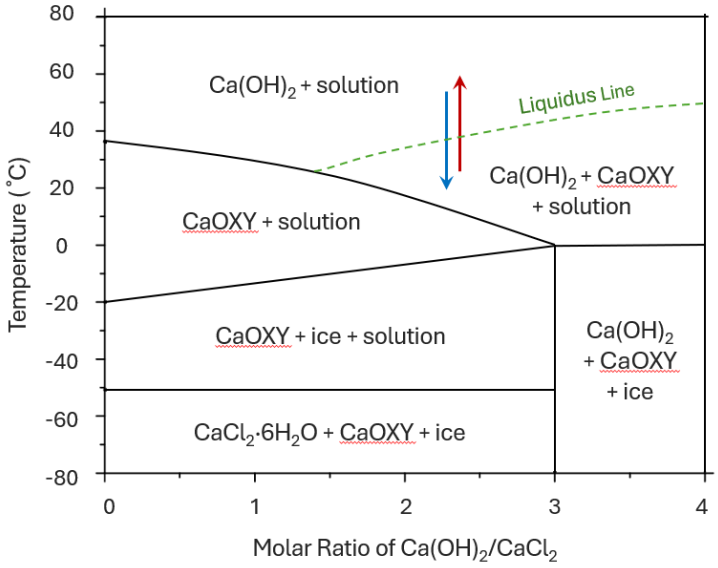

Figure 13 – Phase diagram of $Ca(OH)_2$-$CaCl_2$-H_2O system with 20% $CaCl_2$ solution, after [6, 40, 47].

The formation of CaOXY occurs on cooling and causes a reduction in volume [39, 41, 43]. On reheating, this volume change is reversed, and the material expands. The rearrangement of products during this phase change, accompanied by fluid absorption during cooling, can result in the development of pressure on reheating that may cause damage [15, 24, 48-50]. While studies have documented the overall volume changes associated with CaOXY formation [47, 51], there is a lack

of information about the distribution of the phases and how this causes damage to the concrete. This work uses X-ray micro computed tomography (Micro-CT) to capture 3D images of the same sample at different levels of CaOXY damage.

Micro-CT is a non-destructive x-ray tool that can be used to investigate the three-dimensional microstructure of materials [52, 53]. It has been widely used in medical science to investigate biological organisms [54-56]. This method has also been used to study construction materials to analyze crack propagation [57-59] and air void distribution [60-63]. The Micro-CT captures a series of radiographs from different angles. These radiographs can be used to build a three-dimensional model of the structure called a tomograph. This tomograph can then be used for qualitative and quantitative analyses [64-69]. Because Micro-CT is non-destructive, each sample can be scanned over time to observe changes. Previous examples of this to study the microstructure of concrete and mortar samples that have been exposed to freezing and thawing cycles [69-73]. However, for this study, the samples will not be exposed to freezing temperatures to ensure that the damage is only caused by CaOXY phase changes. Micro-CT will be used to quantify the product growth in air voids and crack formation within each sample at a high level of Degree of Saturation (DOS).

2.0 Experimental Methods

2.1 Concrete Materials and Mixture Proportions

Table 1 provides the oxide composition for the cementitious materials used in this study. The cement was an ASTM C150 Type I ordinary portland cement. The fly ash was an ASTM C618 Class C fly ash. Crushed limestone and natural sand from Oklahoma were used as aggregates. Both the fine and coarse aggregates met ASTM C33 standards. The maximum nominal aggregate size of the limestone was 19 mm (3/4 in). Table 2 shows the admixtures used that met the ASTM C260 and ASTM C494 standards.

Table 4 – Oxide composition of cementitious materials

Oxide (%)	SiO_2	Al_2O_3	Fe_2O_3	CaO	MgO	SO_3	Na_2O	K_2O	C_3S	C_2S	C_3A	C_4AF	LOI
Cement	21.1	4.7	2.6	62.1	2.4	3.2	0.2	0.3	56.7	17.8	8.2	7.8	2.7
Fly Ash	27.0	18.1	4.6	30.5	6.4	2.6	2.7	1.1	-	-	-	-	0.12

An air entraining admixture (AEA) was used in this study. The AEA is a wood rosin (WROS). Table 2 shows the two different mixture proportions studied in the laboratory testing. All the mixtures used a Class C fly ash replacement of 20% or 40% of the portland cement by weight. Each mixture also contained an air content of about 2.5% and 6%. This created four different concrete mixtures.

Table 5 – Concrete Mixture Proportions at SSD

Mixture	w/cm	Cement kg/m^3	Fly-Ash kg/m^3	Paste Volume (%)	Coarse Aggregate kg/m^3	Fine Aggregate kg/m^3	Water kg/m^3	Admixture Used
20FA	0.45	202	36	21	981	971	125	WROS
40FA	0.45	218	145	29	1098	712	163	WROS

2.1.2 Concrete Mixing

Aggregates from outdoor storage piles were gathered and moved indoors to a controlled temperature of 23° C +/- 1°C. After 24 hours, the aggregates were loaded into the mixer and spun. Samples were collected from the mixer for moisture correction. After moisture corrections were calculated, all the aggregate and two-thirds of the water were placed in the mixer and spun for three minutes [ASTM C566]. This time allowed for evenly distributed aggregates and for the aggregates to be closer to saturated surface dry (SSD).

The residual water, cement, and fly ash were added next and mixed for three minutes. While the mixing drum was scraped, the concrete mixture rested for two minutes. Following the rest time, the admixtures were added, and the mixer spun for an additional three minutes.

2.2 Concrete and Mortar Sampling and Testing

2.2.1 Sampling of Concrete and Mortar

Immediately after mixing the concrete was tested for slump (ASTM C143) and unit weight (ASTM C138) [74, 75]. Two 7L samples were tested simultaneously with the SAM (AASHTO T 395) by different operators [76]. These were used to find the average SAM Number of a

mixture. One hardened air-void analysis (ASTM C457) sample was made from each concrete mixture for testing [77].

After the concrete samples were made, mortar samples were prepared. The mortar samples were obtained from the same concrete mixture [78]. using a wet-sieving process. A 9.5 mm sieve was used to remove the coarse aggregate from the concrete. Two mortar cylinders were made from each sieved sample in 102 mm by 203 mm molds. Further testing was completed on these samples that will be discussed in section 2.3.

2.2.2 Sequential Air Method (SAM)

The SAM testing was performed as defined in AASHTO T 395 [76]. The SAM device applies three sequential pressures to fresh concrete and the equilibrium pressures are recorded. After the first pressure step, the air content is found like the ASTM C 231 Type B meter [79]. The pressure is then released, and the same steps are applied again to the fresh concrete. The SAM Number is calculated by taking the numerical difference between the final pressure steps. The difference between the pressure responses has been shown as indication of the air void size and spacing in the concrete [80].

2.2.3 Hardened Air Void Analysis Sample Preparation

Concrete samples were cut into 19 mm thick slabs and polished with sequentially finer grits [77]. The surface of the sample was preserved with an acetone and lacquer mixture to strengthen the surface before it was inspected under a stereo microscope. After an acceptable surface was obtained, the sample is cleaned with acetone. The surface was then colored with a black permanent marker, the air voids were filled with less than 1 μm white barium sulfate powder, and the air voids within the aggregates were blackened under a stereo microscope. This process makes the concrete sample black and the voids in the paste white. Sample preparation details can be found in other publications [81, 82]. The sample analyzed with ASTM C457 method C using Rapid Air 457 from Concrete Experts, Inc. A single threshold value of 185 was used for all samples in this research and the results do not include chords smaller than 30 μm. A traverse length of 2286 mm was used for all samples to satisfy the requirements of ASTM C457. These settings and sample processing methods are like methods used in other publications [82-84]. All air voids were used for the volume of chords less than 300 μm [85].

2.3 Mortar Testing

2.3.1 Measurement of $Ca(OH)_2$

Thermogravimetric Analysis (TGA) was performed on the ground powder from the mortar samples to determine $Ca(OH)_2$. The test was performed using approximately 30 mg of ground powder from the mortar. The sample was heated to 1000 °C at a rate of 10 °C/min under a nitrogen atmosphere. Corrections were made for the loss on ignition of the constituent ingredients in their relative volume. The amount of calcium hydroxide in the paste was estimated based on its mass loss during decomposition between 380 °C and 460 °C. For reference, a tested samples of plain cement paste had a coefficient of variation of $Ca(OH)_2$ of approximately 1% [86, 87].

2.3.2 Coring and Saturation of Samples

After curing, the mortar samples (obtained by wet sieving) were demolded and cut using a water-cooled diamond saw into 30 mm thick discs before being cored to cylinders with 10 mm diameter and 30 mm heights [47]. The cylinders were then trimmed using a water-cooled, precision diamond saw to have parallel surfaces [88]. The final dimensions of the cylindrical cores are nominally 10 mm in diameter and 20 mm in height. The cores were then exposed to 60°C temperature until reaching a constant mass (mass evolution over 24 hours is less than 0.01%). The samples were then vacuum saturated with lime-water solution under a vacuum pressure of 6 Torr. The mortar cores were immersed in lime solution for an additional 24 hours at 23 ± 2°C. They were then kept immersed in lime solution at 50 ± 1°C for an additional 24 hours.

Table 6 – Mortar samples investigated.

Sample ID	% Fly Ash	Fresh Concrete Properties		Hardened Concrete Properties		Hardened Mortar Properties	
		Air Content	SAM Number	Spacing Factor [µm]	Specific Surface [mm^{-1}]	Initial Mass [g]	Initial Length [mm]
20FA	20	5.4%	0.16	157	27.9	3.40	19.16
40FA	40	5.9%	0.10	163	29.3	3.70	21.45

2.3.3 Mortar Sample Mass and Length Measurements

All the samples were measured for mass using a scale with accuracy of 0.01g and length using a micrometer with accuracy of 0.00254 mm. The samples were measured at the completion of each cycle.

2.3.4 Temperature Cycling of Samples

To prepare the samples for CaOXY formation a thermal cycling process was used. Figure *2* outlines the temperature cycling and scanning timeline for each sample. After the samples were removed from the lime solution, they were scanned (Scan1) using the Micro-CT. Following the scan, the samples were placed directly in 20% $CaCl_2$ solution that was equilibrated at 50 ± 1°C for an additional 24 hours, then scanned (Scan2) again using the Micro-CT. The amount of the solution was three times the volume of the sample. Based on a pore volume of 20%, this results in an actual concentration of 18.75% $CaCl_2$ in the pore solution. With the binding of chlorides within hydration products, the $CaCl_2$ concentration in the pore solution will further decrease. The immersion in salt solution at 50°C was to increase the penetration of the salts into the pores of the mortar before forming CaOXY [47, 51]. After scanning the sample, it was placed in a temperature-controlled chamber to be cycled through a series of temperatures: 5°C for 12 hours, 23°C for 10 hours, and 50°C for 30 minutes. This cycle time was based on [47].

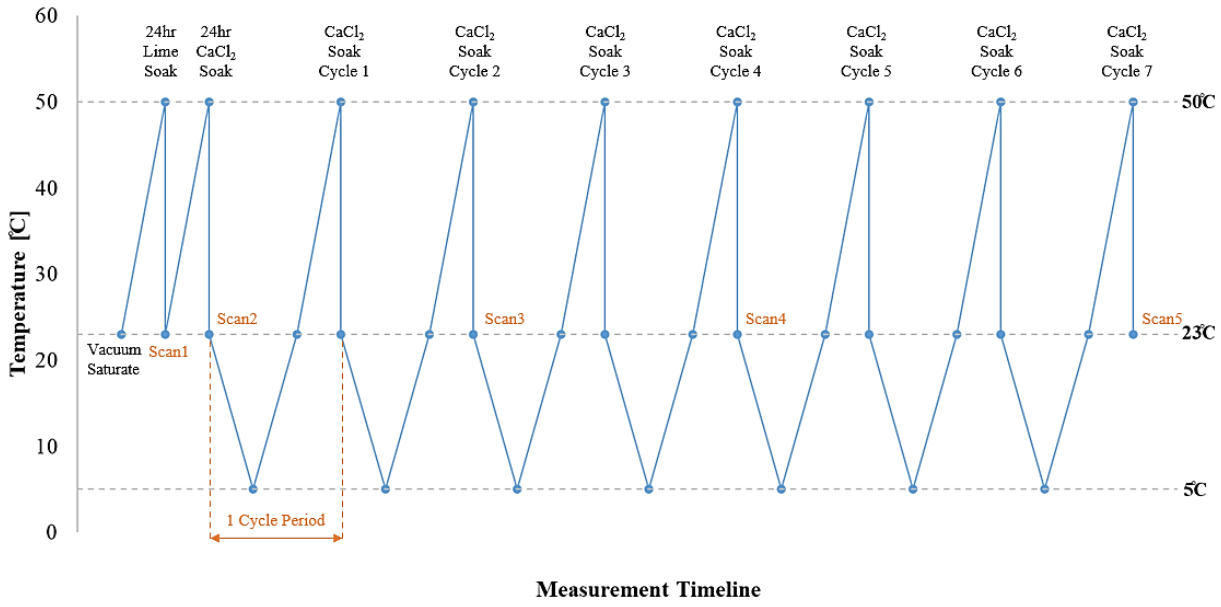

Figure 14 – Temperature cycling versus time. The timing for each scan is also shown.

The mortar samples were scanned with the Micro-CT at different stages throughout the process. These stages are listed in Table 4.

Table 7 – Scans throughout soaking and temperature cycling

Sample ID	% Fly Ash	Micro-CT Scans				
		Scan1	Scan2	Scan3	Scan4	Scan5
		24hr Lime Soak @ 50C	24hr CaCl Soak Solution @ 50C	CaCl Soak Solution for 2 cycles	CaCl Soak Solution for 5 cycles	CaCl Soak Solution for 7 cycles
20FA M1	20	1	1	1	1	1
40FA M1	40	1	1	1	1	1

2.4 Micro Computed Tomography (Micro-CT)

The scanning was done by a ZEISS XRADIA 410 with a photon energy of 90 keV at a resolution of 4.97 µm/pixel using glass filter LE6 from the manufacturer. The volume of the interest (VOI) was a cylinder 5.0 mm in diameter and 5.0 mm in height located near the surface of the sample as shown in Figure 3. The Micro-CT x-ray settings for each scan are shown in Table 5.

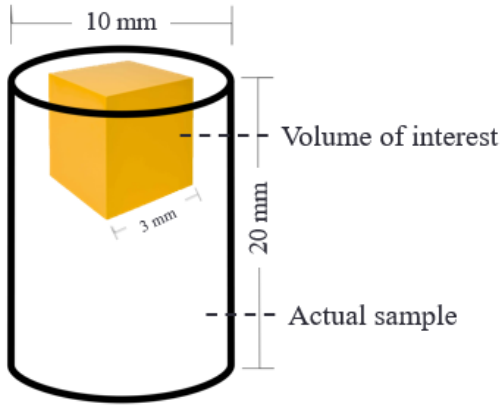

Figure 15 – Location and dimension of the investigated volume of interest (VOI).

Table 8 – ZEISS XRADIA 410 scan settings.

Resolution	4.97 µm/pixel
Source Energy	90 keV
Optical Magnification	4X
Exposure Time	8.5 seconds
Number of Projections	2100
Total Exposure Time	5.5 hours

The images were reconstructed using XMReconstructor to create a library of 2D cross-sectional images. These images were stacked to enable a 3D image of the entire scan. A dataset from a

representative sample is shown in Figure 4. This shows a 3D tomography, a 2D cross-section of the reconstructed image, and the corresponding grayscale histogram for a sample [66]. Each 16-bit image consists of pixels with gray values ranging from 0 to 255 corresponding to x-ray absorption which is a function of density and composition of the material [89, 90]. The range in gray values can be used to separate the sample into different elemental phases by an image segmentation process [57, 61, 91]. The main mortar components are air voids, paste, and aggregates. The x-ray absorption for air voids is the lowest because they are the least dense. The lower the density of the element, the darker the voxels in the reconstructed images. The aggregates and un-hydrated cement particles have higher densities, which makes them appear lighter gray to nearly white. The paste of the sample falls somewhere between the voids and aggregate gray values. This can all be observed in Figure 4.

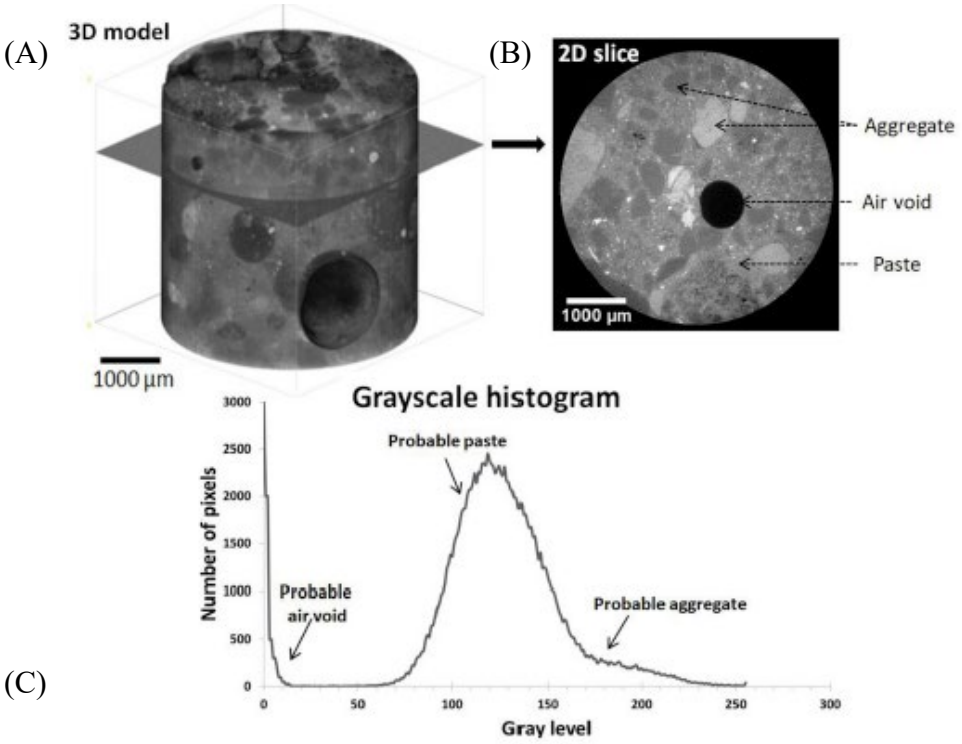

Figure 16 – (A) An example of the Micro-CT dataset with the 3D tomography, (B) a 2D cross-section of the reconstruction image, and (C) the corresponding grayscale histogram for a sample [66].

2.5 Image Processing and Analysis

All images were processed, investigated, and visualized using ImageJ software and MATLAB codes. These techniques were used to provide quantitative and qualitative data from Micro-CT images. Each set of images was aligned with the initial set of images. This alignment would improve accuracy for segmentation and phase identification of each set.

2.5.1 Alignment of Micro-CT Datasets

For each set of images, 16-bit reconstruction images were created. To compare each sample from one scan to another, alignment was necessary. Before aligning the images, a histogram shift was used to match the grayscales in the images [62, 66, 69]. This would correct any grayscale shift in values between scans due to automatic normalization during reconstruction. Matlab coding was then used to align the Micro-CT image datasets from one cycle to another. The alignment algorithm was used with Scan2 as the reference scan for the subsequent scans. In this process, some identifiable feature regions such as void clusters or high-density sand grains were handpicked throughout all scans, and their coordinates were used to find the 3D affine transformation matrices to align the following scans with the reference scan. Details of the technique can be found in other publications [57, 92, 93]. However, this alignment technique did not fully account for the rigid body movement of the sample between the scans. If the regions of the sample moved in different directions from changes in the microstructure from the formation of cracks, it is difficult to find a single affine matrix that could consider those individual movements. That makes the full region of the sample difficult to align using this technique. To solve this, the alignment was completed on a smaller region so that the relative movements would be small and so the alignment was still possible. For quantitative analyses, some small regions with some identifiable features with the dimensions of 1 mm x 1 mm x 1 mm were cropped and aligned individually to compare between different scans.

2.5.2 Segmentation

Segmentation of the Micro-CT imaging was used to create quantitative data. In this study, a threshold value was chosen to segment the regions of voids. This paper uses the term void to

describe the measurements that do not contain solids. There are voids that are below the resolution of the Micro-CT that are not included in this analysis. The threshold value was adjusted and then chosen when the overall void percentage of Scan 1 matched the results from the fresh testing. The voids observed in the initial scan are labeled "air voids". This same segmentation process was used in subsequent scans. If a void space was observed in subsequent scans that did not exist in the initial scan, then this volume is labeled as a "crack" as this is void space that has formed in the hardened matrix. It was also observed that volumes that were initially air voids in Scan 1 were later filled with a solid with additional temperature cycles. These volumes were labeled as "products" as they are materials that are forming in previously existing void space.

3.0 Results

3.1 $Ca(OH)_2$ Content

The $Ca(OH)_2$ content in the 20% fly ash and 40% fly ash mixtures was determined to be equal to 10.6 $g/100g_{paste}$ and 4.5 $g/100g_{paste}$ respectively [47]. This decrease in $Ca(OH)_2$ content is caused by the pozzolanic reaction with fly ash that was added. The lower amount of $Ca(OH)_2$ will decrease the CaOXY content, which is expected to decrease the damage to the sample. The CaOXY content in each sample is equal to 13.6 $g/100g_{paste}$ and 5.4 $g/100g_{paste}$ for mixtures containing 20% and 40% fly ash respectively [47]. This also shows that the sample with 40% fly ash replacement is expected to have less damage than the 20% fly ash sample.

3.2 Mortar Sample Mass and Length Changes

Figure 5 shows the results from the measurements for the 20FA M1 sample and the 40FA M1 sample. Each percent change in length measurement is labeled by the cycle time and scan. The percent change in length is the length of the sample minus its initial length divided by its initial length. The figure shows that the sample with 40% fly ash stays below 0.50 percent length change, while the sample with 20% fly ash steadily increases in length after cycle 2. The increase in length could be internal damage from the formation of cracks. This damage will be discussed later in the paper. At cycle 7, the sample was visibly damaged with crumbling particles falling off the edges of the sample.

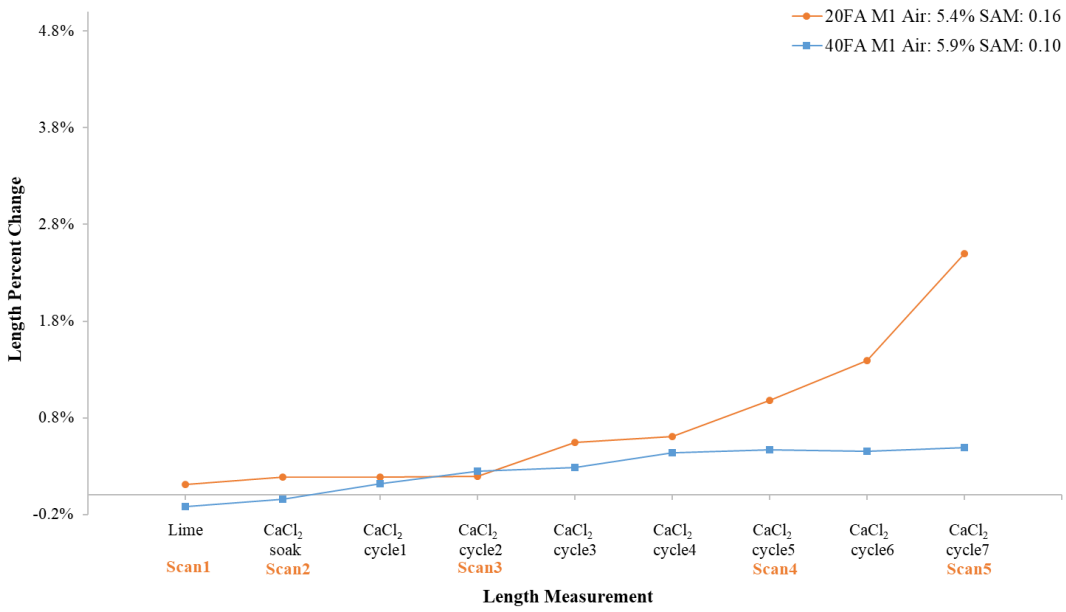

Figure 17 – Length measurement versus percent change.

3.3 Micro-CT Imaging Analysis

3.3.1 Micro-CT Imaging Compared to Segmentation of Voids

Table 6 shows a 3 mm square scan from an interior volume from the 20FA M1 mixture. This is the sample that showed expansion in Figure 5. The first row of images are the raw scans from different cycles. The second row of images shows the segmented voids. The black represents the solids within the sample and the white represents air. At cycle 5, there is a decrease in the volume of the air voids and an increase in cracking. Cycle 7 shows further damage to the sample. The cracks primarily form at the transition zone around the aggregate. The cracks may form here because the transition zone is expected to have a higher concentrations of $Ca(OH)_2$ than the other parts of the structure which has been often seen in field samples with damage around aggregate. Further, the cracks may start at the interface due to dissimilar stiffness, moisture content, and coefficients of thermal expansion between the paste and aggregate resulting in stress concentrations [94].

Table 9 – Images from the grayscale histogram correction process and segmentation of voids for the 20FA M1 sample. Each image is 3 mm x 3 mm in size.

Description	Lime 50C soak	$CaCl_2$ 50C soak	$CaCl_2$ cycle 2	$CaCl_2$ cycle 5	$CaCl_2$ cycle 7
Image after gray value histogram correction	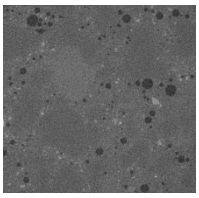	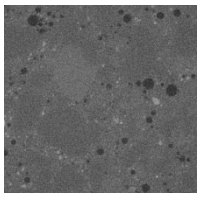	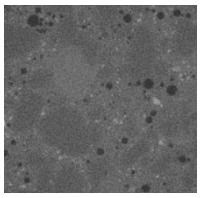	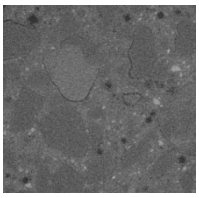	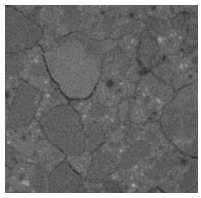
Segmentation of voids	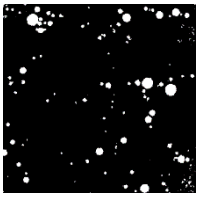	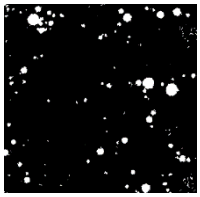	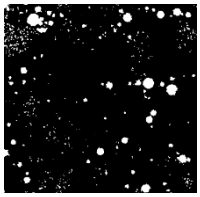	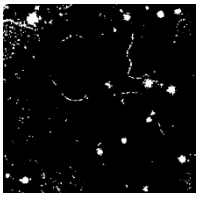	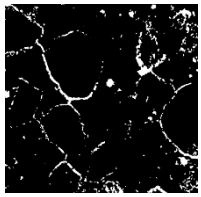

Table 7 shows a slice from a 3 mm cube from the interior VOI displayed in Figure 3 for 40FA M1 mixture. This is the sample that showed minimal expansion after 7 cycles in Figure 5. The first row of images shows a slice without segmentation and the second row of images shows the same slice after segmentation. This matches what is shown in Table 7. The voids in these scans are not changing in size and there is no cracking observed as the temperature cycles increase. The lack of damage is due to the higher fly ash replacement, which decreases the level of $Ca(OH)_2$ within the mixture [95, 96].

Table 10 – Images from the grayscale histogram correction process and segmentation of voids for the 40FA M1 sample. Each image is 3 mm x 3 mm in size.

Description	Lime 50C soak	$CaCl_2$ 50C soak	$CaCl_2$ cycle 2	$CaCl_2$ cycle 5	$CaCl_2$ cycle 7
Image after gray value histogram correction	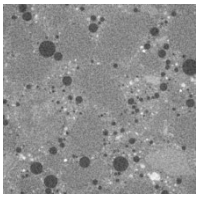	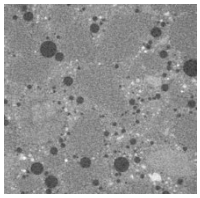	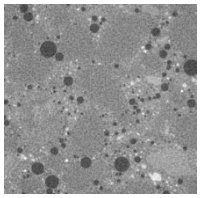	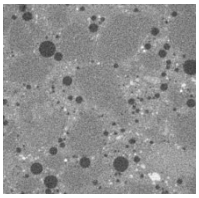	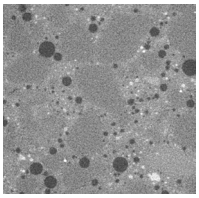
Segmentation of voids				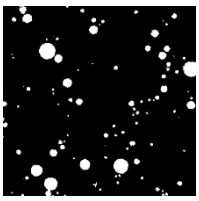	

3.3.2 Quantifying Damage within Samples

To quantify the damage within the sample throughout each scan, the total volume of voids is plotted for different temperature cycles. In Figure 6, the 20FA M1 sample shows an increase in the volume of air voids and cracks in the sample. This matches the visual observations from Table 7 but this provides quantitative evidence. The increase in cracks begin after the second temperature cycle where the sample is soaked in $CaCl_2$. The 40FA M1 sample shows a consistent volume of air voids and cracks within the sample. This result agrees with the images shown in Table 7.

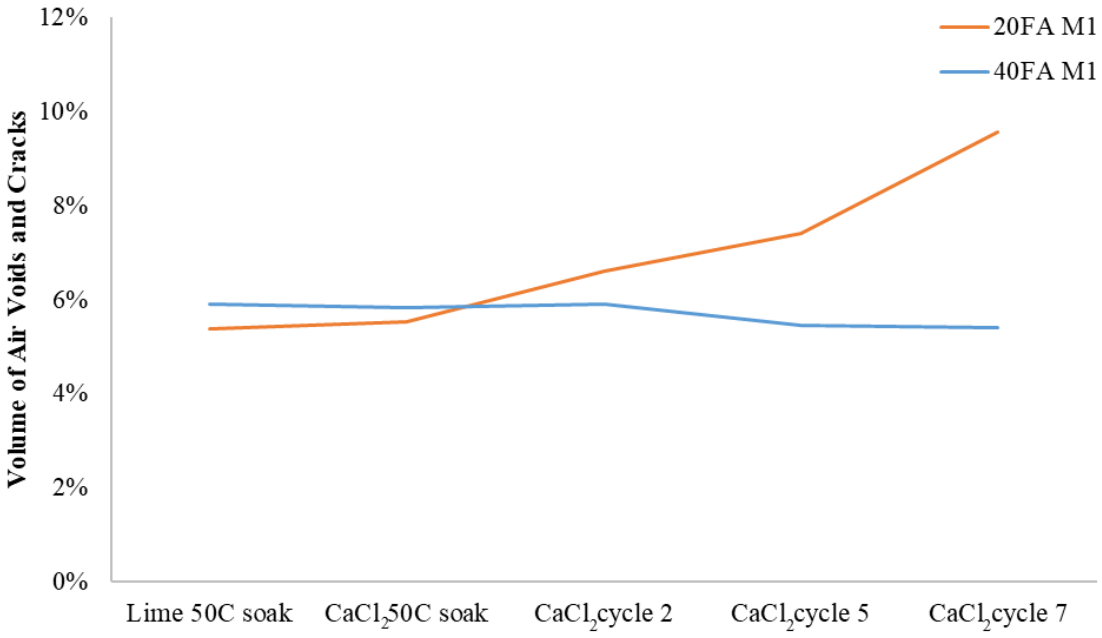

Figure 18 – Total volume of air per scan for 20 percent and 40 percent fly ash replacement.

To obtain more information about the distribution of the voids in the sample, the samples were evaluated from the surface of the sample to a depth of 3.8 mm. The plot shown in Figure 6 shows the change in the volume of air voids and cracks over the depth of the sample. Figure 7 also contains slices from a depth near the surface and 3.0 mm from the surface from $CaCl_2$ solution cycle 7 for the 20FA M1 sample. This plot shows the change in volume of air voids and cracks compared to the initial scan taken after placing the sample in lime water solution at 50ºC. The data is plotted this way to help show the difference between the scans. For example, the total volume of voids at the surface (0.0 mm) for $CaCl_2$ cycle 7 was 7.3% greater than the volume of voids at the surface for the lime soak. The image included in the figure shows the surface of the sample and the significant cracking that is observed. There are several large cracks visible around the aggregates in the image. These changes are noticeable starting at cycle 2. The change in volume of voids for cycle 7 at 3.0 mm depth was 1.5%. This is 5.8% less void volume than at the surface. This means that there is more damage at the surface of the sample compared to the interior. This is probably because the surface of the sample was in contact with the $CaCl_2$ solution. As damage increases this will allow more solution to enter the concrete and damage the sample.

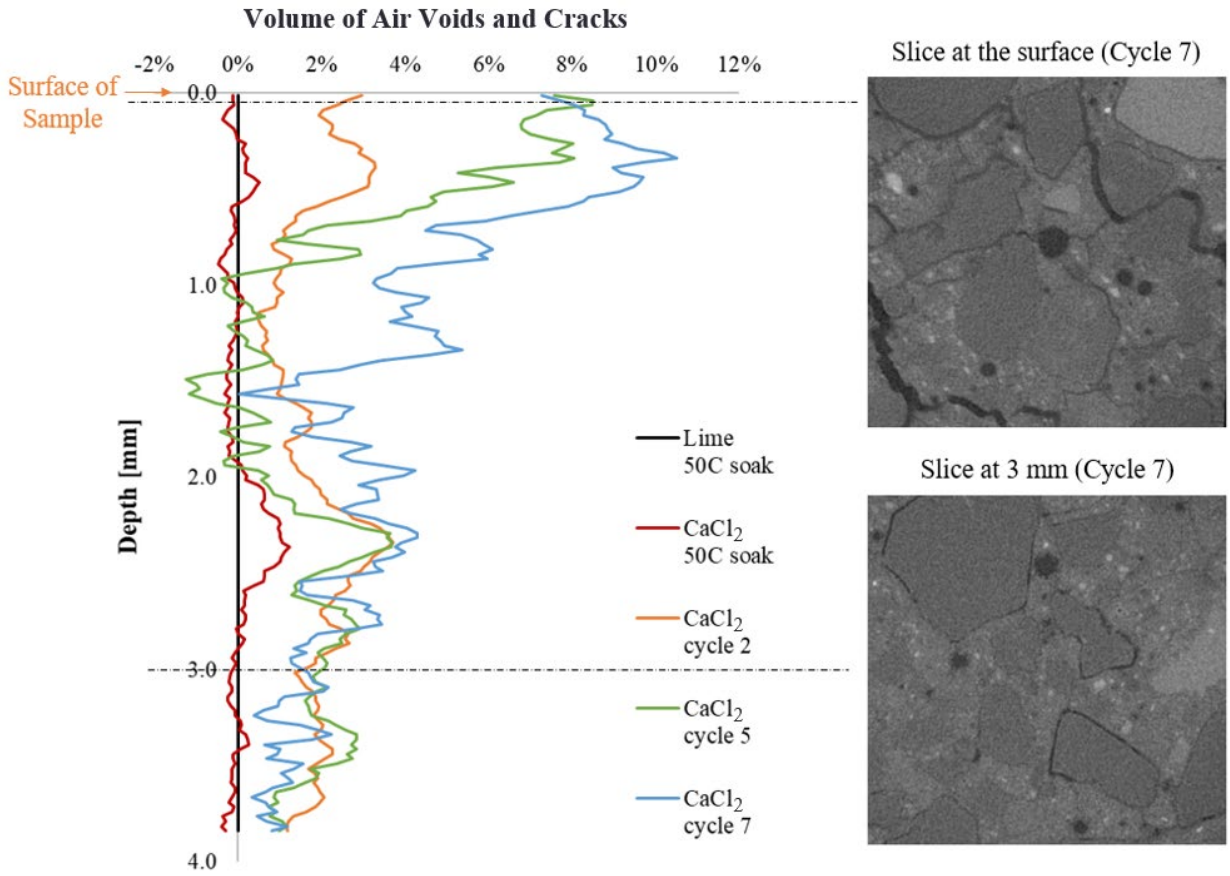

Figure 19 – Change in the total volume of air over the depth of the 20 percent fly ash sample. Each image is 3 mm x 3 mm in size.

Figure 8 shows the same plot and slices as Figure 7, but for the 40 percent fly ash sample. There was minimal change in the volume of air voids and cracks for each cycle. These small changes are likely caused by noise in the images. Cross section images are included from the surface and at a depth of 3.0 mm. The difference in performance is because the damaged sample in Figure 7 used 20% fly ash replacement and contained 10.6 g/100g_{paste} of $Ca(OH)_2$ and the sample in Figure 8 with 40% fly ash replacement contains 4.5 g/100g_{paste} of $Ca(OH)_2$.

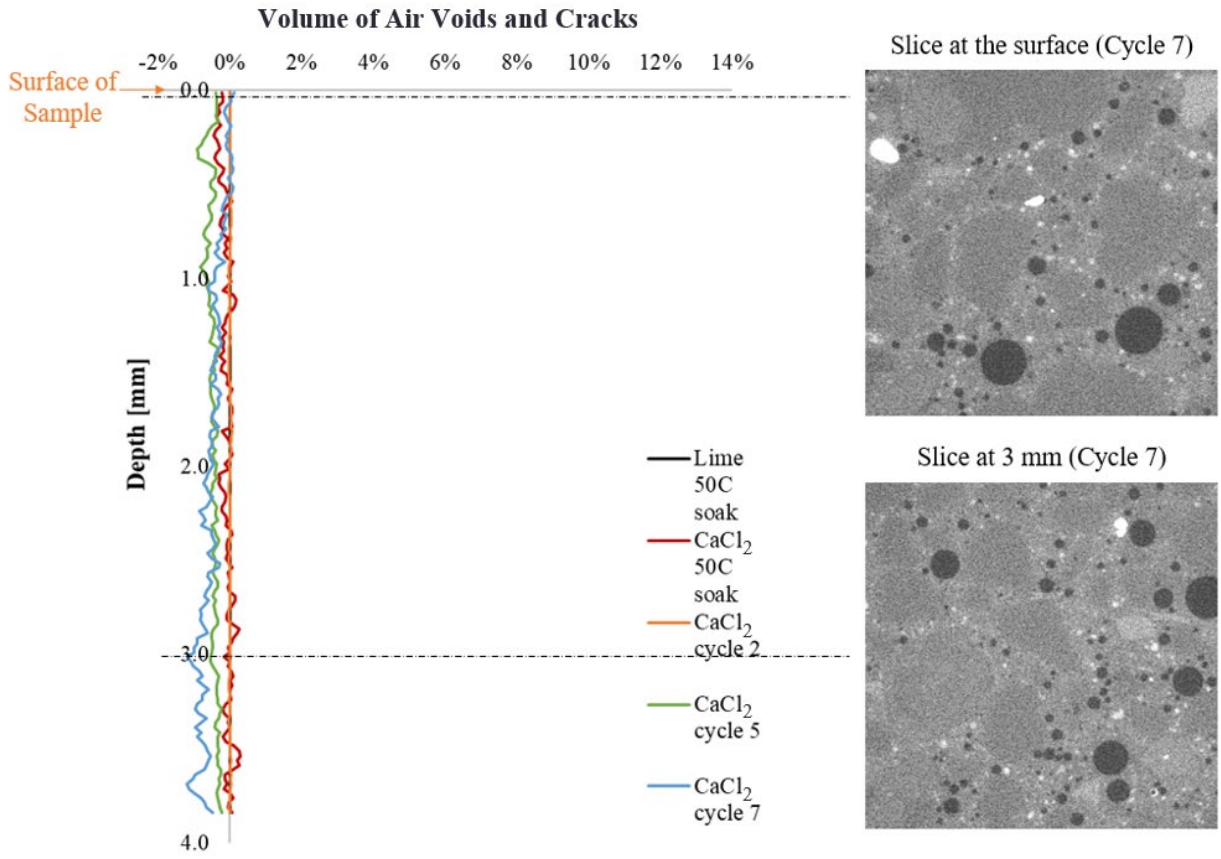

Figure 20 – Change in the total volume of air over the depth of the 40 percent fly ash sample. Each image is 3 mm x 3 mm in size.

3.3.3 Micro-CT Imaging of Individual Voids

Smaller regions of the sample were investigated to follow the changes of individual voids. In Table 8, a raw scan from each cycle for sample 20FA M1 is shown along with a segmented version of the image, a 3D model of an individual air void, the volume of that air void, and the change in measured volume compared to the initial scan. Each image represents a 1 mm cube within the 3 mm cube previously studied.

The segmentation of voids shows air voids filling and cracks forming as the sample was cycled through temperature changes. The 3D model shows how the volume of a single air void changed over time, which is circled in the segmented image. The percentage of initial void starts at 100 percent for the lime soak at 50ºC. By cycle 5, the volume of air void has reduced to 66 percent of the initial void volume and by cycle 7, it has reduced to 43 percent of the initial air volume. These air voids appear to fill with solids over time. These solids may be formed by water being forced into the voids by the phase change of the CaOXY. If the air voids are filled over time by solids, then these voids can no longer protect the concrete from freezing

events or from the pore pressure increases by the CaOXY phase change. Although this study did not examine the chemical makeup of the material in the voids, others have investigated this and determined that it is made up of ettringite and CH [69].

Table 11 – Imaging and air volume analysis of 20FA M1 scans 1 through 5. Each image is 1 mm x 1 mm in size.

Description	Lime 50C soak	$CaCl_2$ 50C soak	$CaCl_2$ cycle 2	$CaCl_2$ cycle 5	$CaCl_2$ cycle 7
Image after gray value histogram correction	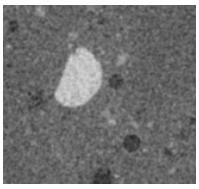	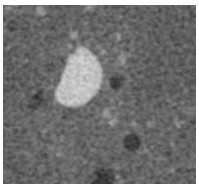	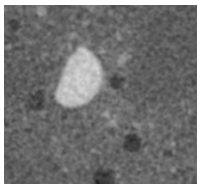	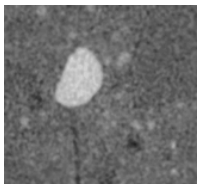	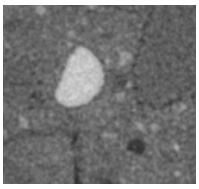
Segmentation of voids	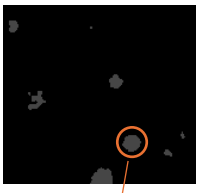	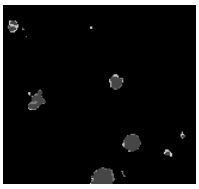	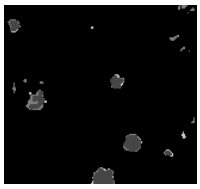	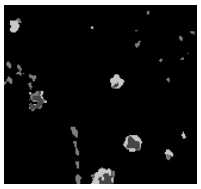	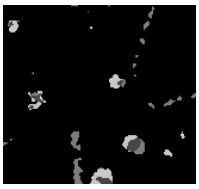
3D void model	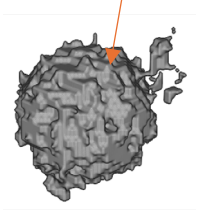	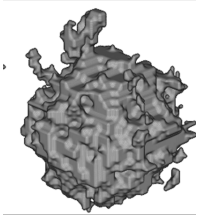	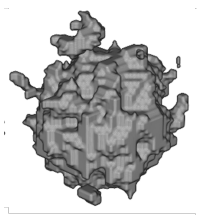	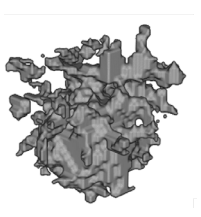	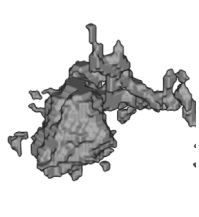
Volume of void [μm^3]	1171125	1129250	1152125	768750	501750
Volume change compared to Lime 50C soak	100%	96%	98%	66%	43%

In Table 9, each cycle for sample 40FA M1 is shown that mirrors Table 8. The most volume reduction observed is 3%. This is a minimal decrease in volume compared to the 57% reduction in volume shown in Table 9. The 3D images also show minimal change in the void. Minimal damage is observed because of the higher fly ash replacement and therefore the reduced CaOXY formation.

Table 12 – Imaging and air volume analysis of 40FA M1 scans 1 through 5. Each image is 1 mm x 1 mm in size.

Description	Lime 50C soak	$CaCl_2$ 50C soak	$CaCl_2$ cycle 2	$CaCl_2$ cycle 5	$CaCl_2$ cycle 7
Image after gray value histogram correction	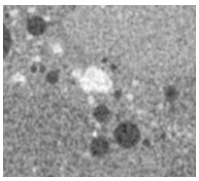	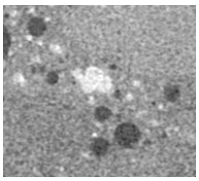	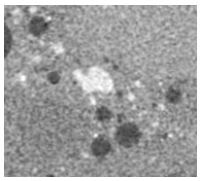	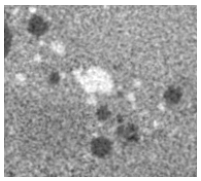	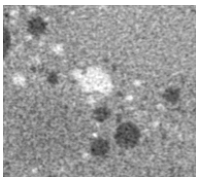
Segmentation of voids		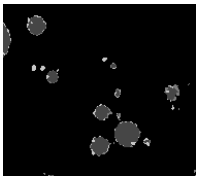	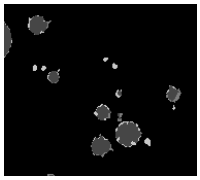	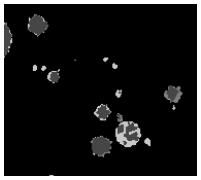	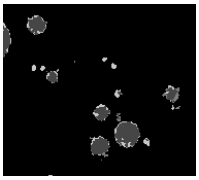
3D void model	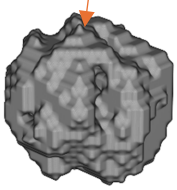	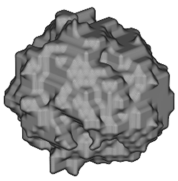	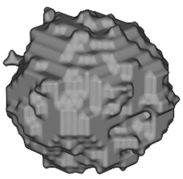	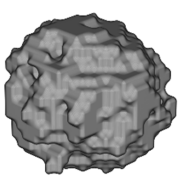	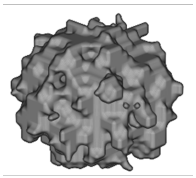
Volume of void [μm^3]	441500	434875	440375	454375	427250
Volume change compared to Lime 50C soak	100%	98%	100%	103%	97%

Figures 9 and 10 extend the results from Tables 9 and 10 to the entire sample. The results reported do not include cracks. The air voids are determined in the scan after soaking the sample in 50ºC lime water and these same volumes are revisited in subsequent scans to determine their change in volume.

In Figure 9 and 10, the line for the sample soaked in lime water at 50ºC shows the initial air void distribution. As the lines move lower this shows a decrease in the air void volume. In both figures, the sample soaked in $CaCl_2$ for the first and second cycles is slightly lower than the initial air volume. This is possibly due to pore filling. Also, there is minimal difference between the "$CaCl_2$ 50C soak" scan and the "$CaCl_2$ cycle 2". This shows that the experimental method is repeatable.

In Figure 9, significant changes in the total volume of air begin to occur starting at cycle 2. The results show that the cumulative air void volume has decreased by roughly 56% by cycle 5 and 70% by cycle 7. This shows the significant air void filling that occurs from temperature

cycling in the 20% $CaCl_2$ solution. As stated previously, once these air voids fill, the protection against freeze thaw and CaOXY damage is reduced.

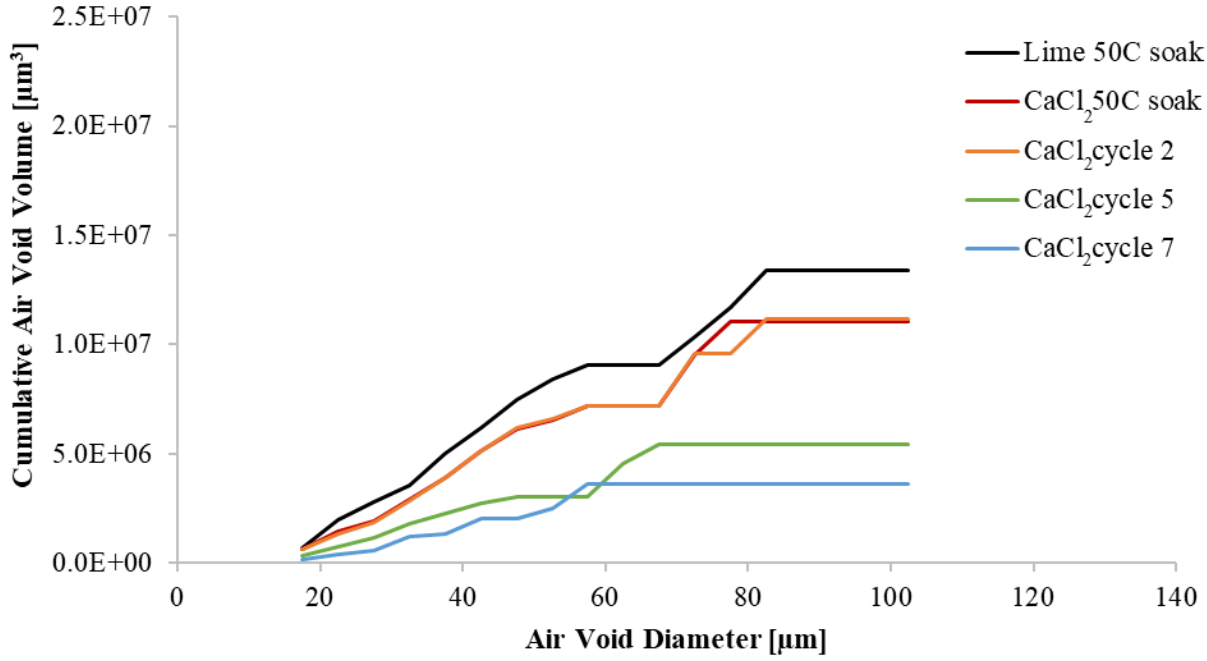

Figure 21 – Cumulative air void volume for the 20% fly ash sample. The results reported do not include cracks. The air voids are determined in the scan after the 50ºC lime soak, and these same volumes are revisited in subsequent scans to determine their change in volume.

The 40% fly ash sample shows a significantly different performance when compared to the sample with 20% fly ash. The total reduction in air void volume is only 20% at the end of the testing. Also, this volume change occurs in voids with a diameter greater than 80 µm. It is important to note that these larger voids are not as critical in providing protection against freeze thaw damage compared to the smaller voids [97]. This occurs because less CaOXY is expected to form in this sample because of the higher fly ash replacement level.

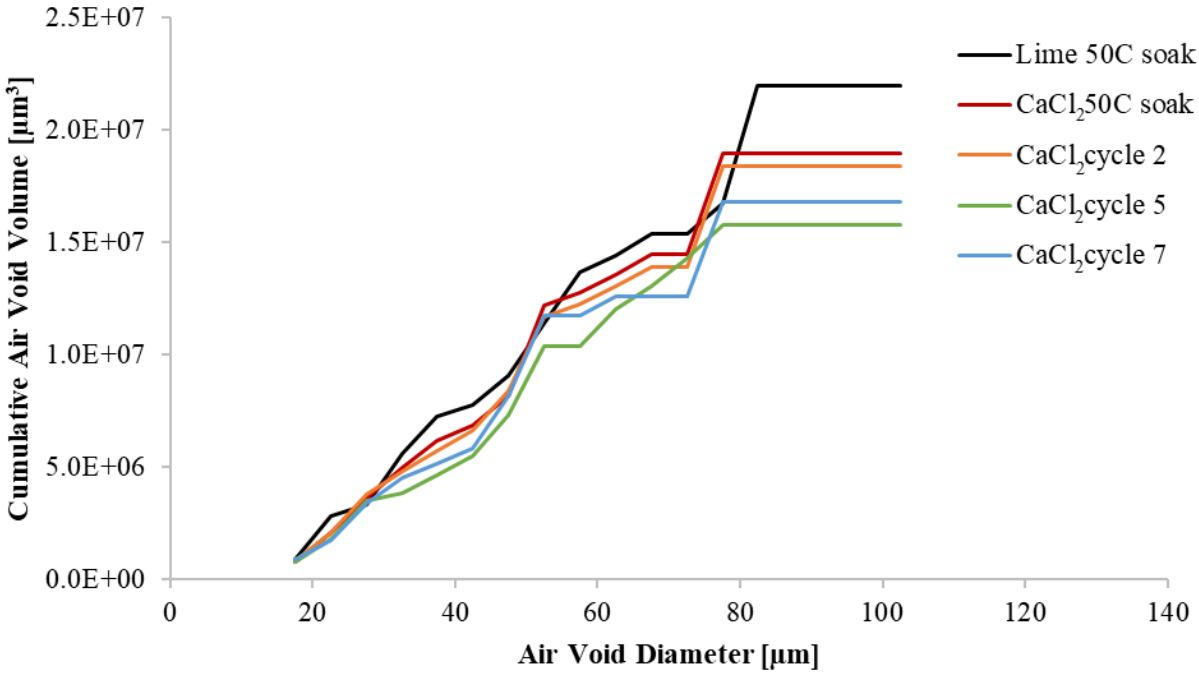

Figure 22 – Cumulative total volume of air in relation to the air void diameter for each scan of sample 40FA M1. The results reported do not include cracks. The air voids are determined in the scan after the 50ºC lime soak, and these same volumes are revisited in subsequent scans to determine their change in volume.

4.0 Mechanisms of CaOXY Damage

This work provides a direct observation of the progressive damage caused by CaOXY in concrete. This provides insights into the location, rate, and volume of damage. Since this work investigated a 20% fly ash sample that was damaged and a 40% fly ash sample that was not damaged then this allows a comparison to be made of the accuracy and repeatability of the experimental techniques.

Figure 7 shows that between cycle 2 and cycle 5, the sample with 20% fly ash shows an increase in damage from the surface to 1 mm deep within the sample. At this same time, the air voids are starting to fill, and the sample is changing length. This continues between temperature cycle 5 and cycle 7. The damage continues to increase at the surface and extends up to 1.5 mm deep within the sample. By the end of cycle 7, the air voids between 20 µm and 100 µm lose 70% of their volume from infilling.

The higher damage at the sample surface occurs because that is where the 20% $CaCl_2$ solution is in direct contact with the sample. As the concrete cracks, this allows a higher amount of $CaCl_2$ within the sample, which reacts to form more CaOXY. As the cycles increase, this causes more damage to the sample. Within the sample, the cracking is first observed in the transition zone around the aggregates. This occurs because the transition zone is expected to have a higher concentration of $Ca(OH)_2$.

The air void filling is likely due to high concentration of dissolved ions in the pore solution. As the temperature decreases, the CaOXY phase change will occur, causing an increase in volume. This increase in volume forces the solution from the capillary pores into the air voids. These air voids are likely empty because the sample is below the critical degree of saturation. Once the forced pore solution reaches the air void, the pressure is relieved because the pore solution is no longer confined. Once the pressure is reduced, the ions saturated in the pore solutions will form solids. As the temperature rises, the CaOXY phase change occurs causing a decrease in volume. This allows the solution in the voids to drain into the capillary pores leaving the formed solids in the air voids. As this process repeats, the air voids will continue to fill with solids. As the air voids decrease in volume, this reduces the amount of protection from future CaOXY phase changes.

5.0 Practical Significance

The damage observed in this paper resembles the damage observed at sawed joints with poor drainage in field pavements that receive chloride deicing chemicals. Because of the sawing, these joints often have aggregates with exposed transition zones that can react with the salt solution. Many field projects have observed air void filling near the joints [98]. The observations and mechanisms discussed in this paper explain why this occurs.

It is important to note that the temperature cycling that causes damage occurs at moderate temperatures and does not require temperatures typical of freezing water. This means that the temperature cycles can be experienced outside winter months and so the cycles caused by CaOXY may be high for these pavements.

If the air voids within the sample fill because of the CaOXY phase change then the air voids will lose their effectiveness to protect the concrete from both CaOXY and freeze thaw damage. This means that concrete could be damaged in the winter from freeze thaw and continue to be

damaged in other months by CaOXY. This is why the damage can be so rapid and severe in the field.

A critical takeaway from this work is that CaOXY damage can be stopped by using enough fly ash in the mixture to reduce the $Ca(OH)_2$ in the sample below a critical limit. While the air void content is helpful, it will only temporarily delay the CaOXY damage if enough $Ca(OH)_2$ is present. One practical method to address CaOXY is to use a supplementary cementitious material like fly ash and to entrain air in the sample. This has been investigated in previous research and for typical air contents of 6% and when fly ash is used at 30% replacement by mass, this seems to be sufficient to prevent damage from CaOXY [47].

6.0 Conclusions

For this study, mortar samples that were wet sieved from concrete were examined using Micro-CT imaging and length change measurements. Both samples had similar values of entrained air but different fly ash replacement levels. One sample used 20% fly ash replacement and the other had 40% fly ash replacement. Throughout the study it shows that the sample with 20% replacement experiences more air void filling and cracking than the 40% fly ash sample. The following can be observed from this work:

- For the 20% fly ash sample, the length change steadily increased by 2.50% between cycles 2 and 7, while there was only 0.50% length change for the 40% fly ash sample.
- The cracks were primarily observed around the aggregates. This may be because of the higher amount of $Ca(OH)_2$ in the transition zone that may form CaOXY.
- For the sample with 20% fly ash replacement, there was an 8% increase in volume at the surface and a 2% increase in volume at 3 mm from the surface from CaOXY damage. There was no cracking observed in the 40% fly ash replacement sample under the same conditions.
- The sample with 20% fly ash replacement had a 56% reduction in the air voids between cycle 2 and 5, and a 70% reduction in the air voids between cycles 2 and 7. While the sample with 40% fly ash replacement showed no changes.

This work provides fundamental insights into the changes in the microstructure and air voids caused by the formation of CaOXY. The observations in this work also match previous field observations and other publications [47]. CaOXY is an issue that has caused significant destruction, and these observations provide insights and discussions about the mechanisms of CaOXY formation and how the damage propagates in concrete and reduces the ability to resist freeze thaw damage.

7.0 Acknowledgements

The authors would like to acknowledge funding from the Oklahoma Transportation Center and Pooled Fund TPF-5(448) and the supporting states. Special thanks to Jason Weiss for the discussion over this work. We would also like to thank David Porter, Sonia Li, Stephanie Castro, Rachel Schwartz, and Lizzie Long for their assistance in preparing and analyzing samples.

8.0 References

1. Del Mar Arribas-Colón, M., et al., *Investigation of Premature Distress Around Joints in PCC Pavements: Parts I & II*. 2012, Joint Transportation Research Program, Indiana Department of Transportation and Purdue University, West Lafayette, Indiana: Publication FHWA/IN/JTRP-2012/25 & FHWA/IN/JTRP-2012/26.
2. Jones, W., et al., *An Overview of Joint Deterioration in Concrete Pavement: Mechanisms, Solution Properties, and Sealers*. 2013: West Lafayette, Indiana.
3. Castro, J., et al., *Durability of saw-cut joints in plain cement concrete pavements*. 2011, Purdue University. Joint Transportation Research Program.
4. Graveen, C., et al., *Performance Related Specifications (PRS) for Concrete Pavements in Indiana, Volume 2: Technical Report.* 2009.
5. Olek, J., M. Radlinski, and M. del Mar Arribas. *Premature deterioration of joints in selected Indiana portland cement concrete pavements*. 2007.

6. Qiao, C., P. Suraneni, and J. Weiss, *Phase diagram and volume change of the $Ca(OH)_2$-$CaCl_2$-H_2O system for varying $Ca(OH)_2/CaCl_2$ molar ratios.* Journal of Materials in Civil Engineering, 2018. **30**(2): p. 04017281.

7. Jones, C., et al., *Calcium oxychloride: a critical review of the literature surrounding the formation, deterioration, testing procedures, and recommended mitigation techniques.* Cement and Concrete Composites, 2020. **113**: p. 103663 %@ 0958-9465.

8. Smith, S., et al., *Service-life of Concrete in Freeze-Thaw Environments: Critical Degree of Saturation and Calcium Oxychloride Formation.* Cement and Concrete Research, Under review.

9. Cai, H. and X. Liu, *Freeze-thaw durability of concrete: ice formation process in pores.* Cement and Concrete Research, 1998. **28**: p. 1281-1287.

10. Tanesi, J. and R. Meininger, *Freeze-thaw resistance of concrete with marginal air content.* Transportation research record, 2007. **2020**(1): p. 61-66 %@ 0361-1981.

11. Janssen, D.J. and M.B. Snyder, *Resistance of concrete to freezing and thawing*. 1994.

12. Sutter, L., et al., *Petrographic evidence of calcium oxychloride formation in mortars exposed to magnesium chloride solution.* Cement and Concrete Research, 2006. **36**(8): p. 1533-1541.

13. Monosi, S. and L. Collepardi, *Chemical attack of calcium chloride on the Portland cement paste.* Cemento, 1989. **86**(2): p. 97-104.

14. Monosi, S. and M. Collepardi, *Research on $3CaO{\cdot}CaCl_2{\cdot}15H_2O$ identified in concretes damaged by CaCl2 attack.* Cemento, 1990. **87**(1): p. 3-8.

15. Collepardi, M., L. Coppola, and C. Pistolesi. *Durability of concrete structures exposed to $CaCl_2$ based deicing salts*. in *Proceedings of the 3rd CANMENT/ACI International Conference*. 1994. France: American Concrete Institute.

16. Sutter, L., et al., *The Deleterious Chemical Effects of Concentrated Deicing Solutions on Portland Cement Concrete* 2008, Michigan Tech Transportation Insitute South Dakota Department of Transportation p. 216.

17. Shi, X., et al., *Freeze–thaw damage and chemical change of a portland cement concrete in the presence of diluted deicers.* Materials and Structures, 2010. **43**(7): p. 933-946.

18. Janusz, A.E., *Investigation of deicing chemicals and their interactions with concrete materials.* 2010.

19. Lee, H., et al., *Effects of various deicing chemicals on pavement concrete deterioration.* 2000.

20. Wang, K., D.E. Nelsen, and W.A. Nixon, *Damaging effects of deicing chemicals on concrete materials.* Cement and Concrete Composites, 2006. **28**(2): p. 173-188.

21. Lawrence, M. and H.E. Vivian, *Action of calcium chloride on mortar and concrete.* 1960.

22. Van Niejenhuis, C.B. and C.M. Hansson, *Detrimental Effects of Anti-Icing Brines on Concrete Durability.* Concrete International, 2019. **41**(11): p. 30-34.

23. Ghazy, A. and M.T. Bassuoni, *Resistance of concrete to different exposures with chloride-based salts.* Cement and Concrete Research, 2017. **101**: p. 144-158.

24. Chatterji, S., *Mechanism of the CaCl2 attack on Portland cement concrete.* Cement and Concrete Research, 1978. **8**(4): p. 461-467.

25. Li, W., et al., *Water absorption and critical degree of saturation relating to freeze-thaw damage in concrete pavement joints.* Journal of Materials in Civil Engineering, 2012. **24**(3): p. 299-307.

26. Litvan, G.G., *Frost action in cement in the presence of de-icers.* Cement and Concrete Research, 1976. **6**(3): p. 351-356 %@ 0008-8846.

27. Spragg, R.P., et al., *Wetting and drying of concrete using aqueous solutions containing deicing salts.* Cement and Concrete Composites, 2011. **33**(5): p. 535-542.

28. Taylor, P., L. Sutter, and J. Weiss, *Investigation of deterioration of joints in concrete pavements.* 2012.

29. Sutter, L., et al., *Long-term effects of magnesium chloride and other concentrated salt solutions on pavement and structural Portland cement concrete.* Transportation research record, 2006. **1979**(1): p. 0361-1981.

30. Pour-Ghaz, M., et al. *Numerical and experimental assessment of unsaturated fluid transport in saw-cut (notched) concrete elements*. 2009.

31. Golias, M., et al., *Can Soy Methyl Esters Improve Concrete Pavement Joint Durability?* Transportation research record, 2012. **2290**(1): p. 60-68 %@ 0361-1981.

32. Hall, K.T., et al., *Performance of Sealed and Unsealed Concrete Pavement Joints*. 2009, United States. Federal Highway Administration.

33. MacInnis, C. and Y.R. Nathawad, *The effects of a deicing agent on the absorption and permeability of various concretes*, in *Durability of Building Materials and Components*. 1980, ASTM International.

34. Castro, J., et al., *Portland cement concrete pavement performance relative to permeability.* JTRP Rep. SPR-3093, Indiana Department of Transportation, West Lafayette, IN, 2010.

35. Barde, V., et al., *Relating material properties to exposure conditions for predicting service life in concrete bridge decks in Indiana.* 2009.

36. Rangaraju, P.R., *Investigating premature deterioration of a concrete highway.* Transportation research record, 2002. **1798**(1): p. 1-7 %@ 0361-1981.

37. Peterson, K., et al., *Observations of chloride ingress and calcium oxychloride formation in laboratory concrete and mortar at 5° C.* Cement and Concrete Research, 2013. **45**: p. 79-90.

38. Demediuk, T., W.F. Cole, and H.V. Hueber, *Studies on magnesium and calcium oxychlorides.* Australian Journal of Chemistry, 1955. **8**(2): p. 215-233.

39. Mori, H., et al., *Deterioration of hardened cement pastes immersed in calcium chloride solution.* Cement Science and Concrete Technology, 2012. **66**(1): p. 79-86.

40. Qiao, C., et al., *The Influence of calcium chloride on flexural strength of cement-based materials*, in *High Tech Concrete: Where Technology and Engineering Meet: Proceedings of the 2017 fib Symposium, held in Maastricht, The Netherlands, June 12–14, 2017*, D.A. Hordijk and M. Luković, Editors. 2018, Springer International Publishing: Cham. p. 2041-2048.

41. Qiao, C., P. Suraneni, and J. Weiss, *Flexural strength reduction of cement pastes exposed to CaCl2 solutions.* Cement and Concrete Composites, 2018. **86**: p. 297-305.

42. Julio-Betancourt, G.A. and R.D. Hooton. *Calcium and magnesium chloride attack on cement-based materials: formation, stability, and effects of oxychlorides*. 2009.

43. Farnam, Y., et al., *The influence of calcium chloride deicing salt on phase changes and damage development in cementitious materials.* Cement and Concrete Composites, 2015. **64**: p. 1-15.

44. Berntsson, L. and S. Chandra, *Damage of concrete sleepers by calcium chloride.* Cement and Concrete Research, 1982. **12**(1): p. 87-92.

45. Smolczyk, H.G. *Chemical Reactions of strong Chloride-Solution with Concrete*. 1968.

46. Chatterji, S. and J. Ad, *Studies of the mechanism of calcium chloride attack on Portland cement concrete.* 1975.

47. Rita M. Ghantous, K.Z., Hope Hall Becker, Amir Behravan, M. Tyler Ley, O. Burkan Isgor, and W. Jason Weiss, *The Influence of Air Voids and Fluid Absorption on Salt-Induced Calcium Oxychloride Damage.* Cement and Concrete Composites, 2022.

48. Winkler, E.M. and P.C. Singer, *Crystallization pressure of salts in stone and concrete.* Geological society of America bulletin, 1972. **83**(11): p. 3509-3514.

49. Scherer, G.W., *Crystallization in pores.* Cement and Concrete Research, 1999. **29**(8): p. 1347-1358.

50. Scherer, G.W., *Stress from crystallization of salt.* Cement and Concrete Research, 2004. **34**(9): p. 1613-1624.

51. Qiao, C., P. Suraneni, and J. Weiss, *Measuring volume change due to calcium oxychloride phase transformation in a $Ca(OH)_2$-$CaCl_2$-H_2O system.* Advances in Civil Engineering Materials, 2017. **6**(1): p. 157-169.

52. Landis, E.N., et al., *Technique to measure 3D work-of-fracture of concrete in compression.* Journal of engineering mechanics, 1999. **125**(6): p. 599-605.

53. Lu, S., E. Landis, and D. Keane, *X-ray microtomographic studies of pore structure and permeability in Portland cement concrete.* Materials and structures, 2006. **39**(6): p. 611-620.

54. Christiansen, B.A., *Effect of micro-computed tomography voxel size and segmentation method on trabecular bone microstructure measures in mice.* Bone reports, 2016. **5**: p. 136-140.

55. Hu, Q., et al., *Direct three-dimensional observation of the microstructure and chemistry of C3S hydration.* Cement and concrete research, 2016. **88**: p. 157-169.

56. Romão, M., et al., *Micro-computed tomography and histomorphometric analysis of human alveolar bone repair induced by laser phototherapy: a pilot study.* International journal of oral and maxillofacial surgery, 2015. **44**(12): p. 1521-1528.

57. Nguyen, T.T., *Modeling of complex microcracking in cement based materials by combining numerical simulations based on a phase-field method and experimental 3D imaging*. 2015, Paris Est.

58. Kim, K.Y., T.S. Yun, and K.P. Park, *Evaluation of pore structures and cracking in cement paste exposed to elevated temperatures by X-ray computed tomography.* Cement and Concrete Research, 2013. **50**: p. 34-40.

59. Sinha, S.K. and P.W. Fieguth, *Automated detection of cracks in buried concrete pipe images.* Automation in construction, 2006. **15**(1): p. 58-72.

60. Moradian, M., et al., *Direct in-situ observation of early age void evolution in sustainable cement paste containing fly ash or limestone.* Composites Part B: Engineering, 2019. **175**: p. 107099.

61. Hu, Q., et al., *Combined three-dimensional structure and chemistry imaging with nanoscale resolution.* Acta materialia, 2014. **77**: p. 173-182.

62. Hu, Q., et al., *3D chemical segmentation of fly ash particles with X-ray computed tomography and electron probe microanalysis.* Fuel, 2014. **116**: p. 229-236.

63. Ley, M., et al. *Combining nano X-ray tomography and nano X-ray fluorescence to create time-dependent three dimensional constitutive maps*. in *2nd International Conference on Tomography of Materials and StructuresQuebec City, Canada*. 2015.

64. Gallucci, E., et al., *3D experimental investigation of the microstructure of cement pastes using synchrotron X-ray microtomography (μCT).* Cement and Concrete Research, 2007. **37**(3): p. 360-368.

65. Hu, Q., et al., *Direct measurements of 3d structure, chemistry and mass density during the induction period of C3s hydration.* Cement and concrete research, 2016. **89**: p. 14-26.

66. Sokhansefat, G., *Feature Investigation using Micro Computed Tomography within Materials*. 2018, Oklahoma State University.

67. Fukuda, D., et al., *Investigation of self-sealing in high-strength and ultra-low-permeability concrete in water using micro-focus X-ray CT.* Cement and Concrete Research, 2012. **42**(11): p. 1494-1500.

68. Zolghadr, A., et al., *Biomass microspheres–A new method for characterization of biomass pyrolysis and shrinkage.* Bioresource technology, 2019. **273**: p. 16-24.

69. Sokhansefat, G., et al., *Using X-ray computed tomography to investigate mortar subjected to freeze-thaw cycles.* Cement and Concrete Composites, 2020. **108**: p. 103520.

70. Promentilla, M.A.B. and T. Sugiyama, *X-ray microtomography of mortars exposed to freezing-thawing action.* Journal of Advanced Concrete Technology, 2010. **8**(2): p. 97-111.

71. Sugiyama, T., et al., *Application of synchrotron microtomography for pore structure characterization of deteriorated cementitious materials due to leaching.* Cement and Concrete Research, 2010. **40**(8): p. 1265-1270.

72. Tekin, I., R. Birgul, and H.Y. Aruntas, *Determination of the effect of volcanic pumice replacement on macro void development for blended cement mortars by computerized tomography.* Construction and Building Materials, 2012. **35**: p. 15-22.

73. Farnam, Y., et al., *Measuring freeze and thaw damage in mortars containing deicing salt using a low-temperature longitudinal guarded comparative calorimeter and acoustic emission.* Advances in Civil Engineering Materials, 2014. **3**(1): p. 316-337.

74. *ASTM C138/C138M-17a Standard Test Method for Density (Unit Weight), Yield, and Air Content (Gravimetric) of Concrete*, A. International, Editor. 2017: West Conshohocken, PA.

75. *ASTM C143/C143M-20 Standard Test Method for Slump of Hydraulic-Cement Concrete*, A. International, Editor. 2020.

76. *AASHTO T 395 LRFD Bridge Design Specifications*, A.A.o.S.H.a.T. Officials, Editor. 2017: Washington, D.C.

77. *ASTM C457/C457M-16 Standard Test Method for Microscopical Determination of Parameters of the Air-Void System in Hardened Concrete*, A. International, Editor. 2016: West Conshohocken, PA.

78. *ASTM C172/C172M-17 Standard Practice for Sampling Freshly Mixed Concrete*, A. International, Editor. 2017: West Conshohocken, PA.

79. *ASTM C231/C231M-17a Standard Test Method for Air Content of Freshly Mixed Concrete by the Pressure Method*, A. International, Editor. 2017: West Conshohocken, PA.

80. Hover, K.C., *Analytical investigation of the influence of air bubble size on the determination of the air content of freshly mixed concrete.* Cement, concrete and aggregates, 1988. **10**(1): p. 29-34.

81. Welchel, D., *Determining the Size and Spacing of Air Bubbles in Fresh Concrete*. 2014, Oklahoma State University.

82. Ley, M.T., *The effects of fly ash on the ability to entrain and stabilize air in concrete*. 2007: ProQuest.

83. Jakobsen, U., et al., *Automated air void analysis of hardened concrete—a Round Robin study.* Cement and Concrete Research, 2006. **36**(8): p. 1444-1452.

84. Peterson, K., L. Sutter, and M. Radlinski, *The practical application of a flatbed scanner for air-void characterization of hardened concrete*, in *Recent Advancement in Concrete Freezing-Thawing (FT) Durability*. 2010, ASTM International.

85. Dąbrowski, M., et al., *Validation of sequential pressure method for evaluation of the content of microvoids in air entrained concrete.* Construction and Building Materials, 2019. **227**: p. 116633.

86. Qiao, C., P. Suraneni, and J. Weiss, *Phase Diagram and Volume Change of the Ca (OH) 2─ CaCl 2─ H 2 O System for Varying Ca (OH) 2/CaCl 2 Molar Ratios.* Journal of Materials in Civil Engineering, 2018. **30**(2): p. 04017281.

87. Qiao, C., P. Suraneni, and J. Weiss, *Measuring Volume Change Caused by Calcium Oxychloride Phase Transformation in a Ca (OH) 2-CaCl 2-H 2 O System.* Advances in Civil Engineering Materials, 2017. **6**(1): p. 157-169.

88. Ghantous, R.M., et al., *Examining the influence of the Degree of Saturation on Length Change and Freeze Thaw Damage.* Submitted to Advances in Civil Engineering Materials, 2018.

89. Otsu, N., *A threshold selection method from gray-level histograms.* IEEE transactions on systems, man, and cybernetics, 1979. **9**(1): p. 62-66.

90. Markoe, A., *Analytic tomography*. Vol. 13. 2006: Cambridge University Press.

91. Wong, R. and K.T. Chau, *Estimation of air void and aggregate spatial distributions in concrete under uniaxial compression using computer tomography scanning.* Cement and Concrete Research, 2005. **35**(8): p. 1566-1576.

92. De Borst, R., et al., *Fundamental issues in finite element analyses of localization of deformation.* Engineering computations, 1993.

93. Lenoir, N., et al., *Volumetric digital image correlation applied to X-ray microtomography images from triaxial compression tests on argillaceous rock.* Strain, 2007. **43**(3): p. 193-205.

94. Mehta, P.K. and P. Monteiro, *Concrete: microstructure, properties, and materials.* (No Title), 2006.

95. Marsh, B.K. and R.L. Day, *Pozzolanic and cementitious reactions of fly ash in blended cement pastes.* Cement and concrete research, 1988. **18**(2): p. 301-310.

96. Saeki, T. and P.J. Monteiro, *A model to predict the amount of calcium hydroxide in concrete containing mineral admixtures.* Cement and Concrete Research, 2005. **35**(10): p. 1914-1921.

97. Powers, T.C. and T. Willis. *The air requirement of frost resistant concrete*. in *Highway Research Board Proceedings*. 1950.

98. Weiss, W.J., et al., *Synthesis: Accelerating implementation of research findings to reduce potential concrete pavement joint deterioration*. 2018, Purdue University. Joint Transportation Research Program.

Field-Based Measurement of Freeze–Thaw Damage in Cementitious Materials

Bahaa N. Abdelrahman, M.Sc.,[1] M. Tyler Ley, Ph.D., P.E.,[2] Lichun Chen, Ph.D.[3], Nicholas F. Materer, Ph.D.[4], Jair Simon[5], Andrew Young[6]

[1]Ph.D. Candidate, Dept. of Civil & Environmental Engineering, Oklahoma State Univ., 217 Engineering North, Stillwater, OK 74078 (Corresponding author).

Email: bahaa.abdelrahman@okstate.edu

[2]Professor, Dept. of Civil & Environmental Engineering, Oklahoma State Univ., 217 Engineering North, Stillwater, OK 74078. Email: tyler.ley@okstate.edu

[3]Ph.D., Dept. of Civil & Environmental Engineering, Oklahoma State Univ., 217 Engineering North, Stillwater, OK 74078. Email: lichun.chen@okstate.edu

[4]Professor, Dept. of Chemistry, Oklahoma State Univ., 107 Physical Science, Stillwater, OK 74078. Email: nicholas.materer@okstate.edu

[5]Student, Dept. of Civil & Environmental Engineering, Oklahoma State Univ., 217 Engineering North, Stillwater, OK 74078. Email: jair.simon@okstate.edu

[6]Student, Dept. of Civil & Environmental Engineering, Oklahoma State Univ., 217 Engineering North, Stillwater, OK 74078. Email: andrew.young12@okstate.edu

Abstract

This research represents four years of direct, concrete field data of degree of saturation (DOS) and damaging freeze-thaw (FT) cycles from 42 sites in 14 states in the U.S. While present methods of estimating FT damage are either using regional climatic data, or a result of lab tests, this research directly measures site-specific variations in concrete moisture and temperature that affect FT durability. The results show that damaging FT cycles occur only when low temperatures and high DOS levels overlap. Therefore, this overlap can differ widely even within the same regions. Based on these observations, four climate zones are identified and mapped. Also, this study analyzes how DOS, total FT cycles, and damaging FT cycles vary

across locations. Overall, this work reveals the importance of using site-specific evaluations for designing concrete with FT durability.

Keywords: Resistivity, Freeze-Thaw Durability, Damaging Freeze-Thaw Cycles, Degree of Saturation, Freeze-Thaw Maps.

1.0 Introduction

FT damage is one of the main concrete durability challenges in cold and wet climates (Kosior-Kazberuk and Jezierski 2004; Jacobsen 2005). Thus, predicting damaging FT cycles accurately is important for designing concrete mixtures that are more durable in cold regions. However, many previous studies relied on laboratory testing or broad climate zones that do not always represent what concrete experiences in the field (ASTM 2015; RILEM TC 117-FDC 2004; Li et al. 2012; Yu et al. 2013; Abdelrahman and Ley 2024; ACI Committee 201 2016; Schaefer and Wang 2006). Current standards, such as the Long-Term Pavement Performance (LTPP) Climate Region Classification (FHWA 2013) and ACI 318 (ACI Committee 318 2019), provide general exposure guidance, but they are not based on field measurements recorded directly from concrete, and they do not account for local weather variability within a single region. Therefore, this work presents concrete field measurements of DOS and FT cycles at different locations across the U.S. to better understand the actual performance of the concrete under real environmental conditions.

FT damage is mainly controlled by freezing temperature and moisture content in the concrete, which is commonly represented by the DOS (Beaudoin and MacInnis 1974; Bentz et al. 2001; Sutter et al. 2006; Sun et al. 2007; Leech et al. 2008). However, local weather conditions such as air temperature, humidity, and precipitation can significantly change both the freezing temperature and the DOS within the concrete (Akita et al. 1999; Liu et al. 2016). DOS stands for percentage voids in concrete saturated with water, and it plays a major role in determining

concrete susceptibility to FT damage (Ghantous et al. 2019; Fagerlund 1977). Several factors influence DOS, such as porosity, air content, pore structure, and the amount of free water within the concrete. Although air void spacing does not directly change DOS, it affects the critical DOS, the critical saturation level when damage starts to develop (Li et al. 2012; Fagerlund 1977; Moradllo et al. 2019; Fagerlund 1973). The critical DOS is typically between 78% and 90% (Li et al. 2012; Fagerlund 1977; Moradllo et al. 2019; Fagerlund 1973), and FT cycles are considered damaging when the DOS in concrete is above the critical DOS.

Temperature is also a key factor in FT damage. In cold, wet regions, when the concrete temperature drops below freezing, water inside the concrete freezes, resulting in hydraulic and crystallization pressures. As a result, cracks will develop, especially when the DOS is above the critical value, leading to more concrete durability issues (Fagerlund 1977; Powers 1945; Shang and Yi 2013; Barham et al. 2021; Obaidat et al. 2020). Therefore, measuring DOS and detecting ice formation in real time under field conditions has historically been a challenge.

To address this challenge, a novel field-based method was developed that uses electrical resistivity and temperature measurements to measure DOS, ice formation, and ice melting inside concrete in real time (Chen et al. 2023). This study showed a direct relationship between DOS and freezing temperature, as higher DOS increases the freezing temperature of cementitious materials, while lower DOS results in freezing at lower temperatures (Chen et al. 2023; Bager and Sellevold 1986; Farnam et al. 2015). Thus, this work showed that damaging FT cycles can be detected in situ, offering a practical way to quantify the number of damaging FT cycles. However, the method was only applied at two locations throughout one winter.

This study extends earlier work (Chen et al. 2023) by expanding the field measurements to 42 sites in 14 U.S. states, monitored over four consecutive winters from September to April (2020–

2024), to investigate how the DOS and the FT cycles change in real environmental conditions across different locations.

This novel dataset of field location-specific measurements offers a valuable methodology for establishing tools and maps that can identify and measure damaging FT cycles for various climatic conditions. Therefore, it becomes feasible for these tools and maps to help enhance durability design and analysis, which are currently a prominent missing area in available literature.

2.0 Experimental Materials and Methods

2.1 Field Sample Preparation

The samples for this work were prepared using cylindrical specimen mortar samples with a diameter of 152.4 mm, a height of 127.0 mm, a water-to-cement ratio of 0.45, and no supplementary cementitious materials were included to minimize variability in resistivity over time (Chen et al. 2023). This mixed design for the samples ensures that all locations have identical samples. Another reason for using a mortar sample in this test is that it provides easy construction, calibration, and measurement for electrical resistivity. Since FT durable coarse aggregates are not expected to absorb much moisture, this test result will also work for concrete.

A fiber-reinforced concrete cover was constructed to protect the samples and wiring using a 0.45 w/c mix with 2% macro synthetic fibers by volume. The final concrete block measured 457 mm × 305 mm × 178 mm, providing structural support and insulation (Chen et al. 2023). Each field sample block contained two mortar specimens, allowing for redundant measurements for data reliability. More details about the mixture design are available in Appendix A.

2.2 Instrumentation and Data Collection

Each field sample block was embedded with four thermocouples for temperature monitoring, and stainless-steel rods, referred to as electrodes, were used for resistivity measurements. The electrodes had a horizontal spacing of 92.7 mm and were centered in the middle of the 152.4 mm diameter cylinder. The rods are vertically spaced at 12.7 mm from the surface to create seven levels of measurement. Thermocouples were also installed to measure the temperature of the sample at 12.7 mm from the surface, and then at 50.8 mm and 88.9 mm from the surface. Based on previous publications, the rods are 51 mm from the surface. This was chosen as the previous research (Chen et al. 2023) has shown that this depth experiences the most FT cycles and the highest DOS. Therefore, this depth is considered the worst-case scenario for evaluating FT damage in this study. These findings were also verified with the sites investigated for this work.

The uppermost steel rods and thermocouples were exposed above the mortar surface to capture water accumulation and air temperature readings (Chen et al. 2023). To simulate poor drainage conditions, the mortar surface was set 25.4 mm below the top of the mold, allowing precipitation to collect and evaporate naturally. This was done to simulate an area of poor drainage on a pavement or bridge deck. Fig. 1 illustrates the configuration of the mortar samples. Samples were connected to an instrument box with a data logger mounted on a post. Temperature and resistivity measurements were recorded every 30 minutes and stored on an SD card. Fig. 2 describes in detail the samples used in the field for monitoring the mortar specimens. Additionally, Fig. 3 illustrates the monitored samples installed in the field. Further information on data processing is in Appendix B.

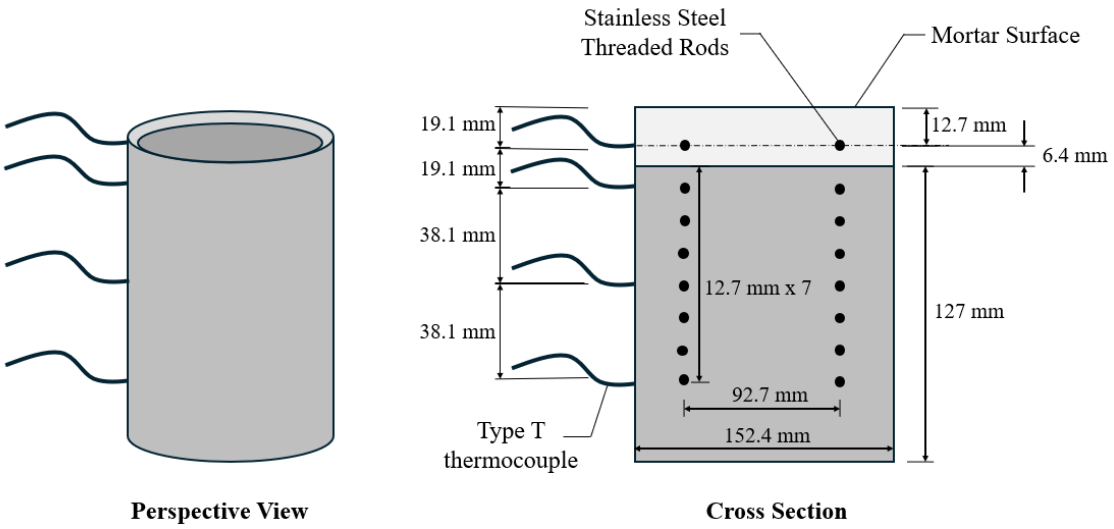

Fig. 1. Mortar cylindrical specimen configuration (acquired from Chen et al. 2023).

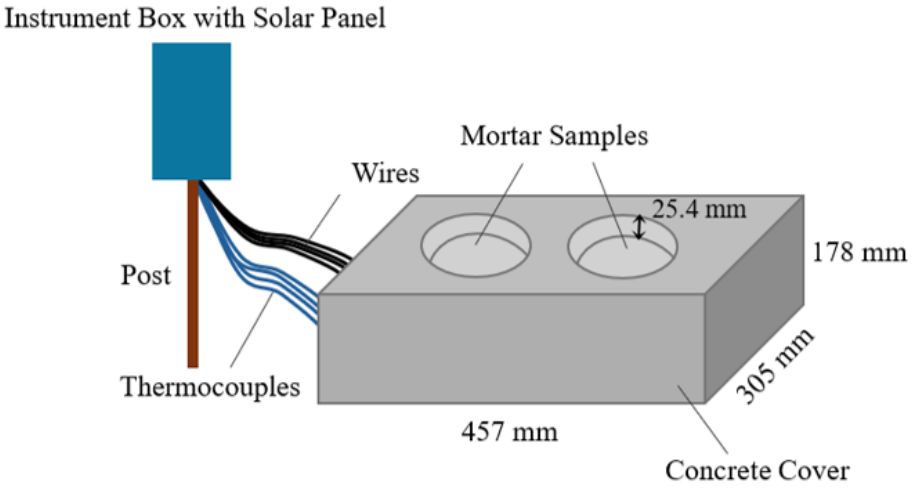

Fig. 2. Configuration of the field samples setup, showing the concrete block dimensions, instrument box, and solar panel connection.

Fig. 3. Installed field samples, with the instrumentation box and solar panel set up for data collection**.**

2.3 Field Samples Placement

To test how FT cycles affect concrete durability, concrete samples were distributed in 14 states in the U.S. The reasons for this are that these states are expected to expose their concrete to varying amounts of FT cycles, and these are also states that are sponsoring this research. The period of this experiment lasted for four successive winter periods: 2020, 2021, 2022, and 2023. Every winter period lasted from September to April. This is tabulated in Table 1. The locations and states are shown on the map in Fig. 4. Each state contains three instrumented blocks placed at three different locations. The field sites in each state are labeled A, B, and C, starting with the furthest west site. The layout is shown in Fig. 4. Detailed locations for each field site are provided in Appendix C.

Table 1. Study Periods for the Field Samples.

Year	Period
Winter of 2020	September 2020 – April 2021
Winter of 2021	September 2021 – April 2022
Winter of 2022	September 2022 – April 2023
Winter of 2023	September 2023 – April 2024

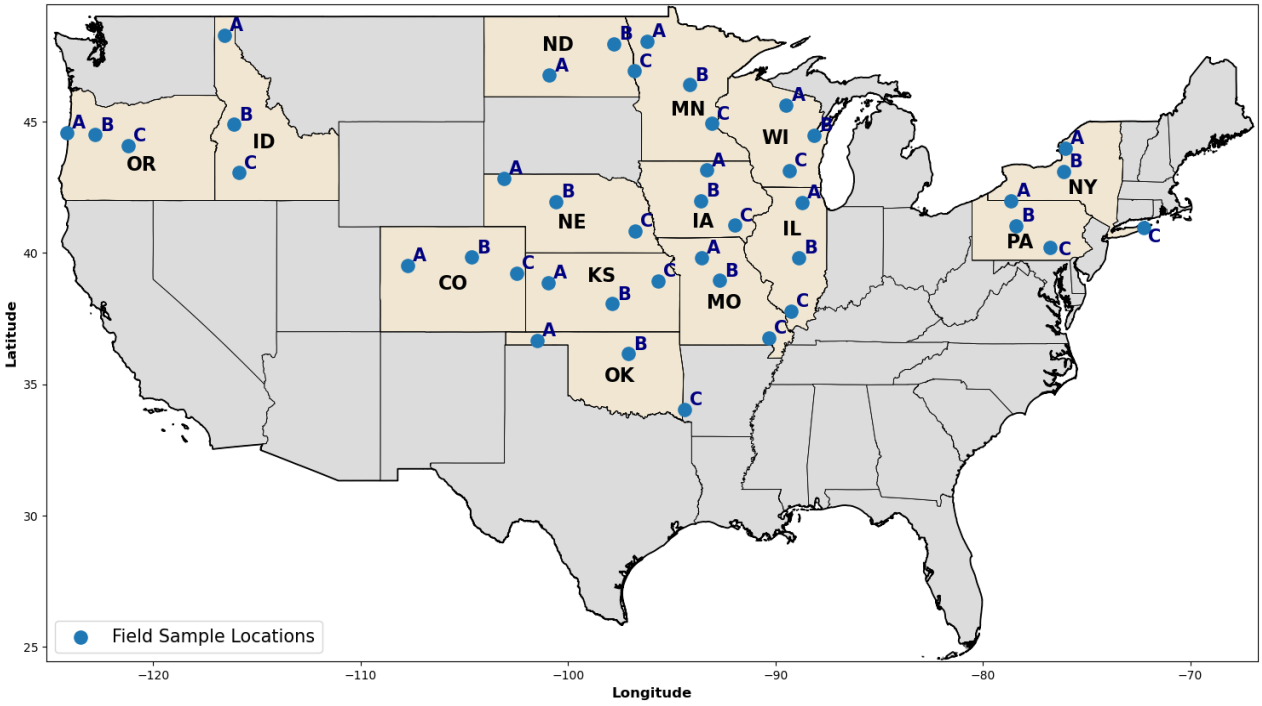

Fig. 4. Locations of the 42 field samples across 14 U.S. states.

2.4 Determining the Number of FT Cycles

The detection of FT cycles is based on the relationship between the DOS and freezing temperature (Chen et al. 2023). The freezing temperature is defined as the temperature at which the water inside the concrete begins to freeze, and this temperature depends on the DOS of the concrete (Chen et al. 2023). Fig. 5 shows the relationship between DOS and freezing temperatures, which was developed from previous work (Chen et al. 2023). More details about this relationship can be found in Appendix D.

Fig. 5 shows that concrete samples with higher DOS values freeze at higher temperatures than the samples with lower DOS. This means it is easier for the concrete to freeze and be damaged from ice formation at high DOS. For this study, the FT cycle is defined as a temperature drop below the freezing temperature followed by a rise above 0°C. The analysis uses the rods located 51 mm below the surface, as this is where the samples showed the highest DOS (Chen et al. 2023).

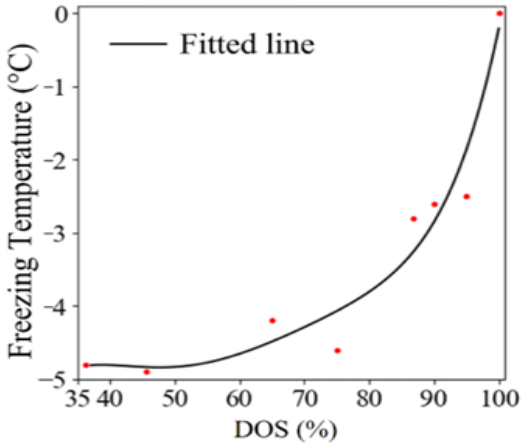

Fig. 5. DOS vs. freezing temperature relationship (acquired from Chen et al. 2023).

2.5 Determining the Number of Damaging FT Cycles

In this study, the FT cycle is considered damaging if the DOS increases above 80% and ice forms within the sample. The 80% DOS limit was selected as it represents a conservative lower limit when FT damage is likely to occur. Setting the critical DOS at 80% ensures caution, as the potential for damaging FT cycles is reduced below this value, and ice formation within the sample is less likely to cause damage. Therefore, this value helps avoid underestimating potential FT damage and aligns with findings from previous studies, which identify the critical DOS range as 78–90% (Li et al. 2012; Fagerlund 1977; Moradllo et al. 2019; Fagerlund 1973). This provides further justification for selecting 80% as a conservative value to account for potential measurement variability and ensure a margin of safety in evaluating FT damage. Thus, in this study, FT damage is detected when the concrete has frozen, based on the freezing

temperature shown in Fig. 5, and coincides with a DOS above the critical 80%. Any FT cycles occurring below this critical DOS are not considered damaging cycles.

3.0 Results and Discussion

3.1 Variation of DOS Based on Month, Region, and Year

Fig. 6 shows the average DOS at the 42 locations during winter 2020–2021, along with regional variation. Results for other winters are provided in Appendix E, and the average monthly DOS data are presented in Appendix F. Across the four winters, Oregon Location C has the highest Coefficient of Variation (CV) at 5.6% and a standard deviation of 4.9%. This indicates that the DOS values were generally consistent over the winters for each location measured. The high CV at this site was likely due to local weather variability, though the variation remained relatively small. The variation in the damaging FT cycles is discussed later in the document.

Fig. 6 shows that different regions have different DOS levels. As explained previously, locations where the DOS is high will freeze at higher temperatures (see Fig. 5) and will be damaged more easily from the FT cycles. While locations with low DOS require lower temperatures to freeze (see Fig. 5), they are less of a concern for FT damage. This observed variability in DOS means that using a single FT strategy for an entire state or region may be inaccurate, since moisture levels can vary widely in the same region. This highlights the need for location-based FT exposure assessments based on actual field measurements to better analyze and design more durable concrete in cold regions. The variation in the DOS between sites is impacted by a complex combination of weather. Understanding how different weather factors impact the DOS will be discussed in other publications.

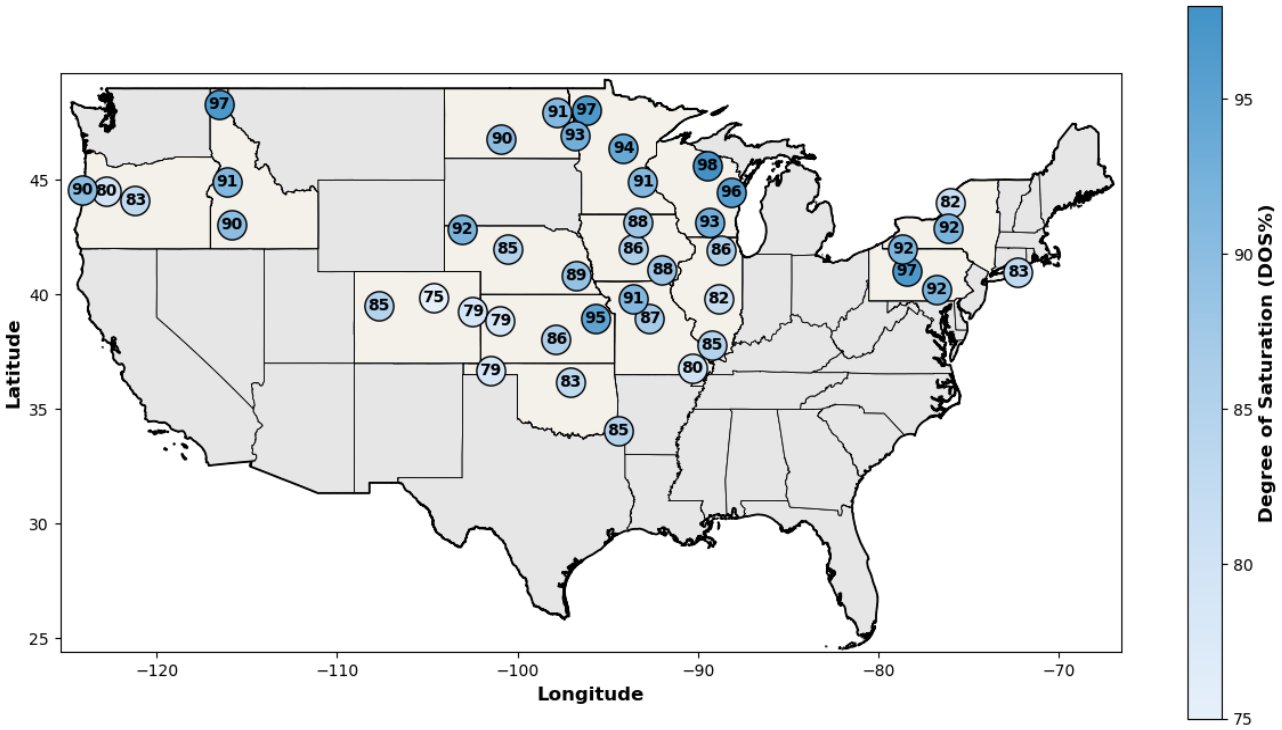

Fig. 6. Location-specific average DOS (%) measured at field sites during winter 2020–2021.

3.2 Total and Damaging FT Cycles

This section presents the total and damaging FT cycles measured in field concrete samples across U.S. states during winter 2020–2021. Results for other years are presented in Appendix G. Fig. 7 shows the total and damaging FT cycles measured in the field concrete samples, where the first number represents the total cycles and the second number indicates the damaging cycles (i.e., cycles occurring when the DOS exceeds 80%). Based on the DOS and FT data, each location can be grouped into different regions, which are summarized in Table 2 and illustrated in Fig. 8.

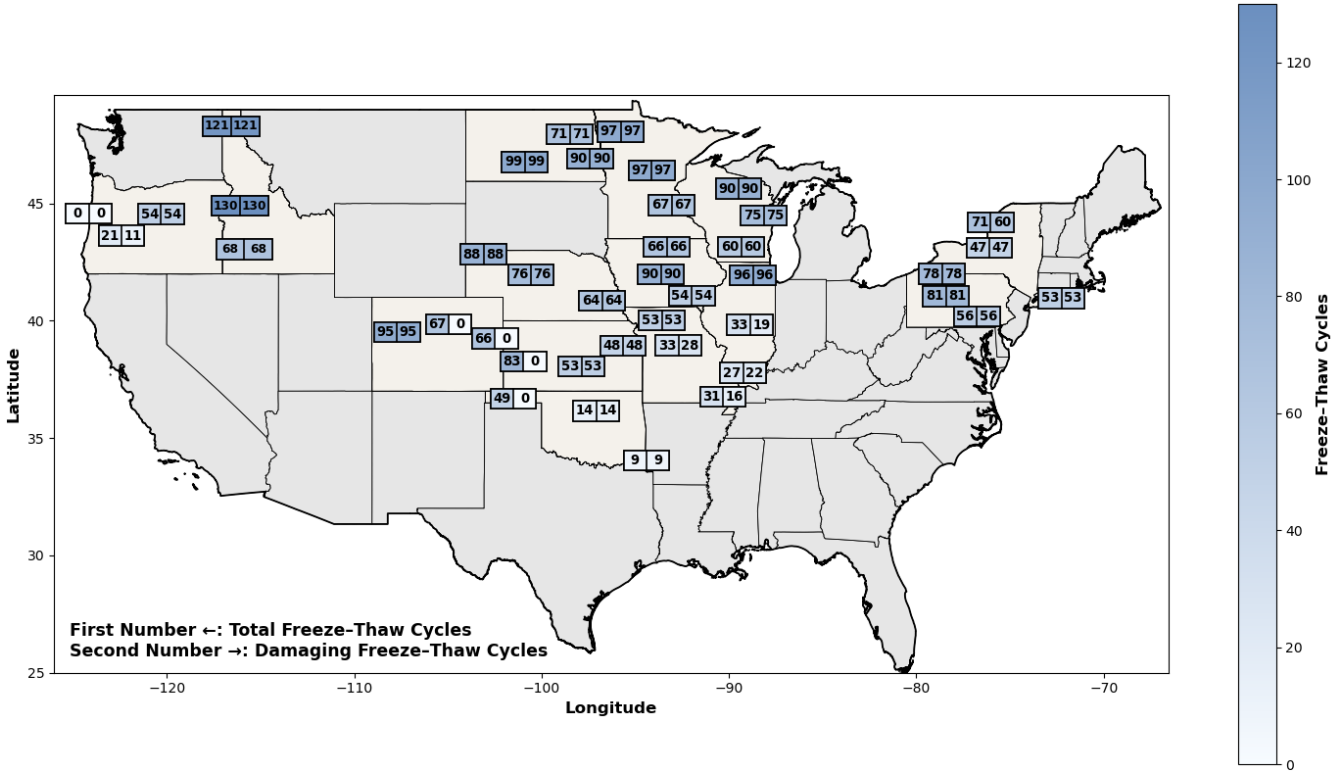

Fig. 7. Total and damaging field-measured FT cycles during winter 2020–2021.

Table 2. Summary of Environmental Conditions and Freezing Event Scenarios.

Possible Case	Wet + FT	Dry + FT	Wet + Low FT	Variable Saturation + FT
Precipitation	High	Low	High	Moderate
DOS%	High (>80%)	Low (<80%)	High (>80%)	Variable (> or < 80%)
FT Cycles	High	High	Low (<15 Cycles)	High
Damaging FT Cycles	High	No	Low (<15 Cycles)	Moderate
Example Location	Minnesota (A)	Oklahoma (A)	Oregon (A)	Illinois (B)

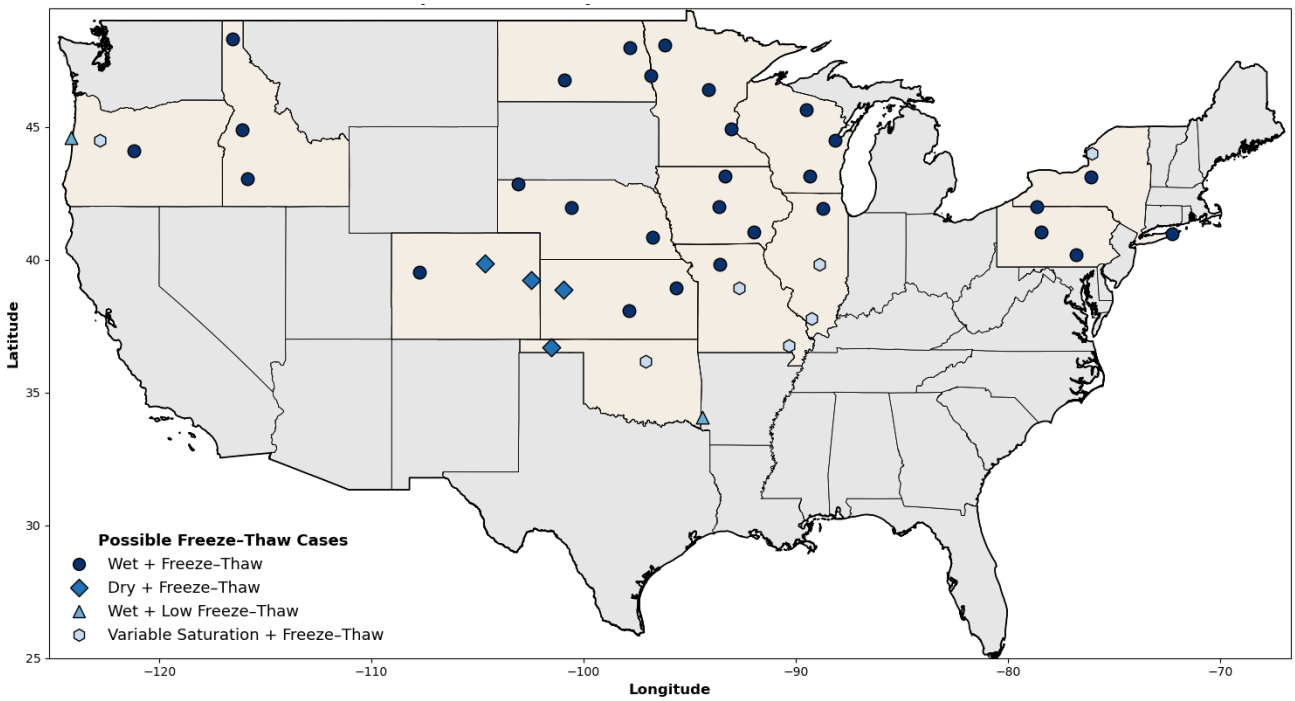

Fig. 8. Geographic distribution of FT cases assigned to each field location.

3.2.1 Wet + FT

Fig. 7 shows that in northern states like Idaho, North Dakota, Minnesota, Wisconsin, Iowa, Nebraska, and Pennsylvania, every FT cycle was damaging, as the DOS consistently exceeded 80% during freezing. This shows the vulnerability of colder, wetter regions where the DOS remains above 80%.

3.2.2 Dry + FT

While some locations experienced frequent FT cycles, these do not always lead to damage. This occurs because the DOS was always <80% during freezing at these locations. This highlights that damaging FT cycles are not caused by freezing alone but by the coincidence of freezing events with high DOS. This can be seen in Fig. 7 in locations B and C in Colorado. These locations experience freeze–thaw cycles (67 and 66), but none were damaging because the DOS stayed below 80% (75% and 79%). A similar pattern was observed at Location A in both Oklahoma and Kansas, where high cycle counts were not damaging because the DOS was

below the critical DOS (both had a DOS of 79%). It should be noted that all of these locations were in a dry climate, which can explain why the DOS of this concrete was lower.

3.2.3 Wet + Low FT

Some locations had an average DOS above the critical threshold of 80% but experienced relatively few freeze–thaw cycles. For this work, a few FT cycles are defined as fewer than 15 cycles over the winter season. In these cases, nearly all FT cycles were damaging, but the total number of FT cycles was limited due to warmer temperatures. For example, Oregon Location A and Oklahoma Location C had average DOS values above 80% during winter, yet recorded only a small number of FT cycles. This shows that even in wet regions where concrete remains highly saturated, limited freezing events can reduce the overall FT damage. However, when freezing does occur, the high DOS ensures that nearly every cycle contributes to damage.

3.2.4 Variable Saturation + FT

It is also possible that the DOS is sometimes above the critical limit of 80% and sometimes it is below. This can be seen at Illinois Locations B and C. For example, 33 and 27 FT cycles were recorded, but only 19 and 22 were damaging. Although the average DOS for this region is 82% and 85%, temporary drops in the DOS below 80% by drying before a freeze meant that some of the FT cycles were not damaging. This shows that it is not enough to know the average DOS, but instead it is important to know the DOS when the freezing event occurs. This work classified any location where this occurred as having variable saturation.

To show a detailed example, individual measurements of the temperature and DOS from December 2020 for Location B in Illinois are shown in Fig. 9. The dashed blue vertical lines indicate points where the concrete has frozen. The vertical dashed green lines then indicate where the concrete has thawed. Note that the temperature may be below 0°C, but this is not low enough for the concrete to freeze based on the DOS of the sample. However, it should be

emphasized that if the DOS is below 80% then the freezing event will not cause damage. Examples of this are shown in Fig. 9b.

This shows that even at sites with a high average DOS, it is possible that variations in the moisture content can create non-damaging FT cycles. This highlights the importance of the DOS of the sample and the timing of the FT event.

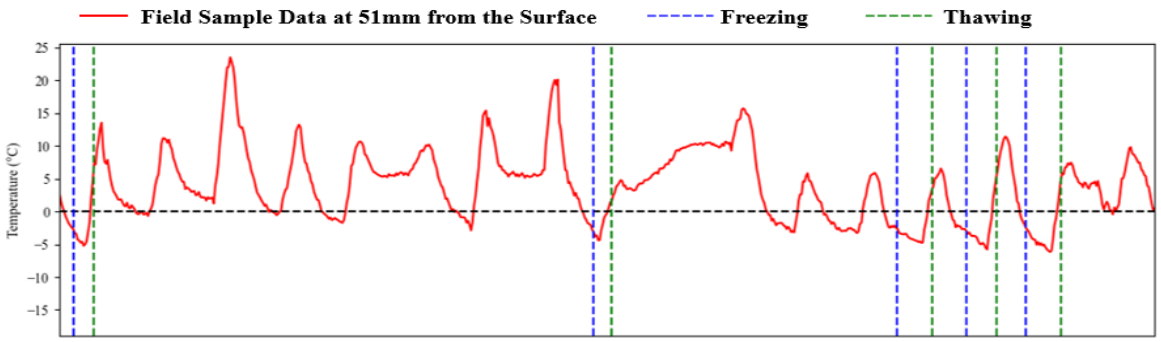

(a)

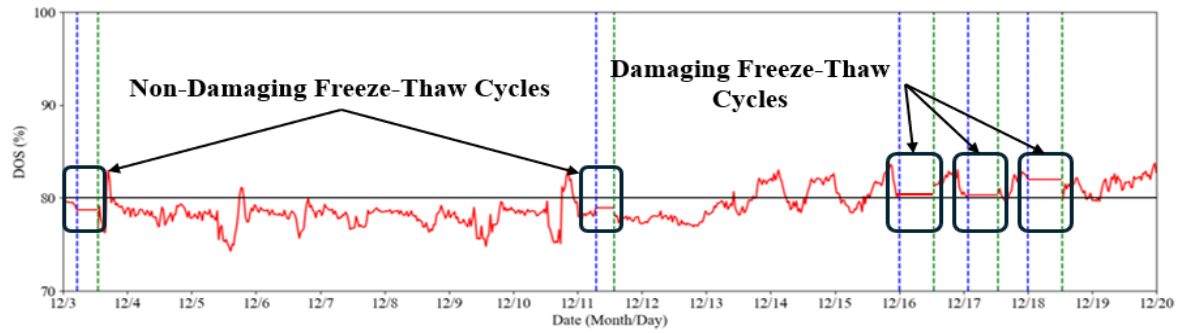

(b)

Fig. 9: Temperature and DOS at Illinois Location B in December 2020, highlighting damaging and non-damaging FT cycles; (a) temperature, (b) DOS.

3.3 Comparison to Other Climate Models

Current standards classify FT exposure by using broad regional climate categories, but they often overlook the site-specific conditions that cause actual damage. Thus, it is important to understand the limitations of these standards as they affect the concrete durability of design

decisions and analysis. For instance, the LTPP (FHWA 2013) divides regions into wet and dry zones based on precipitation. Wet regions are defined as receiving more than 508 mm of precipitation per year, while dry regions receive less. Freeze severity is then described using the Freezing Index (FI), which adds up the degree-days below 0°C in a year and is meant to indicate how severe the freezing exposure is. Areas with FI values below 50 are classified as No-Freeze, those between 50 and 400 as Moderate-Freeze, and those above 400 as Deep-Freeze (FHWA 2013). One problem with this approach is that it does not consider whether freezing happens when the concrete is highly saturated. As shown in this study, even if the average DOS is higher than the critical threshold, short-term drops in saturation during freezing events can reduce the number of damaging FT cycles. Many locations move above and below the 80% DOS level throughout the winter, and this variability is not captured by LTPP categories. Another limitation is that the LTPP zones describe only the severity of freezing but do not indicate how many damaging FT cycles occur at a location, which is a key factor in durability.

ACI 318 (ACI Committee 318 2019) has exposure classes (F0–F3) based on whether or not concrete will freeze in moist conditions, but it does not provide engineers with clear guidance on how to determine this, leading most to make conservative assumptions.

This work has used location-specific field data in combination with measured DOS and timing of freezing events. This allows regional variability to be taken into account and offers a much more accurate assessment and basis for design for FT exposure and durability of concrete in cold regions. It also more accurately represents the true exposure of concrete to damaging cycles than the zones that are offered by some guidelines, but misrepresent local conditions, and can either overestimate or underestimate actual FT exposure.

3.4 Year-to-Year Variability in FT Cycles

Table 3 groups sites by CV and lists the percentage of locations in each variability group; results for individual locations are given in Appendix G. A low CV of less than 15% indicates little variation from year to year and suggests that sites had relatively stable FT behavior. Moderate variability between 15% and 40% still shows some noticeable variation over the years in terms of FT cycles. High variability of greater than 40% suggests that there were substantial differences between years in FT cycle numbers. Locations with a very low number of FT cycles, in general, had inflated values of CV as the effect of even minor variations is magnified. Consequently, only locations that have more than five FT cycles per year have their CV reported as values at sites where there are a very small number of cycles that can be easily inflated and are not very meaningful. The resulting values show that the plurality of locations had low variability (52%), and a very large portion had moderate variability (43%). This suggests that there was year-to-year variability in damaging FT cycles at many locations, but only 5% had high variability. The year-to-year changes are largely the result of annual variations in the weather and the DOS. This finding emphasizes the point that measuring FT cycles for just one year is not sufficient, and multiple years of monitoring are necessary to improve understanding and predictability of FT damage. In general, there was a stable pattern of damaging FT cycles at most locations for the duration of the study. This will be investigated in more detail in future publications.

Table 3. Classification of Site Variability Based on CV for FT Cycles (Only Sites with >5 Cycles per Year are Included).

CV (%)	Variability	Number of Locations for Damaging FT Cycles
<15%	Low	52%
15 – 40%	Moderate	43%
>40%	High	5%

4.0 Practical Significance

This research provides the first large-scale, field-based dataset of damaging FT cycles measured directly in concrete. The results show that FT damage occurs only when freezing temperatures coincide with high saturation levels. Many locations experience FT cycles, but they do not damage concrete because the DOS remains below the critical DOS. This highlights the importance of site-specific evaluations for designing more durable concrete to better capture the complex relationship between DOS and freezing events.

Contrary to conventional methods that are dependent on large climatic areas, these results imply that present design practices either overlook regions with high potential for damaging FT cycles or result in designs that are excessively conservative when, in reality, low potential for damaging cycles exists. These findings also indicate that a level of variation in damaging cycles, as well as in air content requirements, exists in a given area.

Furthermore, this research examines the annual variation of DOS values and damaging cycles of FT, illustrating how a region can experience considerable variation in damaging cycles of FT from year to year. On this basis, it provides for better decisions concerning FT durability, design and maintenance. Lastly, this research has found four different types of FT climatic conditions and has produced a map of their geographic distribution among the regions analyzed.

This lays the groundwork for developing a measurement-based mapping system to quantify damaging FT cycles and to establish procedures that incorporate local weather data for predicting FT cycles using machine learning or other data-driven models that are the focus of future work. This could create a significant improvement to current methods of classifying FT exposure.

5.0 Conclusions

This research builds on work (Chen et al. 2023) by extending the methodology to a larger number of locations and seasons and providing a more detailed understanding of damaging FT cycles in the field. This study evaluated FT exposure using a combination of electrical resistivity and temperature data collected from 42 field locations in the United States over four consecutive winters. A damaging FT cycle was determined as a cycle where ice developed when the value of DOS exceeded 80%. This research effort, in total, adds to a realistic, practical understanding of FT damage as a function of the inclusion of comprehensive field measurement data over a period of four winters. The observations derived from this research effort are as follows:

1. The findings show that FT durability is strongly dependent on both freezing temperature and DOS. Areas with consistently high DOS and frequent freezing, such as Wisconsin, Minnesota, and North Dakota, experienced a high number of damaging FT cycles each year. Conversely, locations like Oklahoma recorded frequent freezing but minimal damage due to low DOS. This difference highlights the importance of accounting for both temperature and DOS, rather than temperature alone, when evaluating FT damage.
2. In dry climates, some locations experienced many FT cycles without damage because the DOS stayed below 80% during freezing. This verifies that the FT cycles do not cause damage if the DOS is low.
3. At some locations, the average DOS was above the critical DOS of 80%, but temporary drops in DOS during freezing prevented damage. This shows that seasonal average DOS alone is not enough; the timing of saturation relative to freezing determines

whether cycles are damaging. This highlights the importance of location-specific evaluations to understand the complex relationship between DOS and FT cycles.

4. Although some locations with high DOS experienced limited overall damage due to the few FT cycles, every cycle that was detected was damaging. This highlights the critical role of DOS in determining FT damage.
5. The relationship between DOS cycles and FT cycles was grouped into four different groups, including: (Wet + FT), (Dry + FT), (Wet + Low FT), and (Variable Saturation + FT), as per actual data of field observations and actual conditions that are not represented in current standards.
6. Over the four winters, the CV for DOS was low at all locations. Oregon Location C had the highest variability, with a CV of 5.6% and a standard deviation of 4.9%. These low values indicate that DOS did not change much from year to year, aside from small weather-related variations.
7. Most sites (95%) had low to moderate variability in damaging FT cycles (CV <40%). Only about 5% showed high variability, with CV values above 40%. This suggests that damaging FT cycles are consistent at most locations, but some sites do experience large year-to-year variations due to small weather variations.

This study shows that location-specific field measurements provide a more accurate and realistic evaluation of FT damage risk. Consequently, this will provide a more reliable design against FT damage. Categorizing the observed exposure conditions into four distinct categories and providing limits for this classification is an important step in developing a weather-based recommendation for FT durability design methods. This work also supports an artificial intelligence-based approach to use more specific weather data to predict the number of damaging FT cycles. This is an area of future work.

Acknowledgment

The authors would like to thank Dr. W. Jason Weiss for his valuable feedback and guidance during this work.

References

Kosior-Kazberuk, M., and Jezierski, W. (2004). "Surface scaling resistance of concrete modified with bituminous addition." *Journal of Civil Engineering and Management*, **10**(1), 25–30.

Jacobsen, S. (2005). "Calculating liquid transport into high-performance concrete during wet freeze/thaw." *Cement and Concrete Research*, **35**(2), 213–219.

ASTM. (2015). *Standard test method for resistance of concrete to rapid freezing and thawing (ASTM C666/C666M-15).* ASTM International, West Conshohocken, PA.

RILEM TC 117-FDC. (2004). "CIF test—Capillary suction, internal damage and freeze–thaw test: Test method for assessing the resistance of concrete to freeze–thaw with capillary suction of deicing salt solution." *Materials and Structures*, **37**(273), 743–753. https://doi.org/10.1007/BF02481627

Li, W., Pour-Ghaz, M., Castro, J., and Weiss, J. (2012). "Water absorption and critical degree of saturation relating to freeze–thaw damage in concrete pavement joints." *Journal of Materials in Civil Engineering*, **24**(3), 299–307. https://doi.org/10.1061/(ASCE)MT.1943-5533.0000383

Yu, X., Kim, J. S., and Weiss, J. (2013). "Assessment of climate-induced freeze–thaw damage risk for concrete pavements." *Transportation Research Record*, **2342**(1), 19–28. https://doi.org/10.3141/2342-03

Abdelrahman, B., and Ley, M. T. (2024). “The effects of concrete temperature on air-void parameters in pumped concrete.” *Materials and Structures*, **57**(2), 33.

ACI Committee 201. (2016). *Guide to durable concrete (ACI 201.2R-16).* American Concrete Institute, Farmington Hills, MI.

Schaefer, V. R., and Wang, K. (2006). *Mix design development for pervious concrete in cold weather climates.* Iowa Department of Transportation, Highway Division, Ames, IA, Rep. No. 2006-01.

Federal Highway Administration (FHWA). (2013). *Long-term pavement performance climate region classification.* FHWA-HRT-13-062, Washington, DC.

ACI Committee 318. (2019). *Building code requirements for structural concrete (ACI 318-19) and commentary (ACI 318R-19).* American Concrete Institute, Farmington Hills, MI.

Beaudoin, J. J., and MacInnis, C. (1974). “The mechanism of frost damage in hardened cement paste.” *Cement and Concrete Research*, **4**(2), 139–147.

Bentz, D. P., Ehlen, M. A., Ferraris, C. F., and Garboczi, E. J. (2001). “Sorptivity-based service life predictions for concrete pavements.” *Proc., 7th Int. Conf. on Concrete Pavements*, Vol. 1, 181–193.

Sutter, L., Van Dam, T., Peterson, K. R., and Johnston, D. P. (2006). “Long-term effects of magnesium chloride and other concentrated salt solutions on pavement and structural portland cement concrete.” *Transportation Research Record*, **1979**(1), 60–68.

Sun, Z., Kumpf, D., and Scherer, G. W. (2007). “Kinetics of ice growth in concrete.” *Proc., 12th Int. Congress on the Chemistry of Cement*, Montreal, Canada.

Leech, C., Lockington, D., Hooton, R. D., Galloway, G., Cowin, G., and Dux, P. (2008). "Validation of Mualem's conductivity model and prediction of saturated permeability from sorptivity." *ACI Materials Journal*, **105**(1), 44–52.

Akita, H., Andrade, C., Sarría, J., and Alonso, C. (1999). "Relative humidity in the interior of concrete exposed to natural and artificial weathering." *Cement and Concrete Research*, **29**(8), 1249–1259.

Liu, P., Song, L., et al. (2016). "Quantitative moisture model of interior concrete in structures exposed to natural weather." *Construction and Building Materials*, **102**, 76–83.

Ghantous, R. M., Madland, H., Kwong, J., and Weiss, W. J. (2019). "Examining the influence of the degree of saturation on length change and freeze–thaw damage." *Advances in Civil Engineering Materials*, **8**(1), 365–374.

Fagerlund, G. (1977). "The critical degree of saturation method of assessing the freeze/thaw resistance of concrete." *Materials and Structures*, **10**(58), 217–229.

Moradllo, M. K., Qiao, C., Hall, H., Ley, M. T., Reese, S. R., and Weiss, W. J. (2019). "Quantifying fluid filling of the air voids in air-entrained concrete using neutron radiography." *Cement and Concrete Composites*, **104**, 103407.

Fagerlund, G. (1973). *Critical degrees of saturation at freezing of porous and brittle materials.* Doctoral dissertation, Lund University, Lund, Sweden.

Powers, T. C. (1945). "A working hypothesis for further studies of frost resistance of concrete." *Journal of the American Concrete Institute*, **41**(1), 245–272.

Shang, H.-S., and Yi, T.-H. (2013). "Freeze–thaw durability of air-entrained concrete." *The Scientific World Journal*, **2013**, 650791.

Barham, W., Obaidat, Y., and Abdelrahman, B. (2021). "Experimental study on bond behavior between heat-damaged recycled asphalt pavement concrete and NSM-CFRP strips." *Case Studies in Construction Materials*, **14**, e00543. https://doi.org/10.1016/j.cscm.2021.e00543

Obaidat, Y., Barham, W., and Abdelrahman, B. (2020). "Effect of elevated temperature on the bond behavior between near-surface-mounted CFRP and recycled aggregate concrete." *Construction and Building Materials*, **251**, 118968. https://doi.org/10.1016/j.conbuildmat.2020.118970

Chen, L., Ley, M. T., Ghantous, R. M., Weiss, W. J., and Master, N. F. (2023). "Measuring damaging freeze–thaw cycles in the field." *Construction and Building Materials*, **387**, 131660.

Bager, D. H., and Sellevold, E. J. (1986). "Ice formation in hardened cement paste, part I—Room temperature cured pastes with variable moisture contents." *Cement and Concrete Research*, **16**(5), 709–720.

Farnam, Y., Todak, H., Spragg, R., and Weiss, J. (2015). "Electrical response of mortar with different degrees of saturation and deicing salt solutions during freezing and thawing." *Cement and Concrete Composites*, **59**, 49–59.

Appendixes

Appendix A: Field Samples Mix Design

Table A1. Mortar mixture summary (acquired from Chen et al. 2023).

Cement (kg/m^3)	Water (kg/m^3)	Fine Aggregate (SSD kg/m^3)
603.7	265.7	1514.2

Table A2. Type I cement oxide analysis (acquired from Chen et al. 2023).

Oxide (%)	SiO_2	Al_2O_3	Fe_2O_3	CaO	MgO	SO_3	Na_2O	K_2O	C_3S	C_2S	C_3A	C_4AF	LOI
Cement	21.1	4.8	3.1	64.5	2.33	3.2	0.17	0.58	50	23	7	9	2.6

Table A3. Concrete mixture summary (acquired from Chen et al. 2023).

Cement (kg/m^3)	Water (kg/m^3)	Fine Aggregate (SSD kg/m^3)	Coarse Aggregate (SSD kg/m^3)
366.4	157.8	728.6	1071.4

References

Chen, L., Ley, M. T., Ghantous, R. M., Weiss, W. J., and Master, N. F. (2023). "Measuring damaging freeze–thaw cycles in the field." *Construction and Building Materials*, 387, 131660.

Appendix B: Resistivity and Temperature Calculation

Resistivity Calculation

This work builds on a previous study (Chen et al. 2023) that used the AD5933, a 12-bit impedance converter, to measure resistivity. The AD5933 combines a frequency generator with a high-precision 12-bit analog-to-digital converter (ADC) capable of sampling at 1 mega-sample per second (MSPS). To provide accurate results, calibration was performed using resistors of 560 Ω and 2000 Ω. In working mode, it calculates the magnitude and phase of impedance at a particular frequency (Chen et al. 2023).

The AD5933 gathers signals from the sample via its ADC during use. Using its DSP system, it applies DFT to these signals. The DFT yields real (R) and imaginary (I) values representing impedance, which are stored in the data registers for further processing. The calculation for the magnitude of the impedance is given by Eq. 1:

$$\text{Magnitude} = \sqrt{(R^2 + I^2} \quad (1)$$

Here, *R* represents the real impedance, and *I* represents the imaginary impedance.

A scaling factor, called the gain factor, multiplies the magnitude to get the impedance value. During the calibration process, the gain factor is calculated by using an already-known value of impedance of a resistor. Calibration in this study was done using resistors with values of 560 Ω and 2000 Ω at 4 kHz frequency. Using Eq. 2, the magnitude value received from the calibration gave the gain factors as 1.43E-7 and 4.84E-8, respectively. Using these gain factors, the unknown impedance of each mortar layer was calculated using Eq. 3, where the magnitude of the unknown layer is determined through the DFT process described in Eq. 1.

$$\text{Gain Factor} = \frac{1}{Magnitude\ Calibration} \quad (2)$$

$$\text{Impedance} = \frac{1}{(Gain\ Factor\ x\ Magnitude\ Unknown)} \quad (3)$$

Temperature Measurement

The MAX31855T thermocouple-to-digital converter was utilized for temperature measurements in the previous study (Chen et al. 2023). This advanced chip includes a 14-bit analog-to-digital converter (ADC) and provides cold-junction compensation for accurate sensing and correction. Different versions of the MAX31855T are available to work with various thermocouple types, and the T-type thermocouple was selected for this research. The MAX31855T incorporates signal-conditioning hardware that converts the thermocouple's output signal into a voltage compatible with the ADC input channels. To minimize noise-induced errors, the thermocouple wires (T+ and T−) were connected directly to the data logger. The device assumes a linear relationship between temperature and voltage, providing output data based on this approximation. For a T-type thermocouple, the voltage output changes approximately by 52.18 μV/°C. This relationship can be modeled by Eq. 4, where V_{OUT} represents the thermocouple's output voltage (μV), T_R is the temperature of the remote thermocouple junction (°C), and T_R is the temperature of the device (Analog Devices 2007; Maxim Integrated 2015).

$$V_{\text{OUT}} = (52.18\ \mu\text{V/°C})\ \text{x}\ (T_R - T_{\text{AMB}}) \quad (4)$$

References

Chen, L., Ley, M. T., Ghantous, R. M., Weiss, W. J., and Master, N. F. (2023). "Measuring damaging freeze–thaw cycles in the field." *Construction and Building Materials*, 387, 131660.

Analog Devices, Inc. (2007). *AD5933 impedance converter, network analyzer datasheet.* Analog Devices, Inc., Wilmington, MA. https://www.analog.com/media/en/technical-documentation/data-sheets/AD5933.pdf

Maxim Integrated. (2015). *MAX31855 cold-junction compensated thermocouple-to-digital converter datasheet.* Maxim Integrated, San Jose, CA.

Appendix C: Field Locations Details for FT Analysis

Table C1. Field locations for FT analysis.

State	Location	Latitude	Longitude
Oklahoma	Stillwater	36.16238°	-97.08931°
	McCurtain County	34.04799°	-94.40157°
	Texas County	36.68185°	-101.50515°
Illinois	Spring Field (Central)	39.83079°	-88.87192°
	Dixon (Northern)	41.93167°	-88.70806°
	Carbondale (Southern)	37.78329°	-89.24533°
Wisconsin	Green Bay	44.47958°	-88.1371°
	Madison	43.14069°	-89.34521°
	Rhinelander	45.63143°	-89.4824°
New York	Watertown	43.98872°	-76.02609°
	Clifton Park	43.1111°	-76.10384°
	Hauppauge	40.95956°	-72.25183°
Minnesota	Baxter	46.40206°	-94.12734°
	Maplewood	44.93234°	-93.05586°
	Thief River Falls	48.06667°	-96.18333°
North Dakota	Bismarck Site	46.7680°	-100.894°
	Grand Forks Site	47.96667°	-97.4000°
	Fargo Site	46.92424°	-96.81186°
Pennsylvania	Clearfield	41.04647°	-78.4112°
	Cyclone	41.79835°	-78.63543°
	Harrisburg	40.1962°	-76.77249°
Nebraska	Lincoln	40.84781°	-96.76467°
	Thedford	41.96444°	-100.56861°
	Chadron	42.83736°	-103.09806°
Iowa	Fairfield	41.05306°	-91.97889°
	Mason City	43.1544°	-93.32611°
	Ames	41.99045°	-93.61852°
Colorado	Denver	39.84657°	-104.65623°
	Seibert	39.24148°	-102.28192°
	Glenwood	39.52791°	-107.71965°
Kansas	Oakley	38.8701°	-100.9627°
	Hutchinson	38.06824°	-97.86075°
	Topeka	38.94144°	-95.65125°
Idaho	Coeur d Alene US-95	48.29944°	-116.5600°
	Mt Home I-84	43.0500°	-115.86667°
	Paddy Flat SH-55	44.89425°	-116.09978°
Oregon	Bend	44.0950°	-121.200°
	Hinsdale Wave Research Lab	44.5000°	-123.28333°
	Newport	44.58333°	-124.0500°
Missouri	Central Laboratory	38.9470°	-92.6830°
	Northwest District	39.819848°	-93.576951°
	Southeast District	36.76973°	-90.32241°

Appendix D: Relationship Between Resistivity, Temperature, and DOS for Mortar Samples

The DOS for a mortar sample can be estimated using temperature and resistivity data through a two-step linear interpolation process, based on the calibration sample dataset. For instance, Fig. D1 illustrates an isotherm at 20°C, derived through interpolation between the data points at 21°C and 17°C. Given a resistivity value of 0.4 kΩ·cm, the corresponding DOS can be calculated as 70% by performing a second step of linear interpolation along the isotherm. This method allows for the practical estimation of DOS under varying temperature and resistivity conditions.

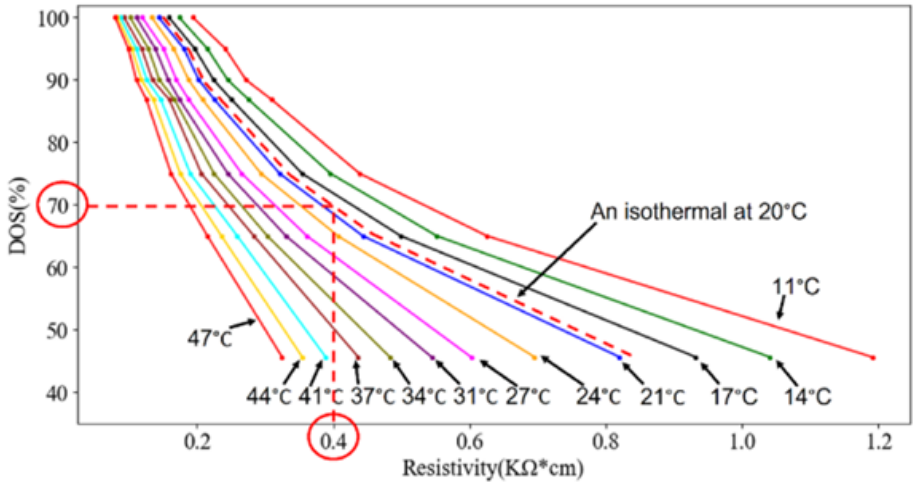

Fig. D1. DOS evaluation using two-step linear interpolation (adapted from Chen et al. 2023).

The relationship between Freezing Temperature and DOS is expressed by the following equation:

$$FT = a_0 \,.\, DOS^5 + a_1 \,.\, DOS^4 + a_2 \,.\, DOS^3 + a_3 \,.\, DOS^2 + a_4 \,.\, DOS + a_5 \quad (1)$$

Table D1. Parameter values in eq. 1 (acquired from Chen et al. 2023).

Parameters	a_0	a_1	a_2	a_3	a_4	a_5
Value	3.81e-08	1.2e-05	1.4e-03	-8.1e-02	2.3e+00	-2.9e+01

References

Chen, L., Ley, M. T., Ghantous, R. M., Weiss, W. J., and Master, N. F. (2023). "Measuring damaging freeze–thaw cycles in the field." *Construction and Building Materials*, 387, 131660.

Appendix E: Year-Specific DOS Maps by Location Across Four Winter Seasons (2020–2024)

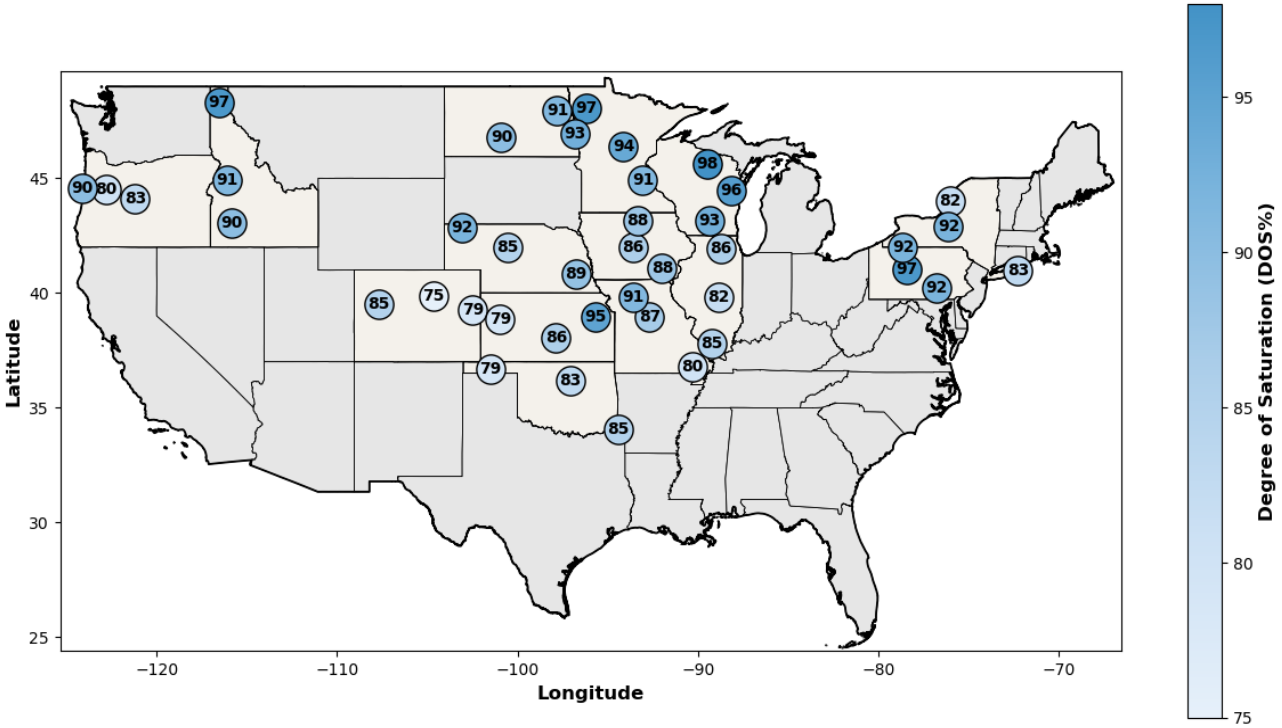

(a)

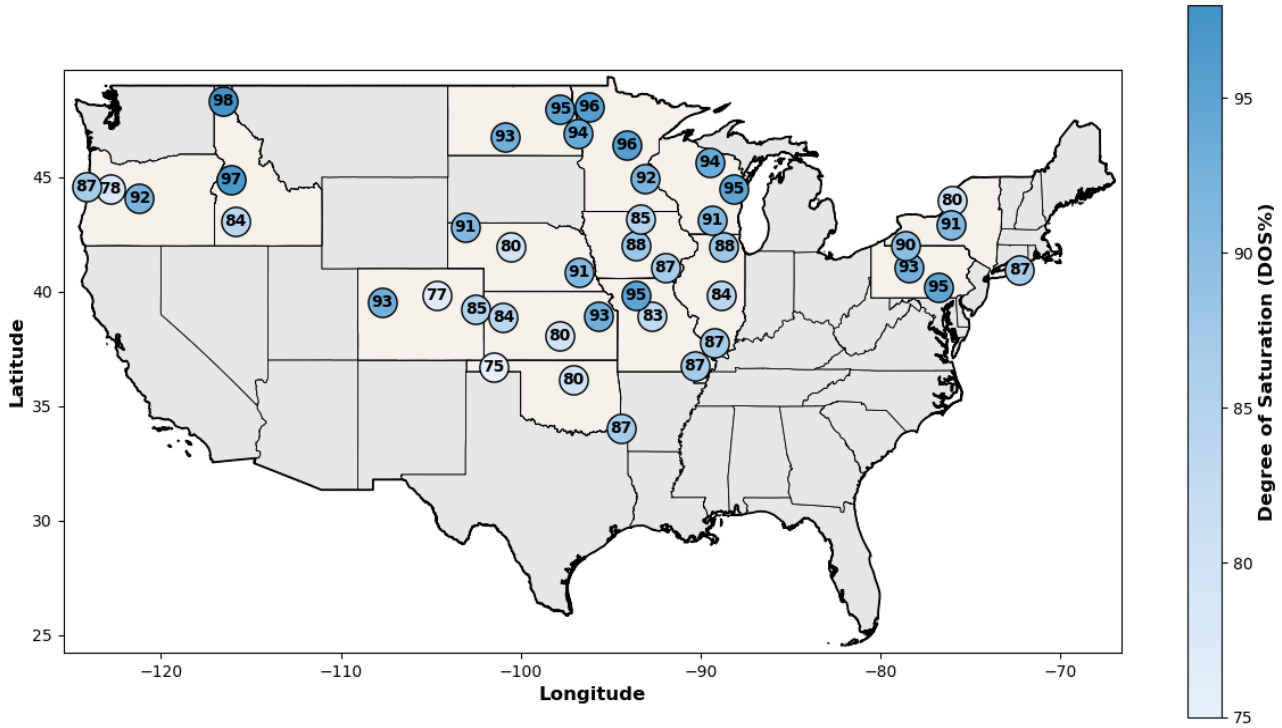

(b)

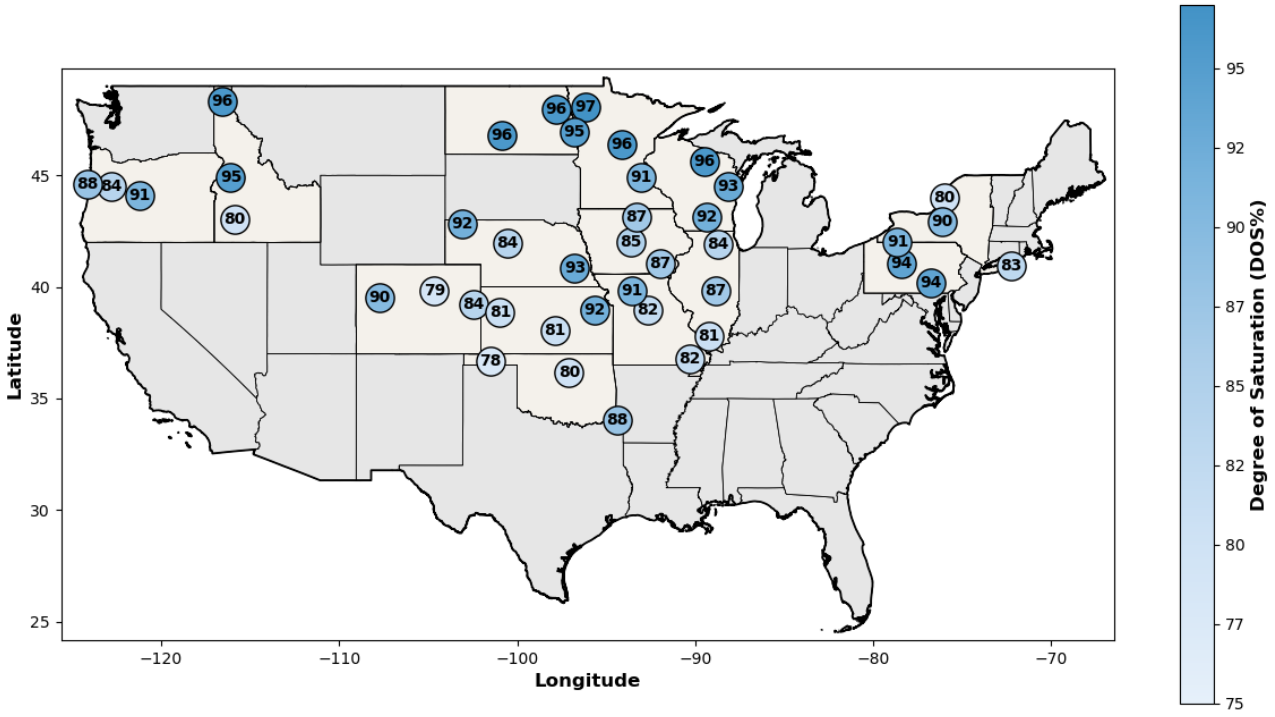
Latitude
Longitude
Degree of Saturation (DOS%)

(c)

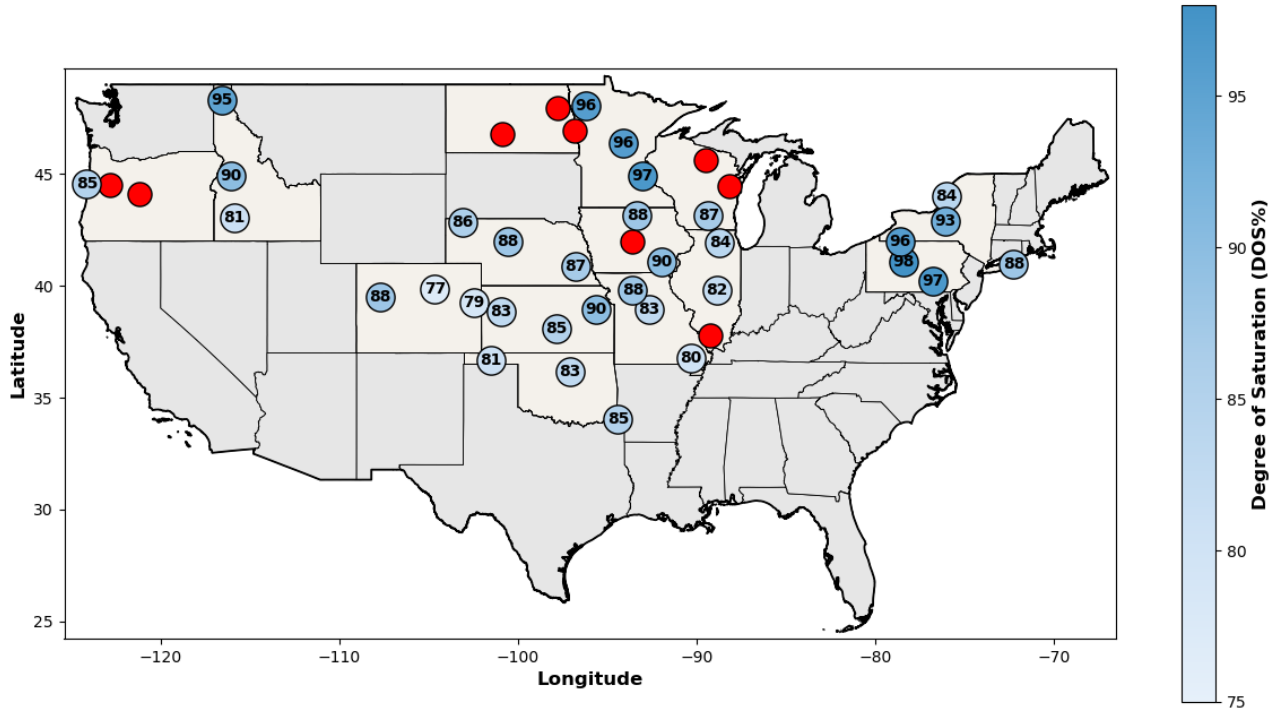
Latitude
Longitude
Degree of Saturation (DOS%)

(d)

Fig. E1. Location-specific average DOS (%) measured at field sites: (a) winter 2020–2021, (b) winter 2021–2022, (c) winter 2022–2023, (d) winter 2023–2024.

Appendix F: Average Monthly DOS Data and Variability Metrics

Table F1. Average monthly DOS data and variability metrics (September 2020 – April 2021).

State	Location	Average DOS (%)								Total Average*	Standard Deviation**	CV (%)***
		Sep	Oct	Nov	Dec	Jan	Feb	Mar	Apr			
Idaho	A	94	96	97	97	98	98	97	95	97	1.4	1.5
	B	88	87	90	91	92	93	93	91	91	2.2	2.4
	C	88	91	90	92	91	89	88	88	90	1.6	1.8
Oregon	A	90	93	89	91	90	89	91	90	90	1.3	1.4
	B	77	78	77	79	81	83	81	80	80	2.1	2.7
	C	80	83	85	85	84	82	84	84	83	1.7	2.0
North Dakota	A	89	89	91	92	91	90	91	90	90	1.1	1.2
	B	88	90	92	93	91	90	91	92	91	1.6	1.7
	C	91	93	93	94	95	91	92	92	93	1.4	1.5
Minnesota	A	92	98	96	98	98	97	97	96	97	2.0	2.1
	B	92	93	95	96	96	95	94	94	94	1.4	1.5
	C	90	91	92	92	91	89	91	90	91	1.0	1.1
Wisconsin	A	97	96	98	98	99	97	98	97	98	0.9	0.9
	B	95	94	96	98	97	96	95	95	96	1.3	1.3
	C	91	90	94	92	97	95	93	91	93	2.4	2.5
Nebraska	A	90	89	93	94	94	93	93	92	92	1.8	2.0
	B	81	83	86	88	89	86	85	84	85	2.6	3.1
	C	87	90	90	89	90	88	87	88	89	1.3	1.5
Iowa	A	88	87	87	86	87	89	88	88	88	0.9	1.1
	B	85	87	86	88	87	85	86	85	86	1.1	1.3
	C	84	88	89	89	90	91	87	88	88	2.1	2.4
Colorado	A	81	83	85	88	86	87	87	86	85	2.3	2.7
	B	72	73	75	76	76	75	75	75	75	1.4	1.9
	C	77	77	76	79	80	81	79	79	79	1.7	2.2
Kansas	A	76	79	77	78	79	82	80	79	79	1.8	2.3
	B	82	88	86	88	88	85	86	84	86	2.2	2.5
	C	92	93	96	96	96	95	94	94	95	1.5	1.6
Missouri	A	89	89	90	93	94	94	91	90	91	2.1	2.3
	B	88	85	89	87	90	88	86	84	87	2.0	2.3
	C	74	78	81	82	82	80	80	80	80	2.6	3.3
Illinois	A	88	85	88	86	87	85	84	83	86	1.8	2.1
	B	80	81	84	85	82	81	81	82	82	1.7	2.1
	C	84	84	88	87	87	85	82	82	85	2.3	2.7
Oklahoma	A	77	77	79	80	78	79	79	79	79	1.1	1.4
	B	79	81	84	85	86	83	82	81	83	2.3	2.8
	C	78	83	89	85	86	84	86	85	85	3.2	3.7
Pennsylvania	A	92	92	91	92	94	91	90	92	92	1.2	1.3
	B	95	95	97	98	97	99	98	94	97	1.8	1.8
	C	93	91	92	94	91	93	92	92	92	1.0	1.1
New York	A	81	84	83	82	80	83	80	80	82	1.6	2.0
	B	90	91	93	92	94	91	91	90	92	1.4	1.5
	C	79	82	81	84	85	83	84	82	83	1.9	2.3
Maximum Value										**97.5**	**3.2**	**3.7**
Minimum Value										**74.6**	**0.9**	**0.9**

*** Average Value of the Average Monthly DOS Values.**
**** Standard Deviation of the Monthly Average DOS Values.**
***** Coefficient of Variation (%) of the Monthly Average DOS Values.**

Appendix G: Year-Specific Total and Damaging FT Cycles Maps by Location Across Four Winter Seasons (2020–2024)

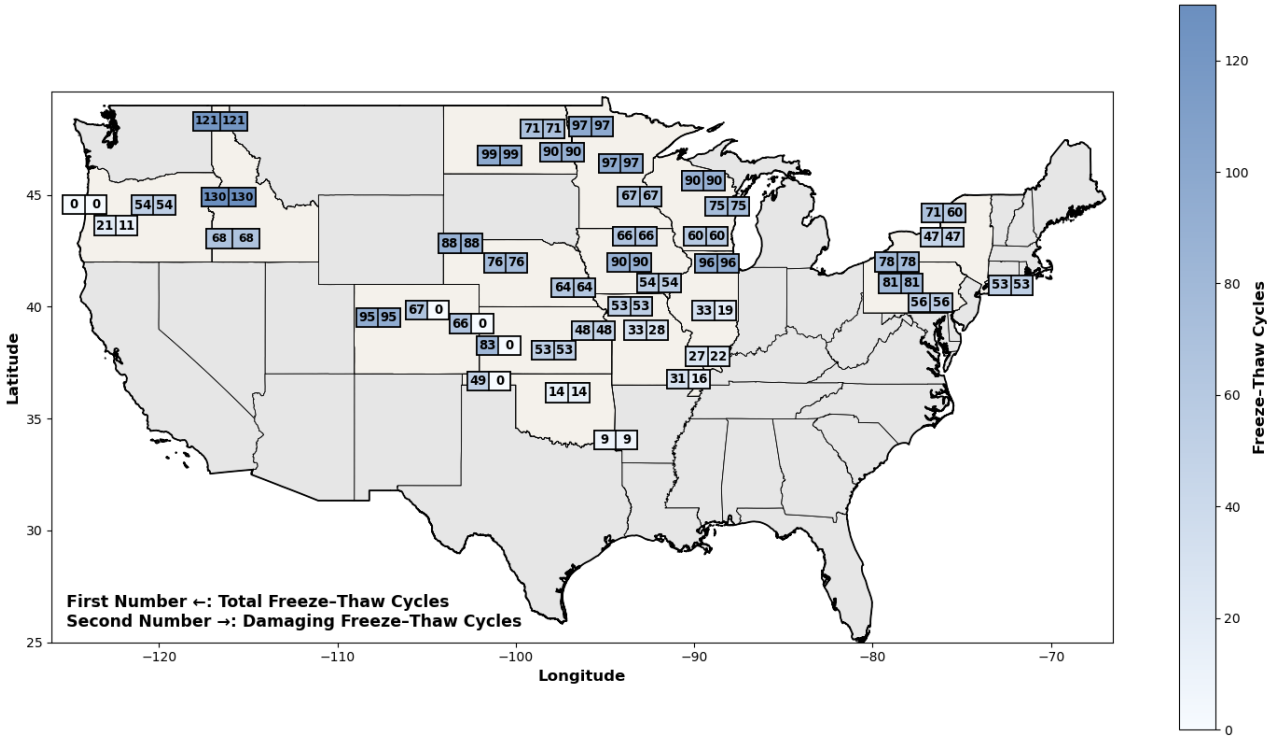

(a)

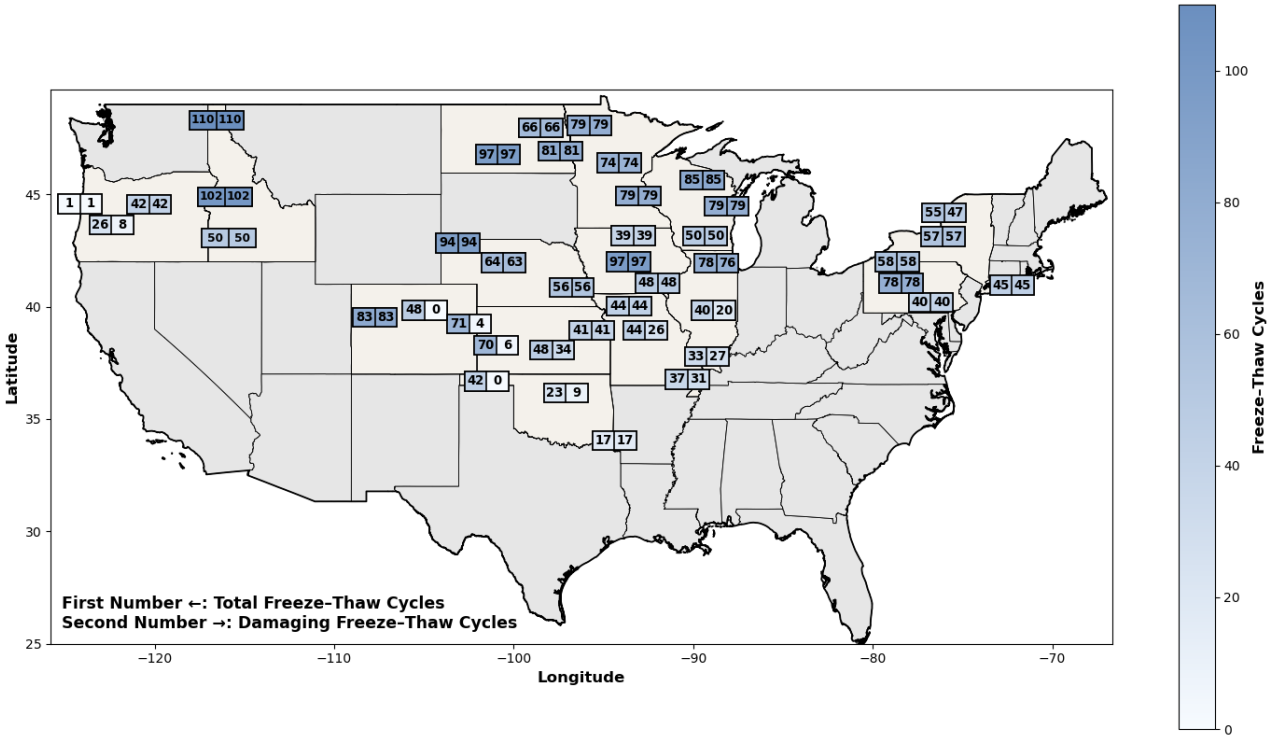

(b)

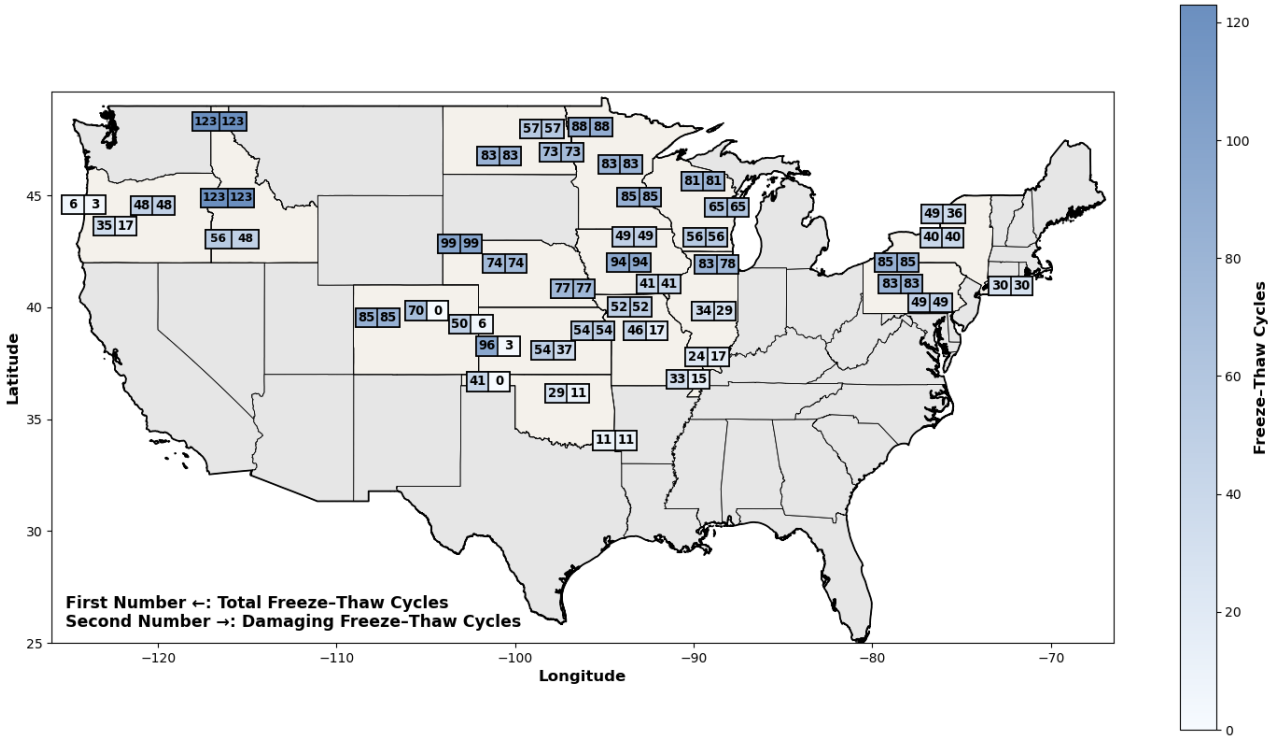

(c)

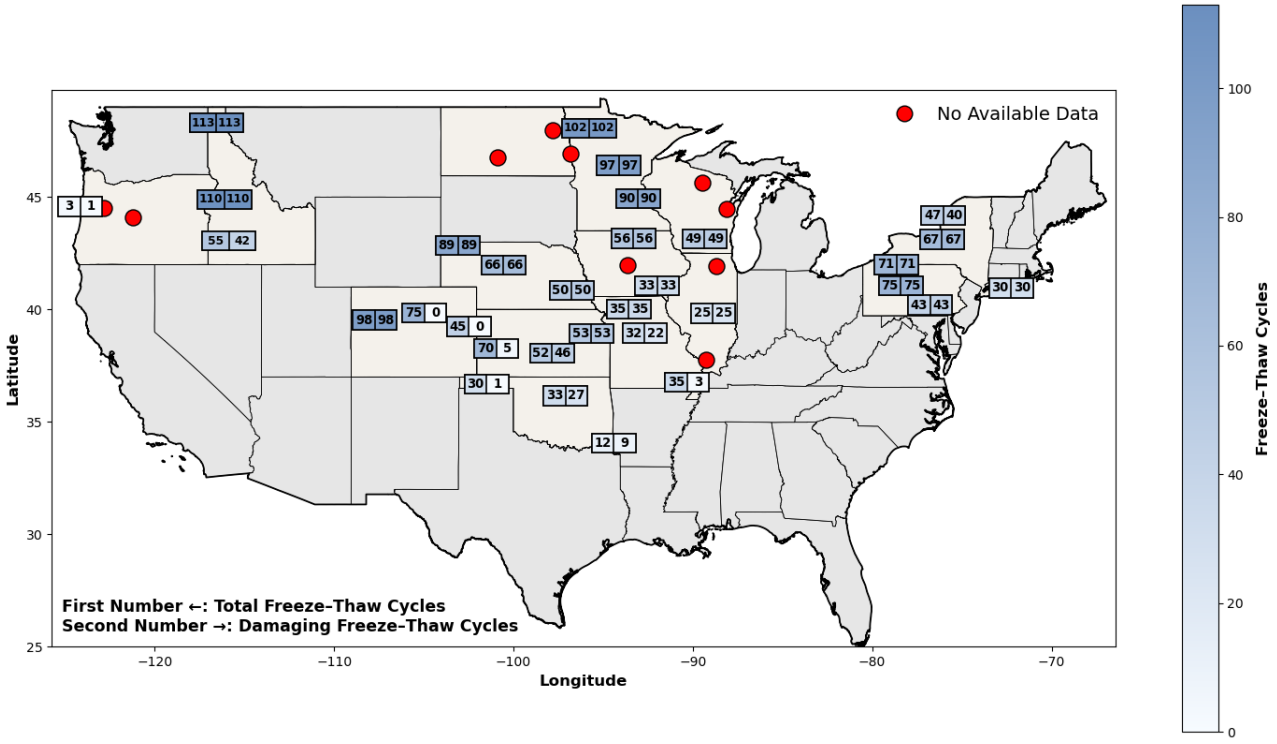

(d)

Fig. G1. Total and damaging field-measured FT cycles: (a) winter 2020–2021, (b) winter 2021–2022, (c) winter 2022–2023, (d) winter 2023–2024.

Appendix H: Standard Deviation and Coefficient of Variation (CV) of DOS, Total, and Damaging FT Cycles Across the Four Winter Seasons.

Table H1. Yearly field-measured DOS at each location with Corresponding Standard Deviation and CV.

State	Location	DOS (%)				4-Year DOS Average	Standard Deviation of DOS	CV (%) of DOS
		Year 1	Year 2	Year 3	Year 4			
Idaho	A	97	98	96	95	97	1.3	1.3
	B	91	97	95	90	93	3.3	3.5
	C	90	84	80	81	84	4.5	5.4
Oregon	A	90	87	81	82	88	2.1	2.4
	B	80	78	84	NA	81	3.1	3.8
	C	83	92	91	NA	89	4.9	5.6
North Dakota	A	90	93	96	NA	93	3.0	3.2
	B	91	95	96	NA	94	2.7	2.8
	C	93	94	95	NA	94	1.0	1.1
Minnesota	A	97	96	97	96	97	0.6	0.6
	B	94	96	96	96	96	1.0	1.0
	C	91	92	91	97	93	2.9	3.1
Wisconsin	A	98	94	96	NA	96	2.0	2.1
	B	96	95	93	NA	95	1.5	1.6
	C	93	91	92	87	91	2.6	2.9
Nebraska	A	92	91	92	86	90	2.9	3.2
	B	85	80	84	88	84	3.3	3.9
	C	89	91	93	87	90	2.6	2.9
Iowa	A	88	85	87	88	87	1.4	1.6
	B	86	88	85	NA	86	1.5	1.8
	C	88	87	87	90	88	1.4	1.6
Colorado	A	85	93	90	88	89	3.4	3.8
	B	75	77	79	77	77	1.6	2.1
	C	79	85	84	79	82	3.2	3.9
Kansas	A	79	84	81	83	82	2.2	2.7
	B	86	80	81	85	83	2.9	3.5
	C	95	93	92	90	93	2.1	2.3
Missouri	A	91	95	91	88	91	2.9	3.1
	B	87	83	82	83	84	2.2	2.6
	C	80	87	82	80	82	3.3	4.0
Illinois	A	86	88	84	84	86	1.9	2.2
	B	82	84	87	82	84	2.4	2.8
	C	85	87	81	NA	84	3.1	3.6
Oklahoma	A	79	75	78	81	78	2.5	3.2
	B	83	80	80	83	82	1.7	2.1
	C	85	87	88	85	86	1.5	1.7
Pennsylvania	A	92	90	91	96	92	2.6	2.9
	B	97	93	94	98	96	2.4	2.5
	C	92	95	94	97	95	2.1	2.2
New York	A	82	80	80	84	82	1.9	2.3
	B	92	91	90	93	92	1.3	1.4
	C	83	87	83	88	85	2.6	3.1

Table H2. Yearly field-measured **total** FT cycles with standard deviation and CV.

State	Location	Total FT Cycles				FT Cycles Average	Total FT Cycles Standard Deviation	Total Freeze-FT CV (%)
		Year 1	Year 2	Year 3	Year 4			
Idaho	A	121	110	123	113	117	6	5
	B	130	102	123	110	116	13	11
	C	68	50	56	55	57	8	13
Oregon	A*	0	1	6	3	3	3	-
	B	21	26	35	NA	27	7	26
	C	54	42	48	NA	48	6	13
North Dakota	A	99	97	83	NA	93	9	9
	B	71	66	57	NA	65	7	11
	C	90	81	73	NA	81	9	11
Minnesota	A	97	79	88	102	92	10	11
	B	97	74	83	97	88	11	13
	C	67	79	85	90	80	10	12
Wisconsin	A	90	85	81	NA	85	5	5
	B	75	79	65	NA	73	7	10
	C	60	50	56	49	54	5	10
Nebraska	A	88	94	99	89	93	5	6
	B	76	64	74	66	70	6	8
	C	64	56	77	50	62	12	19
Iowa	A	66	39	49	56	53	11	22
	B	90	97	94	NA	94	4	4
	C	54	48	41	33	44	9	21
Colorado	A	95	83	85	98	90	7	8
	B	67	48	70	75	65	12	18
	C	66	71	50	45	58	13	22
Kansas	A	83	70	96	70	80	13	16
	B	53	48	54	52	52	3	5
	C	48	41	54	53	49	6	12
Missouri	A	53	44	52	35	46	8	18
	B	33	44	46	32	39	7	19
	C	31	37	33	35	34	3	8
Illinois	A	96	78	83	NA	86	9	11
	B	33	40	34	25	33	6	19
	C	27	33	24	NA	28	5	16
Oklahoma	A	49	42	41	30	41	8	19
	B	14	23	29	33	25	8	33
	C	9	17	11	12	12	3	28
Pennsylvania	A	78	58	85	71	73	12	16
	B	81	78	83	75	79	4	4
	C	56	40	49	43	47	7	15
New York	A	71	55	49	47	56	11	20
	B	47	57	40	67	53	12	22
	C	53	45	30	30	40	12	29

*** CV values are only reported for sites with more than five cycles per year; sites with lower averages are marked with (–).**

Table H3. Yearly field-measured **damaging** FT cycles with standard deviation and CV.

State	Location	Damaging FT Cycles				FT Cycles Average	Damaging FT Cycles Standard Deviation	Damaging FT Cycles CV (%)
		Year 1	Year 2	Year 3	Year 4			
Idaho	A	121	110	123	113	117	6	5
	B	130	102	123	110	116	13	11
	C	68	50	48	42	52	11	22
Oregon	A*	0	1	3	1	1	1	-
	B	11	8	17	NA	12	5	38
	C	54	42	48	NA	48	6	13
North Dakota	A	99	97	83	NA	93	9	9
	B	71	66	57	NA	65	7	11
	C	90	81	73	NA	81	9	11
Minnesota	A	97	79	88	102	92	10	11
	B	97	74	83	97	88	11	13
	C	67	79	85	90	80	10	12
Wisconsin	A	90	85	81	NA	85	5	5
	B	75	79	65	NA	73	7	10
	C	60	50	56	49	54	5	10
Nebraska	A	88	94	99	89	93	5	6
	B	76	63	74	66	70	6	9
	C	64	56	77	50	62	12	19
Iowa	A	66	39	49	56	53	11	22
	B	90	97	94	NA	94	4	4
	C	54	48	41	33	44	9	21
Colorado	A	95	83	85	98	90	7	8
	B*	0	0	0	0	0	0	-
	C*	0	4	6	0	3	3	-
Kansas	A*	0	6	3	5	4	3	-
	B	53	34	37	46	43	9	20
	C	48	41	54	53	49	6	12
Missouri	A	53	44	52	35	46	8	18
	B	28	26	17	22	23	5	21
	C	16	31	15	3	16	12	71
Illinois	A	96	76	78	NA	83	11	13
	B	19	20	29	25	23	5	20
	C	22	27	17	NA	22	5	23
Oklahoma	A*	0	0	0	1	0	1	-
	B	14	9	11	27	15	8	53
	C	9	17	11	9	12	4	33
Pennsylvania	A	78	58	85	71	73	12	16
	B	81	78	83	75	79	4	4
	C	56	40	49	43	47	7	15
New York	A	60	47	36	40	46	11	23
	B	47	57	40	67	53	12	22
	C	53	45	30	30	40	12	29

*** CV values are only reported for sites with more than five cycles per year; sites with lower averages are marked with (–).**

Predicting Concrete Freeze–Thaw Damage with Weather Data-Based Machine Learning

Bahaa N. Abdelrahmana,*, M. Tyler Leya, Guoliang Fanb, Lichun Chena

a Department of Civil and Environmental Engineering, Oklahoma State University, Stillwater, OK 74078, USA

b School of Electrical Computer Engineering, Oklahoma State University, Stillwater, OK 74078, USA

Keywords: Freeze-Thaw Durability, Damaging Freeze-Thaw Cycles, Degree of Saturation, Genetic Algorithms, Weather Data, Machine Learning, Predictive Modeling.

Abstract

This paper presents a machine learning model to predict the number of damaging freeze-thaw (FT) cycles based on weather data. The model combines a genetic algorithm (GA) to identify the most effective environmental thresholds for six major weather variables across four regions in the United States. Training was performed on data from 42 sites within 14 states over the course of a year, then testing was performed using data from the subsequent three years. The model correctly predicted the DOS category 89% of the time for all years and regions. Based on a 95% confidence interval, the number of predicted FT cycles and damaging FT cycles were within 15% of the measured values in all years and regions, meaning that the model provides reliable and consistent performance across varying climatic conditions. Thus, this model allows for an important new ability to predict FT cycles from weather only. This can aid in improving these predictions and lead to the development of better tools to aid specifiers in getting the needed FT durability of their concrete.

1. Introduction

Freeze-thaw (FT) durability of concrete is often critical to the longevity of concrete structures in cold regions. The FT resistance of concrete is primarily a function of its internal degree of saturation (DOS) [1,2]. Damage from FT occurs when water freezes and expands within the pore structure, leading to microcracking, scaling, and long-term degradation [3,4]. The phenomenon was first modeled by Powers [5] and Fagerlund [6], who discovered damage when the material became saturated, and the temperature fell to the freezing point. Critical DOS is the moisture level above which the growth of stresses created by the freezing of water can damage the concrete, which subsequently leads to gradual deterioration [5-7]. It has been demonstrated that the critical degree of saturation was between 78–90% [7-10]. This range is impacted by the size, spacing, and overall volume of air voids within the concrete, which can allow for relief of the hydraulic pressure due to the ice formation [11-14]. A FT cycle occurs when the temperature of the concrete falls below the freezing temperature and then returns back above 0°C. Therefore, a damaging FT cycle occurs when the DOS is at or above the

critical DOS. If the cycle occurs when the DOS is below this critical value, then the cycle does not count as a damaging cycle [7, 14-16].

Presently, concrete design for FT durability is typically prescriptive exposure classes (ACI 201.2R, ACI 318) [16,17]. These documents use the designer or specifier to determine the appropriate exposure category based on the severity of the freezing and thawing to be experienced. While this is simple to understand, the specifier must make assumptions about local weather, the saturation level within the concrete, and the anticipated frequency of FT cycles. This can lead to either under-design or over-design of the structure. In contrast, the desired tool should utilize local climatic information and provide recommendations on both the level of saturation in the concrete and the frequency of FT cycles.

Machine Learning (ML) has been an increasingly common research direction in concrete research. Concrete properties of value are often the targets to be predicted. The nature of concrete research data is nonlinear and multivariate, leading to well-suited for ML approaches. Numerous studies have developed predictive models of concrete properties, including compressive strength [18–22], crack propagation [23], thermal expansion [24], and other mechanical properties [25–28]. The common thread among these papers is that they demonstrate the ability of ML models to capture and represent the complex behavior of these materials. ML has been widely used to model the mechanical properties of concrete. However, only a few studies have explored its potential for assessing concrete durability, particularly under FT conditions. A handful of authors have developed ML models to predict FT resistance based on mixture design parameters and laboratory test results [29]. A few studies have proposed using a framework to extract microstructural features (pore structures) with deep learning and image-based data for the assessment of FT durability indices [30,31]. ML techniques have also been used to predict the FT behavior of aggregates [32]. However, this is still a reduced system and does not represent the full complexities of concrete systems exposed to real-world conditions.

Predicting the FT performance in concrete requires understanding how the moisture content, temperature, and ice formation evolve over time. Previous work has collected this information from 42 different field locations over the course of four years [33,34]. This work aims to employ ML techniques to relate the DOS and the number of damaging FT cycles to local weather parameters. Extensive previous research has been completed in predicting the soil moisture content of an area based on the local weather parameters [35-44]. The research was

consistent in identifying six key weather parameters. This included: temperature, precipitation, relative humidity, solar radiation, wind speed, and air pressure [35-44]. These same parameters will be used to predict the moisture content of concrete. However, in order to predict FT cycles, they will be used to predict damaging FT cycles by incorporating the moisture information to predict the number of damaging FT cycles.

Traditional ML models often struggle to represent the complex relationships between environmental factors such as temperature, relative humidity, and precipitation [45–47]. These variables interact in nonlinear ways that make it difficult for models to identify the specific conditions that cause damaging FT cycles. For example, in this study, ten machine learning models were assessed, and the GAs showed the best overall performance; further details are discussed later in the results section and also in Appendix D. The GA uses one year of training data, including measured DOS, FT cycles, and six key weather parameters, to predict the number of damaging FT cycles in a concrete slab.

This work addresses a major gap by providing a data-driven approach to directly connect local weather conditions to concrete DOS and FT performance using a large field dataset from 42 locations across the U.S. This tool can use either measured or simulated weather data to provide estimates of FT damage under different environments. This paper lays the foundation for developing measurement-based mapping systems and tools of damaging FT cycles for different locations using long-term historical weather records, which offer practical guidance for FT durability design, which will be developed in a future study.

2. Methodology

2.1. Data Collection and Preprocessing

2.1.1. Field-Measured DOS Data

The DOS represents the proportion of voids in concrete that are filled with water and is an important factor in determining its FT durability. Field-measured DOS data from 42 locations across the United States were collected in a previous study over four consecutive winters [34]. The locations were chosen to capture a wide range of climate variability and include the state agencies that funded the research.

A single, mortar mixture was used for all field samples at each location. The use of the same mixture at each location enables direct comparison of DOS behavior. However, the results are specific to this material and mixture design. The mixture design chosen was representative of

pavement and bridge deck concrete, and so this makes this work applicable to a wide variety of applications. For this study, the DOS data from each location were averaged for each month, and these monthly average values were grouped into three categories representing practical thresholds of FT vulnerability. By using monthly averages from the concrete and the weather data, this minimizes the short-term variability. This approach allows the model to capture more meaningful relationships between the environmental conditions and the saturation level of the concrete.

Previous studies identified the critical DOS range to be between 78% and 90% [7-10]. Thus, 80% 80% was chosen as a practical lower limit and was a convenient place to segment the data. Locations with a DOS <80% are considered to have minimal risk for FT damage, locations with a DOS between 80% and 90% suggest a moderate risk, and DOS values >90% have the highest risk of FT damage. The developed predictive model is used to classify the DOS of a location into one of these ranges based on six weather parameters.

To account for geographic variability, the field sites were divided into four regions, Northwest, South, North, and Northeast, based on climate variations. Climate variation strongly influences both DOS and FT durability of concrete, with northern regions generally experiencing lower temperatures and greater FT exposure than southern states. Some states, such as Illinois and Missouri, have regions that are assigned to the north and south regions because of their differences in weather. These regional distinctions are used because the weather was found to be different in each region, so the prediction was improved by using a ML model that is specific to the region. These regions are shown in Fig. 1.

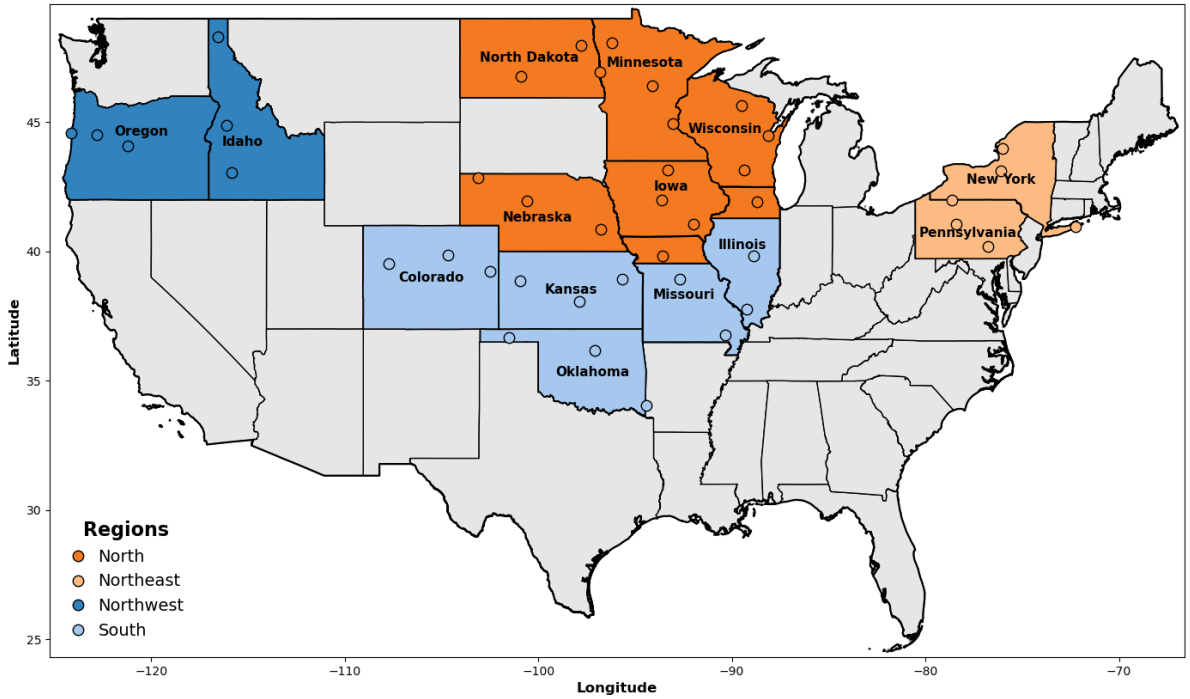

Fig. 1. Regional classification used for FT cycle prediction, showing the four regions applied to field samples.

2.1.2. Weather Data

The study considered six weather variables presented in Table 1. These parameters were chosen as they are the most commonly used in the soil literature for the assessment of environmental impact on the saturation and drying process of porous media such as soils [35–44]. Thus, these same parameters also control moisture movement and retention within concrete, making them suitable inputs for predicting DOS and FT cycles. Precipitation is the liquid-equivalent of rain and snowfall combined. Snowfall amounts were converted to liquid-equivalent precipitation amounts, using the standard water-equivalent amounts that weather stations report, so that rain and snow contributions to total precipitation can be compared on a common volumetric basis across areas.

Solar radiation was expressed as Global Horizontal Irradiance (GHI) in kWh/m², which quantifies the total solar energy incident on a horizontal surface. Weather data for each field location across the United States were collected from the Open-Meteo API [48], an open-source, research-oriented climate database that compiles long-term, quality-controlled records from established meteorological networks and provides broad spatial coverage. Because precipitation accumulates over time, monthly totals were calculated by summing the daily precipitation values. In contrast, the remaining parameters, air temperature, relative humidity,

solar radiation, wind speed, and air pressure, reflect average environmental conditions and were therefore averaged over each month to reduce random short-term fluctuations. This allowed an average DOS to be used for each location.

Table 1

Selected weather variables and their relevance to moisture behavior in concrete.

Variable	Unit	Role and Relevance
Air Temperature	°C	Governs evaporation, condensation, and FT cycles.
Precipitation	mm	Represents the moisture ingress into concrete pores.
Relative Humidity	%	regulates vapor exchange and internal drying
Solar Radiation (GHI)	kWh/m²/day	Influences surface heating, drying rates, and temperature gradients within concrete.
Wind Speed	m/s	Affects convective moisture loss from exposed concrete surfaces and accelerates drying.
Air Pressure	kPa	Impacts vapor diffusion and moisture transport through capillary pores.

2.1.3. Data Collection Period and Study Timeframe

The DOS and weather data were collected during the winter seasons, spanning from September to April, over four consecutive years (September 2020 to April 2024). The model was trained and developed using data from the first winter season (September 2020 to April 2021). It was then used to predict the DOS category and FT cycles for the following three winters, as shown in Table 2.

Table 2

Summary of Model Training and Prediction Periods.

Purpose	Time
Training Year 1	September 2020 to April 2021
Prediction Year 1	September 2021 to April 2022
Prediction Year 2	September 2022 to April 2023
Prediction Year 3	September 2023 to April 2024

2.2. Model Development

The predictive model was developed using a GA framework, selected for its ability to efficiently explore complex, nonlinear relationships between environmental variables and DOS. GA is an optimization technique based on the concept of natural selection. A population of candidate solutions to an optimization problem is evolved toward better solutions by repeatedly selecting and applying genetic operators like selection, crossover, and mutation to individual candidates in the population [49-56]. In this work, the GA was used to determine the combination of thresholds of the six weather variables that most accurately predict the measured DOS categories.

2.2.1. Segmenting the Data

ML algorithms are more efficient when the data are binned into discrete classes. This limits the number of possible results and minimizes the impact of scale and units of measurement. As a preprocessing step for modelling, it was decided to sort each weather parameter with two thresholds (Threshold 1 and Threshold 2), which can be used as a boundary value to separate the weather data into high, medium, or low with respect to the DOS of the concrete. This segmentation procedure can be organized with a trinary code. The trinary code is summarized below:

$$\textbf{Trinary Code} = \begin{cases} 0, & \text{if } x \leq \text{Threshold 1} \\ 1, & \text{if Threshold 1} < x \leq \text{Threshold 2} \\ 2, & \text{if } x > \text{Threshold 2} \end{cases}$$

Where x represents the value of the weather parameter.

The GA continuously adjusts the thresholds for each weather parameter to determine the combination of threshold values that best predicts the measured DOS for the regions shown in Fig. 1. Once these threshold values have been found, each measurement location can be categorized by a six-digit number made up of a 0, 1, or 2 in each digit $(x_1, x_2, x_3, x_4, x_5, x_6)$. The value of 0, 1, or 2 is determined by comparing the average monthly weather parameter in comparison to the threshold values. Each digit in the code corresponds to a specific weather variable in the following order: air temperature, precipitation, relative humidity, solar radiation, wind speed, and air pressure. This was done to enable effective categorization.

The thresholds for each parameter were initially defined based on statistical analysis of the four-year dataset, where the lower and upper thresholds correspond to the 33rd and 66th percentiles of each feature's distribution. This ensured that the coding captured low, medium, and high ranges representative of realistic weather variability across all sites. These threshold values were then optimized by GA, which iteratively adjusted the values to improve the

model's classification accuracy for predicting the DOS. The established upper and lower limits from the GA model are shown in Appendix A.

2.2.2. Fitness Function: Bhattacharyya Distance

In GAs, the fitness function determines the objective numerical value for each member of the population of solutions. A good fitness function helps the algorithm drive better threshold combinations that enhance DOS class separation by progressively selecting threshold sets that can offer greater degrees of separation for each optimization cycle [57]. In this case, the fitness function calculates a measure of separability between the distributions of weather-variable threshold combinations that belong to different measured DOS categories. This process is essential to the model development as it helps the model identify how different weather conditions impact the DOS of concrete and its vulnerability to FT damage. The selection of weather-variable threshold combinations that result in the highest degree of separability between measured DOS categories should result in a model that can better represent the impact of temperature, precipitation, relative humidity, solar radiation, wind speed, and air pressure on moisture accumulation and its associated damage.

The Bhattacharyya distance was used as the fitness function. The Bhattacharyya distance is a nonparametric, distribution-based measure that directly compares two probability distributions [57–59]. Unlike distance-based measures of performance, it is independent of any parametric assumptions on the data and is well-suited for nonlinear environmental datasets. The Bhattacharyya distance can range from 0 to infinity, with higher values indicating lower overlap between DOS categories and better classification performance [57–59].

2.2.2.1. Converting Trinary Codes to Probability Distributions

The frequency of each six-digit trinary weather code in the training set was counted and then normalized by the total counts in that category so that the probabilities summed to 1. The resulting distributions, denoted *P* (for <80%), *Q* (for 80–90%), and *R* (for >90%), represent the likelihood of each six-digit code occurring within its respective DOS category, and were compared pairwise using the Bhattacharyya distance to quantify separability.

For instance, consider the category *P* corresponding to DOS <80%. Suppose the six-digit trinary code (e.g., *000000*) appears 10 times within this category, and the total number of codes recorded for *P* is also 10. The probability of observing this code within the category is therefore

$$p_i = \frac{\text{Count of six-digit trinary code } (e.g. 000000) \text{ in category } P}{\text{Total number of six-digit trinary codes in category } P} = \frac{10}{10} = 1.0$$

indicating that this particular trinary code $(e.g., 000000)$ occurs in all observations within the <80% DOS category. Conversely, if the same six-digit code does not appear in the other categories (Q (for 80–90%), or R (for > 90%)), its probability becomes zero ($q_i = 0$ and $r_i = 0$), indicating that this $\text{six} - \text{digit trinary code}$ is unique to the <80% DOS category. Thus, differences in code probabilities across categories capture distinct weather–DOS relationships, which are later quantified using the Bhattacharyya distance.

Because six weather features each have three possible trinary codes (0, 1, 2), there are $3^6 = 729$ unique combinations (bins), each representing a distinct weather pattern. These normalized probability distributions (P, Q, and R) were then used to compute the Bhattacharyya coefficient (BC), which measures the overlap between the probability distributions of any two DOS categories.

2.2.2.2. Computing the Bhattacharyya Coefficient and Distance

The *Bhattacharyya coefficient* (BC) measures the similarity between two probability distributions. In this study, the three distributions P, Q, and R represent the normalized trinary weather-code probabilities for the three DOS categories, where P corresponds to DOS (<80%), Q to DOS (80–90%), and R to DOS (>90%). The BC quantifies how much the two distributions overlap, $(P\ vs.\ Q), (P\ vs.\ R), and\ (Q\ vs.\ R)$, which is a critical property when the goal is to separate classes effectively. For the first pair, P and Q, the BC is calculated as shown in Equation (1) [57]:

$$BC\ (P, Q) = \sum_{i=1}^{n} \sqrt{p_i . q_i} \qquad \text{Equation (1)}$$

where p_i and q_i represent the normalized probability values of the weather variable across two DOS categories being compared. Similarly, the BC was computed for the other two category pairs, (P vs. R) and (Q vs. R).

The square root term in Equation (1) plays an important role. Multiplying p_i and q_i without the square root, the coefficient is dominated by the high probability regions. In this case, a low-probability but meaningful overlap between the two distributions will have less influence on the value of the coefficient. Taking the square root counteracts this compression of high values and expansion of lower values and leads to a more uniform, symmetric measure of overlap that

is not dominated by one of the distributions even in the case when the two distributions are very different (e.g. one distribution is much sharper or more skewed than the other) [60].

Since the BC ranges from 0 to 1, the *Bhattacharyya distance* (D_B) transforms this coefficient into a measure of dissimilarity through a logarithmic function, as shown in Equation (2) [57,58]:

$$D_B\,(P, Q) = -\ln\,(BC) \qquad \text{Equation (2)}$$

The negative natural log transformation yields an infinite range (0 to ∞), in which larger D_B values represent better separability between DOS categories. Logarithmic transformation mathematically changes multiplicative relationships between probabilities into additive ones, and this renders the metric more sensitive to small differences in overlap and therefore more amenable to optimization in the GA setting [61, 62].

For example, if the trinary code (2, 0, 0, 0, 2, 2) appears only in the >90% DOS category and never in the <80% or 80–90% categories, the corresponding probabilities are p_i (>90%) = 1, $q_{i,}$ (<80%) = 0 and r_i (80–90%) = 0. For this case, the coefficient between the >90% and <80% categories is $BC = \sqrt{1 \times 0} = 0$, giving $D_B = -\ln\,(0) = \infty$. This means that the trinary code here is unique, and there is no overlap between these two categories of DOS. The same logic holds for each other category pair in Table 3. This represents perfect separability where the weather pattern of this code is uniquely characteristic of the >90% DOS category.

For comparison, if a trinary code occurs equally across two DOS categories, the probabilities would be $p_i = q_i = 0.5$, giving $BC = \sqrt{0.5 \times 0.5} = 0.5$ and $D_B = -\ln\,(0.5) = 0.69$, which represents overlap between the categories.

Thus, larger $D_B$values indicate greater separability between the DOS categories. When two DOS categories have nearly identical probability distributions, $BC \approx 1$ and $D_B \approx 0$, indicating complete overlap. Conversely, when their distributions are entirely distinct, $BC \approx 0$ and $D_B \approx \infty$, representing maximum separation between the DOS categories [57]. In our study, we consider higher D_B values to be more desirable. In this case, the probability distributions of the two DOS categories overlap minimally, and the GA can find weather-variable thresholds to create better distinctions. This metric helps to ensure the model is as effective as possible at predicting outcomes. It is important to make this distinction, as the fundamental goal of the GA model is to create distinctions between the DOS categories by determining the best weather-variable thresholds. By making the Bhattacharyya distance the fitness function of the

algorithm, we can directly optimize how distinct these categories are in probabilistic terms and ensure the resulting model is effective at not only differentiating between DOS categories but also capturing information about the environmental effects on FT durability.

Table 3
Example Calculation of the Bhattacharyya Coefficient and Distance for the Trinary Code (2, 0, 0, 0, 2, 2).

DOS Category Pair and Probability Substitution	Bhattacharyya coefficient (BC)	Bhattacharyya distance ($\boldsymbol{D_B}$) = - ln (*BC*)	Interpretation
$\boldsymbol{p_i}$ (>90%) = 1, $\boldsymbol{q_i}$ (<80%) = 0	$BC(P,Q) = \sqrt{p_i q_i}$ $= \sqrt{1 \times 0} = 0$	$D_B(P,Q) = -\ln(0)$ $= \infty$	Perfect separation; no overlap
$\boldsymbol{p_i}$ (>90%) = 1, $\boldsymbol{r_i}$ (80–90%) = 0	$BC(P,R) = \sqrt{p_i r_i}$ $= \sqrt{1 \times 0} = 0$	$D_B(P,R) = -\ln(0)$ $= \infty$	Perfect separation; no overlap
$\boldsymbol{r_i}$ (80–90%) = 0, $\boldsymbol{q_i}$ (<80%) = 0	$BC(Q,R) = \sqrt{r_i q_i}$ $= \sqrt{0 \times 0} = 0$	$D_B(Q,R) = -\ln(0)$ $= \infty$	Perfect separation; no overlap

2.2.2.3. Fitness Function Evaluation and Optimization

The fitness was determined as the negative value of the sum of the Bhattacharyya distances between all pairs of DOS categories as per Equation (3) [57,58].

$$Fitness\ Score = -\sum_{k=1}^{3} D_B^k \qquad \text{Equation (3)}$$

where 3 represents the number of DOS categories.

This approach allows the GA to favor solutions that produce greater separation between DOS categories. Since larger D_B values indicate better distinction, summing them captures the total separability across all categories. The negative sign is used because GA evaluates fitness by minimizing the objective function. Since larger D_B indicate greater separation between DOS categories, taking the negative sum reverses the direction of optimization. This way, minimizing the fitness value corresponds to maximizing the overall separability among the DOS categories.

2.2.3. Genetic Algorithms Framework

The algorithm begins by generating an initial population, which in this case consists of possible threshold sets for the six weather variables. In this study, a population size of 200 was chosen, meaning that 200 different combinations of weather thresholds were created in the first generation. This number was chosen to provide sufficient diversity for reliable convergence without excessive computational time. Each threshold set represents one possible way that

weather conditions could be divided to classify the DOS categories. The algorithm then evaluates how well each threshold set separates the measured DOS categories using the fitness function. By starting with a broad and diverse population, the algorithm increases its chances of identifying combinations that best capture the complex, nonlinear relationships between weather variables and concrete saturation behavior [63–65].

2.2.3.1. Mutation

Mutation is performed on the first population to diversify and explore the parameter search space for new combinations. Mutation slightly perturbs the existing threshold combinations to create new candidate threshold combinations that have the potential to perform better at separating DOS categories [65, 66]. Mutation is an essential part of this operation as without it the algorithm would converge prematurely and limit itself to a small portion of the search space. Mutation allows for the exploration of new areas of the parameter space through the generation of new combinations of weather thresholds that may or may not be represented in the initial population.

This process is essential to identifying the most appropriate weather thresholds that will separate the two measured DOS categories. The weather thresholds that most accurately reflect environmental conditions will result in DOS distributions with the least overlap between categories. This work used the Differential Evolution (DE/rand/1) mutation strategy. This strategy was used because it is a simple yet effective mutation scheme that maintains population diversity while simultaneously biasing the search toward better-performing individuals. It achieves this by generating new members through a combination of randomly selected threshold sets [65, 66]. The method is computationally inexpensive and exploits the search space between existing members to improve performance.

A mutation factor of 0.2 was used to control the extent of the change introduced with each mutation step. A smaller factor would have led to small changes, resulting in slow exploration. A larger factor would have been computationally expensive and led to an unstable search. The value of 0.2 was empirically selected as it offered a good balance between exploration and exploitation.

2.2.3.2. Crossover

Once a mutation generates new threshold combinations, the algorithm proceeds to the crossover step, which mixes the weather-variable thresholds from different threshold

combinations. This step creates a new trial combination of thresholds by taking a portion of a newly mutated threshold set and combining it with a portion of a previously existing threshold set. The purpose of crossover is to further combine the best thresholds (those that most effectively separate the DOS categories) from different sets while still maintaining diversity in the trial runs [63–67].

For this study, a crossover rate of 0.8 was used, which means that approximately 80% of threshold values in a new combination were inherited from the mutated set, with the remaining 20% of the values being inherited from the original set. This way, the algorithm can preserve useful threshold patterns that may have been developed in earlier generations, while still exploring the full space of possible threshold combinations that could lead to improved classification.

Conceptually, crossover can be thought of as a controlled form of experimentation. The algorithm tests to see if taking thresholds from different, but still well-performing, sets of weather variables can lead to a better overall separation of the DOS categories. For example, a combination of thresholds that is effective for temperature could be combined with a combination that better represents the effects of relative humidity, and an improved overall set of thresholds could result.

This step is important as it maintains diversity in the population and allows the algorithm to test multiple, potentially promising, paths simultaneously. Without crossover, the population of threshold combinations could quickly become too similar from generation to generation, and the algorithm would be less able to identify new and more effective threshold configurations to describe the DOS of the concrete [63–67].

2.2.3.3. Selection

For each generation after crossover, the algorithm has to decide which threshold combination should continue. This selection process essentially determines which candidates are fittest in terms of being able to separate the different DOS categories. Several selection strategies are available, but in this case the fitness function described earlier is simply used to compare the fitness values of the newly generated (trial) and the existing threshold sets and the one with a better (higher) fitness value is carried forward to the next generation (replaces the other if the trial set is fitter) [50, 68].

In a conceptual sense, the selection process is essentially the judgment phase of the optimization process. It determines which set of weather-threshold values is best at distinguishing the different saturation states of concrete, and it only lets the fittest combinations survive and be subject to further variation. By iteratively and automatically performing this selection process over many generations, the algorithm applies a kind of survival of the fittest pressure on the evolving threshold combinations.

In this way, the overall fitness of the population is slowly but continuously improved. The algorithm eventually converges when the incremental improvements of the fitness function become insignificant, and the algorithm then converges to the set of weather thresholds that most effectively discriminate between different saturation states in concrete [50, 68].

2.2.3.4. Optimization and Convergence

During this optimization process, the algorithm automatically monitored the best fitness value in each generation to track convergence, and the algorithm was deemed to have converged when improvements in the best fitness score became negligible. In this study, optimal thresholds refer to a particular set of threshold values for the six weather variables that most effectively separate the measured DOS categories. This particular set of thresholds is associated with a particular set of environmental limits that may be used to directly associate weather conditions and the DOS of the concrete.

For repeatability of the optimization procedure and thus produce the same results each time, a fixed random seed of 42 was used in both the initialization and the evolutionary phases of the GAs. The random seed marks the start of the sequence of pseudorandom numbers, which are later used to determine how the initial population is generated and which mutations are applied in the subsequent evolutionary steps of the algorithm. Fixing the random seed to the same value thus implies that with every restart of the algorithm, the same sequence of random operations is generated and that the complete optimization procedure can therefore be repeated bit by bit with identical results [69].

The value 42 was chosen arbitrarily, but consistently for all weather variables and all runs of the model. This procedure allows for complete transparency and repeatability of the model, both of which are essential for judging the predictive performance of the developed model.

2.3. Lookup Table and Prediction Process for New Data

Once the best thresholds were defined, a lookup table was generated that associates the various combinations of weather values with the corresponding categories of DOS. This table acts as a kind of summary of all the relations discovered between weather variables and measured DOS values in the training data. It encodes each combination of the six weather variables and the DOS category that was observed with those conditions. In other words, it reduces the complex relations between weather and concrete DOS into a simple reference system. This allows for fast and direct classification of new weather data, while still being exactly the same as the trained model.

When a new weather dataset is presented, the same thresholds are used to assign each variable to a low, medium or high value. The combination of these categories together can be considered a simple pattern that describes the overall state of the weather. The algorithm then looks up this pattern or the most similar one in the lookup table and assigns the associated category of DOS.

If an exact match for the new pattern does not exist in the lookup table, the algorithm selects the closest match using the Hamming distance, which counts how many positions differ between two patterns. In simpler terms, it finds the trinary code that is most similar to the new one [70-73]. For instance, if the new weather pattern differs from an existing one in only a single variable (e.g., temperature slightly higher but all other variables similar), that closest match is used to predict the DOS category.

In cases where a trinary code does not exactly match any existing code but shows equal similarity to multiple classified codes, the category that appears most frequently in the training data is selected. For example, if a specific trinary code has been associated with both the 80–90% and >90% DOS categories, but that trinary code occurred more often in the DOS >90% category in the training data (e.g., a trinary code observed 15 times in DOS >90% and 3 times in DOS 80-90%), the algorithm will assign >90% to that trinary code. When both categories occur with equal frequency, the higher DOS category is chosen, as it represents a more saturated and potentially more critical condition for FT damage.

2.4. Prediction Evaluation

The model's accuracy is evaluated through two metrics: correct predictions and incorrect predictions.

- **Correct Prediction**: A prediction is considered correct if the predicted trinary code exactly matches a code from the training data, and the corresponding DOS category is the same.

Alternatively, if the predicted trinary code does not exactly match but is the closest to a code in the training data (based on the Hamming distance), and the predicted DOS category matches the measured value from the field, then this is considered a correct prediction.

- **Incorrect Prediction**: A prediction is considered incorrect if the predicted trinary code matches a code from the training data, but the predicted DOS category does not align with the measured DOS category.

2.5. Predicting FT Cycles

2.5.1. Detecting Actual FT Cycles

The detection of field freezing events was based on the relationship between the DOS and the freezing temperature of concrete. The freezing temperature is defined as the point at which the pore solution within the concrete begins to freeze, and this temperature depends directly on the DOS of the material [33,34]. As illustrated in Fig. 2, concrete with a higher DOS freezes at warmer temperatures, meaning it is more susceptible to ice formation and potential freeze–thaw damage. Conversely, concrete with a lower DOS requires colder temperatures to reach the freezing point.

The field-measured FT cycle, defined as a temperature below the freezing temperature that was followed by a rise to temperatures above 0°C, was used in this study to compare with the values predicted by the model. The analyses of the field-measured data were limited to the sensors 51 mm below the surface since this depth had the highest DOS values in all cases [33,34].

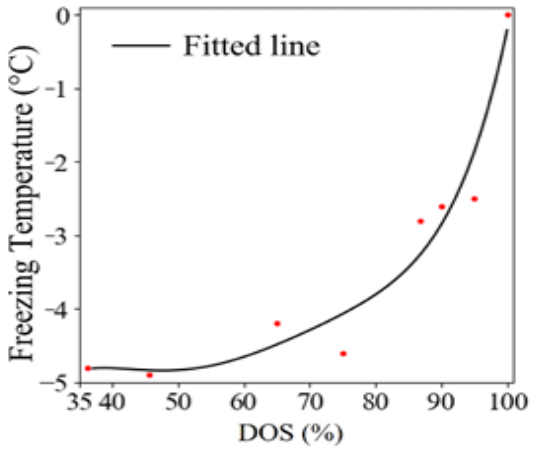

Fig. 2. Relationship between freezing temperature and DOS (adapted from [33]).

2.5.2. Predicting FT Cycles

Fig. 2 shows how the freezing temperature varied for samples with different DOS. Instead of using the curve shown in Fig. 2, a single freezing temperature was assigned to each DOS category to simplify the analysis. The values used for the analysis are listed in Table 4. These values were selected by testing multiple freezing temperatures within the range of each DOS category, as shown in Fig. 2, to determine which provided the most accurate prediction of freeze–thaw cycles. More details are provided in Appendix B.

In summary, a freeze event was defined as any period when the air temperature dropped to or below the freezing temperature outlined in Table 3, based on the DOS category for the location, based on the weather, and a thaw event occurred when the air temperature increased to or above 0°C. A complete freeze–thaw cycle was identified when the sample goes from a freezing point to a thawing point.

Table 4

Selected Freezing Temperatures Assigned to Each DOS Category.

DOS Category	Freezing Temperature (°C)
<80%	-4.0
80–90%	-3.5
>90%	-1.5

2.5.3. Detecting Damaging FT Cycles

The FT cycles were considered damaging only when the moisture level exceeded the critical DOS, which is assumed to be 80% or higher for this study. This threshold was selected based on previous research that identified the critical DOS range to be approximately 78–90% [7–10]. The chosen 80% cutoff has the advantage of giving a conservative lower limit on FT damage. This is cautious, in that it is less likely that ice formation below 80% will lead to severe damage. Given that the temperature, DOS, and presence of ice were known, it was possible to assess whether the observed freezing event occurred when the DOS was at or above 80%. This approach allowed for the quantification of potentially damaging FT cycles. Specifically, FT cycles for predicted DOS categories >90% and 80–90% were considered damaging, while those with DOS <80% were not deemed damaging.

3. Results and Discussions

3.1. Air and Concrete Temperatures Relationship

In this research, air temperature was employed instead of concrete temperature for a few reasons. Air temperatures are available from numerous sources and monitored frequently by weather stations. Their data are consistent and easily accessible as well. Air temperature is a practical and cost-effective means of detection of FT cycles, and it performs well for this purpose if the difference between air and concrete temperature at 51 mm from the surface is minimal, and the coefficient of correlation between the two is high.

A statistical test was performed to show whether air temperature can replace concrete temperature in FT. In order to determine the consistency between air and concrete temperature data, these two datasets were compared. For determining whether the difference in means of air and concrete temperature was statistically significant, the Z-test was used.

The Z-test for two population means is the test for differences in the population means of two samples of continuous data drawn from a normal distribution when each sample has more than 30 records [74, 75]. The Z-score is calculated based on the following formula:

$$Z = \frac{\bar{X}_1 - \bar{X}_2}{\sqrt{\frac{\sigma_1^2}{n_1} + \frac{\sigma_2^2}{n_2}}} \quad \text{Equation (4)}$$

where $\bar{X}_1$ and $\bar{X}_2$ are the sample means, σ_1 and σ_2 are the standard deviations, and n_1, n_2 are the sample sizes. The sample sizes were large and equal, justifying the use of the Z-test over a t-test [75].

In this study, one location was selected from each geographical region to prevent any bias or generalization and to represent the diversity of regions. The selected location was presented with the detailed value of each statistical test in Table 5, and the rest were reported in Table 6. The results of the Z-test for all four locations showed no statistically significant difference ($p \geq 0.05$) (Tables 5 and 6). These results mean that the measured air temperature and concrete temperature at 51 mm from the surface are statistically similar. Pearson's correlation coefficient was also computed to more closely assess the relationship between the two variables. This test determines the strength and direction of the linear relationship between two continuous variables [75,76]. A Pearson correlation close to +1 indicates a strong positive relationship. All locations showed strong positive correlations ($r > 0.85$), confirming that concrete and air temperatures are statistically similar. Plots showing the relationship are included in Appendix C.

This supports using air temperature as a reliable input for assessing FT cycles in large-scale analyses. This is useful where direct concrete temperature measurements are not available.

Table 5

Statistical Comparison of Air and Concrete Temperatures from September 2021 to April 2022 at Four Different Locations, Including Z-Test Results and Pearson Correlation Coefficients.

Location	North (Wisconsin – Green Bay)	South (Oklahoma - Texas County)	Northeast (Pennsylvania – Cyclone)	Northwest (Idaho – Coeur d'Alene US-95)
Sample Size	11,616	11,616	11,616	11,616
Mean Concrete Temperature (°C)	1.53	8.43	6.73	6.66
Mean Air Temperature (°C)	1.44	8.13	6.70	6.45
Standard Deviation (Concrete) (°C)	9.287	11.901	7.977	9.189
Standard Deviation (Air) (°C)	9.063	10.085	7.417	9.239
Standard Error (Concrete) (°C)	0.107	0.124	0.385	0.097
Standard Error (Air) (°C)	0.104	0.136	0.094	0.122
Standard Error of Difference (°C)	0.149	0.185	0.369	0.156
Z-score	0.599	1.589	0.075	1.348
P-value	0.549	0.112	0.940	0.178
Significance (α=0.05)	***Not Significant (p ≥ 0.05)***	***Not Significant (p ≥ 0.05)***	***Not Significant (p ≥ 0.05)***	***Not Significant (p ≥ 0.05)***
Pearson Correlation	*0.952*	*0.937*	*0.968*	*0.963*

Table 6

Pearson Correlation Coefficients of Air and Concrete Temperatures from September 2021 to April 2022.

State	Location	Pearson Correlation	P- Value
Oklahoma	Cooper Lab	**0.954**	**0.235**
	McCurtain County	**0.922**	**0.552**
	Texas County	**0.937**	**0.112**
	Spring Field (Central)	**0.945**	**0.531**
	Dixon (Northern)	**0.903**	**0.203**
	Carbondale (Southern)	**0.958**	**0.640**
Wisconsin	Green Bay	**0.952**	**0.549**
	Madison	**0.960**	**0.460**
	Rhinelander	**0.924**	**0.335**
New York	Watertown	**0.953**	**0.197**
	Clifton Park	**0.922**	**0.756**
	Hauppauge	**0.900**	**0.623**
Minnesota	Baxter	**0.860**	**0.101**
	Maplewood	**0.887**	**0.267**
	Thief River Falls	**0.967**	**0.310**

Pennsylvania	Clearfield	**0.913**	**0.554**
	Cyclone	**0.968**	**0.940**
	Harrisburg	**0.947**	**0.910**
Nebraska	Lincoln	**0.925**	**0.646**
	Thedford	**0.939**	**0.501**
	Chadron	**0.915**	**0.397**
Iowa	Ames	**0.908**	**0.631**
	Fairfield	**0.956**	**0.241**
	Mason City	**0.895**	**0.200**
Colorado	Denver	**0.923**	**0.122**
	Seibert	**0.898**	**0.298**
	Glenwood	**0.909**	**0.534**
Kansas	Oakley	**0.927**	**0.115**
	Hutchinson	**0.945**	**0.621**
	Topeka	**0.969**	**0.322**
Idaho	Coeur d Alene US-95	**0.963**	**0.178**
	Mt Home I-84	**0.911**	**0.386**
	Paddy Flat SH-55	**0.893**	**0.476**
Oregon	Bend	**0.975**	**0.678**
	Hinsdale Wave Research Lab	**0.913**	**0.834**
	Newport	**0.967**	**0.568**
Missouri	Central Laboratory	**0.905**	**0.178**
	Northwest District	**0.922**	**0.433**
	Southeast District	**0.930**	**0.754**
North Dakota	Bismarck Site	**0.889**	**0.756**
	Grand Forks Site	**0.914**	**0.989**
	Fargo Site	**0.927**	**0.854**

3.2. DOS Prediction Evaluation

3.2.1. Regional Threshold Development

This section shows the values of the upper and lower boundaries of each weather variable that are found to be optimal for distinguishing the measured values into DOS categories, referred to as thresholds. These thresholds for each region are found using the training dataset of 1 year (September 2020–April 2021), and the GA model is run.

The result suggests that different regions have different threshold values, as listed in Table 7. This is also a representation of the fact that regional climate behavior is a dominant feature in dictating the DOS classification. For instance, the threshold of air temperatures in the North and the South are between –7.6 and 5.3°C and between 10.8 and 14.8°C, respectively. This is a concrete example showing that the climate of a region determines the classification of a particular weather condition into a specific DOS category. By using the regionally varying thresholds, the proposed model is more representative of the weather behavior of different regions and therefore improves prediction accuracy.

The regional thresholds are then utilized to predict the DOS categories of the following three winter seasons, i.e., September 2021–April 2022, September 2022–April 2023, and September 2023– April 2024.

3.2.2. Development and Application of the Lookup Table for DOS Prediction

A lookup table was established during the training to link each trinary code to a DOS category during training. When the model is applied to new monthly weather data, the regional thresholds obtained from the GA training period are used to generate trinary codes for each location and month. These codes are then matched to their corresponding DOS categories using the lookup table. This lookup-based approach simplifies the prediction process by turning the complex relationships between weather and concrete DOS into an easy-to-use reference system. It allows rapid classification of new weather data while maintaining consistency with the trained model.

Table 8 summarizes the lookup table results generated from the 2020–2021 training data and presents an example from Lincoln, Nebraska (North Region) for one representative year (September 2021–April 2022). These results illustrate how the lookup table was used to predict DOS categories for each month within that region and year. The prediction results for the other regions are presented in the following section.

Table 7

Optimal Thresholds of Weather Variables for Each Region.

Weather Feature	Region	Threshold 1[a]	Threshold 2[a]
Average Air Temperature (°C)	**Northwest**	-0.2	8.4
	North	-7.6	5.3
	South	10.8	14.8
	Northeast	4.1	7.6
Total Precipitation (mm)	**Northwest**	228.6	260.0
	North	44.9	152.4
	South	269.0	273.0
	Northeast	140.0	148.0
Average Relative Humidity (%)	**Northwest**	51.3	67.6
	North	63.2	82.5
	South	65.6	70.1
	Northeast	60.4	74.8
Solar Radiation GHI (kWh/m²)	**Northwest**	4.6	4.8
	North	4.2	4.7
	South	4.7	4.9
	Northeast	4.3	4.5
Average Wind Speed (m/s)	**Northwest**	2.8	3.1
	North	3.6	4.7
	South	2.3	3.1
	Northeast	2.8	3.3
Average Air Pressure (kPa)	**Northwest**	92.7	97.0
	North	92.6	94.3
	South	86.0	90.0
	Northeast	93.0	98.0

[a] Obtained from the Genetic Algorithms Model.

Table 8
Lookup Table Example for DOS Prediction in Lincoln, Nebraska (September 2021–April 2022).

North Region								
	Training Data (September 2020 – April 2021)			Predicted Performance (September 2021 – April 2022)			Conclusion	
Month	**Trinary Code**	**DOS Category (%)**	**Overlap (%)**	**Trinary Code**	**Predicted DOS Category (%)**	**Overlap (%)**	**Does the Trinary Code Match?**	**Does the DOS Category Match?**
September	002012	>90	0	002012	>90	0	YES	YES
October	111002	>90	0	111002	>90	0	YES	YES
November	221102	>90	0	221102	>90	0	YES	YES
December	201012	80-90	0	201012	80-90	0	YES	YES
January	202102	80-90	0	202102	80-90	0	YES	YES
February	210002	80-90	0	210002	80-90	0	YES	YES
March	112002	>90	0	112012	>90	0	Closest Match	YES
April	201022	80-90	0	201022	>90	0	YES	NO
Prediction Accuracy (%)[a]							**87.5**	

[a] $\text{Prediction Accuracy (\%)} = \frac{\text{Number of Correct DOS Predictions}}{\text{Total Number of Months Evaluated}} \text{x} 100$ Equation (5)

3.2.3. DOS Prediction Accuracy Across Years and Regions

Table 9 shows the results for ten traditional ML models. The best performing model was the GA model, as the other models did not perform well. This is likely because of the imbalance in the dataset. There were fewer training data points in the <80% DOS category than in the 80–90% and >90% DOS categories. The models had less information from which to learn the properties of this category, and the prediction accuracy for it was particularly low, as presented in Appendix D. The GA approach, unlike traditional ML models, is able to accommodate the imbalanced and non-uniform distribution of data in the three DOS categories [49–51]. The result is a large improvement in the accuracy of predicting the DOS category, which speaks to the robustness of the GA model and its applicability in making predictions of DOS for different years with confidence from weather data.

Table 10 shows more details of the predictions of the GA model. The table shows where the predicted DOS category matches the measured values over three forecasted years. Across all regions, the average prediction accuracy was 89%, indicating that the GA model and its derived thresholds achieved nearly 90% accuracy in predicting DOS categories over multiple years.

Table 9
Predicting DOS Category Results for the year September 2021 to April 2022.

Model	Model Accuracy in Predicting the DOS Category (%)
Random Forest Classifier	56
Multilayer Perceptron	31
Support Vector Machines	31
SVM with RBF Kernel	31
Gradient Boosting Classifier	31
Decision Tree Classifier	44
LSTM Model (10 epochs)	33
LSTM Model (60 epochs)	33
Linear Regression	25
Nonlinear Regression	30
Artificial Neural Network (ANN)	35
Genetic Algorithms	***89***

Table 10
Prediction Accuracy of DOS Categories for Three Years.

Time	Region	Correct Prediction	Incorrect Prediction
September 2021 to April 2022	Northwest	85%	15%
	North	86%	14%
	South	89%	11%
	Northeast	87%	13%
September 2022 to April 2023	Northwest	84%	16%
	North	87%	13%
	South	97%	3%
	Northeast	93%	6%
September 2023 to April 2024	Northwest	89%	11%
	North	87%	13%
	South	95%	5%
	Northeast	91%	9%
Average		**89%**	**11%**

3.3. FT Cycles Prediction

The comparison of the predicted FT cycles is shown in Table 11 for all 42 field locations over three years for both total and damaging FT cycles. Some field samples from September 2023 to April 2024 were damaged, and this caused sensor malfunction. These affected sites are labeled as NA in Table 11. In total, 9 out of the 42 locations did not yield actual FT cycle measurements for this winter season.

The predicted DOS categories generated by the GA model were combined with the predefined freezing temperatures (Table 4) and the air temperature data to estimate the number of total and

damaging FT cycles for each field location. A cycle was considered as damaging when the air temperature dropped below the predefined freezing temperature for that DOS category (Table 4), and the predicted DOS category corresponded to either 80–90% or >90%. FT cycles occurring during months with a predicted DOS <80% were considered non-damaging.

Table 11 summarizes the percentage differences between the predicted and measured FT cycles across all locations and years. The measured FT cycles were obtained from instrumentation boxes used in the field over four winter seasons. Detailed actual and predicted values for total and damaging FT cycles are provided in Appendices E and F.

On average, the predicted results are within 2% of the measured values for both total and damaging FT cycles. To quantify the accuracy of the proposed method, the standard deviation of measurements was analyzed. The standard deviation of damaging FT cycles was 7%, meaning that the number of predicted damaging FT cycles will be within the 14% of the measured value 95% of the time. This is reasonably consistent with this study, as the maximum error in this study was 15%, close to the anticipated 14%. The prediction of the total number of FT cycles at a 95% confidence interval has a smaller standard deviation of 5%. The GA-based approach could, therefore, be considered a practical tool for predicting the FT behavior of concrete in a wide range of climatic zones. Minor deviations between the predicted and the measured FT cycles were, in most cases, linked to a difference in the actual freezing temperatures at field locations and the predefined freezing temperatures for each category of DOS. The model tends to overpredict the FT cycles when the actual freezing temperature is lower than the predefined value, and underpredict when the actual temperature is higher. In some cases, the mismatch of predicted and measured DOS category also plays a role in the variations. These differences reflect the inherent variability in local weather conditions and the nonlinear relationship between DOS and freezing temperature, but remained within acceptable limits for the intended predictive accuracy of the model.

Additionally, it is important to note that the model predictions in this study are based on field measurements obtained from mortar without entrained air. This represents a worst-case scenario for FT susceptibility, as air-entrained concrete or concrete with different mixture proportions would experience fewer damaging cycles under the same environmental conditions. Therefore, the predicted number of damaging FT cycles presented here should be interpreted as mixture-dependent, and different concrete mixtures may show reduced or altered damage potential.

Table 11
Regional and Overall Percent Differences Between Predicted and Measured FT Cycles.

Region	State	Location	FT Cycles % Difference[a]					
			Year 1[b]		Year 2[c]		Year 3[d]	
			Total	Damaging	Total	Damaging	Total	Damaging
North	North Dakota	Bismarck Site	0	-2	0	0	NA[e]	NA
		Grand Forks Site	0	-8	0	0	NA	NA
		Fargo Site	0	-11	0	0	NA	NA
	Minnesota	Baxter	0	-5	0	0	-4	-4
		Maplewood	6	11	0	0	2	2
		Thief River Falls	3	-4	0	5	-4	-2
	Wisconsin	Green Bay	-4	-1	-8	8	NA	NA
		Madison	-8	-10	-4	-4	0	0
		Rhinelander	-5	1	0	2	NA	NA
	Iowa	Ames	-3	1	-2	-3	NA	NA
		Fairfield	-8	-8	-7	-7	0	0
		Mason City	8	-3	-4	-4	0	0
	Nebraska	Lincoln	-7	-7	0	0	14	8
		Thedford	2	-6	0	-8	3	3
		Chadron	-5	4	0	0	1	10
	Illinois	Dixon (Northern)	-4	-1	-2	10	NA	NA
	Missouri	Northwest District	-5	-5	0	0	-3	-3
	Average (%)		-2	-3	-2	0	1	1
	Standard Deviation		5	6	3	5	5	5
South	Colorado	Denver	0	0	1	0	-1	0
		Seibert	-4	0	-4	0	0	0
		Glenwood	-1	4	-5	0	-1	-1
	Kansas	Oakley	-1	0	0	0	1	0
		Hutchinson	2	-12	0	-8	4	-9
		Topeka	-10	-10	-15	-7	-4	-4
	Oklahoma	Cooper Lab	0	0	0	9	6	-11
		McCurtain County	0	0	0	-9	8	-11
		Texas County	0	0	0	0	0	0
	Illinois	Spring Field (Central)	-5	-10	-12	-10	12	12
		Carbondale (Southern)	0	-11	0	-12	13	12
	Missouri	Central Laboratory	0	-12	0	-12	6	-14
		Southeast District	-3	-13	0	13	0	0
	Average (%)		-2	-5	-3	-3	3	-3
	Standard Deviation		3	6	5	8	5	7
Northwest	Oregon	Bend	-10	-12	0	-4	NA	NA
		Hinsdale Wave Research Lab	-8	0	-9	-12	NA	NA
		Newport	0	0	0	0	0	0
	Idaho	Coeur d'Alene US-95	5	-5	0	2	-1	14
		Mt Home I-84	-12	-12	0	-15	-7	-12
		Paddy Flat SH-55	9	2	0	7	-5	-5
	Average (%)		-3	-4	-2	-4	-3	-1
	Standard Deviation		9	6	4	8	3	11
Northeast	Pennsylvania	Clearfield	-5	10	0	0	-3	-3
		Cyclone	-8	10	0	0	-6	-6
		Harrisburg	-8	-8	0	-2	7	7
	New York	Watertown	0	-6	4	-11	3	3
		Clifton Park	-8	4	-10	-13	4	4
		Hauppauge	0	11	0	0	10	10
	Average (%)		-5	4	-1	-4	3	3
	Standard Deviation		4	9	5	6	6	6

All Years and Regions	Average Difference (%)	Standard Deviation (%)	Maximum Difference (%)	Minimum Difference (%)

Total FT Cycles	-1	5	14	-15
Damaging FT Cycles	-2	7	14	-15

[a] Difference (%) = $\frac{Measured\ FT\ Cycles - Predicted\ FT\ Cycles}{Measured\ FT\ Cycles}\ x\ 100$ Equation (6)

[b] Year 1: September 2021 – April 2022.
[c] Year 2: September 2022 – April 2023.
[d] Year 3: September 2023 – April 2024.
[e] NA: No Available data due to the damaged field sample.

4. Practical Significance

The main contribution of this research is the ability to provide a field-validated, scalable model to predict the damaging FT cycles of concrete using weather data. By accurately predicting the DOS categories to 89% accuracy and damaging FT cycles within 15% of measured values Based on a 95% confidence interval in all years and regions. This model enables a specifier to perform a reliable evaluation of FT durability without the need for physical measurements, which may be costly and time-consuming.

A single, uniform concrete mixture was used for all field samples at each location. The use of the same mixture at each location enables direct comparison of DOS behavior across locations. However, the results described here are specific to this material and mixture design. It is encouraging that this mixture is representative of a common bridge deck or pavement.The developed model has significance in that it is based on easily acquired and generally available weather data. Therefore, the end-user needs only to know the geographic location of a project to predict its risk to FT. This research is not only novel, but it has never previously existed. Most existing models are based on generalized or region-wide climatic assumptions and therefore result in designs that are either overly conservative or under-designed for FT durability.

The developed model could also be used to develop FT maps or web-based tools to allow users to input a location and provide predicted FT damage based on historical weather data or forecasts. Publications are also being developed that focus on the development of these tools. The tools will provide valuable information for data-informed decision-making in construction planning, infrastructure maintenance, and resilience strategies, particularly in regions where climatic conditions are changing.

The model will also be expanded in the future by the addition of new field measurements from different regions and the use of different concrete mixtures to continue to validate and refine the performance. As data are obtained from adjoining climatic zones more widely, the hope is to be able to develop a universally applicable model.

5. Conclusions

This work provides a scalable, regionalized framework to predict the DOS, FT cycles, and damaging FT cycles for concrete, given accessible weather data from 42 separate locations. To

characterize a wide range of climatic conditions, GA-based optimization was used to determine thresholds for 6 environmental variables, which differ by region, to be used as model inputs for the classification of the three DOS categories. Region-specific thresholds were used with trinary encoding and the Bhattacharyya distance as a fitness function to accurately predict the DOS. The model was also validated against measured FT cycles and damaging FT cycles in the field and was shown to provide statistically equivalent and interchangeable results compared to the measured values. The field measurements used for both the development and validation of this framework were performed on the same standard concrete mixture to allow for direct comparison of DOS and FT behavior between locations. As a result, the presented findings and suggested thresholds are specific to this mixture design and may need to be adjusted when applied to other concrete mixtures. The following conclusions can be drawn:

1. The GA model that used trinary encoding and Bhattacharyya distance as a fitness function yielded an average DOS accuracy of 89% using 1 year of training data and 3 years of validation data.

2. Based on a 95% confidence interval, the number of predicted FT cycles and damaging FT cycles were within 15% of the measured values in all years and regions, meaning that the model provides reliable and consistent performance across varying climatic conditions.

3. The statistical analysis indicates that there is no statistical difference between air temperature and concrete temperature at 51 mm, and the Pearson correlation coefficient (r) is greater than 0.93, showing that they have a strong positive linear relationship. The air temperature can be used as an effective substitute for the concrete temperature for large-scale applications where concrete temperature is not available for determining FT cycles.

4. A model that uses a simplified freezing temperature based on the DOS was developed. The temperatures used were –4.0°C for DOS <80%, –3.5°C for 80–90%, and –1.5°C for >90%. This allowed for simplified calculations to determine when freezing occurred within the concrete.

In summary, this framework represents a significant step towards the state-of-the-art in predictive modeling of concrete durability, while also providing a foundation for future expansion to larger geographic regions as additional field data becomes available. By establishing a strong linkage between environmental exposure conditions and actual field measurements, this framework provides a scalable and validated solution for the assessment and mitigation of FT damage in infrastructure.

References:

[1] Wang, R., Zhao, Q., Zhang, S., & Gao, X. (2022). Review on the deterioration and approaches to enhance the durability of concrete in the freeze–thaw environment. *Construction and Building Materials*, 321, 126371.

[2] Marchand, J., Jolin, M., & Machabée, Y. (2005). Deicer salt scaling resistance of supplementary cementing material concrete: Laboratory results against field performance. In Proceedings of the 6th International Congress Global Construction: Ultimate Concrete Opportunities, Dundee, UK, 5–7 July 2005.

[3] Guo, J., Xu, H., Zhang, J., & Li, Q. (2022). Damage mechanism and modeling of concrete in freeze–thaw cycles: A review. *Buildings*, 12(9), 1317.

[4] Sun, Z., and Scherer, G.W. (2010). Effect of air voids on salt scaling and internal freezing. Cement and Concrete Research, 40(2), 260–270.

[5] Powers, T.C. (1945). A working hypothesis for further studies of frost resistance of concrete. ACI Journal Proceedings, 41(4), 245–272.

[6] Fagerlund, G. (1973). Critical degrees of saturation at freezing of porous and brittle materials. Durability of Building Materials, 1(1), 19–29.

[7] Li, W., Pour-Ghaz, M., Castro, J., & Weiss, J. (2012). Water absorption and critical degree of saturation relating to freeze-thaw damage in concrete pavement joints. Journal of Materials in Civil Engineering, 24(3), 299–307.

[8] Fagerlund, G. (1977). The critical degree of saturation method of assessing the freeze/thaw resistance of concrete. Materials and Structures, 10(58), 217–229.

[9] M.K. Moradllo, C. Qiao, H. Hall, M.T. Ley, S.R. Reese, W.J. Weiss, Quantifying fluid filling of the air voids in air-entrained concrete using neutron radiography, Cem. Concr. Compos. 104 (2019) 103407.

[10] Wen, J., Li, F., Zhang, H., & Niu, D. (2024). A review of new methods for measuring saturation of concrete and its impact on concrete properties. *Journal of Building Engineering*, 96, 110664.

[11] Moradllo, M. K., Qiao, C., Ghantous, R. M., Zaw, M., Hall, H., Ley, M. T., & Weiss, W. J. (2020). Quantifying the freeze-thaw performance of air-entrained concrete using the time to reach critical saturation modelling approach. *Cement and Concrete Composites*, *106*, 103479.

[12] Ley, M. T., Welchel, D., Peery, J., Khatibmasjedi, S., & LeFlore, J. (2017). Determining the air-void distribution in fresh concrete with the Sequential Air Method. *Construction and Building Materials*, *150*, 723-737.

[13] Scherer, G. W. (2004). *Stress from crystallization of salt and ice. Cement and Concrete Research*, 34(9), 1613–1624.

[14] Abdelrahman, B., & Ley, M. T. (2024). The effects of concrete temperature on air void parameters in pumped concrete. *Materials and Structures*, 57(10), 228.

[15] Zhang, W., Liu, J., Guo, J., & Li, Q. (2020). Influence of damage degree on the degradation of concrete under freezing–thawing cycles. *Construction and Building Materials*, 260, 119903.

[16] ACI Committee 201. (2016). *Guide to Durable Concrete (ACI 201.2R-16).* American Concrete Institute, Farmington Hills, MI, USA.

[17] ACI Committee 318. (2019). *Building Code Requirements for Structural Concrete (ACI 318-19) and Commentary (ACI 318R-19)*. American Concrete Institute.

[18] Chou, J. S., Tsai, C. F., Pham, A. D., & Lu, Y. H. (2014). Machine learning in concrete strength simulations: Multi-nation data analytics. Construction and Building Materials, 73, 771–780.

[19] Tran, V. Q., Dang, V. Q., & Ho, L. S. (2022). Evaluating compressive strength of concrete made with recycled concrete aggregates using machine learning approach. Construction and Building Materials, 323, 126578.

[20] Nguyen, H., Vu, T., Vo, T. P., & Thai, H. T. (2021). Efficient machine learning models for prediction of concrete strengths. Construction and Building Materials, 266, 120950.

[21] Bayar, G., & Bilir, T. (2019). A novel study for the estimation of crack propagation in concrete using machine learning algorithms. Construction and Building Materials, 215, 670–685.

[22] Hadzima-Nyarko, M., Nyarko, E. K., Lu, H., & Zhu, S. (2020). Machine learning approaches for estimation of compressive strength of concrete. The European Physical Journal Plus, 135(8), 682.

[23] Khambra, G., & Shukla, P. (2023). Novel machine learning applications on fly ash based concrete: an overview. Materials Today: Proceedings, 80, 3411–3417.

[24] Chaabene, W. B., Flah, M., & Nehdi, M. L. (2020). Machine learning prediction of mechanical properties of concrete: Critical review. Construction and Building Materials, 260, 119889.

[25] Nilsen, V., Pham, L. T., Hibbard, M., Klager, A., Cramer, S. M., & Morgan, D. (2019). Prediction of concrete coefficient of thermal expansion and other properties using machine learning. Construction and Building Materials, 220, 587–595.

[26] Bello, S. A., Oyedele, L., Olaitan, O. K., Olonade, K. A., Olajumoke, A. M., Ajayi, A., et al. (2022). A deep learning approach to concrete water-cement ratio prediction. Results in Materials, 15, 100300.

[27] Yuan, Z., Wang, L. N., & Ji, X. (2014). Prediction of concrete compressive strength: Research on hybrid models genetic based algorithms and ANFIS. Advances in Engineering Software, 67, 156–163.

[28] Chopra, P., Sharma, R. K., & Kumar, M. (2016). Prediction of compressive strength of concrete using artificial neural network and genetic programming. Advances in Materials Science and Engineering, 2016, 7648467.

[29] Li, Y., Jin, K., Lin, H., Shen, J., Shi, J., & Fan, M. (2024). Analysis and prediction of freeze-thaw resistance of concrete based on machine learning. Materials Today Communications, 39, 108946.

[30] Luo, D., Qiao, X., & Niu, D. (2025). A predictive model for the freeze-thaw concrete durability index utilizing the DeepLabV3+ model with machine learning. Construction and Building Materials, 459, 139788.

[31] Li, F., Luo, D., & Niu, D. (2025). Durability evaluation of concrete structure under freeze-thaw environment based on pore evolution derived from deep learning. Construction and Building Materials, 467, 140422.

[32] Kahraman, E., & Ozdemir, A. C. (2022). The prediction of durability to freeze–thaw of limestone aggregates using machine-learning techniques. Construction and Building Materials, 324, 126678.

[33] Chen, L., Ley, M.T., Ghantous, R.M., Weiss, W.J., Master, N.F. (2023). Measuring damaging freeze-thaw cycles in the field. Construction and Building Materials, 387, 131660.

[34] Abdelrahman, B. N., Ley, M. T., Chen, L., Materer, N. F., Simon, J., & Young, A. (2025). *Field-Based Measurement of Freeze–Thaw Damage in Cementitious Materials*. Manuscript submitted for publication.

[35] Hong, Z., Kalbarczyk, Z., & Iyer, R. K. (2016). A data-driven approach to soil moisture collection and prediction. 2016 IEEE International Conference on Smart Computing (SMARTCOMP). IEEE.

[36] Cai, Y., Zheng, W., Zhang, X., Zhangzhong, L., & Xue, X. (2019). Research on soil moisture prediction model based on deep learning. PLOS ONE, 14(4), e0214508.

[37] Matei, O., Rusu, T., Petrovan, A., & Mihuţ, G. (2017). A data mining system for real-time soil moisture prediction. Procedia Engineering, 181, 837–844.

[38] Gill, M. K., Asefa, T., Kemblowski, M. W., & McKee, M. (2006). Soil moisture prediction using support vector machines. JAWRA Journal of the American Water Resources Association, 42(4), 1033–1046.

[39] Acharya, U., Daigh, A. L., & Oduor, P. G. (2021). Machine learning for predicting field soil moisture using soil, crop, and nearby weather station data in the Red River Valley of the North. Soil Systems, 5(4), 57.

[40] Brocca, Luca; Moramarco, Tommaso; Melone, Fulvio; Wagner, Wolfgang (2011). Assimilation of surface- and root-zone ASCAT soil moisture products into rainfall–runoff modeling. IEEE Transactions on Geoscience and Remote Sensing, 50(7), 2542–2555.

[41] Entekhabi, D., et al. (2010). The Soil Moisture Active Passive (SMAP) mission. Proceedings of the IEEE, 98(5), 704–716.

[42] Mohanty, B.P., Skaggs, T.H., Famiglietti, J.S. (2000). Analysis and mapping of field-scale soil moisture variability using high-resolution ground-based data during the SGP97 Hydrology Experiment. Water Resources Research, 36(4), 1023–1031.

[43] Pan, M., Cai, X., Chaney, N.W., Wood, E.F. (2016). An initial assessment of SMAP soil moisture retrievals using high-resolution in situ and modeled data. Geophysical Research Letters, 43(18), 9662–9668.

[44] Vereecken, H., Huisman, J.A., Bogena, H., Vanderborght, J., Vrugt, J.A., Hopmans, J.W. (2008). On the value of soil moisture measurements in vadose zone hydrology: A review. Water Resources Research, 44(12).

[45] Chawla, N. V., Bowyer, K. W., Hall, L. O., & Kegelmeyer, W. P. (2002). SMOTE: Synthetic minority over-sampling technique. Journal of Artificial Intelligence Research, 16, 321–357.

[46] Fernández, A., García, S., Galar, M., Prati, R. C., Krawczyk, B., & Herrera, F. (2018). Learning from imbalanced data sets. Springer.

[47] García, S., Fernández, A., Luengo, J., & Herrera, F. (2015). Advanced nonparametric tests for multiple comparisons in the design of experiments in machine learning research. Information Sciences, 180(10), 2044–2064.

[48] Open-Meteo. (2024). *Open-Meteo: Free weather forecast and historical data API for scientists and developers.* Retrieved from https://open-meteo.com.

[49] Haupt, R. L., & Haupt, S. E. (2004). Practical Genetic Algorithms (2nd ed.). Wiley.

[50] Deb, K. (2000). An efficient constraint handling method for genetic algorithms. *Computer Methods in Applied Mechanics and Engineering*, 186(2–4), 311–338.

[51] Holland, J. H. (1975). Adaptation in Natural and Artificial Systems. University of Michigan Press.

[52] Kara, A., Pekel, E., Ozcetin, E., & Yıldız, G. B. (2024). Genetic algorithm optimized a deep learning method with attention mechanism for soil moisture prediction. Neural Computing and Applications, 36(4), 1761–1772.

[53] Wang, J., Wu, Y., Zhang, Y., Wang, H., Yan, H., & Jin, H. (2024). A genetic algorithm-optimized backpropagation neural network model for predicting soil moisture content using spectral data. Journal of Soils and Sediments, 24(7), 2816–2828.

[54] Wang, H., Zhang, L., Zhao, J., Hu, X., & Ma, X. (2022). Application of hyperspectral technology combined with genetic algorithm to optimize convolution long- and short-memory hybrid neural network model in soil moisture and organic matter. Applied Sciences, 12(20), 10333.

[55] Nguyen, T. T., Ngo, H. H., Guo, W., Chang, S. W., Nguyen, D. D., Nguyen, C. T., & Hoang, N. B. (2022). A low-cost approach for soil moisture prediction using multi-sensor data and machine learning algorithm. Science of the Total Environment, 833, 155066.

[56] Dumedah, G., Berg, A. A., & Wineberg, M. (2011). An integrated framework for a joint assimilation of brightness temperature and soil moisture using the nondominated sorting genetic algorithm II. Journal of Hydrometeorology, 12(6), 1596–1609.

[57] Bhattacharyya, A. (1943). *On a measure of divergence between two statistical populations defined by their probability distributions*. Bulletin of the Calcutta Mathematical Society, **35**, 99–109.

[58] Kailath, T. (1967). *The divergence and Bhattacharyya distance measures in signal selection*. IEEE Transactions on Communication Technology, 15(1), 52–60.

[59] Xuan, G., Zhu, X., Chai, P., Zhang, Z., Shi, Y. Q., & Fu, D. (2003). *Feature selection based on the Bhattacharyya distance*. Pattern Recognition, 36(8), 1703–1709.

[60] Knuth, K. H. (2016, July). Why square roots of probabilities?. In *AIP Conference Proceedings* (Vol. 1757, No. 1, p. 020001). AIP Publishing LLC.

[61] Crooks, G. E. (2015). *On Measures of Entropy and Information*. (See discussion on fidelity / Bhattacharyya coefficient and the negative-log transformation.)

[62] Aherne, F. J., et al. “The Bhattacharyya Metric as an Absolute Measure of Divergence.” *Kybernetika*, 1998. (Shows taking −ln of the coefficient to get a divergence measure with additive properties.)

[63] Price, K., Storn, R., & Lampinen, J. (2005). *Differential Evolution: A Practical Approach to Global Optimization*. Springer.

[64] Lampinen, J. (2002). *A Constraint Handling Approach for the Differential Evolution Algorithm*. Proceedings of the IEEE CEC, 1468–1473.

[65] Gong, W., Cai, Z., & Liang, D. (2014). Adaptive ranking mutation operator-based differential evolution for constrained optimization. *IEEE transactions on cybernetics*, *45*(4), 716-727.

[66] Gong, W., & Cai, Z. (2013). Differential evolution with ranking-based mutation operators. *IEEE Transactions on Cybernetics*, 43(6), 2066–2081.

[67] Wang, B. C., Li, H. X., Li, J. P., & Wang, Y. (2018). Composite differential evolution for constrained evolutionary optimization. *IEEE Transactions on Systems, Man, and Cybernetics: Systems*, *49*(7), 1482-1495.

[68] Takahama, T., & Sakai, S. (2006). Constrained optimization by the ε-constrained differential evolution with gradient-based mutation and feasible elites. *Proceedings of the 2006 IEEE Congress on Evolutionary Computation*, 1–8.

[69] Bergstra, J., & Bengio, Y. (2012). *Random search for hyper-parameter optimization*. Journal of Machine Learning Research, 13(2), 281–305.

[70] Bishop, C. M. (2006). *Pattern Recognition and Machine Learning*. Springer.

[71] Hamming, R. W. (1950). Error detecting and error correcting codes. *Bell System Technical Journal*, 29(2), 147–160.

[72] Bookstein, A., Kulyukin, V. A., & Raita, T. (2002). Generalized hamming distance. *Information Retrieval*, *5*, 353-375.

[73] Norouzi, M., Fleet, D. J., & Salakhutdinov, R. R. (2012). Hamming distance metric learning. *Advances in neural information processing systems*, *25*.

[74] Montgomery, D. C., & Runger, G. C. (2014). *Applied Statistics and Probability for Engineers* (6th ed.). Wiley.

[75] Moore, D. S., McCabe, G. P., & Craig, B. A. (2012). *Introduction to the Practice of Statistics* (7th ed.). W. H. Freeman.

[76] Rodgers, J. L., & Nicewander, W. A. (1988). Thirteen ways to look at the correlation coefficient. *The American Statistician*, 42(1), 59–66.

Appendices

Appendix A: Initial Threshold Ranges for Weather Variables Before GA Optimization

The boundary values were preselected based on the following considerations:

- ***Data Boundaries**:* The boundaries were chosen to include at least 90% of the data, ensuring they reflect typical conditions while excluding outliers.
- ***Avoiding Extremes**:* Boundaries were intentionally set away from the absolute maximum and minimum values of the weather features to ensure the thresholds remain within reasonable limits.
- ***Optimal Discriminant Power**:* The selected boundaries were found to be most effective in distinguishing between DOS categories, minimizing overlap between them.

This approach ensures that threshold optimization remains grounded in realistic weather conditions, as all threshold values fall within the observed weather data ranges obtained from the Open-Meteo API website [1]. By staying within these bounds, the model maintains physical relevance and improves its generalizability across different regions and years.

Table A1

Weather Feature Threshold Boundaries and Optimized Threshold Values for Each Region, Derived from the Genetic Algorithms Model (Training Period: September 2020 to April 2021).

Region	Weather Feature	Weather Feature Min. Value[a]	Weather Feature Max. Value*	Minimum Threshold Boundary	Maximum Threshold Boundary	Lower Threshold[b]	Upper Threshold[b]
Northwest	Average Air Temperature (°C)	-3.75	15.89	-1	12	**-0.2**	**8.4**
	Total Precipitation (mm)	0.00	504.95	40	450	**228.6**	**260.0**
	Average Relative Humidity (%)	40.94	94.10	45	85	**51.3**	**67.6**
	Solar Radiation GHI (kWh/m²)	4.00	5.50	4.2	5.25	**4.7**	**4.9**
	Average Wind Speed (m/s)	1.37	4.98	2.2	3.5	**2.8**	**3.1**
	Average Air Pressure (kPa)	84.35	101.71	88	99	**92.7**	**97.0**
North	Average Air Temperature (°C)	-16.24	17.58	-12	12	**-7.6**	**5.3**
	Total Precipitation (mm)	0.00	269.49	30	200	**44.9**	**152.4**
	Average Relative Humidity (%)	53.00	93.22	60	85	**63.2**	**82.5**
	Solar Radiation GHI (kWh/m²)	4.00	5.75	4.2	5.25	**4.25**	**4.9**
	Average Wind Speed (m/s)	2.17	6.04	3	5.2	**3.56**	**4.7**
	Average Air Pressure (kPa)	90.01	99.51	92	99	**92.6**	**94.3**
South	Average Air Temperature (°C)	-6.17	20.64	-2	16	**10.8**	**14.8**
	Total Precipitation (mm)	0.00	657.86	40	450	**269.0**	**273.0**
	Average Relative Humidity (%)	38.98	90.02	45	80	**65.6**	**70.1**
	Solar Radiation GHI (kWh/m²)	4.00	5.75	4.2	5.25	**4.7**	**4.9**
	Average Wind Speed (m/s)	1.53	6.16	2.2	5.0	**2.3**	**3.1**
	Average Air Pressure (kPa)	82.96	102.25	85	99	**86.0**	**90.0**
Northeast	Average Air Temperature (°C)	-5.17	19.86	-1	12	**4.1**	**7.6**
	Total Precipitation (mm)	30.23	282.45	70	250	**140.0**	**148.0**
	Average Relative Humidity (%)	57.20	84.87	60	80	**60.4**	**74.8**
	Solar Radiation GHI (kWh/m²)	4.00	4.75	4.25	4.5	**4.3**	**4.5**
	Average Wind Speed (m/s)	1.64	4.70	2.2	4.0	**2.8**	**3.3**
	Average Air Pressure (kPa)	93.57	101.89	94	101	**93.0**	**98.0**

[a] Obtained from Open-Meteo API website [1].

[b] Obtained from the Genetic Algorithms Model.

Appendix B: Freezing Temperature Optimization for Predicting FT Cycles

Fig. B1 represents the freezing temperature ranges for each DOS category, selected on the DOS–freezing temperature curve. For instance, as shown in Fig. B1, freezing temperatures between –3.9°C and –4.9°C are the selected range for the DOS <80% category. Several values within this range were tested, and the freezing temperature at which the best agreement between predicted and observed FT cycles was found was –4.0°C. The same method was used to select the best freezing temperature ranges for the other DOS categories in order to ensure high accuracy and best matching between predicted and observed FT cycles.

As a result, a large number of tests at various locations have confirmed that the freezing temperatures in Table B1 resulted in the most accurate FT cycle predictions in terms of the best matching with the observed number of freeze–thaw cycles at all of the tested locations (as presented in the results section).

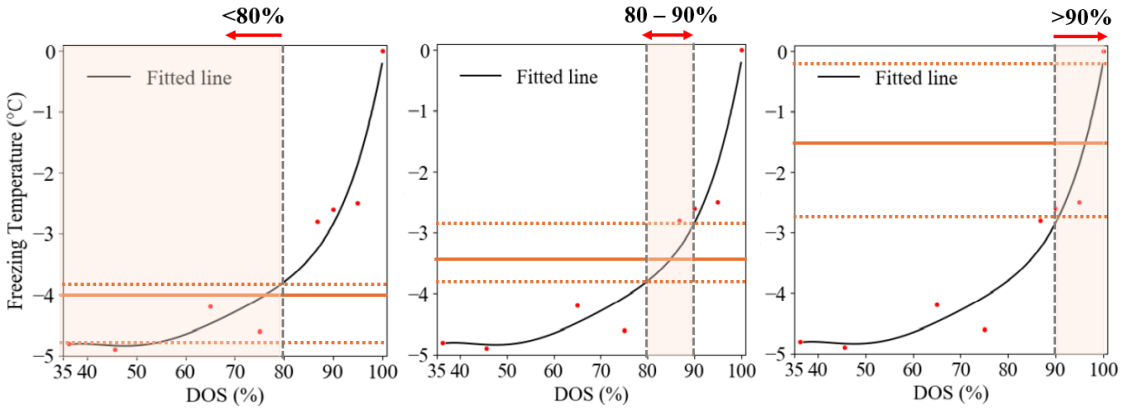

Fig. B1. Freezing temperature ranges associated with each DOS category, derived from the DOS vs. freezing temperature relationship [2]: (a) <80%, (b) 80–90%, and (c) >90%.

B.1 Optimal Freezing Temperatures for DOS >90%

To identify the best fitting predefined freezing temperature in terms of predicting FT cycles in the locations with the predicted DOS category >90%, appropriate freezing temperatures for the considered category were determined with the DOS–freezing temperature relationship shown in Fig. B1. For this purpose, three freezing temperatures were chosen within the temperature range shown for this category in Fig. B1(c) (between –0.6 and –2.8°C), namely 1, –1.5, and –2°C. These were used to test which of these temperatures most accurately predicted the number of FT cycles (Table B1). For the sake of simplicity, it was decided to use locations from different parts of the considered region with predicted DOS values >90%.

The fact that actual DOS values (91–99%) and associated freezing temperatures (–0.6 and –2.8°C) vary significantly supports the notion that the selection of a specific predefined freezing temperature influences the resulting number of FT cycles. Table 11 gives the total number of actual FT cycles and their differences between the values predicted using a given predefined freezing temperature and the actual values (predicted from September 2021 to April 2022) for the selected locations.

It is clear from the results that the predefined freezing temperatures of –1 and –2°C lead to large differences between the predicted and actual values. This means that neither of these temperatures is a good fit for the locations with the DOS >90%. In contrast, the predefined temperature of –1.5°C has very small variations and can be deemed to be the best fitting freezing temperature for predicting the number of FT cycles in this category.

Table B2 shows the average, maximum, and minimum values of actual and predicted FT cycles, as well as the differences between the predicted and actual numbers of FT cycles. It can be seen that predictions using the predefined freezing temperature of –1.5°C have smaller absolute differences compared with those using the predefined temperature of –2°C. In other words, the predicted numbers of FT cycles at –1.5°C are closer to the actual values. Smaller differences at a predefined temperature of –1.5°C also have a tighter range with a minimum and a maximum of –8 and 7, respectively, than at –2°C, for which a minimum and maximum of –7 and 15, respectively, were calculated. For example, a large maximum difference of 15 at a predefined freezing temperature of –2°C might cause a bias in results for a location. On the other hand, predictions using the predefined freezing temperature of –1°C are clearly lower than the actual number of FT cycles, which is evident from the negative values of differences (Table B2).

In summary, using the predefined freezing temperature of –1.5°C leads to the most accurate and consistent predictions of FT cycles in the DOS >90% category. It minimizes the difference between actual and predicted numbers of FT cycles, as well as the range of these differences, and avoids systematic underestimation or overestimation of the numbers of FT cycles.

Table B1

Evaluation of Predicted FT Cycles Using Different Predefined Freezing Temperatures for DOS Category >90%.

Region	Location, State	Actual FT Cycles[a]	Predicted FT Cycles[a]	Difference (Actual – Predicted)
Predefined Freezing Temperature (-1.0°C)				
Northwest	Coeur d'Alene US-95, Idaho	61	123	-62
Northwest	Paddy Flat SH-55, Idaho	74	83	-9
Northeast	Cyclone, Pennsylvania	44	64	-20
Northeast	Harrisburg, Pennsylvania	40	51	-11
North	Chadron, Nebraska	94	119	-25
North	Madison, Wisconsin	50	67	-17
North	Baxter, Minnesota	54	67	-13
South	Glenwood, Colorado	70	72	-2
South	McCurtain County, Oklahoma	31	50	-19
South	Topeka, Kansas	41	56	-15
	Average	55.9	75.2	-19.3
	Minimum Value	31	50	-62
	Maximum Value	94	123	-1
Predefined Freezing Temperature (-1.5°C)				
Northwest	Coeur d'Alene US-95, Idaho	61	58	3
Northwest	Paddy Flat SH-55, Idaho	74	67	7
Northeast	Cyclone, Pennsylvania	44	52	-8
Northeast	Harrisburg, Pennsylvania	40	43	-3
North	Chadron, Nebraska	94	99	-5
North	Madison, Wisconsin	50	54	-4
North	Baxter, Minnesota	54	54	0
South	Glenwood, Colorado	70	71	-1
South	McCurtain County, Oklahoma	31	31	0
South	Topeka, Kansas	41	45	-4
	Average	55.9	57.4	-1.5
	Minimum Value	31	31	-8
	Maximum Value	94	99	7
Predefined Freezing Temperature (-2.0°C)				
Northwest	Coeur d'Alene US-95, Idaho	61	52	9
Northwest	Paddy Flat SH-55, Idaho	74	59	15
Northeast	Cyclone, Pennsylvania	44	51	-7
Northeast	Harrisburg, Pennsylvania	40	40	0
North	Chadron, Nebraska	94	93	1
North	Madison, Wisconsin	50	49	1
North	Baxter, Minnesota	54	50	4
South	Glenwood, Colorado	70	69	1
South	McCurtain County, Oklahoma	31	35	-4
South	Topeka, Kansas	41	41	0
	Average	55.9	53.9	2.0
	Minimum Value	31	35	-7
	Maximum Value	94	93	15

[a] Total Number of FT Cycles from September 2021 to April 2022.

B.2 Optimal Freezing Temperatures for DOS 80-90%

To reduce complexity, multiple locations from different regions with variable DOS values in the range of 80–90% (Table B2) were chosen for this specific category to identify the most suitable predefined freezing temperature. This DOS range covers the widest spectrum of actual DOS values and their corresponding actual freezing temperatures (Fig. B1(b), approximately from −3.8 to −2.8°C). Consequently, three predefined freezing temperatures, 2.5°C, −3.0°C, and −3.5°C, were chosen for comparison and testing.

The actual FT cycles from the selected multiple locations in the DOS 80–90% category (Table B2) were used to conclude the most reasonable predefined freezing temperature. As a result, −3.5°C is recommended as the predefined freezing temperature to calculate FT cycles in this category (Table B2). This is because, in comparison to −2.5°C and −3.0°C, differences between actual and predicted FT cycles at −3.5°C generally have smaller absolute values, i.e., they are relatively closer to zero, which implies that the prediction using −3.5°C is, on average, closer to the actual values. Besides, as shown in Table B2, the predefined freezing temperature of −3.5°C produces the smallest average absolute difference (≈1.3) as opposed to −2.5°C (≈10.1) and −3.0°C (≈5.3), which further indicates that the latter two cases have more extreme values (−18 and −10, respectively) that would disproportionately affect the results and make predictions less accurate at certain locations. The absolute average differences between actual and predicted FT cycles at −2.5°C are also generally large and consistently negative, which would suggest an underestimation bias in those cases. Although those at −3.0°C are much closer to zero on average, there are still more positive and extreme values present that could cause occasional overestimations.
On the contrary, differences at −3.5°C are not only on average smaller in magnitude but also lack a strong positive or negative direction. As such, it can be concluded that −3.5°C would lead to more accurate predictions on average, compared to the two other cases.

Table B2
Evaluation of Predicted FT Cycles Using Different Predefined Freezing Temperatures for DOS Category 80%-90%.

Region	Location, State	Actual FT Cycles[a]	Predicted FT Cycles[a]	Difference (Actual – Predicted)
Predefined Freezing Temperature (-2.5°C)				
Northwest	Newport, Oregon	1	2	-1
Northwest	Mt Home I-84, Idaho	50	61	-11
Northeast	Hauppauge, New York	18	33	-15
North	Lincoln, Nebraska	56	74	-18
North	Mason City, Iowa	39	44	-5
South	Seibert, Colorado	71	87	-16
South	Hutchinson, Kansas	48	53	-5
Average		40.4	50.6	-10.1
Minimum Value		1	2	-18
Maximum Value		71	87	-1
Predefined Freezing Temperature (-3.0°C)				
Northwest	Newport, Oregon	1	1	0
Northwest	Mt Home I-84, Idaho	50	60	-10
Northeast	Hauppauge, New York	18	26	-8
North	Lincoln, Nebraska	56	63	-7
North	Mason City, Iowa	39	40	-1
South	Seibert, Colorado	71	80	-9
South	Hutchinson, Kansas	48	50	-2
Average		40.4	45.7	-5.3
Minimum Value		1	1	-10
Maximum Value		71	80	0
Predefined Freezing Temperature (-3.5°C)				
Northwest	Newport, Oregon	1	1	0
Northwest	Mt Home I-84, Idaho	50	56	-6
Northeast	Hauppauge, New York	18	18	0
North	Lincoln, Nebraska	56	60	-4
North	Mason City, Iowa	39	36	3
South	Seibert, Colorado	71	74	-3
South	Hutchinson, Kansas	48	47	1
Average		40.4	41.7	-1.3
Minimum Value		1	1	-6
Maximum Value		71	74	3

[a] Total Number of FT Cycles from September 2021 to April 2022.

B.3 Optimal Freezing Temperatures for DOS <80%

The results for the DOS category <80% show the effect of the chosen value of predefined freezing temperature on the predicted values. Table B3 presents the actual and predicted number of FT cycles for three different predefined freezing temperatures (–4.0°C, –4.5°C, and –4.7°C) for locations in Texas County, Oklahoma, and Denver, Colorado. The chosen range of temperatures is based on the range of actual DOS values and corresponding freezing temperatures shown in Fig. B1(a).

When the predefined freezing temperature is set to –4.0°C, the actual and predicted FT cycles are perfectly aligned with no difference in any of the metrics (average, minimum, and maximum). This would make the predefined temperature of –4.0°C an ideal choice. At a predefined freezing temperature of –4.5°C, there is a clear difference between the actual and predicted values. The predicted values underestimate the number of FT cycles with a difference ranging from 3 to 5, with an average of 4. When the predefined freezing temperature is further lowered to –4.7°C, the difference between actual and predicted values increases, with a range from 5 to 7 and an average of 6. This pattern of results shows that lower predefined temperatures cause a larger underestimation of the actual values, which affects the prediction accuracy in a negative way.

In conclusion, the most suitable predefined freezing temperature for the <80% DOS category is –4.0°C, as it results in a perfect match between actual and predicted FT cycles with no difference in the selected locations.

Table B3
Evaluation of Predicted FT Cycles Using Different Predefined Freezing Temperatures for DOS Category <80%.

Region	Location, State	Actual FT Cycles[a]	Predicted FT Cycles[a]	Difference (Actual – Predicted)
Predefined Freezing Temperature (-4.0°C)				
South	Texas County, Oklahoma	42	42	0
South	Denver, Colorado	48	48	0
	Average	45	45	0
	Minimum Value	42	42	0
	Maximum Value	48	48	0
Predefined Freezing Temperature (-4.5°C)				
Northwest	Texas County, Oklahoma	42	39	3
Northwest	Denver, Colorado	48	43	5
	Average	45	41	4
	Minimum Value	42	39	3
	Maximum Value	48	43	5
Predefined Freezing Temperature (-4.7°C)				
Northwest	Texas County, Oklahoma	42	37	5
Northwest	Denver, Colorado	48	41	7
	Average	45	39	6
	Minimum Value	42	37	5
	Maximum Value	48	41	7

[a] Total Number of FT Cycles from September 2021 to April 2022.

Appendix C: Comparison of Air Temperature and Concrete Temperature

Fig. C1 shows the air and concrete temperatures at all selected locations from September 2021 to April 2022. Fig. C1 indicates that air temperature generally tracked the concrete temperature over time at each location.

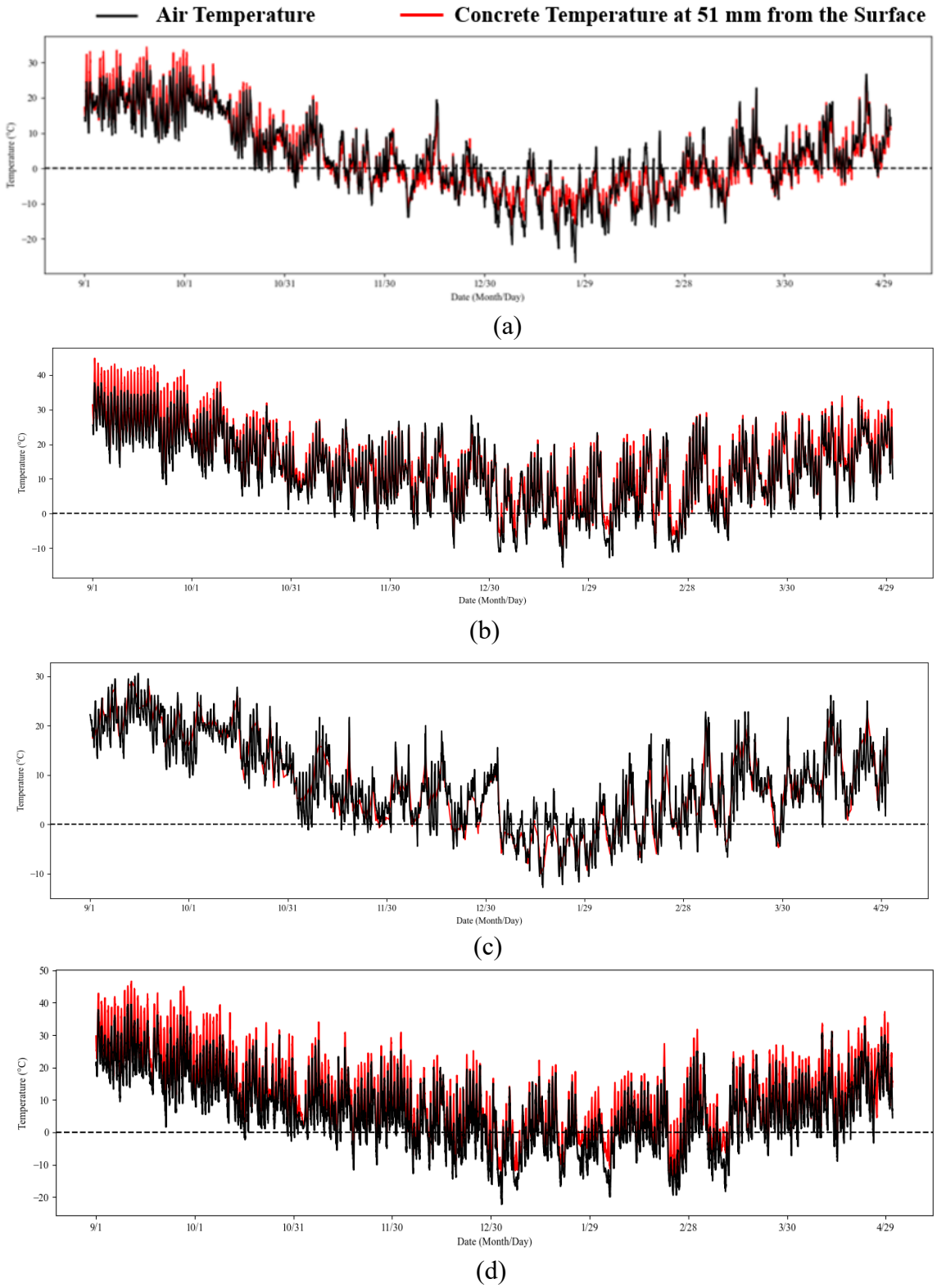

Fig. C1: Comparison of air temperature and concrete temperature from September 2021 to April 2022 at the following locations: (a) North – Wisconsin (Green Bay), (b) South – Oklahoma (Texas County), (c) Northeast – Pennsylvania (Cyclone), and (d) Northwest – Idaho (Coeur d'Alene, US-95).

Appendix D: Comparison with Traditional Machine Learning Models

Initially, standard ML models were applied to the dataset to predict the DOS categories. The performance of all models was mediocre, which was further compounded by the low performance in the most important class, the <80% DOS category (Table D1). The best-performing traditional ML model was the Random Forest Classifier, which still only managed to achieve 56% accuracy (Table D1), which is no better than making random predictions (Table D1). The major problem that plagued all traditional ML models was the imbalanced nature of the data. There were fewer data points for the <80% DOS category compared to the 80–90% and >90% categories, which made it more difficult for the models to learn this category, resulting in worse predictive accuracy for it.

Furthermore, the traditional ML models are often not good at representing the intricate and non-linear interactions that can exist between weather variables. This is because the ML models often assume that the inputs to the model are independent from each other, or that their relationship is linear, when in fact the relationship between weather variables is dynamic and mutually dependent. For example, the effect of a single weather variable, such as temperature, on the DOS may change depending on the values of other weather variables, such as humidity or precipitation. These kinds of non-linear and context-dependent effects are difficult to model using traditional ML algorithms, which operate based on simplified assumptions [3-5]. The exhaustive search of the hyperparameter space for the traditional models resulted in only marginal increases in performance, and even then, performance in the DOS <80% category still remained very low (Table D1). As a result of all of the above, it was decided to use GAs. The principal reason for this is that they are able to search through a larger solution space with little to no need for training data [6-8]. GAs is particularly useful for threshold optimizations, and as an added benefit, it can also work with imbalanced and non-uniform distributions of data [6-8]. It was also able to circumvent the manual weighing of the different categories in the decision tree via fitness maximization, which, as seen in the results, automatically enforces the importance of all categories, which also contributed to a large increase in performance in the <80% category.

GAs clearly outperformed the traditional machine-learning method in dealing with the imbalanced data and in threshold optimization, which resulted in a large improvement in the prediction of the DOS categories.

Table D1

Predicting DOS Category Results for the year September 2021 to April 2022.

Model	DOS Category			Overall Model Accuracy (%)
	<80%	80-90%	>90%	
	Prediction Accuracy (%)			
Random Forest Classifier	20	38	76	56
Multilayer Perceptron	0	31	57	31
Support Vector Machines	0	20	67	31
SVM with RBF Kernel	20	20	50	31
Gradient Boosting Classifier	0	14	44	31
Decision Tree Classifier	20	25	67	44
LSTM Model (10 epochs)	0	22	67	33
LSTM Model (60 epochs)	0	0	44	33
Linear Regression	0	22	48	25
Nonlinear Regression	0	33	57	30
Artificial Neural Network (ANN)	0	20	60	35

Appendix E: Predicted and Measured Total FT Cycle Data for All Regions

Tables E1, E2, and E3 display the predicted and measured total FT cycles for all years and regions, as well as the absolute and relative (percentage) differences between measured and predicted total FT cycles.

Table E1

Predicted and Measured Total FT Cycles from September 2021 to April 2022 Across All Regions and Locations.

Region	State	Location	Measured FT Cycles	Predicted FT Cycles	Difference in FT Cycles[a]	% Difference[b]
North	North Dakota	Bismarck Site	97	97	0	0
		Grand Forks Site	66	66	0	0
		Fargo Site	81	81	0	0
	Minnesota	Baxter	54	54	0	0
		Maplewood	49	46	3	6
		Thief River Falls	70	68	2	3
	Wisconsin	Green Bay	79	82	-3	-4
		Madison	50	54	-4	-8
		Rhinelander	59	62	-3	-5
	Iowa	Ames	77	79	-2	-3
		Fairfield	48	52	-4	-8
		Mason City	39	36	3	8
	Nebraska	Lincoln	56	60	-4	-7
		Thedford	64	63	1	2
		Chadron	94	99	-5	-5
	Illinois	Dixon (Northern)	48	50	-2	-4
	Missouri	Northwest District	44	46	-2	-5
South	Colorado	Denver	48	48	0	0
		Seibert	71	74	-3	-4
	Kansas	Glenwood	70	71	-1	-1
		Oakley	70	71	-1	-1
		Hutchinson	48	47	1	2
		Topeka	41	45	-4	-10
	Oklahoma	Cooper Lab	23	23	0	0
		McCurtain County	31	31	0	0
		Texas County	42	42	0	0
	Illinois	Spring Field (Central)	40	42	-2	-5
		Carbondale (Southern)	33	33	0	0
	Missouri	Central Laboratory	44	44	0	0
		Southeast District	37	38	-1	-3
Northwest	Oregon	Bend	42	46	-4	-10
		Hinsdale Wave Research Lab	26	28	-2	-8
		Newport	1	1	0	0
	Idaho	Coeur d'Alene US-95	61	58	3	5
		Mt Home I-84	50	56	-6	-12
		Paddy Flat SH-55	74	67	7	9
Northeast	Pennsylvania	Clearfield1	58	61	-3	-5
		Cyclone	48	52	-4	-8
		Harrisburg	40	43	-3	-8
	New York	Watertown	25	25	0	0
		Clifton Park	25	27	-2	-8
		Hauppauge	18	18	0	0

[a] Difference in FT Cycles = *Measured – Predicted FT cycles*.

[b] Difference (%) = $\frac{Measured\ FT\ Cycles - Predicted\ FT\ Cycles}{Measured\ FT\ Cycles}\ x\ 100$

Table E2

Predicted and Measured Total FT Cycles from September 2022 to April 2023 Across All Regions and Locations.

Region	State	Location	Measured FT Cycles	Predicted FT Cycles	Cycle Difference[a]	% Difference[b]
North	North Dakota	Bismarck Site	63	63	0	0
		Grand Forks Site	57	57	0	0
		Fargo Site	73	73	0	0
	Minnesota	Baxter	83	83	0	0
		Maplewood	85	85	0	0
		Thief River Falls	67	67	0	0
	Wisconsin	Green Bay	51	55	-4	-8
		Madison	56	58	-2	-4
		Rhinelander	60	60	0	0
	Iowa	Ames	94	96	-2	-2
		Fairfield	41	44	-3	-7
		Mason City	49	51	-2	-4
	Nebraska	Lincoln	77	77	0	0
		Thedford	116	116	0	0
		Chadron	99	99	0	0
	Illinois	Dixon (Northern)	65	66	-1	-2
	Missouri	Northwest District	52	52	0	0
South	Colorado	Denver	70	69	1	1
		Seibert	50	52	-2	-4
		Glenwood	85	89	-4	-5
	Kansas	Oakley	96	96	0	0
		Hutchinson	54	54	0	0
		Topeka	55	62	-7	-15
	Oklahoma	Cooper Lab	29	29	0	0
		McCurtain County	4	4	0	0
		Texas County	41	41	0	0
	Illinois	Spring Field (Central)	34	38	-4	-12
		Carbondale (Southern)	24	24	0	0
	Missouri	Central Laboratory	46	46	0	0
		Southeast District	33	33	0	0
Northwest	Oregon	Bend	48	48	0	0
		Hinsdale Wave Research Lab	35	38	-3	-9
		Newport	6	6	0	0
	Idaho	Coeur d Alene US-95	133	133	0	0
		Mt Home I-84	56	56	0	0
		Paddy Flat SH-55	123	123	0	0
Northeast	Pennsylvania	Clearfield1	83	83	0	0
		Cyclone	85	85	0	0
		Harrisburg	49	49	0	0
	New York	Watertown	49	47	2	4
		Clifton Park	41	45	-4	-10
		Hauppauge	30	30	0	0

[a] Difference in FT Cycles = *Measured – Predicted FT cycles*.

[b] Difference (%) = $\frac{Measured\ FT\ Cycles - Predicted\ FT\ Cycles}{Measured\ FT\ Cycles}\ x\ 100$

Table E3

Predicted and Measured Total FT Cycles from September 2023 to April 2024 Across All Regions and Locations.

Region	State	Location	Measured FT Cycles	Predicted FT Cycles	Cycle Difference[a]	% Difference[b]
North	North Dakota	Bismarck Site	NA	115	NA	NA
		Grand Forks Site	NA	105	NA	NA
		Fargo Site	NA	106	NA	NA
	Minnesota	Baxter	97	101	-4	-4
		Maplewood	90	88	2	2
		Thief River Falls	102	107	-5	-4
	Wisconsin	Green Bay	NA	91	NA	NA
		Madison	49	49	0	0
		Rhinelander	NA	89	NA	NA
	Iowa	Ames	NA	55	NA	NA
		Fairfield	33	33	0	0
		Mason City	56	56	0	0
	Nebraska	Lincoln	50	43	7	14
		Thedford	66	64	2	3
		Chadron	75	76	1	1
	Illinois	Dixon (Northern)	NA	43	NA	NA
	Missouri	Northwest District	35	36	-1	-3
South	Colorado	Denver	75	76	-1	-1
		Seibert	45	45	0	0.00
		Glenwood	98	99	-1	-1
	Kansas	Oakley	70	69	1	1
		Hutchinson	52	50	2	4
		Topeka	53	55	-2	-4
	Oklahoma	Cooper Lab	33	31	2	6
		McCurtain County	12	11	1	8
		Texas County	30	30	0	0
	Illinois	Spring Field (Central)	25	22	3	12
		Carbondale (Southern)	16	14	2	13
	Missouri	Central Laboratory	32	30	2	6
		Southeast District	35	35	0	0
Northwest	Oregon	Bend	NA	37	NA	NA
		Hinsdale Wave Research Lab	NA	26	NA	NA
		Newport	3	3	0	0
	Idaho	Coeur d Alene US-95	72	73	-1	-1
		Mt Home I-84	55	59	-4	-7
		Paddy Flat SH-55	110	115	-5	-5
Northeast	Pennsylvania	Clearfield1	75	77	-2	-3
		Cyclone	71	75	-4	-6
		Harrisburg	43	40	3	7
	New York	Watertown	40	39	1	3
		Clifton Park	67	64	3	4
		Hauppauge	30	27	3	10

[a] Difference in FT Cycles = *Measured – Predicted FT cycles*.

[b] Difference (%) = $\frac{Measured\ FT\ Cycles - Predicted\ FT\ Cycles}{Measured\ FT\ Cycles}\ x\ 100$

Appendix F: Predicted and Measured Damaging FT Cycle Data for All Regions

Table F1 presents the predicted and measured damaging FT cycles for all years and regions, as well as the absolute and percentage difference between the observed and predicted. Table F2 shows the monthly predicted and measured values for selected locations.

Table F1

Predicted and Measured Damaging FT Cycles Across All Regions and Locations.

Region	State	Location	Measured Damaging FT Cycles			Predicted Damaging FT Cycles			% Difference[a]		
			Year2[b]	Year3[c]	Year4[d]	Year2[b]	Year3[c]	Year4[d]	Year2[b]	Year3[c]	Year4[d]
North	North Dakota	Bismarck Site	97	83	NA	99	83	NA	-2	0	NA
	North Dakota	Grand Forks Site	66	57	NA	71	57	NA	-8	0	NA
	North Dakota	Fargo Site	81	73	NA	90	73	NA	-11	0	NA
	Minnesota	Baxter	74	83	97	78	83	101	-5	0	-4
	Minnesota	Maplewood	79	85	90	70	85	88	11	0	2
	Minnesota	Thief River Falls	79	88	102	82	84	104	-4	5	-2
	Wisconsin	Green Bay	79	65	NA	80	60	NA	-1	8	NA
	Wisconsin	Madison	50	56	49	55	58	49	-10	-4	0
	Wisconsin	Rhinelander	85	81	NA	84	79	NA	1	2	NA
	Iowa	Ames	97	94	NA	96	97	NA	1	-3	NA
	Iowa	Fairfield	48	41	33	52	44	33	-8	-7	0
	Iowa	Mason City	39	49	56	40	51	56	-3	-4	0
	Nebraska	Lincoln	56	77	50	60	77	46	-7	0	8
	Nebraska	Thedford	63	74	66	67	80	64	-6	-8	3
	Nebraska	Chadron	94	99	89	90	99	80	4	0	10
	Illinois	Dixon (Northern)	76	78	NA	77	70	NA	-1	10	NA
	Missouri	Northwest District	44	52	35	46	52	36	-5	0	-3
			Average						-3	0	1
			Standard Deviation						6	5	5
South	Colorado	Denver	0	0	0	0	0	0	0	0	0
	Colorado	Seibert	4	6	0	4	6	0	0	0	0
	Colorado	Glenwood	83	85	98	80	85	99	4	0	-1
	Kansas	Oakley	6	3	5	6	3	5	0	0	0
	Kansas	Hutchinson	34	37	46	38	40	50	-12	-8	-9
	Kansas	Topeka	41	54	53	45	58	55	-10	-7	-4
	Oklahoma	Cooper Lab	9	11	27	9	10	30	0	9	-11
	Oklahoma	McCurtain County	17	11	9	17	12	10	0	-9	-11
	Oklahoma	Texas County	0	0	1	0	0	1	0	0	0
	Illinois	Spring Field (Central)	20	29	25	22	32	22	-10	-10	12
	Illinois	Carbondale (Southern)	27	17	NA	30	19	NA	-11	-12	NA
	Missouri	Central Laboratory	26	17	22	29	19	25	-12	-12	-14
	Missouri	Southeast District	31	15	3	35	13	3	-13	13	0
			Average						-5	-3	-3
			Standard Deviation						6	8	7
Northwest	Oregon	Bend	42	48	NA	47	50	NA	-12	-4	NA
	Oregon	Hinsdale Wave Research Lab	8	17	NA	8	19	NA	0	-12	NA
	Oregon	Newport	1	3	1	1	3	1	0	0	0
	Idaho	Coeur d'Alene US-95	110	123	113	115	120	97	-5	2	14
	Idaho	Mt Home I-84	50	48	42	56	55	47	-12	-15	-12
	Idaho	Paddy Flat SH-55	102	123	110	100	115	115	2	7	-5
			Average						-4	-4	-1
			Standard Deviation						6	8	11
Northeast	Pennsylvania	Clearfield	78	83	75	70	83	77	10	0	-3
	Pennsylvania	Cyclone	58	85	71	52	85	75	10	0	-6
	Pennsylvania	Harrisburg	40	49	43	43	50	40	-8	-2	7
	New York	Watertown	47	36	40	50	40	39	-6	-11	3
	New York	CliftonPark	57	40	67	55	45	64	4	-13	4
	New York	Hauppauge	45	30	30	40	30	27	11	0	10
			Average						4	-4	3
			Standard Deviation						9	6	6

[a] Difference (%) = $\frac{Measured\ FT\ Cycles - Predicted\ FT\ Cycles}{Measured\ FT\ Cycles}\ x\ 100$

[b] September 2021 – April 2022.

[c] September 2022 – April 2023.

[d] September 2023 – April 2024.

Table F2

Comparison of Predicted and Measured FT Cycles for Selected Locations (September 2021 to April 2022).

Month	Actual DOS (%)[a]	Actual DOS Category (%)	Predicted DOS Category (%)[b]	Actual Number of FT Cycles	Predicted Number of FT Cycles	Difference Between Actual and Predicted FT Cycles
Maplewood, Minnesota (North Region)						
September	87	80-90	80-90	0	0	0
October	92	>90	>90	0	0	0
November	99	>90	>90	6	6	0
December	99	>90	>90	13	10	4
January	99	>90	>90	6	6	0
February	99	>90	>90	7	7	0
March	97	>90	>90	9	9	0
April	97	>90	>90	8	8	0
Total Number of FT Cycles				**49**	**46**	**3**
Percent Error (%)[c]						**6**
Bend, Oregon (Northwest Region)						
September	68	<80	<80	0	0	0
October	73	<80	<80	1	1	0
November	81	80-90	80-90	4	4	0
December	81	80-90	80-90	8	8	0
January	82	80-90	80-90	9	9	0
February	83	80-90	80-90	10	10	0
March	86	80-90	>90	5	9	-4
April	79	<80	<80	5	5	0
Total Number of FT Cycles				**42**	**46**	**-4**
Percent Error (%)[c]						**-10**
Harrisburg, Pennsylvania (Northeast Region)						
September	96	>90	>90	0	0	0
October	95	>90	>90	0	0	0
November	95	>90	>90	1	2	-1
December	93	>90	>90	4	7	-3
January	94	>90	>90	14	14	0
February	96	>90	>90	14	14	0
March	96	>90	>90	8	8	0
April	97	>90	>90	0	0	0
Total Number of FT Cycles				**40**	**43**	**-3**
Percent Error (%)[c]						**-8**
Topeka, Kansas (South Region)						
September	92	>90	>90	0	0	0
October	91	>90	>90	0	0	0
November	93	>90	>90	4	7	-3
December	92	>90	>90	9	10	-1
January	94	>90	>90	14	14	0
February	93	>90	<80	12	14	-2
March	94	>90	>90	5	5	0
April	94	>90	>90	1	2	-1
Total Number of FT Cycles				**41**	**45**	**-4**
Percent Error (%)[c]						**10**

[a] Obtained from the Field Sample [2].

[b] Obtained from Genetic Algorithms Model.

[c] Percent Error (%) = $\frac{Measured\ FT\ Cycles - Predicted\ FT\ Cycles}{Measured\ FT\ Cycles}\ x\ 100$

Appendices References

[1] Open-Meteo. (2024). *Open-Meteo: Free weather forecast and historical data API for scientists and developers.* Retrieved from https://open-meteo.com.

[2] Chen, L., Ley, M.T., Ghantous, R.M., Weiss, W.J., Master, N.F. (2023). Measuring damaging freeze-thaw cycles in the field. Construction and Building Materials, 387, 131660.

[3] Chawla, N. V., Bowyer, K. W., Hall, L. O., & Kegelmeyer, W. P. (2002). SMOTE: Synthetic minority over-sampling technique. Journal of Artificial Intelligence Research, 16, 321–357.

[4] Fernández, A., García, S., Galar, M., Prati, R. C., Krawczyk, B., & Herrera, F. (2018). Learning from imbalanced data sets. Springer.

[5] García, S., Fernández, A., Luengo, J., & Herrera, F. (2015). Advanced nonparametric tests for multiple comparisons in the design of experiments in machine learning research. Information Sciences, 180(10), 2044–2064.

[6] Haupt, R. L., & Haupt, S. E. (2004). Practical Genetic Algorithms (2nd ed.). Wiley.

[7] Deb, K. (2000). An efficient constraint handling method for genetic algorithms. *Computer Methods in Applied Mechanics and Engineering*, 186(2–4), 311–338.

[8] Holland, J. H. (1975). Adaptation in Natural and Artificial Systems. University of Michigan Press.

Creating Maps of Freeze–Thaw Exposure Based for Concrete

Bahaa N. Abdelrahman, M. Tyler Ley, Guoliang Fan, Lichun Chen, Andrew Young

Keywords: Freeze-Thaw Durability, Damaging Freeze-Thaw Cycles, Degree of Saturation, Freeze-Thaw Maps, Machine Learning.

Abstract

Freeze–thaw damage is a major durability concern for concrete in cold regions. This study develops maps based on field instrumentation, weather data, and a correlation based on machine learning. The maps are based on 24 years of data from 574 weather stations. Maps of the average and variation of the combination of freeze-thaw cycles and moisture are combined to measure the amount of damaging freeze-thaw cycles. Since this work provides insights into the average freeze-thaw exposure and its variability, this information can serve as a starting point for performance design against freeze-thaw damage. The map produced is also compared to other freeze-thaw exposure maps, such as those developed by the Long-Term Pavement Performance (LTPP), which do not capture the localized weather exposure.

1.0 Introduction

The durability of concrete can be compromised in cold regions due to freeze–thaw deterioration [1, 2]. Repeated freeze–thaw cycles generate internal stresses when pore water freezes at high saturation levels, leading to cracking, scaling, and premature degradation of concrete structures [3-9]. This highlights the need for reliable methods to predict freeze–thaw damage and improve durability design [10].

The degree of saturation (DOS), defined as the ratio of pore water to total pore volume in concrete, plays a key role in freeze–thaw damage [11,12]. When DOS exceeds a critical threshold, typically between 78% and 90%, the risk of damage increases significantly due to ice formation in the pores [12–15]. Accordingly, damaging freeze–thaw cycles are defined as those that occur when the DOS is at or above the critical DOS, while freeze-thaw events that occur below the critical DOS are not damaging [15–18].

A recent study developed a novel field-based method that combines electrical resistivity and temperature measurements to monitor DOS, ice formation, and ice melting within concrete in real time [19, 20]. This approach provides in-situ detection of damaging freeze–thaw cycles and a practical way to quantify them. The study also showed that higher DOS levels raise the

freezing point of cementitious materials, while lower DOS levels result in freezing at lower temperatures [19–22]. This highlights the importance of accounting for both temperature and moisture conditions when evaluating freeze–thaw exposure, as freeze–thaw damage is primarily influenced by freezing temperature and DOS, both of which are influenced by local weather conditions [23,24].

Building on this framework, the authors' recent work [25] introduced a novel statistical model to predict freeze–thaw cycles directly from weather data. The model was trained on field measurements from 42 sites across 14 states and incorporated critical weather parameters. A genetic algorithm (GA) was applied to optimize thresholds, systematically identifying the most effective cutoff values of the weather variables to classify and distinguish the DOS categories. From this process, a region-specific tool was developed to convert weather data into different levels of DOS within the concrete. Freeze–thaw cycles were determined to occur if the temperature dropped below the freezing temperature based on the moisture of the concrete and then subsequently increased to a temperature above 0°C. If the DOS ≥80%, then the freezing cycle is classified as damaging, and if the DOS <80%, then the freezing cycle is considered non-damaging. The model correctly predicted the DOS in 89% of cases and predicted damaging freeze-thaw cycles with 85% accuracy across all years and regions [25].

This work uses the developed model and combines it with 24 years of weather data from 574 locations. Predictions were only made for regions where field data were used to validate the model. This work aims to provide a starting place for an easy-to-use tool, such as a map or simple website, where the amount of total and damaging freeze-thaw cycles can be determined. This also helps visualize the average, standard deviation, and the coefficient of variation (COV) of this exposure. This offers specifiers and builders a better understanding of regional freeze–thaw risks, and this supports durability-based decision-making in concrete infrastructure design.

2.0 Methodology

2.1 Weather Data Collection and Preprocessing

This study focused on six key weather variables: temperature, precipitation, relative humidity (RH), wind speed, solar radiation, and atmospheric pressure. These parameters were selected because they are widely used in measuring how environmental factors impact the saturation and drying behavior of soils [26-35]. More information can be found in other publications [25].

Weather data were collected from the winter seasons (September through April) between 2000 and 2024 for 574 weather stations across 14 states. A map of these weather stations is shown in Figure 1. The dataset was obtained from the Open-Meteo API [36], an open-source, research-oriented climate database that compiles long-term, quality-controlled records from established meteorological networks and provides wide spatial coverage. The daily records were averaged into monthly values for ease of processing.

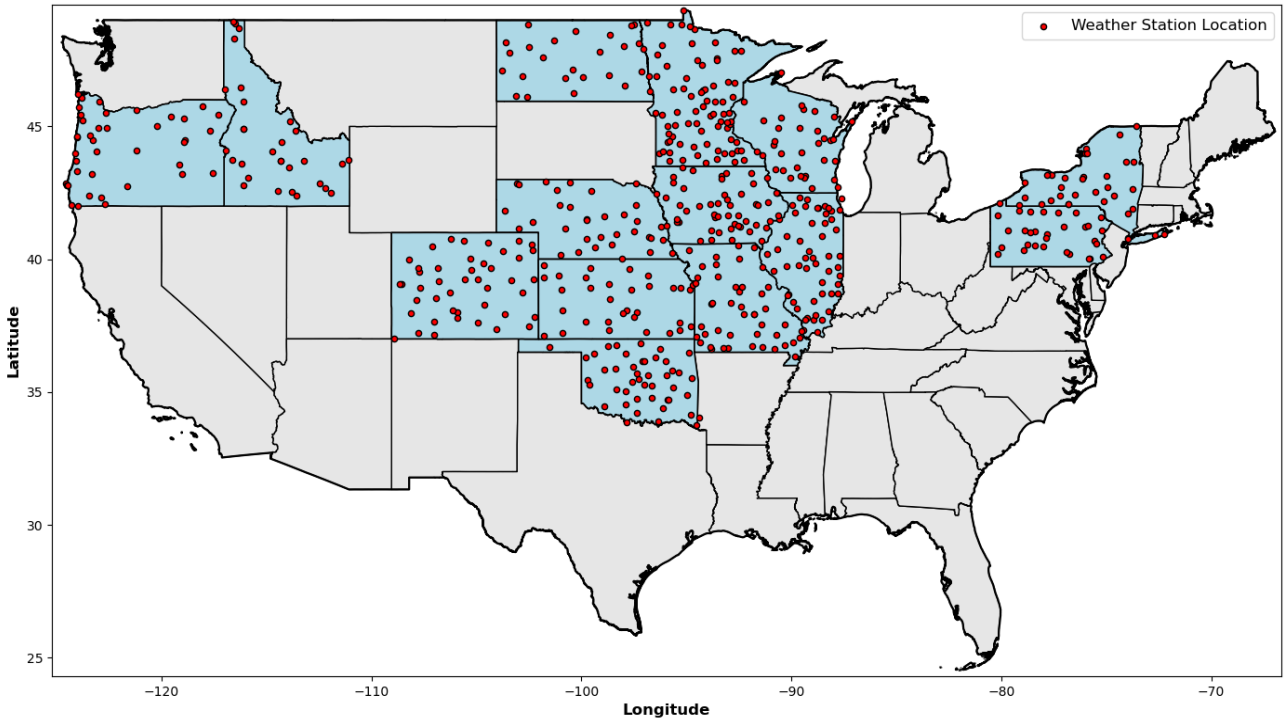

Figure 1: Locations of weather stations used for predicting freeze-thaw cycles in the states analyzed.

2.2 Freeze-Thaw Cycles Prediction

To predict freeze–thaw cycles across all weather stations, this study used the tools developed in the previous study [25]. The approach allowed the conversion of weather data into categorical representations that could be used to estimate the average DOS for each location during each winter season. The regions used are in Appendix A.

The freeze–thaw cycles were predicted using air temperature records from each station in combination with the predicted DOS category. The air temperature has been shown to closely match the temperature at 50 mm from the surface in the concrete, based on field measurements [25]. Each DOS category is associated with a specific freezing temperature, and a cycle is

counted whenever the temperature falls below that freezing temperature and then increases to 0°C. Additional details on this procedure are provided in Appendix B and in a previous publication [25].

Any freeze–thaw cycle that occurred when the predicted DOS was below 80% was considered non-damaging, while all cycles at or above 80% were classified as damaging. This threshold was selected based on previous studies, which identified the critical saturation range for freeze–thaw damage as approximately 78–90% [12–15]. Using 80% as the cutoff provides a conservative and practical criterion that accounts for the measurement variability and ensures a margin of safety when evaluating freeze–thaw durability.

2.3 Development of Freeze–Thaw Cycles Maps

Geospatial interpolation was used to produce continuous surfaces by interpolating between weather measurement sites to visualize the spatial distribution of freeze-thaw cycles to create freeze-thaw maps. Maps of measures of variability (average, standard deviation, and coefficient of variation (COV) were generated across the 24 winter seasons for both total and damaging freeze–thaw cycles. Total freeze–thaw cycle maps represent all cycles occurring when the concrete freezes based on the saturation level, while damaging freeze–thaw cycle maps include only cycles when the DOS exceeded 80%, the critical threshold set for this work.

2.3.1 Interpolation and Smoothing

Spatial interpolation and smoothing are widely used in geospatial analysis to convert irregular point measurements into continuous surfaces that can reveal regional patterns [37,38]. These approaches are particularly valuable when site data are limited or unevenly distributed, as they help reduce noise, fill gaps, and generate maps that are both interpretable and suitable for decision-making.

2.3.1.1 Interpolation Method

Surface interpolation in this study was performed using the Inverse Distance Weighting (IDW) method, which estimates values at locations without data by averaging nearby measurements while giving greater influence to points that are closer. In this approach, the weight of each point decreases with distance according to an inverse power function, meaning that spatially close sites contribute more strongly to the estimated value. IDW was selected because it

performs well with irregularly spaced data, preserves local gradients, and avoids the overshoot artifacts that can occur in polynomial or spline-based interpolation methods [38,39].

The interpolation parameters were empirically tuned to achieve a balance between smoothness and local accuracy. The power value, which typically ranges between 1 and 3, controls how quickly the influence of a point decreases with distance. A power of 1.9 was chosen in this study because it provides an effective balance between emphasizing nearby data points and maintaining regional continuity. A higher power would overly emphasize nearby points, creating sharp local variations, while a lower power would over-smooth the data and obscure meaningful regional trends.

Each grid cell represents a small, regularly spaced unit on the interpolation grid covering the study area, serving as the basic element where the damaging freeze–thaw cycle value is estimated. Interpolating values at each grid cell ensures a continuous surface suitable for mapping and contour visualization. The model used the 16 nearest neighboring stations within a maximum search radius of 1.6° in both longitude and latitude, which defines the geographic range (in degrees) within which nearby stations influence the interpolated value. These settings ensured that interpolation remained constrained to regions with sufficient data coverage, preventing unrealistic extrapolation into data-sparse areas.

Overall, the chosen IDW parameters allowed the interpolated surface to represent realistic spatial transitions in damaging freeze–thaw cycles while maintaining numerical stability and visual continuity. The IDW approach has been shown to perform reliably in environmental mapping applications where preserving local variability without introducing artificial extremes is important [38,39].

2.3.1.2 Smoothing Filters

To reduce small-scale noise and improve the visual clarity of the interpolated surface, two smoothing filters were applied in sequence. First, a median filter was used to remove isolated pixel-level spikes that resulted from local interpolation noise, with a window size of 0.26° in both longitude and latitude. The window size defines the area around each grid cell that the filter considers when computing a new value. This value was chosen empirically to allow random noise to be removed without distorting meaningful spatial gradients. The median filter replaces each grid cell's value with the median of its surrounding cells within the defined neighborhood, effectively removing isolated spikes or speckled noise that may arise from local

measurement variability or interpolation artifacts while preserving genuine spatial boundaries and gradients [40].

After median filtering, a Gaussian filter was applied to further smooth the overall surface. The Gaussian filter performs a weighted average of nearby values, giving higher weights to those closer to the center and progressively lower weights with distance. This produces a gradual, natural-looking transition between neighboring cells rather than abrupt changes. A standard deviation (σ) of 0.32° in both longitude and latitude was used to control the degree of smoothing, while a truncation factor of 2.5 limited the filter's influence on about five times σ in each direction [41,42]. These parameters were selected empirically through sensitivity testing to provide light smoothing that reduced pixel-level irregularities without blurring meaningful regional gradients.

Overall, the combination of median and Gaussian filters effectively enhanced the smoothness and readability of the maps while preserving the true spatial variability of damaging freeze–thaw cycles. The parameters were chosen conservatively to ensure that filtering improved visualization without introducing bias or altering the underlying data trends [41,42]. The filtering effects at each stage of processing are illustrated in Figure 2, which compares the IDW interpolation, IDW with a median filter, and IDW with median and Gaussian filters.

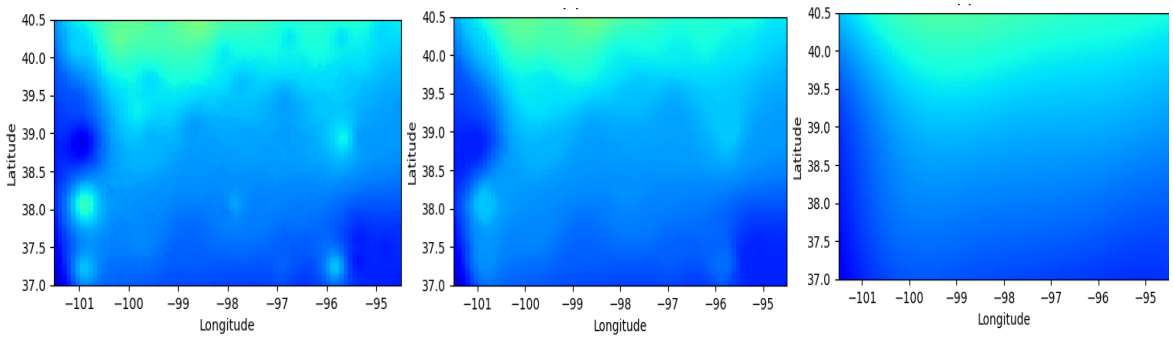

(a) **(b)** **(c)**

Figure 2: Comparison of the effects of interpolation and filtering steps on freeze–thaw cycle maps: (a) IDW interpolation, (b) IDW with median filter, and (c) IDW with median and Gaussian filters.

2.4 Color Mapping and Visualization Design

For this study, filled contour maps were selected to visualize the distributions of freeze–thaw cycles. These maps display continuous color shading to represent regional gradients and

contour lines to mark areas of equal value, providing an intuitive and quantitative representation of spatial variation. Such maps are widely used in environmental and geospatial studies to communicate spatial variation in a way that is both intuitive and quantitative [43,44].

Interpolated grids were displayed as filled rasters, meaning that each grid cell was color-shaded according to its freeze–thaw cycle value using a sequential colormap, with categories increasing in 10-cycle intervals. This continuous color background highlights spatial gradients, while contour lines were added at consistent intervals appropriate for each map to provide additional clarity. A color bar accompanied each figure for easy interpretation of the result [45].

These maps highlight geographic variations in freeze–thaw cycles and their potential impact on concrete durability. They serve as a practical tool for visualizing freeze–thaw exposure, enabling engineers and practitioners to design concrete mixtures suited to specific environmental conditions. By clearly identifying regions at higher risk of damaging freeze–thaw cycles, the maps support informed decision-making in selecting materials and mix designs appropriate for different climates.

3.0 Results and Discussions

3.1 Long-Term Spatial Distribution of Freeze–Thaw Cycles

The maps in this work use 24 years of weather information to find the total and damaging freeze–thaw cycles. Figures 3a and 3b show significant variability over the regions studied. In some regions, damaging freeze–thaw cycles are frequent, while in nearby areas they are minimal. These variations demonstrate how moisture levels can shift over short distances, directly influencing damaging freeze–thaw cycles.

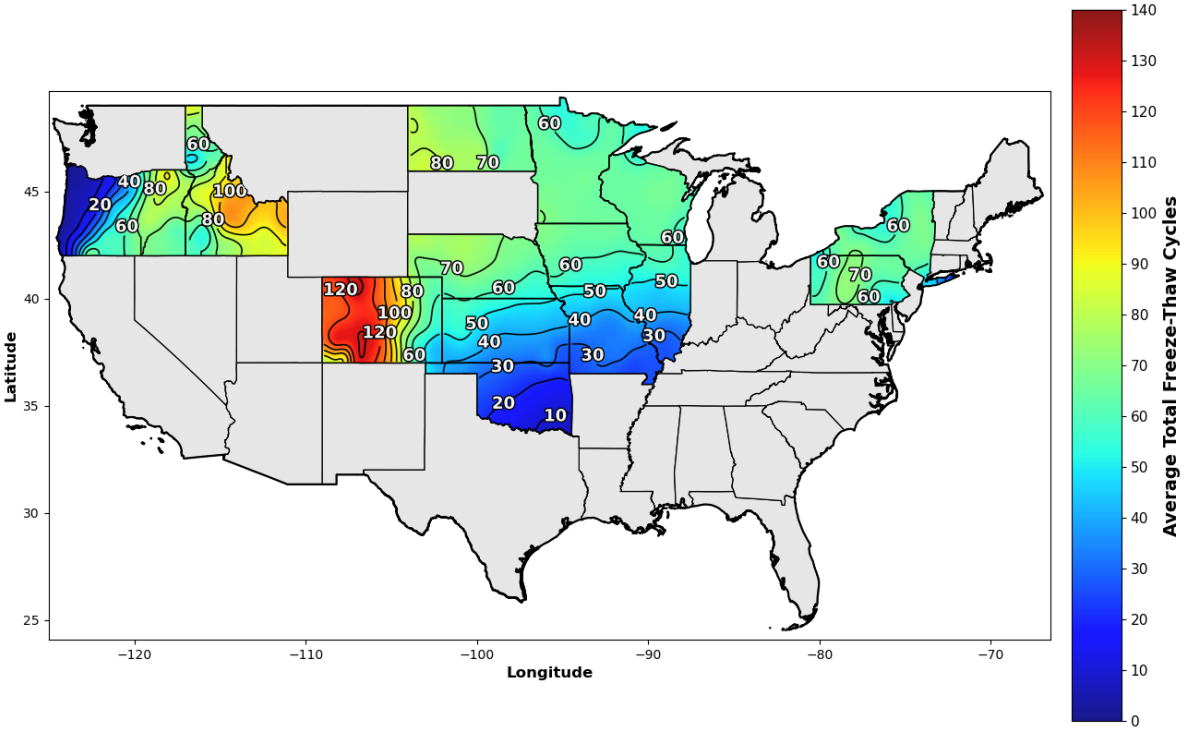

(a)

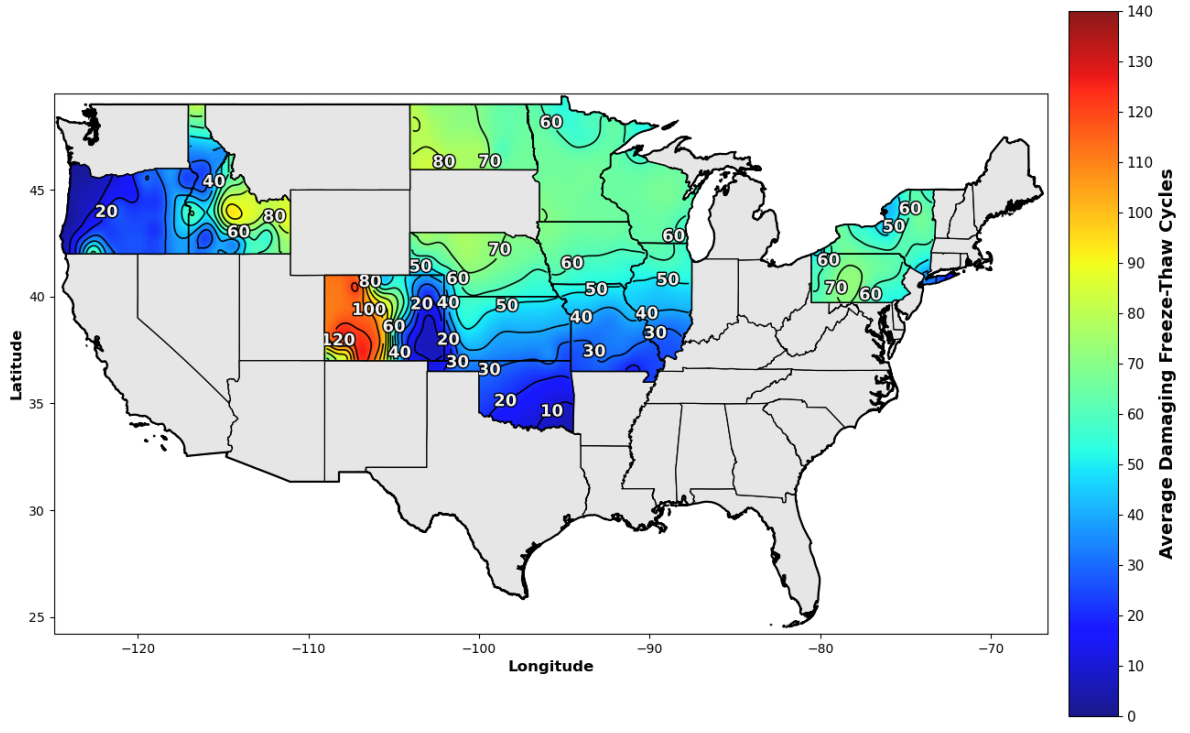

(b)

Figure 3: 24-Year average of predicted freeze–thaw cycles at all weather stations: (a) total freeze–thaw cycles, (b) damaging freeze–thaw cycles.

3.2 Difference Between the Total and Damaging Cycles

Figure 4 shows the average difference between the total and damaging freeze–thaw cycles. Areas with large differences, such as eastern Colorado, Oregon, and western Idaho, experience frequent freeze–thaw cycling, but the moisture content of these areas was often below the critical DOS, resulting in a damage reduction. Conversely, the rest of the regions studied show little to no difference between the damaging and effective freeze-thaw cycles. One reason for this small difference is that the model assumed the average DOS remained constant throughout each month. However, the field data showed that there were periods when the DOS temporarily dropped below 80% before increasing again. These fluctuations were not captured in the model, leading to a conservative estimate of the number of damaging freeze–thaw cycles.

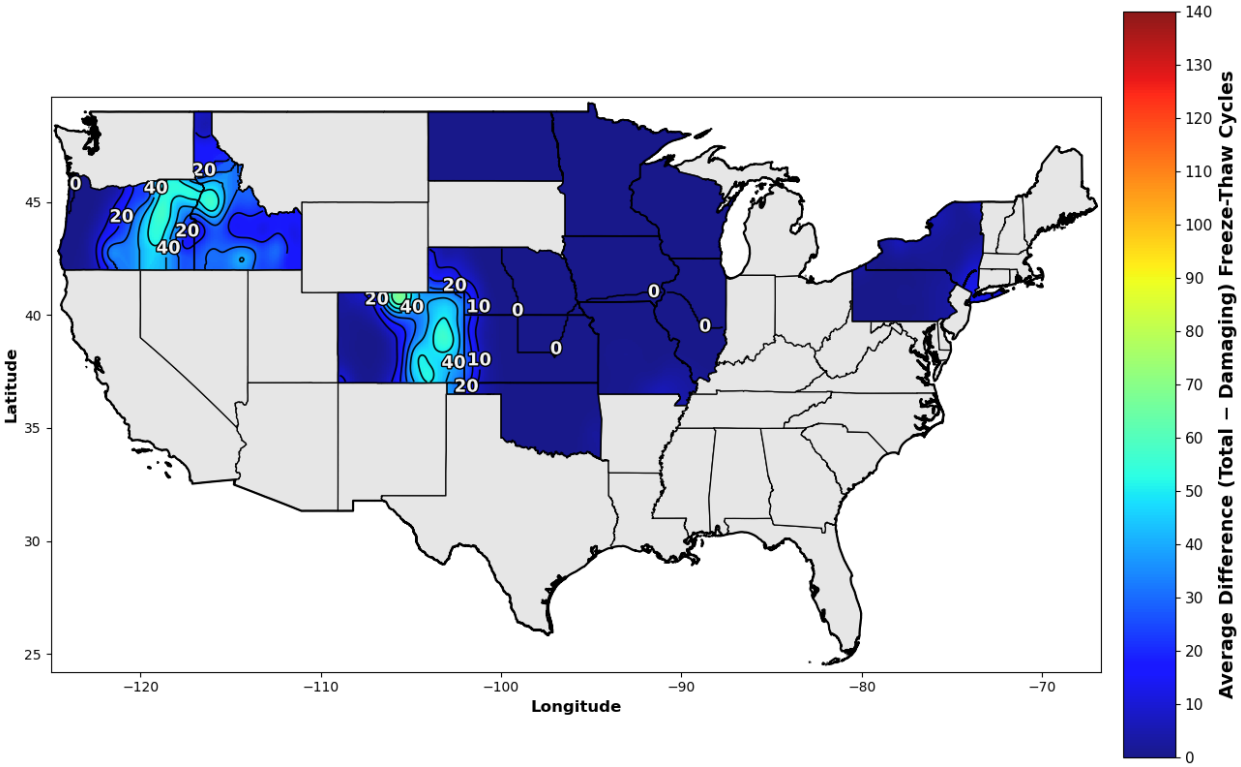

Figure 4: Average difference between total and damaging freeze–thaw cycles.

3.3 Long-Term Variability in Freeze–Thaw Cycles

3.3.1 Standard Deviation of Freeze-Thaw Cycles

Figures 5a and 5b show the standard deviation maps of the total and damaging freeze–thaw cycles. This is helpful to understand the variability in the different winter seasons. While total cycles generally show low variability, ranging from 3 to 21 cycles, the standard deviation for damaging cycles is much higher, reaching up to 45 cycles in regions such as Colorado, Oregon, and Idaho. This demonstrates that these regions have larger variability in the moisture content during the freezing cycles.

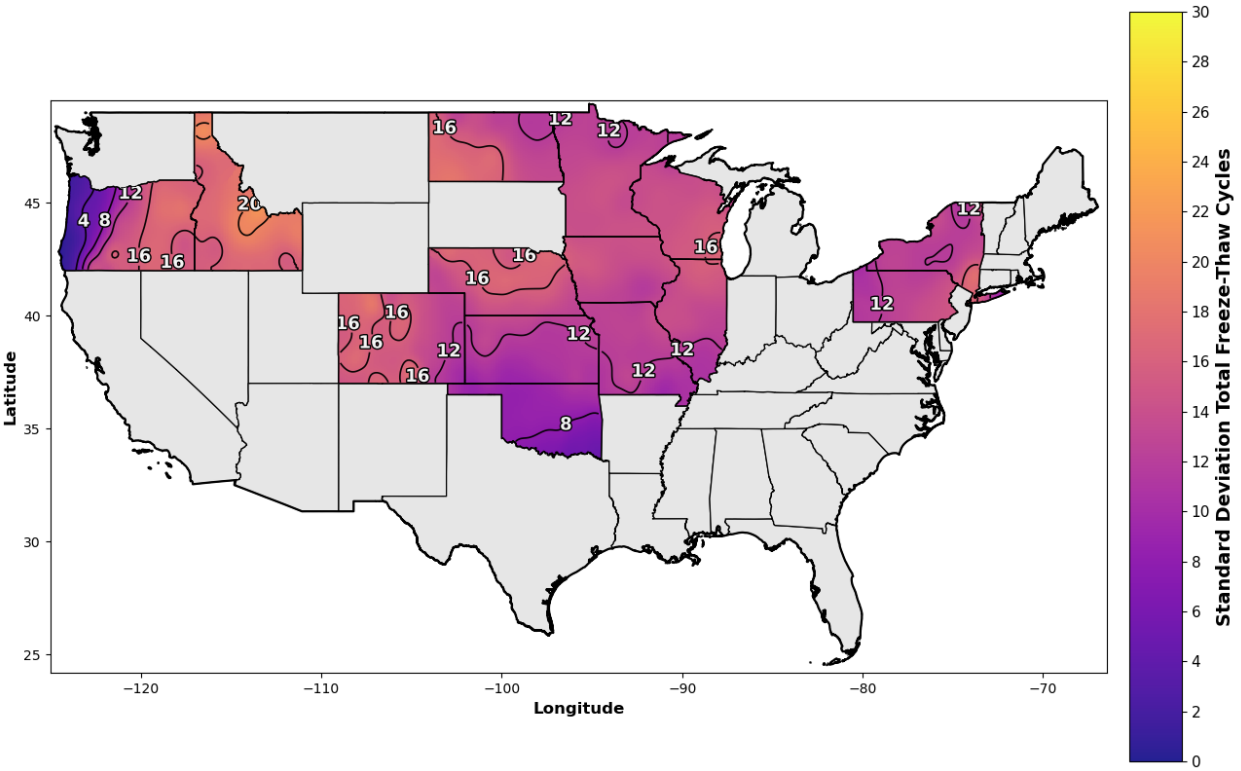

(a)

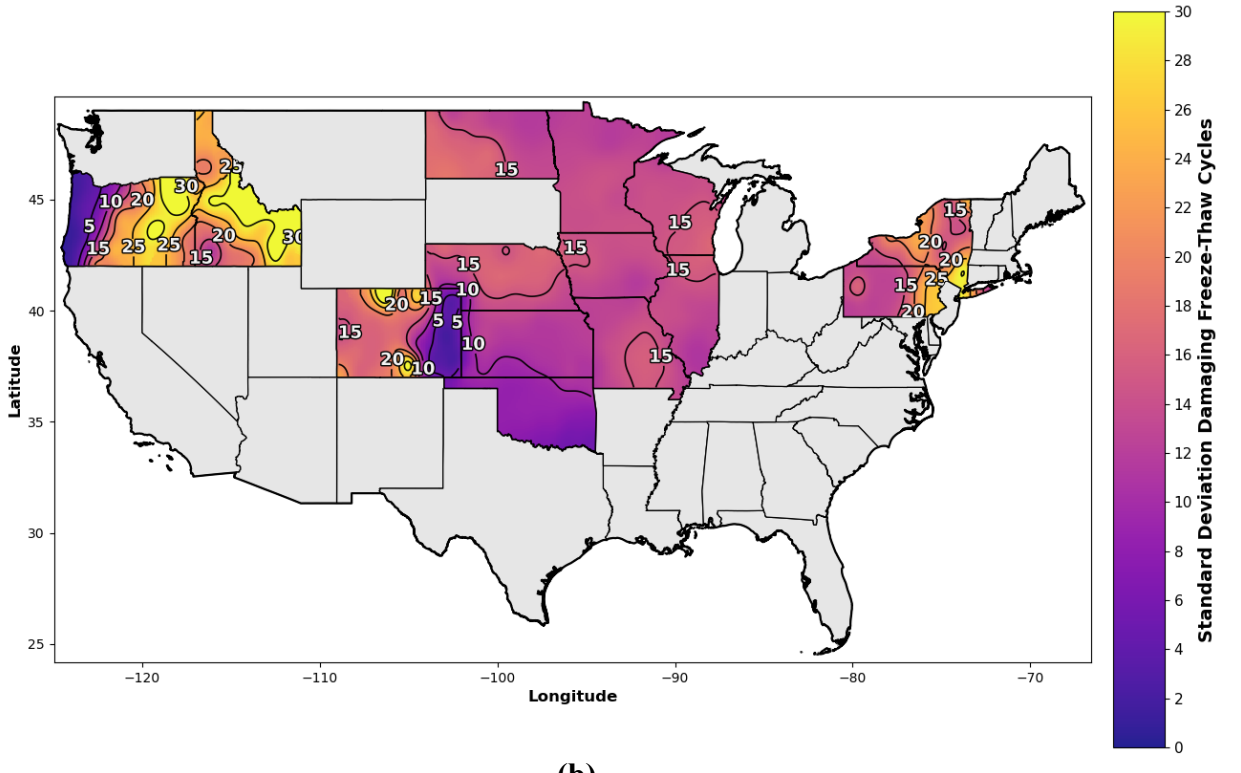

(b)

Figure 5: 24-Year standard deviation of predicted freeze–thaw cycles at all weather stations: (a) total freeze–thaw cycles, (b) damaging freeze–thaw cycles.

3.3.2 Coefficient of Variation to Measure Variability

The average coefficient of variation was used to quantify the variability of the total and the damaging freeze thaw cycles. This was done to create a map of which areas show the most variation in the freeze-thaw damage. The individual plots are included in Appendix C, but Figure 6 is included in the body of the paper as it shows the coefficient of variation of the damaging freeze-thaw cycles in different risk levels. These different groups are a coefficient of variability of Low (<15%), Moderate (15–40%), and High (>40%). The locations in the high category face substantial swings in the damage potential from year to year.

Some of these regions typically have a low number of damaging freeze thaw cycles but they will have a few winters where these numbers increase significantly. It is possible that these regions have variable weather, or that more than 24 years is needed to understand the weather patterns for these regions. Overall, the results highlight regions where freeze–thaw damage potential is more sensitive to year-to-year climate variability.

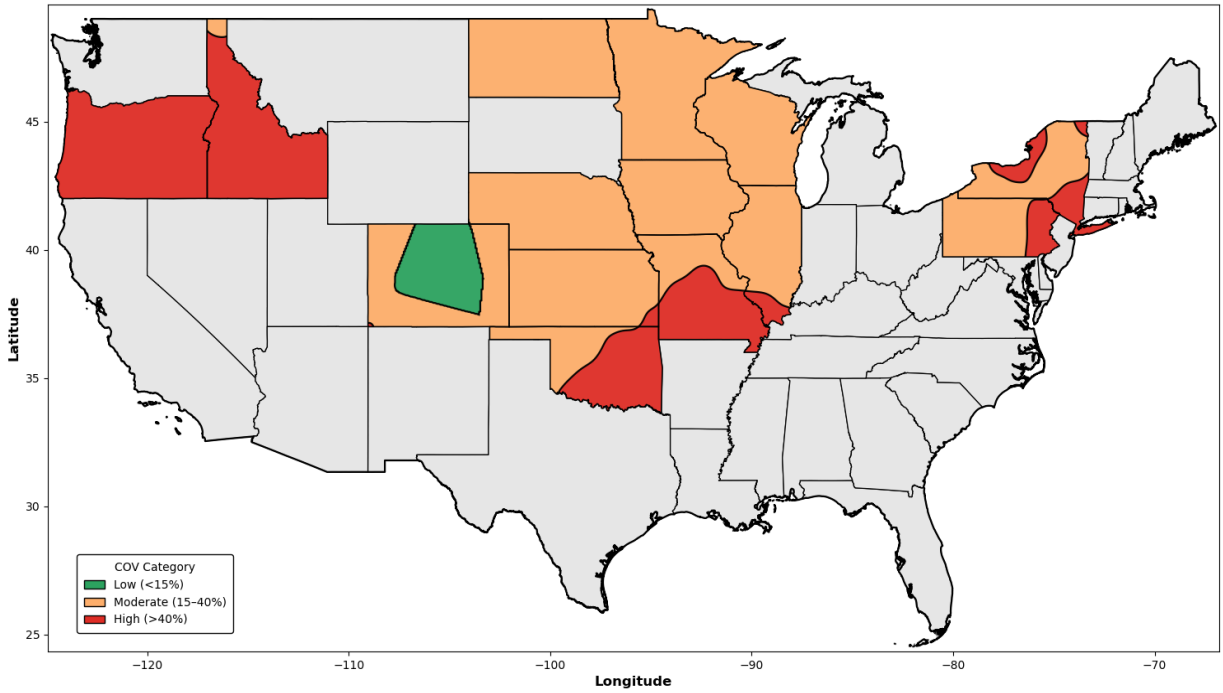

Figure 6: 24-Year spatial categories of CV (%) of predicted damaging freeze–thaw cycles at all weather stations.

3.4 Comparison with Existing Models and Standards

Unlike traditional approaches that rely on broad climate zones or a single freeze–thaw classification for an entire state, the maps developed in this study are based on a predictive model that was developed and validated using real field data [25]. Existing standards classify freeze–thaw exposure using broad regional categories, but such approaches often overlook the site-specific conditions that drive actual damage. Understanding how these models differ is important, as they directly influence durability design decisions for concrete in cold regions.

3.4.1 LTPP Climate Classification

The Long-Term Pavement Performance (LTPP) climate classification [46,47] divides the United States into four general zones, Wet–Freeze, Wet–Non-freeze, Dry–Freeze, and Dry–Non-freeze, based on annual precipitation and the freezing index (FI). The FI is the summation of the average daily air temperature of each day that is below freezing. The data is then classified as No-Freeze (FI < 50), Moderate-Freeze (FI = 50–400), and Deep-Freeze (FI > 400). Wet regions are defined as those receiving more than 508 mm of annual precipitation, while dry regions receive less.

Although this framework provides a generalized national classification, it simplifies the complex interaction between moisture availability and freezing conditions that controls freeze–thaw damage in concrete. Total annual precipitation does not determine whether the concrete remains saturated when freezing occurs. As shown previously [19, 20, 25], the DOS is influenced by several weather variables, and the relationship between concrete and DOS is complex.

Similarly, the freezing index represents an index of the temperature below freezing, but it does not capture the temperature fluctuations around 0 °C that define individual freeze–thaw cycles. Moreover, previous studies have shown that freezing does not always occur exactly at 0°C; concrete with higher DOS freezes at higher temperatures than concrete with lower DOS [19]. As a result, the LTPP classification does not specify how many damaging freeze–thaw cycles occur annually, how severe they are, or how much they vary from year to year.

The maps developed in this study overcome these limitations by using a model trained and validated with field measurements to predict both total and damaging freeze–thaw cycles for specific locations. These maps directly incorporate the effects of temperature and DOS to provide a more realistic assessment of freeze–thaw exposure. Figure 7 overlays the LTPP

climate zones [47], with the 24-year average damaging freeze–thaw cycle map developed in this study for easy comparison. While the general distribution of the Wet–Freeze, Wet–No-Freeze, and Dry–No-Freeze regions align with the LTPP zones, notable differences appear within the Dry–Freeze region. States such as North Dakota, Nebraska, Idaho, Colorado, and Kansas exhibit measurable damaging cycles, indicating that these areas are not as dry as suggested by the LTPP classification. This highlights the need for long-term, location-specific analysis when evaluating freeze–thaw durability.

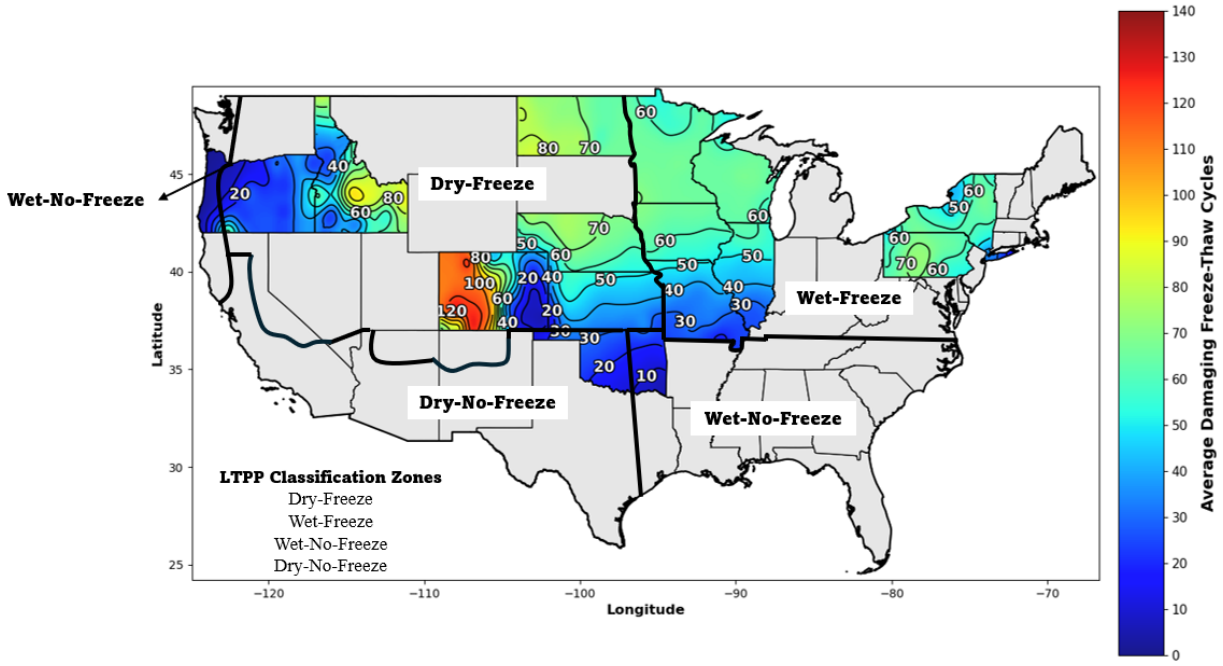

Figure 7: Overlay of LTPP climate zones with the 24-year average damaging freeze–thaw cycles.

3.4.2 ASHRAE 90.1 Climate Zone Map

The ASHRAE 90.1 Standard [48] divides the United States into eight primary climate zones, with further subdivisions based on moisture regime (moist, dry, or marine) (Figure 8). These zones are defined using long-term heating and cooling degree days together with humidity indices and are primarily intended to guide building energy performance and envelope design. In this system, dry (B) zones represent areas with low annual precipitation, humid (A) zones correspond to regions with higher precipitation and significant seasonal humidity, and marine (C) zones are coastal regions with moderate temperatures, high humidity, and mild summers [48].

Figure 9 shows the ASHRAE climate zone boundaries overlaid on the 24-year average damaging freeze–thaw cycle map developed in this study. Although the ASHRAE map was not designed for concrete durability, it shows a noticeable resemblance to the spatial patterns of damaging freeze–thaw cycles. For example, regions classified as moist (A), including Minnesota, North Dakota, Wisconsin, Iowa, Nebraska, and the northern portions of Illinois and Missouri, generally correspond to areas with a higher number of damaging freeze–thaw cycles > 50 for this work. Similarly, the central and southern parts of Illinois and Missouri show fewer damaging cycles (30-40 cycles), aligning with the transitional mixed classification in the ASHRAE map. In addition, the dry (B) regions in the ASHRAE map, such as western Idaho, eastern Colorado, and eastern Oregon, exhibit relatively low damaging freeze–thaw cycles in our map (up to 20 cycles). The marine (C) zones along the Pacific Coast also display limited freezing, consistent with our observations from the western Oregon site [48].

This comparison suggests that both systems reflect similar climatic trends, but the ASHRAE framework does not account for concrete DOS or the actual number of damaging freeze–thaw cycles, which are critical for assessing material durability. Overall, the ASHRAE classification and the maps in this study share some broad climate-driven similarities (e.g., distinguishing dry and wet regions), but only the field-calibrated, DOS-based approach presented here provides an accurate representation of damaging freeze–thaw exposure relevant to concrete durability.

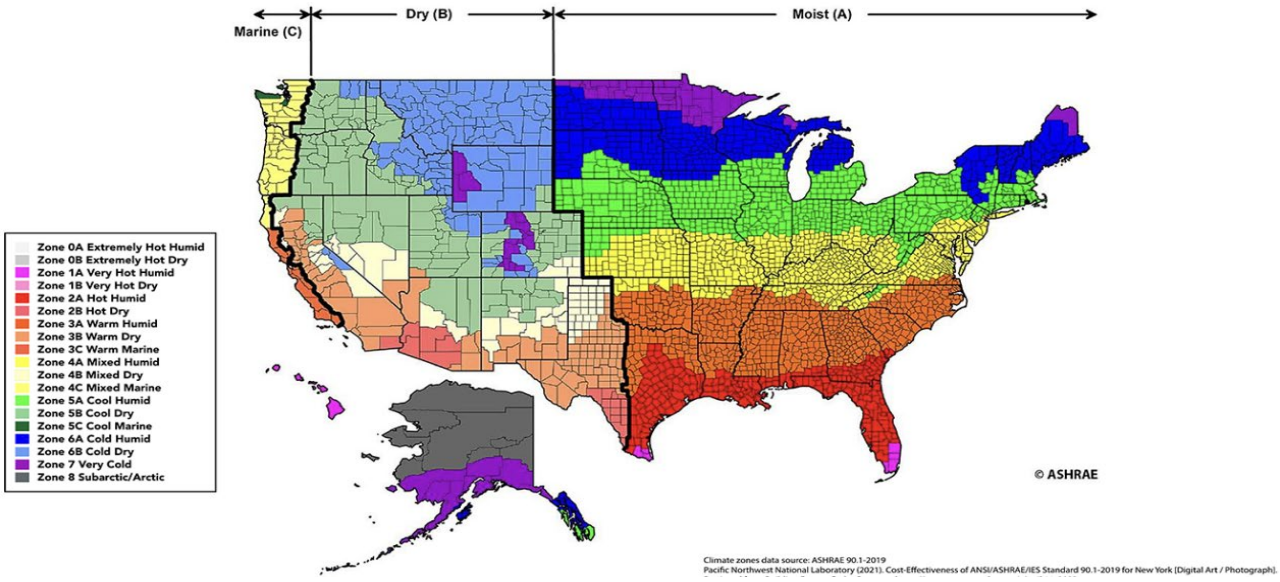

Figure 8: ASHRAE 90.1 climate zone map for the United States (adapted from ASHRAE 90.1-2016 [48]).

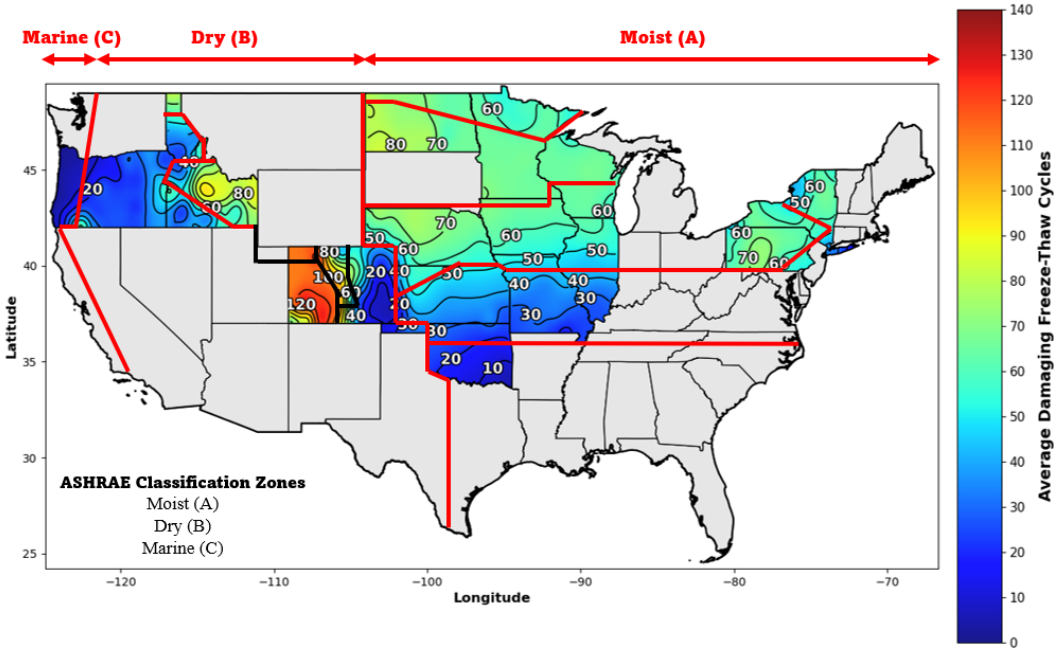

Figure 9: ASHRAE climate zone boundaries overlaid on the 24-year average damaging freeze–thaw cycle map developed in this study.

4. Practical Implications

This research introduces a framework that develops maps of long-term, site-specific damaging freeze–thaw cycles in concrete by using a model trained and validated with field measurements to predict both total and damaging freeze–thaw cycles based on weather data [25]. These maps directly incorporate the effects of local weather conditions and concrete DOS to provide a more realistic assessment of freeze–thaw exposure and durability design. The results show that designing solely on average or assumed regional exposure may overlook areas with high variability or lead to overly conservative designs in regions where the actual risk is low.

Currently, design engineers are responsible for making durability-related decisions about freeze-thaw design, and the maps developed in this work can help them by providing objective, data-driven guidance. For example, ACI 318 [49] uses exposure classes (F0–F3) based on whether concrete is expected to freeze while saturated, but it does not specify how to determine when those conditions occur or how many cycles to design for. As a result, many practitioners rely on conservative assumptions that may not reflect real exposure levels. The maps presented in this study help fill this gap by quantifying damaging freeze–thaw cycles across regions, offering engineers a performance-based and data-driven tool to inform durability design.

It should be noted that in high-variability regions, designing solely based on the average freeze–thaw cycles may be insufficient. A more rational approach can be achieved by incorporating a

safety margin based on the variability of the damaging freeze-thaw cycles. For example, designing for the 95th percentile, assuming a normal distribution, is an approach used in structural reliability-based design. This means the number of damaging freeze-thaw cycles to design for would be to design for the average number of damaging freeze-thaw cycles plus the standard deviation multiplied by 1.65 [51-53]. This approach would account for the years of high and low exposure in the design of the concrete. However, such design guidance is only possible when long-term datasets, such as the 24-year records used for this study.

5. Conclusions

This study developed long-term, data-driven maps of the average total and damaging freeze–thaw cycles across 14 U.S. states using a field-validated model and 24 years of weather data. The work also shows the spatial variation and the difference in the total and damaging freeze-thaw cycles. The following key conclusions can be drawn:

- The presented maps provide engineers with a scalable and validated framework for integrating long-term weather records with field data. This enables location-specific durability design, particularly for specifying air-void systems and other measures to improve concrete resistance to freeze–thaw damage.
- The average difference between the total and damaging freeze–thaw cycles was highest in regions such as eastern Colorado, Oregon, and western Idaho, where the concrete often experienced frequent freezing and thawing but remained below the critical DOS. These areas had lower moisture contents during freezing events, reducing the number of damaging cycles. Conversely, areas in the North, South, and Northeast showed minimal differences, suggesting that their concrete was frequently near or above the critical DOS threshold during freezing periods.
- The highest variation in damaging freeze–thaw cycles was observed in Colorado, Idaho, and Oklahoma, where the standard deviation reached up to ~45 cycles and the COV exceeded 60–70%. These large fluctuations indicate that year-to-year moisture variability significantly impacts the freezing exposure. In contrast, states in the North region, such as Iowa, Wisconsin, and Minnesota, exhibited more consistent patterns with low variability, reflecting more stable winter conditions and moisture behavior across seasons.
- The average number of damaging freeze-thaw cycles determined in this study provides different recommendations than the LTPP framework currently used in pavement design for freeze-thaw exposure. These predictions are different because the maps developed in this work account for the DOS and directly quantify damaging-cycle counts, while the LTPP map relies on average precipitation and the temperature of the days below freezing.

Overall, the maps presented in this study incorporate long-term, site-specific data and account for both regional and intra-state variability, offering a more reliable and practical foundation for freeze–thaw durability design.

References

[1] M. Kosior-Kazberuk, W. Jezierski, Surface scaling resistance of concrete modified with bituminous addition, J. Civ. Eng. Manag. 10 (1) (2004) 25–30.

[2] S. Jacobsen, Calculating liquid transport into high-performance concrete during wet freeze/thaw, Cem. Concr. Res. 35 (2) (2005) 213–219.

[3] Guo, J., Chen, X., Zhang, J., & Sun, W. (2022). Damage mechanism and modeling of concrete in freeze–thaw cycles: A review. *Buildings, 12*(9), 1317.

[4] Trofimov, B. Y., Kramar, L. Y., & Schuldyakov, K. V. (2017). On deterioration mechanism of concrete exposed to freeze–thaw cycles. *IOP Conference Series: Materials Science and Engineering, 262*(1), 012024.

[5] J.J. Beaudoin, C. MacInnis, The mechanism of frost damage in hardened cement paste, Cem. Concr. Res. 4 (2) (1974) 139–147.

[6] Bentz, D. P., Ehlen, M. A., Ferraris, C. F., & Garboczi, E. J. (2001, September). Sorptivity-based service life predictions for concrete pavements. In Proceedings of the 7th International Conference on Concrete pavements (Vol. 1, pp. 181-193).

[7] L. Sutter, T. Van Dam, K.R. Peterson, D.P. Johnston, Long-term effects of magnesium chloride and other concentrated salt solutions on pavement and structural Portland cement concrete, Transp. Res. Rec. 1979 (1) (2006) 60–68.

[8] Sun, Z., Kumpf, D., & Scherer, G. W. (2007). Kinetics of ice growth in concrete. Proc. 12th Int. Cong. Cement Chemistry. Paper W4-07.1. Beaudoin, J. J, Makar, J. M., Raki, L. Ed., National Research Council of Canada, Montreal, Canada.

[9] C. Leech, D. Lockington, R.D. Hooton, G. Galloway, G. Cowin, P. Dux, Validation of Mualem's conductivity model and prediction of saturated permeability from sorptivity, ACI Mater. J. 105 (1) (2008) 44.

[10] Pigeon, M., & Pleau, R. (2014). *Durability of Concrete in Cold Climates* (1st ed.). CRC Press.

[11] Ghantous, R. M., Madland, H., Kwong, J., & Weiss, W. J. (2019). Examining the Influence of the Degree of Saturation on Length Change and Freeze–Thaw Damage. *Advances in Civil Engineering Materials*, 8(1), 365–374.

[12] Fagerlund, G. (1977). The critical degree of saturation method of assessing the freeze/thaw resistance of concrete. Materials and Structures, 10(58), 217–229.

[13] M.K. Moradllo, C. Qiao, H. Hall, M.T. Ley, S.R. Reese, W.J. Weiss, Quantifying fluid filling of the air voids in air-entrained concrete using neutron radiography, Cem. Concr. Compos. 104 (2019) 103407.

[14] G. Fagerlund, Critical degrees of saturation at freezing of porous and brittle materials, Lund University, 1973. Doctoral dissertation.

[15] W. Li, M. Pour-Ghaz, J. Castro, J. Weiss, Water absorption and critical degree of saturation relating to freeze-thaw damage in concrete pavement joints, J. Mater. Civ. Eng. 24 (3) (2012) 299–307.

[16] Yu, X., Kim, J. S., & Weiss, J. (2013). Assessment of climate-induced freeze–thaw damage risk for concrete pavements. *Transportation Research Record*, 2342(1), 19–28.

[17] Abdelrahman, B., & Ley, M. T. (2024). The effects of concrete temperature on air void parameters in pumped concrete. *Materials and Structures*, 57(2), 33.

[18] ACI Committee 201. (2016). *Guide to Durable Concrete (ACI 201.2R-16)*. American Concrete Institute.

[19] L. Chen, M. T. Ley, R. M. Ghantous, W. J. Weiss, N. F. Master, Measuring damaging freeze-thaw cycles in the field, Constr. Build. Mater. 387 (2023) 131660.

[20] B. N. Abdelrahman, M. T. Ley, L. Chen, N. F. Materer, J. Simon, and A. Young, *Field-based measurement of freeze–thaw damage in cementitious materials*, manuscript under review.

[21] D.H. Bager, E.J. Sellevold, Ice formation in hardened cement paste, part I—Room temperature cured pastes with variable moisture contents, Cem. Concr. Res. 16 (5) (1986) 709–720.

[22] Y. Farnam, H. Todak, R. Spragg, J. Weiss, Electrical response of mortar with different degrees of saturation and deicing salt solutions during freezing and thawing, Cem. Concr. Compos. 59 (2015) 49–59.

[23] Akita H., Andrade C., Sarría J., Alonso C. (1999). Relative humidity in the interior of concrete exposed to natural and artificial weathering. Cement and Concrete Research, 29(8): 1249–1259.

[24] Liu P., Song L. et al. (2016). *Quantitative moisture model of interior concrete in structures exposed to natural weather*. Construction and Building Materials, 102: 76–83.

[25] B. N. Abdelrahman, M. T. Ley, G. Fan, and L. Chen, *Predicting concrete freeze–thaw damage with weather data-based machine learning*, manuscript under review.

[26] Entekhabi, D., et al. (2010). The Soil Moisture Active Passive (SMAP) mission. Proceedings of the IEEE, 98(5), 704–716.

[27] Mohanty, B.P., Skaggs, T.H., Famiglietti, J.S. (2000). Analysis and mapping of field-scale soil moisture variability using high-resolution ground-based data during the SGP97 Hydrology Experiment. Water Resources Research, 36(4), 1023–1031.

[28] Pan, M., Cai, X., Chaney, N.W., Wood, E.F. (2016). An initial assessment of SMAP soil moisture retrievals using high-resolution in situ and modeled data. Geophysical Research Letters, 43(18), 9662–9668.

[29] Vereecken, H., Huisman, J.A., Bogena, H., Vanderborght, J., Vrugt, J.A., Hopmans, J.W. (2008). On the value of soil moisture measurements in vadose zone hydrology: A review. Water Resources Research, 44(12).

[30] Chawla, N. V., Bowyer, K. W., Hall, L. O., & Kegelmeyer, W. P. (2002). SMOTE: Synthetic minority over-sampling technique. Journal of Artificial Intelligence Research, 16, 321–357.

[31] Fernández, A., García, S., Galar, M., Prati, R. C., Krawczyk, B., & Herrera, F. (2018). Learning from imbalanced data sets. Springer.

[32] García, S., Fernández, A., Luengo, J., & Herrera, F. (2015). Advanced nonparametric tests for multiple comparisons in the design of experiments in machine learning research. Information Sciences, 180(10), 2044–2064.

[33] Haupt, R. L., & Haupt, S. E. (2004). Practical Genetic Algorithms (2nd ed.). Wiley.

[34] Deb, K. (2000). An efficient constraint handling method for genetic algorithms. *Computer Methods in Applied Mechanics and Engineering*, 186(2–4), 311–338.

[35] Holland, J. H. (1975). Adaptation in Natural and Artificial Systems. University of Michigan Press.

[36] Open-Meteo. (2024). *Free Weather API for non-commercial use*. Retrieved from https://open-meteo.com/.

[37] Burrough, P. A., & McDonnell, R. A. (1998). *Principles of Geographical Information Systems*. Oxford University Press.

[38] Li, J., & Heap, A. D. (2014). *A review of spatial interpolation methods for environmental scientists*. Geoscience Australia, Record 2014/23, Canberra, Australia.

[39] Shepard, D. (1968). *A two-dimensional interpolation function for irregularly spaced data*. Proceedings of the 1968 ACM National Conference, 517–524.

[40] Huang, T. S., Yang, G. J., & Tang, G. Y. (1979). *A fast two-dimensional median filtering algorithm*. IEEE Transactions on Acoustics, Speech, and Signal Processing, 27(1), 13–18.

[41] Gonzalez, R. C., & Woods, R. E. (2018). *Digital Image Processing* (4th ed.). Pearson.

[42] Wahba, G. (1990). *Spline Models for Observational Data*. SIAM.

[43] Brewer, C. A. (1994). *Guidelines for use of the perceptual dimensions of color for mapping and visualization*. In A. M. MacEachren & D. R. F. Taylor (Eds.), Visualization in Modern Cartography (pp. 123–147). Pergamon.

[44] Slocum, T. A., McMaster, R. B., Kessler, F. C., & Howard, H. H. (2009). *Thematic Cartography and Geovisualization* (3rd ed.). Pearson Prentice Hall.

[45] Brewer, C. A., Hatchard, G. W., & Harrower, M. A. (2003). *ColorBrewer in print: A catalog of color schemes for maps*. Cartography and Geographic Information Science, 30(1), 5–32.

[46] Federal Highway Administration. (2013). *Long-Term Pavement Performance Climate Region Classification*. FHWA-HRT-13-062, Washington, D.C.

[47] Federal Highway Administration. (2015). *Evaluation of LTPP Climatic Data for Use in Mechanistic-Empirical Pavement Design Guide (MEPDG) Calibration and Other Pavement Analysis*. FHWA-HRT-15-019, Washington, D.C.

[48] ASHRAE. *ANSI/ASHRAE/IES Standard 90.1-2016: Energy Standard for Buildings Except Low-Rise Residential Buildings.* American Society of Heating, Refrigerating and Air-Conditioning Engineers, Atlanta, GA, 2016

[49] ACI Committee 318. (2019). *Building Code Requirements for Structural Concrete (ACI 318-19) and Commentary (ACI 318R-19)*. American Concrete Institute.

[50] ASTM C33 / C33M-18, *Standard Specification for Concrete Aggregates*. ASTM International, West Conshohocken, PA, 2018.

[51] Jin, W.-L., Ye, Q., & Bai, Y. (2025). *Structural Reliability in Civil Engineering*. Wiley.

[52] Ang, A. H-S., & Tang, W. H. (2007). *Probability, Statistics, and Decision for Civil Engineers* (2nd ed.). Cengage Learning.

[53] Bazant, Z.P., Najjar, L.J. (1972). "Nonlinear water diffusion in nonsaturated concrete." Materials and Structures.

Appendices

Appendix A: Regional Classification Used for Predicting Freeze–Thaw Cycles

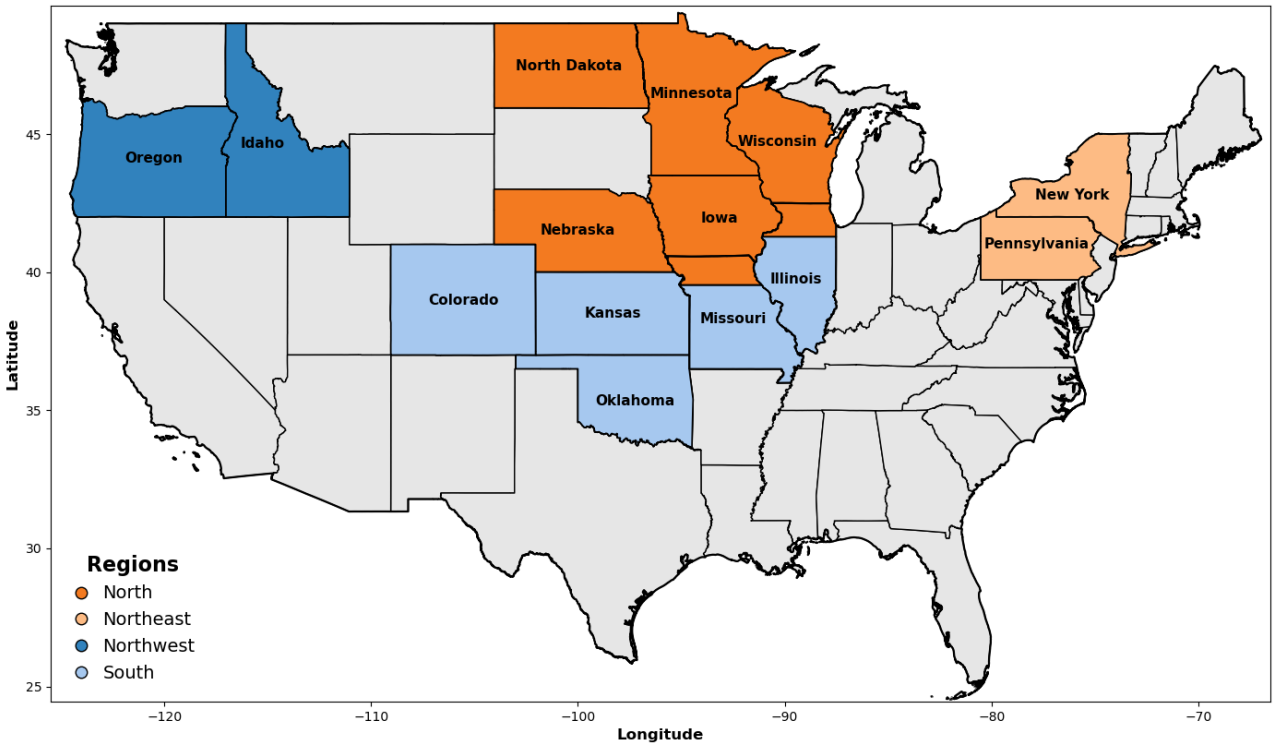

Figure 2: Regional classification used for freeze–thaw cycle prediction, showing the four regions applied to weather stations (adapted from [25]).

Appendix B: Freezing Temperature Thresholds for DOS Categories

Figure B1 shows how freezing temperature thresholds were assigned for each DOS category using the DOS–freezing temperature relationship, where higher DOS levels require warmer temperatures to freeze and cause damage. They were also verified in the previous study [25]] to have the best match between predicted and measured freeze–thaw cycles. For instance, the DOS < 80% category corresponded to a freezing range of approximately –3.9°C to –4.9°C. Several values within this interval were tested to evaluate prediction accuracy, and a threshold of –4.0°C provided the closest match between predicted and observed freeze–thaw cycles [25]. This same process was repeated for the remaining DOS categories to identify the most representative freezing temperatures. The final set of thresholds, summarized in Table B1, produced cycle predictions that closely agreed with measured values across multiple locations. These results confirmed that the selected thresholds gave the most reliable estimation of freeze–thaw cycles, as further discussed in the results section [25].

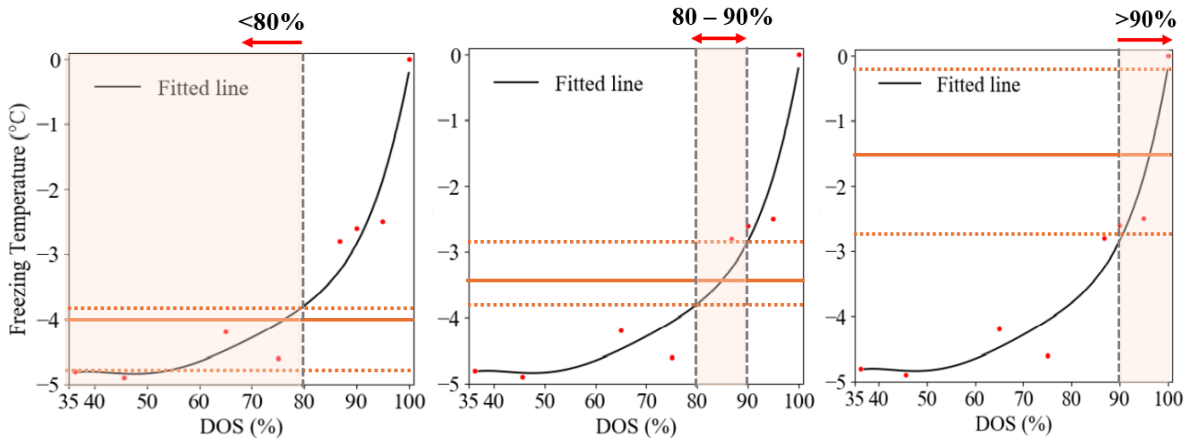

Figure B1: Freezing temperature ranges associated with each DOS category, derived from the DOS vs. freezing temperature relationship (adapted from [9]): a) <80%, b) 80–90%, and c) >90%.

Table B1

Selected Freezing Temperatures Assigned to Each DOS Category.

DOS Category	Freezing Temperature (°C)
<80%	-4.0°C
80–90%	-3.5°C
>90%	-1.5°C

A freeze event was defined as any period during which the air temperature dropped to or below the assigned freezing threshold, while a thaw event occurred when the temperature rose to or above 0 °C. A complete freeze–thaw cycle was therefore identified as the progression from a freezing event to a subsequent thawing event.

Appendix C: Variability Analysis and Coefficient of Variation Maps for Freeze–Thaw Cycles

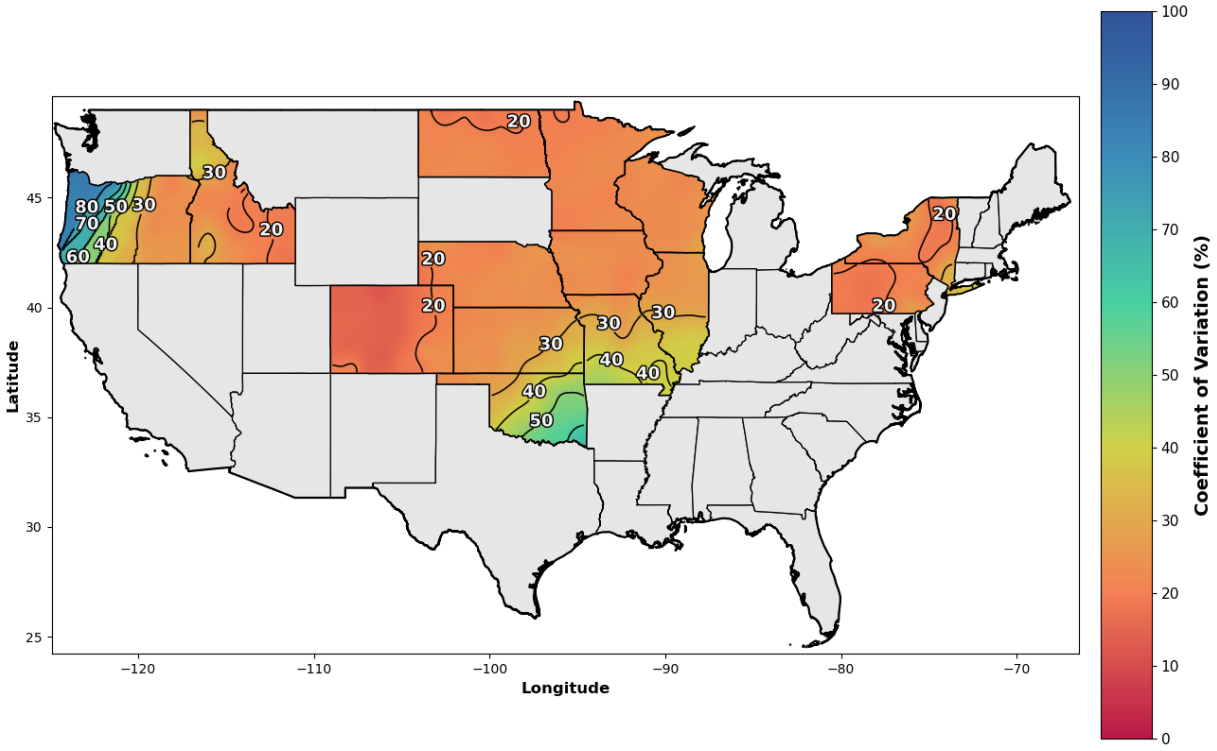

(a)

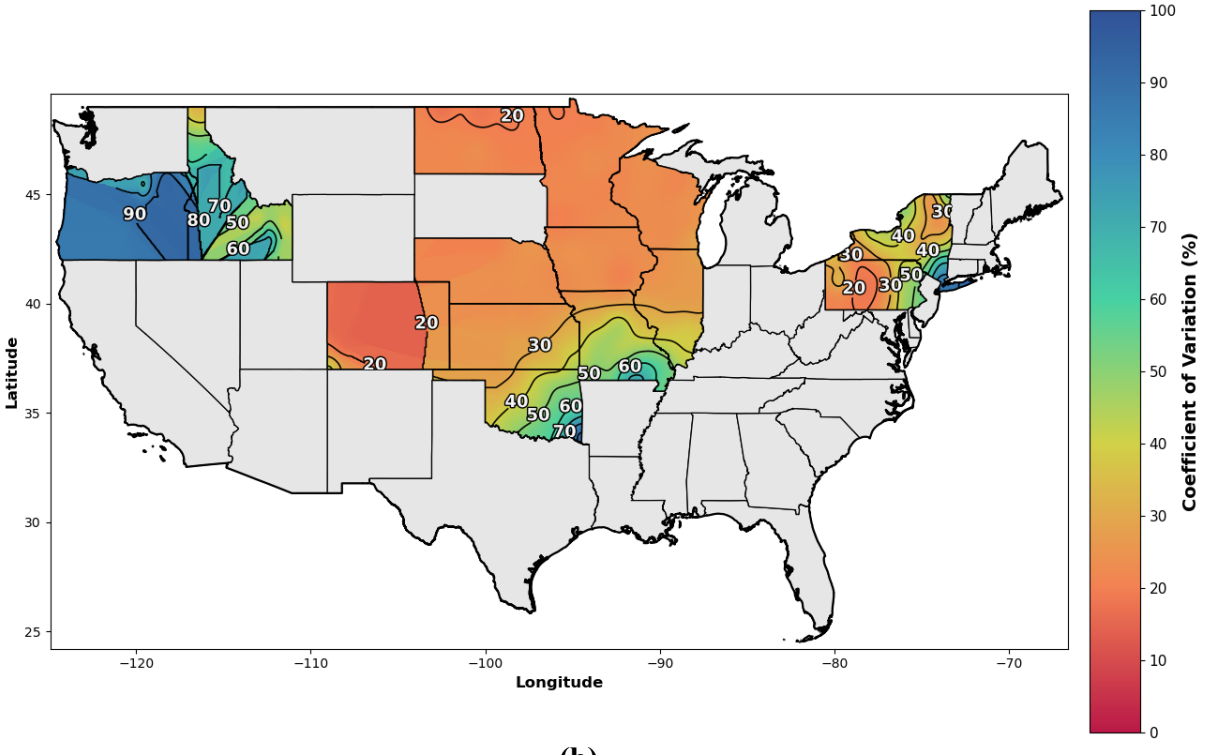

(b)

Figure C1: 24-Year coefficient of variation of predicted freeze–thaw cycles at all weather stations: (a) total freeze–thaw cycles, (b) damaging freeze–thaw cycles.

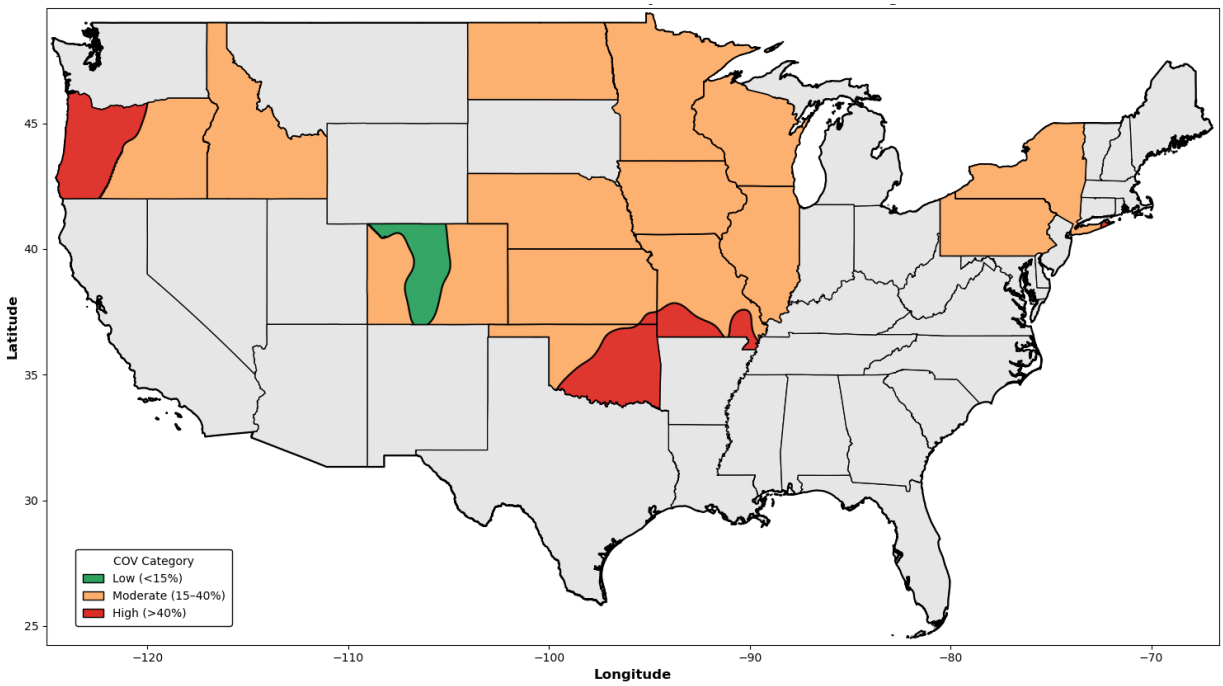

Figure C2: 24-Year spatial categories of CV (%) of predicted total freeze–thaw cycles at all weather stations.

The Effects of Concrete Temperature on Air Void Parameters in Pumped Concrete

Bahaa N. Abdelrahman [1*], and M. Tyler Ley [1]

[1]School of Civil & Environmental Engineering, Oklahoma State University, Stillwater, 74078, Oklahoma, United Stated

*Corresponding author, E-mail: Bahaa.abdelrahman@okstate.edu

Contributing author: tyler.ley@okstate.edu

Abstract

This study investigates the effects of concrete pumping on air content, SAM Number, spacing factor, and freeze-thaw performance. This work focuses on how the air dissolves under pressure and then returns to the concrete at room (30°C/86°F), cold (8°C/46°F), and hot (40°C/104°F) temperatures. The research reveals that concrete pumping leads to a significant reduction in air content, with cold mixtures experiencing higher air loss compared to room temperature and hot mixtures. Despite these changes, freeze-thaw performance remains satisfactory for mixtures with initial air content above 4% and SAM Number below 0.32. The study also observes that the dissolved air bubbles return to the concrete with a similar bubble distribution as was in the original mixture.

Keywords: Air entrainment; air void system; pumping concrete; Super Air Meter; SAM Number; freeze-thaw resistance

1. INTRODUCTION

Concrete pumping is a widely used placement method because of its efficiency, versatility, and reduction in labor [1, 2]. Despite the wide use of pumping, concerns have been raised regarding the impact of pumping on the air void system of fresh concrete [1, 3-6]. This is important in cold regions where air voids play an important role in preventing freeze-thaw damage and ensuring the durability of concrete structures [3, 7-10]. Consequently, to address this concern, specifiers in freeze-thaw environments often mandate measuring the air volume after pumping to ensure that the concrete at placement meets the required air volume specification. Because pumping changes the air volume in an unpredictable manner, this makes it challenging to meet the specified range. This causes issues in practice.

While measuring the air volume in fresh concrete is common in practice, more recent work shows that freeze-thaw durability is ensured by providing a high-quality air void system. Recent research shows that this is done if then the air content in the fresh concrete is at least 4.0% [1, 3, 5, 7] and the Sequential Air Method (SAM) Number is lower than 0.32 [3, 5, 7, 11]. These recommendations are currently used in the AASHTO R101 document for field concrete [12].

Previous research has studied pumping air-entrained concrete, and it has been found that the pressure during pumping caused the dissolution of smaller air bubbles [1, 5, 13, 14]. Several studies have shown that concrete pumping can generate pressures ranging from 2000 to 3500

kPa [11, 13]. Lab and field measurements show that these pressures regularly decrease the air content between 0.5% to 3%, occasionally observing larger losses, and at times even increases in the air volume [1, 4, 11, 13, 15]. This research has gone on to show that the dissolved air bubbles return to the concrete with a similar bubble distribution as measured by the spacing factor prior to pumping [3, 5, 6, 13]. This observation is also supported by satisfactory freeze-thaw performance, and observations of improved bubble spacing over time as measured by the SAM Number.

Others have suggested that the air is knocked out of the concrete by impacting a surface such as a 90-degree elbow during pumping [16]. However, previous work has shown by testing concrete in several different places along the pumping line that the air is lost immediately after pumping and that there is no change in air after a 90-degree elbow [5].

While previous studies have focused on analyzing the air void systems and rheological properties of concrete during pumping [4-6, 13, 15, 20, 21], these studies examined the concrete at ambient temperature or uncontrolled temperatures in the field. This work creates air-entrained concrete mixtures at different temperatures and measures how pumping changes the air volume and the ability of the air to return to the fresh concrete before it has hardened.

2. EXPERIMENTAL METHODS

2.1. Constituent Materials

All concrete mixtures used a type I cement that adhered to ASTM C150 standards [22]. Table 1 presents the oxide analysis and Bogue calculations. The aggregates consisted of locally available crushed limestone and natural sand typically utilized in commercial concrete applications. The crushed limestone featured a maximum nominal aggregate size of 19 mm (3/4 inch), and the natural sand is characterized by a fineness modulus of 2.68. Each mixture incorporated a blend of both coarse and intermediate aggregates. Both the crushed limestone and sand met the specifications outlined in ASTM C33 [23] and are known for good performance in freeze-thaw conditions. The absorption capacity for crushed limestone and sand are 0.66% and 0.55%, respectively. All admixtures used in this study adhered to the requirements outlined in ASTM C260 and ASTM C494 [24, 25]. Various doses of air-entraining admixture were used to create concrete with air contents from 4% to 10%. It's important to note that one cooled mixture and one heated mixture intentionally did not contain AEA. This was done to examine the performance of concrete with a poor air void distribution. A water reducer was used at a constant dosage of 467 mL/100 kg (7 oz./cwt). This was done to get at least a 15 cm (6 in.) slump in the concrete mixture. Additionally, citric acid was added at 0.25% of the cementitious material's weight. Citric acid was used to delay the set time of the concrete to ensure that the concrete did not stiffen over120 minutes, which was needed for pumping and sampling the fresh concrete. This intentional delay in setting time was helpful to isolate any change in air void system from stiffening from concrete hydration. Previous research with these same materials and equipment showed no impact of citric acid on the performance of pumped air-entrained concrete [5].

Table 1
Type I Cement Oxide Analysis.

Oxide (%)	SiO_2	Al_2O_3	Fe_2O_3	CaO	MgO	SO_3	Na_2O	K_2O	TiO_2	P_2O_5	C_3S	C_2S	C_3A	C_4AF
Cement	21.1	4.7	2.6	62.1	2.4	3.2	0.2	0.3	-	-	56.7	17.8	8.2	7.8
Fly Ash	38.7	18.8	5.8	23.1	5.6	1.2	1.8	0.6	1.5	0.4	-	-	-	-

2.2. Mix Proportions

2.2.1. Concrete Mixtures

The mixtures used 362.5 kg/m^3 (611 lbs./yd^3) of cementitious material, with a 20% mass replacement of fly ash and water to the cementitious material ratio (w/cm) of 0.45. The paste content of each mixture was 28.9%, excluding air content from the calculation. Slight adjustments were made to the aggregate proportions in each mixture, aiming to maintain a consistent aggregate gradation between mixtures. This approach was guided by the Tarantula Curve, an aggregate gradation strategy known to enhance concrete pumpability [26]. Table 2 presents the mixture design employed in this study.

Table 2
Concrete Mixture Summary.

Cement (kg/m^3)	Fly Ash (kg/m^3)	Water (kg/m^3)	Coarse (SSD kg/m^3)	Intermediate Coarse (SSD kg/m^3)	Fine (SSD kg/m^3)	Paste Content
290	72	163	660	328	886	28.9%

2.2.2. Grout Mixtures

Before each laboratory pumping session, the pump and pipe network underwent a priming process using grout. Priming involved applying a thin lubricating layer of grout to the inner walls of the pump and pipe network. The grout mixture used a w/cm of 0.40. The mixture is outlined in Table 3.

Table 3
Grout Mixture Summary.

Cement (kg/m^3)	Water (kg/m^3)	Fine (SSD kg/m^3)
597	238.5	1491.5

2.3. Mixing Procedure

2.3.1. Grout Mixtures

Fine aggregates were loaded into the mixer, accompanied by approximately two-thirds of the mixing water. A mixing duration of at least three minutes ensured thorough blending. Subsequently, the binder and the remaining water were mixed for three minutes. Following a two-minute rest period, during which the sides of the mixing drum were scraped, mixing was resumed for an additional three minutes.

2.3.2. Concrete Mixtures

Aggregates were brought from outside stockpiles and placed in a temperature-controlled environment at (25°C/77°F) for at least 24 hours before mixing. Aggregates were added into a mixing drum and spun for a minimum duration of three minutes. To account for moisture content, a representative sample was utilized for moisture content testing and subsequent moisture correction. To simulate different temperatures, some concrete mixtures were either heated or cooled prior to mixing. For these mixtures, the aggregate and water were either heated to (63°C/ 145°F) or cooled to (1.7°C/35°F) prior to mixing. The average concrete temperature was (40°C/104°F) for the heated mixtures, (8°C/46°F) for cooled mixtures, and (30°C/86°F) for the mixtures near room temperature. This paper will refer to (40°C/104°F) as

the “hot mixtures” and (8°C/46°F) as the “cold mixtures”. These temperatures were chosen because they represent the extremes of temperatures that may be used in the field.

During the mixing phase, all aggregates and approximately two-thirds of the required mixing water were loaded into the mixer. This blend was mixed for three minutes to ensure uniform distribution of aggregates and saturation of their surfaces. Subsequently, the cement, fly ash, and remaining water were added and mixed for three minutes. After a two-minute resting period, the sides of the mixing drum were scraped, admixtures were introduced, and the mixing process continued for an additional three minutes.

Care was taken to ensure that the heated and cooled aggregate did not lose water prior to mixing. All storage containers for the aggregate had tight-fitting O-rings, and the weight of the container was compared before and after either heating or cooling to ensure that there was no moisture loss. For the cold mixtures, ice was added to the mixer prior to adding the aggregates to cool the mixer. The ice was 0.25% by weight of the water in the mixture. The equivalent amount of water was withheld from the mixture to ensure an accurate w/cm.

2.4. Equipment and Pipe Configuration

2.4.1. Concrete Pump

The Putzmeister TK 50 concrete pump shown in Fig. 1 was used for testing. This pump operates through two alternating pistons, ensuring an almost continuous concrete flow. As one piston retracts, it draws concrete from the hopper, while the second piston extends to push concrete out. An S-valve alternating delivery system facilitates the shift between delivery cylinders, ensuring a consistent concrete supply. To maintain the concrete's homogeneity, a remixer continuously agitates the concrete within the hopper. The pump settings were 1500 RPM, with the piston volume set at 0.016 m^3 (0.57 ft^3). Both of these parameters were used in previous research and so they were repeated in this work [26].

Fig. 1. The Putzmeister TK 50 Concrete Pump.

2.4.2. Pipe Configurations

The laboratory testing employed a standard pipe network configuration, as shown in Fig. 2. This network used a 0.102 m (4.0 in.) inner diameter (I.D.) single-wall steel pipe. The connection of pipe sections was secured through rubber gaskets and couplings. The pipe

network encompassed a 1 m (3.3 ft.) long single-wall steel pipe reducer, which reduced the pump output from 0.127 m (5.0 in.) I.D. to 0.102 m (4.0 in.). Following the reducer, a 16 m (52.5 ft.) length of 0.102 m (4.0 in.) I.D. steel pipe was incorporated, featuring three 0.457 m (1.5 ft.) radius 90° bends. Concluding the steel pipe network, a flexible rubber hose directed the concrete back to the pump's hopper, creating a continuous flow. The cumulative volume of the pipe network was approximately 0.17 m^3 (6.0 ft^3).

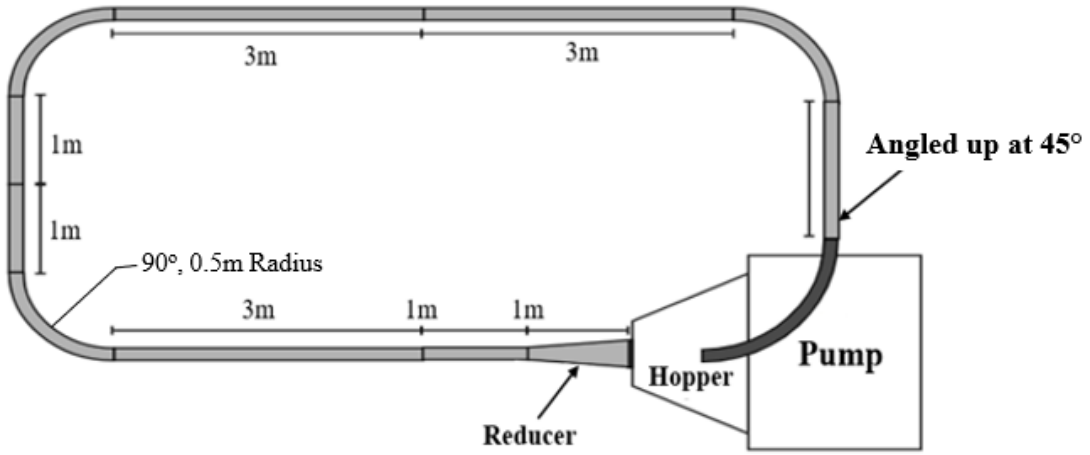

Fig. 2. Pipe Network Configuration.

2.5. Pumping Procedure

The grout was added to the pump, and a few piston strokes were used to add the grout to the pipe. Next, concrete was added to ensure that the hopper remained constantly filled to prevent introducing air into the line. Concrete was added to the pump's hopper, and additional pump strokes were used to push concrete through the pipes. This process persisted until all the mortar was expelled from the flexible rubber hose. The rubber hose was secured to the pump's hopper to redirect the concrete back into the pump. This established a seamless and uninterrupted flow, allowing us to complete a single cycle of concrete pumping.

Once a continuous flow was completed, the rubber hose was detached from the pump's hopper and was used to fill five wheelbarrows with concrete. Wet burlap sheets were carefully draped over the concrete in the wheelbarrows to minimize temperature and moisture loss. One wheelbarrow was tested immediately after pumping, and the other four were tested approximately every 25 minutes. This allowed the change in the fresh properties of the concrete to be measured before and after pumping and regularly over time until about 120 minutes after the concrete was pumped. Fig. 3 illustrates the pumping procedure employed in this study. The tests and timing used are outlined in Table 4.

The following tests were used to evaluate the concrete: Slump (ASTM C143), Unit Weight (ASTM C138), SAM (AASHTO T 395), Freeze-Thaw Resistance (ASTM C666), and Hardened Air Void Analysis (ASTM C457). The SAM was used to measure the air volume and the SAM Number. The slump, unit weight, air volume, and SAM Number were measured at each time- period. Freeze-Thaw Resistance and Hardened Air Void Analysis were run before pumping, immediately after pumping, and 120 minutes after pumping. The number and timing of the tests are outlined in Table 4.

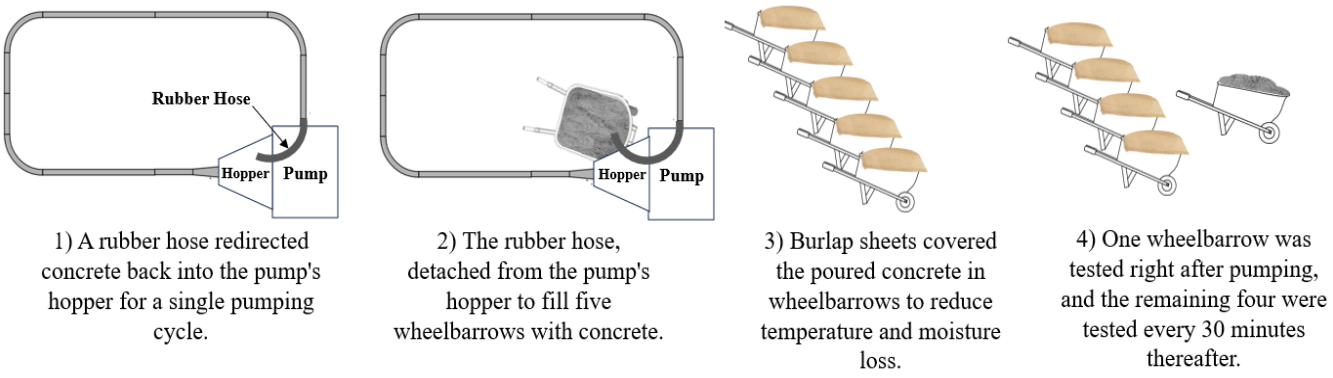

1) A rubber hose redirected concrete back into the pump's hopper for a single pumping cycle.

2) The rubber hose, detached from the pump's hopper to fill five wheelbarrows with concrete.

3) Burlap sheets covered the poured concrete in wheelbarrows to reduce temperature and moisture loss.

4) One wheelbarrow was tested right after pumping, and the remaining four were tested every 30 minutes thereafter.

Fig. 3. Concrete Pumping and Wheelbarrow Filling Procedure.

Table 4

Number and Timing of Conducted Tests.

Time of the Tests (Minutes)	Conducted Tests	Number of Samples
0 (Before Pumping)	1) Unit Weight (ASTM C138). 2) Air % and Sam Number, Super Air Meter (AASHTO T 395). 3) Slump (ASTM C143). 4) Hardened Air Void Analysis (ASTM C457). 5) Freeze-Thaw Resistance (ASTM C666).	3 3 2 2 3
10 (Immediately after Pumping)	1) Unit Weight (ASTM C138). 2) Air % and Sam Number, Super Air Meter (AASHTO T 395). 3) Slump (ASTM C143). 4) Hardened Air Void Analysis (ASTM C457). 5) Freeze-Thaw Resistance (ASTM C666).	3 3 2 2 3
30	1) Unit Weight (ASTM C138). 2) Air % and Sam Number, Super Air Meter (AASHTO T 395). 3) Slump (ASTM C143).	3 3 2
60	1) Unit Weight (ASTM C138). 2) Air % and Sam Number, Super Air Meter (AASHTO T 395). 3) Slump (ASTM C143).	3 3 2
80	1) Unit Weight (ASTM C138). 2) Air % and Sam Number, Super Air Meter (AASHTO T 395). 3) Slump (ASTM C143).	3 3 2
90	1) Unit Weight (ASTM C138). 2) Air % and Sam Number, Super Air Meter (AASHTO T 395). 3) Slump (ASTM C143).	3 3 2
120	1) Unit Weight (ASTM C138). 2) Air % and Sam Number, Super Air Meter (AASHTO T 395). 3) Slump (ASTM C143). 4) Hardened Air Void Analysis (ASTM C457). 5) Freeze-Thaw Resistance (ASTM C666).	3 3 2 2 3

3. RESULTS and discussion

3.1. Change in Air Volume Before and After Pumping

Table 5 provides a comprehensive overview of the fresh and hardened properties of all concrete mixtures, before and after 120 minutes of pumping. Figs. 4a, 5a, and 6a summarize the changes in air volume before and after the pumping for the concretes of different temperatures and Figs. 4b, 5b, and 6b show the same data that has been normalized by the original air content. The normalized air content represents the percentage obtained by multiplying the ratio of air content measured at a specific time after pumping to the air content measured prior to pumping by 100. The data point at zero minutes represents measurements taken before pumping, while the data at ten minutes corresponds to the first measurement taken after pumping. These times were used to make it easier to visualize the data.

Figs. 4, 5, and 6 show that there is a reduction in air content after pumping with the current materials and equipment, regardless of the temperature of the concrete. The reduction in air content is attributed in other research work to the dissolution of smaller air bubbles from the increased pressures that occur during pumping [1,13,14]. It should be noted that other papers have seen that at least a portion of these air bubbles return to the concrete with a similar spacing as before they were pumped [3, 5, 6, 13]. From these Figures, it can be deduced that after pumping, the air volume decreased by at least 20% of the initial value that was present before pumping. In practical terms, if a concrete mixture initially possessed 6% air content before pumping, it would have an air volume of approximately 5% when measured after passing through the pump, as investigated in other research work [6]. This reduction in air content highlights the impact of the pumping process on air voids within the concrete mixture [5]. Based on the presented figures, it can be concluded that the percentage of air loss remains relatively consistent between room temperature and heated mixtures. Notably, the cold mixtures deviate by exhibiting a significantly higher air loss. This implies that colder concretes may see a larger air loss during pumping.

For example, Table 6 shows that the average air content was similar in all three mixtures at 7.4%, 6.8%, and 5.7%. The loss in air content for the room and hot temperature mixtures were similar at 1.9% and 1.7%, respectively, but the colder mixture lost more air at 2.3%. When comparing the percentage loss of air content between the mixtures, the room and hot temperature mixture lost between 26% and 25% of the original air volume, and the cold mixture lost 40%. This suggests that a cold mixture is expected to lose roughly twice as much air as room temperature or hot mixtures. The standard deviations are included in the table to show the relative difference. To investigate this further, a Student t-test was used, and this was found to be a statistically significant difference in the results, as shown in Table 7. The t-test results indicate that the observed differences in air loss percentage between Room Temperature and Hot mixtures are not statistically significant (t-value < t-critical), suggesting comparable behavior. In contrast, the Cold mixture exhibits a significantly higher air loss percentage compared to both Room Temperature and Hot mixtures (t-value > t-critical for both comparisons), emphasizing the considerable impact of lower temperatures on air loss during pumping.

Fig. 7 shows the relationship between measuring the air content before pumping and measurement in the fresh concrete 120 minutes after pumping. This plot features a line of

equality, indicating that a mixture maintaining the same air content before and after pumping would fall on this line. Moreover, the plot highlights significant changes with 0.7% offset lines, exceeding the threshold of two standard deviations. This implies that the sample falls outside the 95% confidence interval can be considered as statistically different. However, for all mixtures tested at different temperatures, a statistically significant reduction in air content was consistently observed after the pumping process.

From Figs. 4, 5, and 6, we can observe that the air volume does not change significantly up to 120 minutes after pumping. However, it should be noted that the air volume measurement may not be the most discerning indicator to the change in the air void system over time. Also, changes may occur after the 120-minute period.

Table 5

Fresh and Hardened Properties of All Concrete Mixtures at Various Temperatures Before and After 120 Minutes of Pumping.

Temperature (°C)		Fresh Properties				HAV Analysis				666 Beams	
		Air%		SAM #		Air%		Spacing Factor (µm)		Durability Factor (%)	
Before*	After 120 min**	Before	After 120 min	Before	After 120 min	Before	After 120 min	Before	After 120 min	Before	After 120 min
30	25	9.1	6.7	0.15	0.10	10.9	8.8	107	160	NA	NA
30	25	7.9	6.0	0.11	0.13	8.5	5.4	130	226	NA	NA
30	25	6.8	4.7	0.17	0.10	7.4	5.8	157	226	NA	NA
30	25	5.9	4.0	0.16	0.32	6.8	4.1	211	188	100	93
12***	22	3.4	2.0	0.63	0.35	4.4	3.6	333	353	32	16
3	15	5.8	3.4	0.15	0.23	6.5	4.6	178	312	100	96
9	17	5.2	3.0	0.24	0.45	6.0	5.7	231	264	96	100
8	19	6.3	3.3	0.30	0.48	8.1	4.9	178	307	100	98
8	19	5.9	3.4	0.20	0.55	8.7	7.2	160	173	83	96
10	20	5.4	3.8	0.33	0.38	7.4	5.9	239	211	104	96
44***	32	3.8	3.0	0.76	0.49	5.3	3.9	257	335	75	19
39	32	7.7	4.6	0.23	0.17	8.6	6.8	135	229	100	100
38	30	7.8	4.5	0.25	0.19	7.5	4.0	173	245	100	96
39	31	6.1	4.4	0.21	0.29	7.9	5.2	175	252	98	98
38	30	5.7	4.3	0.32	0.26	7.6	12.0	165	99	98	100

* Before: Measurements Taken Before Pumping the Concrete.
** After: Measurements Taken 120 Minutes After Pumping Concrete.
*** Non- Air Entrained Mixtures.

Table 6

Average and Standard Deviation of Fresh Concrete Air Content%.

Mixtures	Average Air% of Fresh Concrete (%)		Average Air loss (%)	Percentage Loss of Air Content After Pumping (%)	Standard Deviation of Fresh Concrete Air Content %	
	Before Pumping	Immediately after Pumping		(Avg Air Loss/Air Before Pumping x 100)	Before Pumping	Immediately after Pumping
Room Temperature	6.9	5.5	1.4	20	0.98	0.78
Hot	6.8	5.1	1.7	25	1.08	0.57

Cold	5.7	3.4	2.3	40	0.45	0.36

Table 7
Statistical Analysis of Air Loss Percentage and Standard Deviation Differences in Concrete Mixtures

Mixtures	**Average % change of Air loss (%)**	**Average % Change of Standard Deviation Difference**	**$t_{critical}$**	**Mixtures**	**t_{Value}**	**Comparison**	**Conclusion**
Room Temperature	26	4.1	± 2.365	Room-Hot	0.243	t-Value < t-critical	Not Significant
Hot	25	8.1	± 2.306	Room-Cold	4.096	t-Value > t-critical	Significant
Cold	40	6.7	± 2.262	Hot-Cold	3.331	t-Value > t-critical	Significant

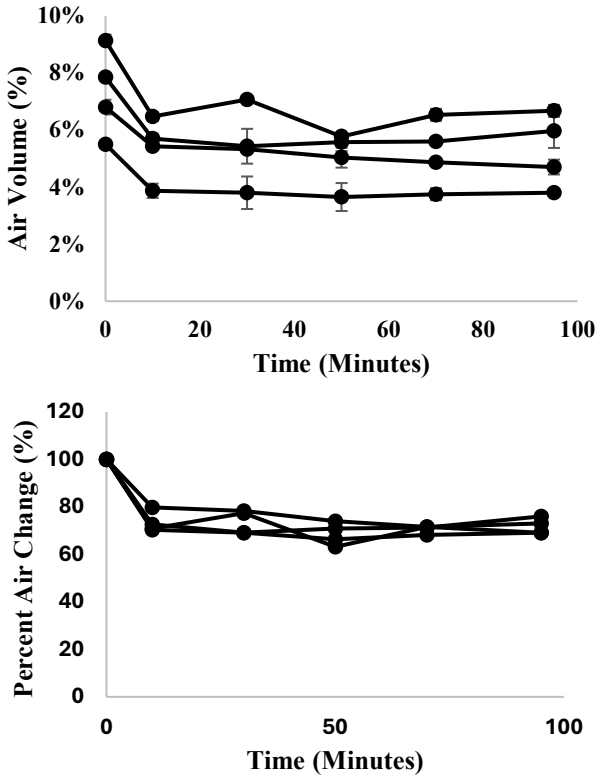

a) Air Content vs. Time. b) Normalized Air Content vs. Time.

Fig. 4. Air Content vs. Time Before and After Pumping of (30°C/86°F) Concrete Mixtures.

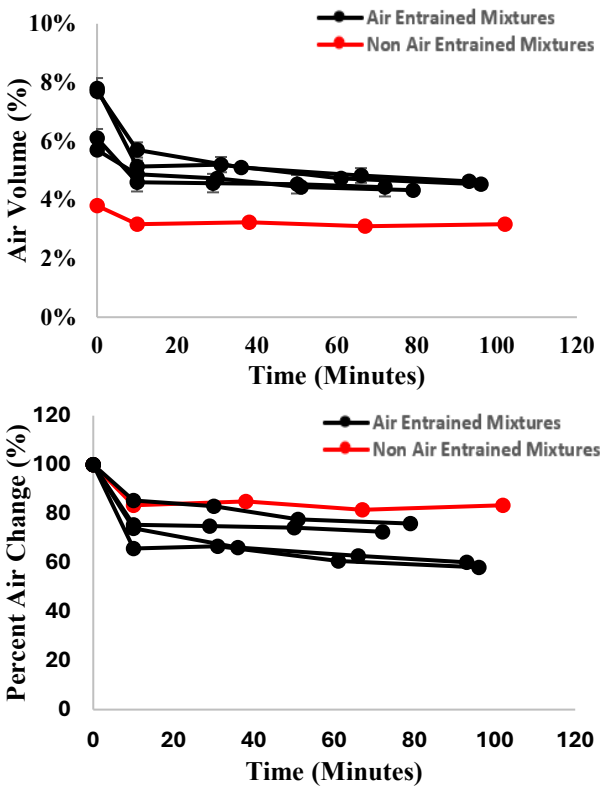

a) Air Content vs. Time. b) Normalized Air Content vs. Time.

Fig. 5. Air Content vs. Time Before and After Pumping of (40°C/104°F) Concrete Mixtures.

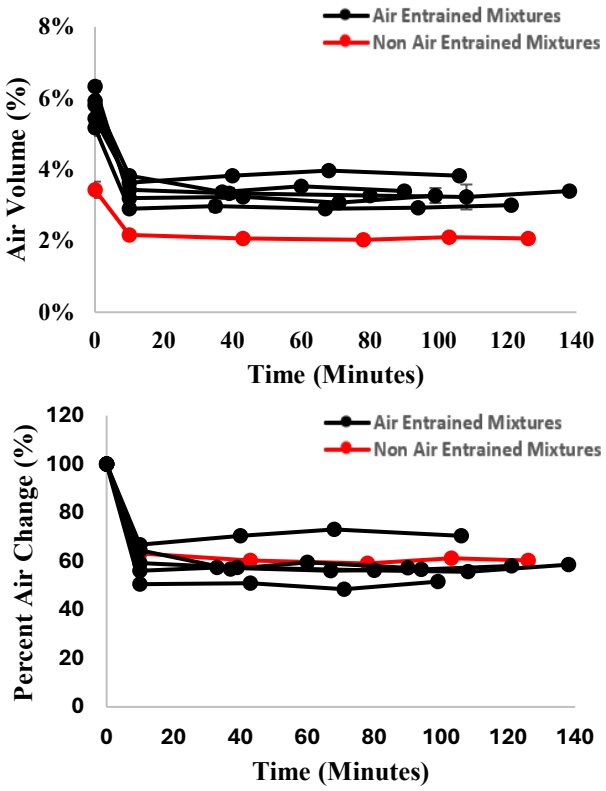

a) Air Content vs. Time. b) Normalized Air Content vs. Time.

Fig. 6. Air Content vs. Time Before and After Pumping of (8°C/46°F) Concrete Mixtures.

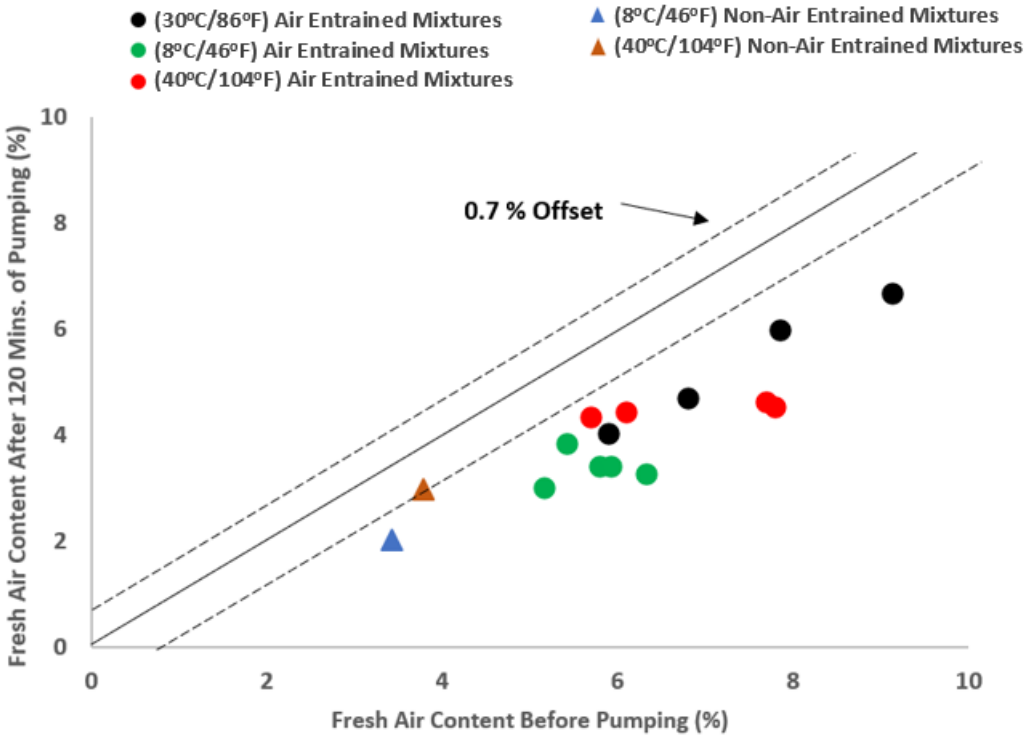

Fig. 7. Plot of Air Content Before Pumping vs. Air Content After Pumping.

3.2. Change in SAM Number Before and After Pumping

Figs. 8a, 9a, and 10a show the change in the SAM Number over time after pumping. The data shows that typically, the SAM Number increases immediately after pumping, followed by a subsequent decrease in the SAM Number with time.

Out of the 13 air-entrained mixtures at three different temperatures, 11 exhibited an increase in the SAM Number immediately after pumping by at least 20% over the SAM Number before pumping. The other two had a SAM Number that increased but not to the same degree. All the air entrained mixtures that showed an increase in the SAM Number also showed a decrease in the SAM Number over time. This decrease in SAM Number suggests that small air voids are returning to the concrete. For the hot and room temperature samples, every air entrained sample that showed an increase in the SAM Number showed a value within 20% of the original value. Recall that the cold samples showed an air volume loss of almost double from pumping over the samples at room temperature and hot samples. The SAM Number for the cold samples increased by almost twice as much as the hot and room temperature samples.

It is interesting to note that 120 minutes after pumping, the SAM Numbers of the hot and room temperature mixtures were close to the original SAM Number. This matches previous data that shows that the small voids lost during pumping are returning to the concrete before the concrete has hardened with a similar air void spacing [3, 5, 6, 13]. However, during the 120 minutes of testing the SAM Numbers of the cold mixtures did not return to the original values. The measurements for the cold mixtures show that the SAM Numbers continue to decrease over time indicating that at the end of the measurement period the small air voids continued to

return to the concrete. This will be discussed in greater detail later with the hardened air void analysis and the freeze thaw-durability testing.

The increase in the SAM Number after pumping and its subsequent decrease over time can be attributed to the temporary dissolution of smaller bubbles during pumping due to increased pressures [5, 6, 11, 13]. After decreasing the pressures from pumping, it appears that the dissolved air voids are re-forming in liquid-filled space. This suggests that the air void system measured immediately after pumping does not accurately represent the characteristics present in the hardened concrete.

An important observation is that the SAM Number seems to be improving without a significant change in the air volume. This may occur because the SAM Number is sensitive to the amount of small bubbles in the concrete while these small bubbles do not have a significant change to the air volume [5, 6].

This difference in the rate of bubbles returning in the cold mixtures could be attributed to a slower rate of gas formation in the low-temperature concrete mixtures compared to room-temperature or high-temperature concrete mixtures [28-32]. However, this lower temperature will increase the set time, which will provide more time for the bubbles to return to the concrete. This could extend past the 120-minute measuring period for fresh concrete used in this study. This will be investigated more with the freeze-thaw and hardened air void analysis.

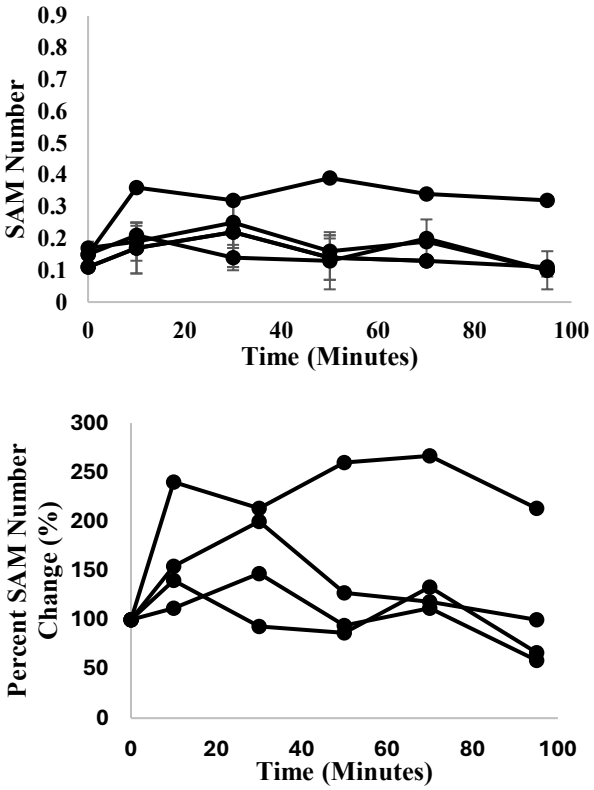

a) SAM Number vs. Time. b) Normalized SAM Number.

Fig. 8. SAM Number vs. Time Before and After Pumping of (30°C/86°F) Concrete Mixtures.

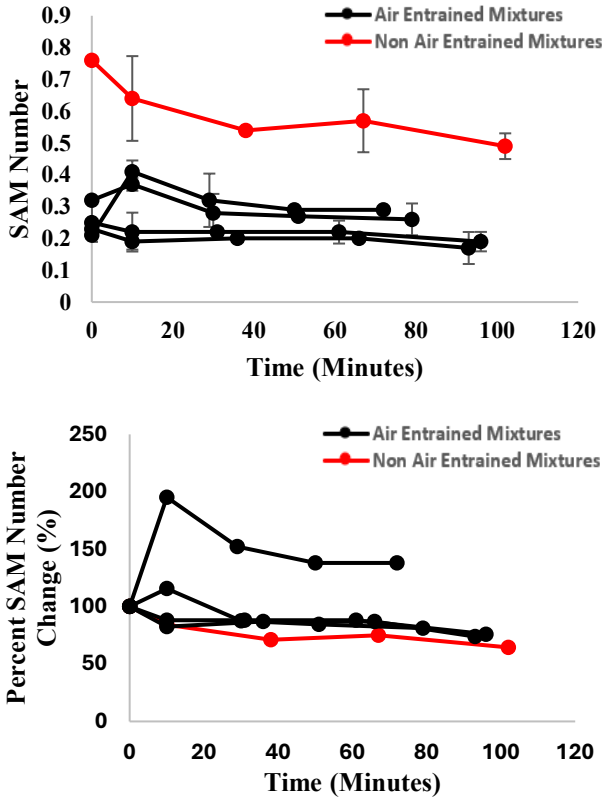

a) SAM Number vs. Time. b) Normalized SAM Number.

Fig. 9. SAM Number vs. Time Before and After Pumping of (40°C/104°F) Concrete Mixtures.

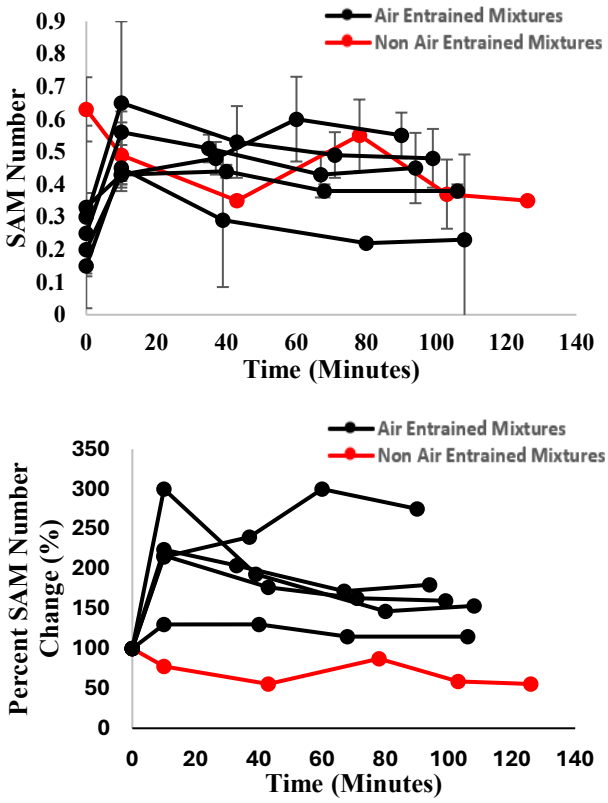

a) SAM Number vs. Time. b) Normalized SAM Number.

Fig. 10. SAM Number vs. Time Before and After Pumping of (8°C/46°F) Concrete Mixtures.

3.3. Freeze Thaw Performance

Fig. 11 illustrates the correlation between the volume of fresh air content and the durability factor. Dashed lines are added at 4% air content and a durability factor of 70%, as these are typical values that have been used with these materials to recommend freeze-thaw durability based on previous work [3, 5, 7]. A data set has been added with light gray dashes. This data uses the same materials from this study to show the performance of air-entrained concrete that was never pumped [3]. These data points highlight that as the air content decreases then so does the durability factor. The filled circles represent the air content measured before pumping, and the opened circles represent the air content measured after pumping. Fig. 11 shows that several measurements measured immediately after pumping had air contents of 4% or lower that showed satisfactory freeze-thaw performance. While this is useful, there are several measurements made of concrete that was not pumped that also showed satisfactory freeze-thaw performance at this air volume.

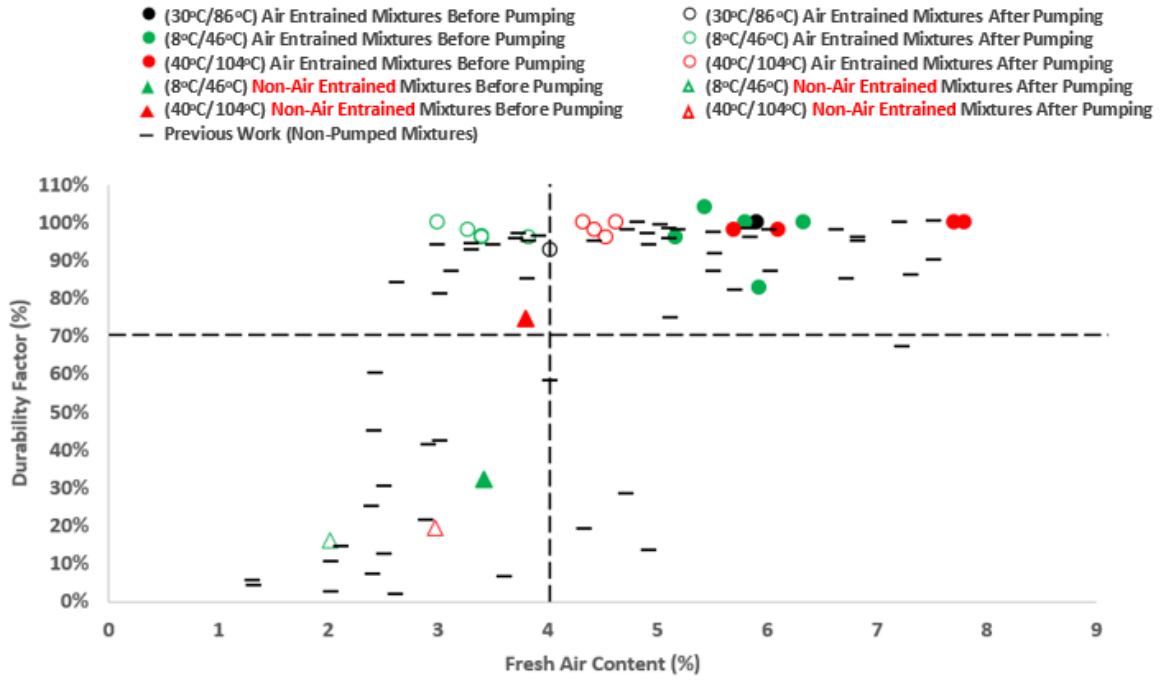

Fig. 11. Plot of Durability Factor vs. Fresh Air Content for Concrete Mixtures at Different Temperatures.

Fig. 12 shows the relationship between the SAM Number and the durability factor from ASTM C 666 testing [33]. The dashed lines show a 0.32 SAM Number and a durability factor of 70%. These are typical values used to recommend freeze-thaw durability based on previous research [3, 5, 7]. A data set has been added with the same materials to show the performance of air entrained concrete that was never pumped [3]. These data points are shown as black dashes. The filled circles represent the SAM Number measured before pumping, and the opened circles represent the SAM Number measured after pumping.

The primary observation in Fig. 12 is that air entrained concrete mixtures with a SAM Number below 0.32 before pumping the concrete showed freeze-thaw resistance in the hardened concrete even if the SAM Number after pumping increased above 0.32. This shows that measurements of the concrete immediately after pumping are not representative of the freeze-thaw performance using recommendations for non-pumped concrete.

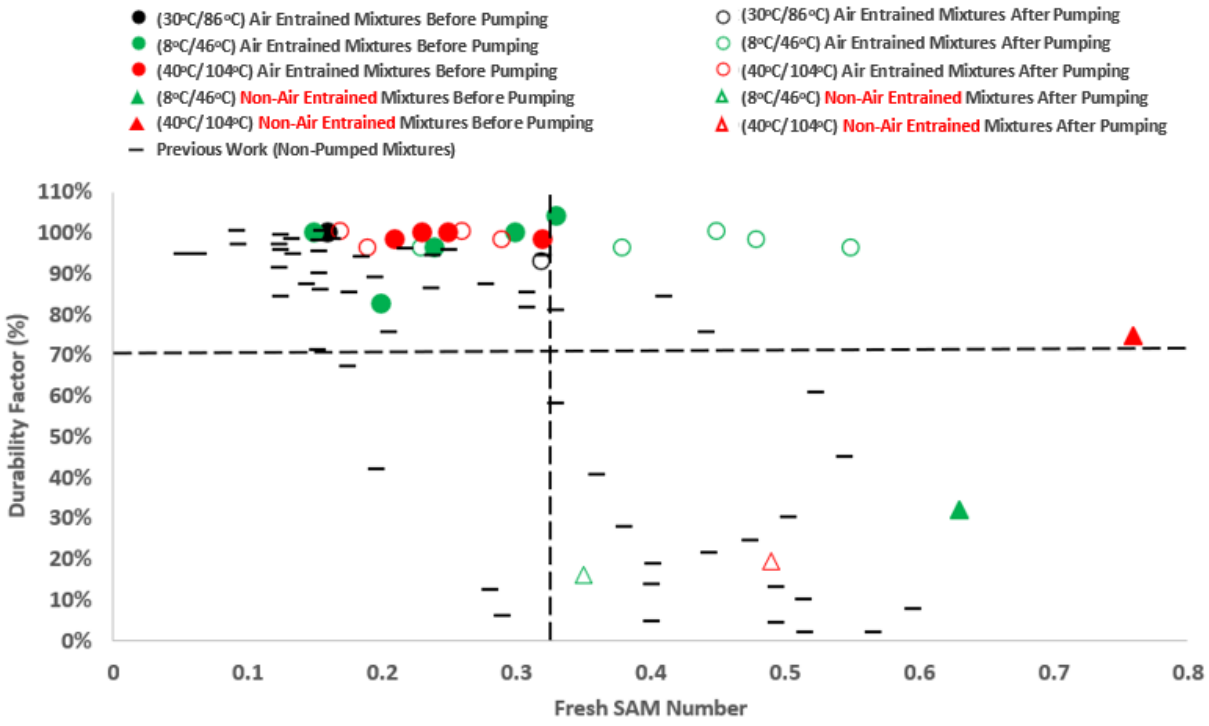

Fig. 12. Plot of Durability Factor vs. Fresh SAM Number for the Concrete Mixtures at Different Temperatures.

3.4. Hardened Air Void Analysis (HAV)

Fig. 13 illustrates the relationship between the spacing factor before and after 120 minutes of pumping for various concrete temperature mixtures. The graph includes a line of equality and lines indicating twice the reported coefficient of variation of the ASTM C 457 test method [34], illustrating the expected variation of the test method with a 95% confidence interval. Notably, all measurements fall within the anticipated variation of the test method, indicating that pumping did not significantly alter the spacing factor of the hardened concrete samples according to this test.

Despite observing a loss of fresh air volume and an increase in the fresh SAM Number in 11 out of 13 of the air-entrained mixtures after pumping, the measurements of the hardened air voids do not indicate a substantial change in the spacing factor after pumping. These findings align with previous studies on air entrained pumped concrete [5, 6].

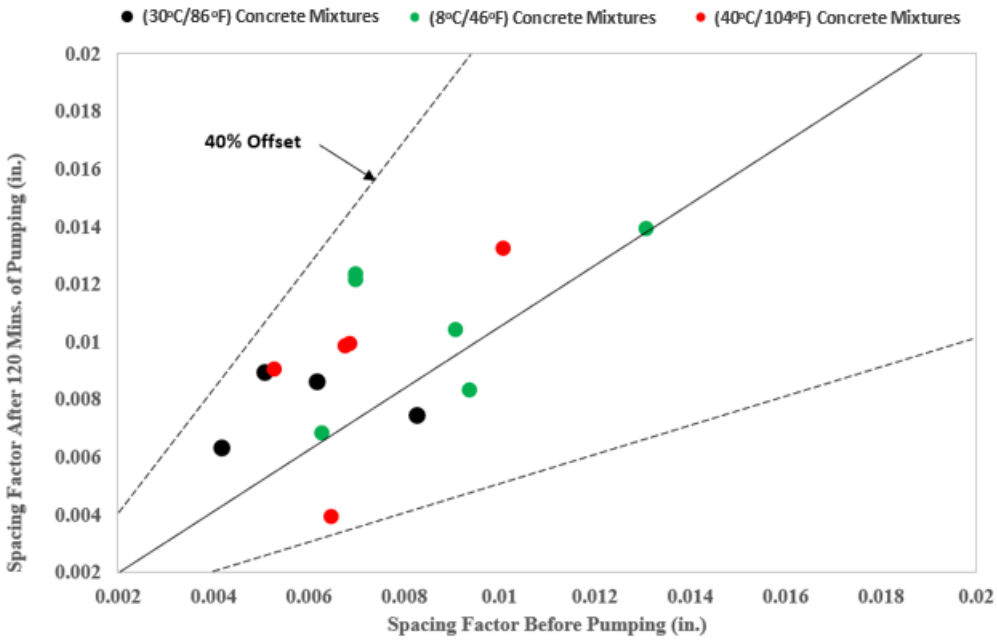

Fig. 13. Plot of Spacing Factor Before Pumping vs. Spacing Factor After 120 Mins. of Pumping.

3.5. Practical Significance

This work shows that when the concrete had an air content greater than 4% and a SAM Number less than 0.32 prior to pumping, then satisfactory freeze-thaw performance was found despite air contents or SAM Numbers outside of these limits being obtained after pumping. This recommendation is held for concretes with measured temperatures from (8°C/46°F) to (40°C/104°F). This suggests that concrete should not be rejected for measurements of air content or SAM Number measured after pumping as the air void system has been temporarily modified by pumping, and there has not been enough time for the air void system to recover. One solution is to only sample the concrete prior to pumping to use the conventional limits for the air content and SAM Number before pumping and to not test concrete after a concrete pump. Another solution is to wait for the air voids to return to the concrete; however, based on this work it may be 50 minutes for the air voids to return at room temperature. Also, this return time will depend on the temperature of the concrete as it took more than 120 minutes from the air voids to return to the (8°C/46°F) concrete mixtures.

4. conclusions

This work examines how different concrete temperatures impact the loss of air during pumping and the rate and efficiency of that air to return to the concrete. Pumping frequently caused changes in the air void system of the fresh concrete in this work. However, these changes did not affect the hardened air void parameters and freeze-thaw performance of concrete mixtures at temperatures between (8°C/46°F) and (40°C/104°F). Here are the key conclusions drawn:

- All mixtures tested at different temperatures showed a significant reduction in air content by at least 20% of the initial value that was present before pumping.

- Despite the hot mixtures (40°C/104°F) and room temperature (30°C/86°F) mixtures showing comparable air losses at 1.4% and 1.7%, respectively, the colder mixtures (8°C/46°F) experience a more significant air loss of 2.3%. When this is normalized, the hot and room temperature mixtures lose between 26% and 25% of the original air volume, while the cold mixture loses 40%. This finding implies that a cold mixture is anticipated to lose roughly twice as much air as its room temperature or hot counterpart.

- Out of the 13 air-entrained mixtures at three different temperatures, 11 exhibited an increase in the SAM Number immediately after pumping by at least 20% over the SAM Number before pumping. The other two had a SAM Number that increased but not to the same degree.

- All the air-entrained mixtures that showed an increase in the SAM Number also showed a decrease in the SAM Number over time to reach a point that is closer or lower than the initial number before pumping. This suggests that the fine air voids are returning to the concrete and that they are forming an air void system that is well dispersed with a similar spacing factor to the concrete that was added to the pump.

- Spacing factors measured before and after pumping across various temperatures exhibited changes within the variation of the test method, indicating that pumping did not significantly alter the spacing factor of hardened concrete samples.

- Mixtures with an air volume > 4% and SAM Number < 0.32 before pumping showed satisfactory performance in ASTM C666 testing, regardless of changes in fresh air content, SAM Number due to pumping, or concrete temperature.

- Cold mixtures (8°C/46°F) experienced an average air content change from 5.73% to 3.40%, resulting in a 41% air loss. This was about double the air loss air loss experienced for the room temperature (30°C/86°F) and hot concrete (40°C/104°F) mixtures. Additionally, for the cold concrete samples, the SAM Number did not return to its original value even 120 minutes after pumping. This phenomenon may be attributed to the slower rate of diffusion in low-temperature concrete mixtures [28-32]. The extended set time in lower temperatures would allow more time for the bubbles to return to the concrete as was shown by the spacing factor and satisfactory freeze thaw performance.

This work replicates previous measurements and reinforces findings that pumping causes a dissolution of smaller air bubbles from the increased pressures and these bubbles seem to return to the concrete before hardening. In summary, these findings indicate that the air volume and SAM Number measured immediately after pumping are not representative of the values in the hardened concrete. Therefore, these parameters should not be used to reject concrete for poor freeze-thaw durability after pumping. Instead, it is recommended to measure the air volume and SAM Number of the concrete before pumping for more accurate assessments.

References

[1] NRMCA Association, CIP21 - Loss of Air Content in Pumped Concrete. NRMCA, 2005.

[2] Jolin M, Chapdelaine F, Gagnon F, Beaupré D. Pumping concrete: a fundamental and practical approach. InShotcrete for underground support X 2006 (pp. 334-347).

[3] Ley MT, Welchel D, Peery J, Khatibmasjedi S, LeFlore J. Determining the air-void distribution in fresh concrete with the Sequential Air Method. Construction and Building Materials. 2017 Sep 30;150:723-37.

[4] Li F, Shen W, Yuan Q, Hu X, Li Z, Shi C. An overview on the effect of pumping on concrete properties. Cement and Concrete Composites. 2022 May 1;129:104501.

[5] Becker, J., Investigation of Concrete Pumping Effects on Air-Entrained Concrete. 2018, Oklahoma State University.

[6] Staffileno, C. J. Field Investigation of Pumping Air Entrained Concrete and Validation of the Sam Test on Lightweight Aggregate Concrete Mixtures. Oklahoma State University. 2020.

[7] Hall, H., Ley, M.T., Welchel, D., Peery, J., Leflore, J., Khatibmasjedi, M., Gudimettla, J.M. and Praul, M., 2020. Field and laboratory validation of the sequential air method. Materials and Structures, 53, pp.1-26.

[8] Jin S, Zhang J, Huang B. Fractal analysis of effect of air void on freeze–thaw resistance of concrete. Construction and Building Materials. 2013 Oct 1;47:126-30.

[9] Powers, T.C. and T. Willis. The air requirement of frost resistant concrete. in Highway Research Board Proceedings. 1950.

[10] Ley, M.T., The effects of fly ash on the ability to entrain and stabilize air in concrete, in Civil, Architectural, and Environmental Engineering. 2007, University of Texas at Austin

[11] Janssen DJ, MacDonald KA, Gardiner AJ. Effects of pumping parameters on the stability of entrained air voids. Concrete Under Severe Conditions, 2001. **2**: p. 1344-1351.

[12] AASHTO R101, Standard Practice for Developing Performance Engineered Concrete Pavement Mixtures.

[13] Elkey W, Janssen DJ, Hover KC. Concrete Pumping Effects on Entrained Air-Voids. Washington State Transortation Center. 1994.

[14] Janssen DJ, Dyer RM, Elkey WE. Effect of Pumping on Entrained Air Voids: role of pressure. in CONSEC 95 Concrete Under Severe Conditions. 1995.

[15] Jang KP, Kwon SH, Choi MS, Kim YJ, Park CK, Shah SP. Experimental observation on variation of rheological properties during concrete pumping. International Journal of Concrete Structures and Materials. 2018 Dec;12(1):1-5.

[16] Ksaibati K, Zeng M, Sellers FR, Dolan CW. Air change in hydraulic concrete due to pumping. Transportation research record. 2003;1834(1):85-92.

[17] Hall, H., Evaluation of the Concrete Mixture Efficiency within Construction Practices. 2018, Oklahoma State University.

[18] Yingling J, Mullings GM, Gaynor RD. Loss of Air Content in Pumped Concrete. Concrete International, October 1992. **14**(10): p. 57-61.

[19] Hover K.C., P.R.J. Impact of Concrete Placing Method on Air Content, Air-void System Parameters, and Freeze-Thaw Durability. Transportation Research Record, 1996. 1532: p. 1-8.

[20] Shen W, Shi C, Khayat K, Yuan Q, Ji Y, Zeng R, Li W, Zhang Z, Chen Z. Change in fresh properties of high-strength concrete due to pumping. Construction and Building Materials. 2021 Sep 20;300:124069.

[21] Vosahlik J, Riding KA, Feys D, Lindquist W, Keller L, Van Zetten S, Schulz B. Concrete pumping and its effect on the air void system. Materials and Structures. 2018 Aug;51:1-5.

[22] ASTM-C150/C150M, ASTM C150/C150M: Standard Specification for Portland Cement. 2011, ASTM International: West Conshohocken, PA. p. 9.

[23] ASTM-C33, Standard Specification for Concrete Aggregates, 2016, ASTM International: West Conshohocken, PA.

[24] ASTM-C260-10a, Standard Specification for Air-Entraining Admixtures for Concrete, 2010, ASTM International: West Conshohocken, PA.

[25] ASTM-C494, Standard Specification for Chemical Admixtures for Concrete, 2005, ASTM International: West Conshohocken, PA.

[26] Seader, N., The Pumpability of Optimized Graded Aggregates, in College of Civil and Environmental Engineering. 2016, Oklahoma State University.

[27] Tunstall LE, Ley MT, Scherer GW. Air entraining admixtures: Mechanisms, evaluations, and interactions. Cement and Concrete Research. 2021 Dec 1;150:106557.

[28] ME Cerro Prada, MJ Vázquez Gallo, JM Alonso Trigueros, AL Romera Zarza. Agent-based model for the effect of curing temperature on cement hydration. 2011.

[29] Kaleta-Jurowska A, Jurowski K. The Influence of Ambient Temperature on High Performance Concrete Properties. Materials (Basel). 2020. 18;13(20):4646. doi: 10.3390/ma13204646.

[30] Obaidat YT, Barham WS, Abdelrahman BN. Effect of elevated temperature on the bond behavior between near Surface Mounted-Carbon Fiber Reinforced Polymers strips and Recycled Aggregate concrete. Construction and Building Materials. 2020 Aug 10;251:118970.

[31] A. Farahani, H. Taghaddos, M. Shekarchi, Prediction of long-term chloride diffusion in silica fume concrete in a marine environment, Cement Concr. Compos. (59) 2015 10–17.

[32] D. Panesar, S. Chidiac, Effect of cold temperature on the chloride-binding capacity of cement, J. Cold Reg. Eng. 25 (4) 2011 133–144.

[33] ASTM C666/C666M-15, in Standard Test Method for Resistance of Concrete to Rapid Freezing and Thawing. 2015.

[34] ASTM International C457/C457M-16, in Standard Test Method for Microscopical Determination of Parameters of the Air-Void System in Hardened Concrete. 2016.